Dissertation

submitted to the

Combined Faculties of the Natural Sciences and Mathematics

of the Ruperto-Carola-University of Heidelberg. Germany

for the degree of

Doctor of Natural Sciences

Put forward by

Diana Elizabeth Kossakowska

born in Fremont, CA, USA

Oral examination: July 8, 2020

MODELING AND DETERMINING ORIGINS OF SIGNALS FOUND IN RADIAL VELOCITY DATA

Referees:

Prof. Dr. Thomas Henning

PD Dr. Sabine Reffert

Abstract

Thanks to the current *TESS* space mission, the number of exoplanets with both precise radius and mass measurements is continually growing, providing more promising candidates for the next era in the exoplanet field of atmosphere characterization. A key ingredient is to understand all the signals that appear in the data, to ensure that we obtain the correct planetary parameters. I was involved in developing the `juliet` package, which allows for easy model comparison between models of combined transit and radial velocity datasets. The methodology is based on modern statistical concepts, such as Bayesian statistics, Nested Sampling, and Gaussian Processes, which are presently gaining popularity among the community. Within the CARMENES consortium, I was heavily engaged in demonstrating how to construct the appropriate models and also how to interpret the results. Hence, for this thesis, I present a guideline on how to build an intuition using this code, covering the small nuances and common misconceptions.

I employed `juliet` on a variety of planets/systems: TOI-150 b, one of the most eccentric transiting hot Jupiters known to date whose obliquity can be measured; TOI-163 b, another hot Jupiter with an inflated radius ideal for future atmospheric characterization in the *JWST* continuous viewing zone; TOI-1201 b, currently one of the most optimal transiting mini-Neptunes for atmospheric characterization to aid in determining the origins of these planets; and AD Leo, a case study of a highly-active star that continues to puzzle how stellar activity influences radial velocity measurements as it often masquerades as a planet. These projects showcase the wide application of the code as well as the importance of implementing the correct methodology to contribute well-constrained planetary parameters. To end the thesis, I discuss the need for a better understanding of how stellar activity affects radial velocities to better mitigate the effects, and as well I urge the community to take a standardized approach for modeling in order to avoid misleading interpretations.

Zusammenfassung

Dank der aktuellen Weltraummission *TESS* wächst die Zahl der Exoplaneten mit präzisen Radius- und Massenmessungen kontinuierlich an und liefert viele weitere vielversprechende Kandidaten für die kommende Ära im Bereich der Atmosphärencharakterisierung von Exoplaneten. Ein wichtiger Bestandteil ist dabei ein tiefgehendes Verständnis aller Signale, die in den Daten auftauchen, um sicherzustellen, dass wir die richtigen Planetenparameter bestimmen. Ich war an der Entwicklung des `juliet`-Pakets beteiligt, das einen einfachen Vergleich zwischen verschiedenen Modellen für kombinierte Transit- und Radialgeschwindigkeitsdatensätze ermöglicht. Die Methodik basiert sich auf modernen statistischen Konzepten wie Bayessche Statistik, Nested Sampling und Gaußschen Prozessen, die alle derzeit in der Fachwelt an Popularität gewinnen. Innerhalb des CARMENES-Konsortiums war ich in diesem Zusammenhang maÃgeblich daran beteiligt anderen zu erklären, wie man die entsprechenden Modelle konstruiert und wie man die Ergebnisse interpretiert. Daher präsentiere ich in dieser Arbeit einen Leitfaden der helfen soll eine Intuition für den Code zu bekommen und der all die kleinen Feinheiten und häufigen Missverständnisse abdeckt.

Ich habe `juliet` für die Charakterisierung einer Vielzahl von Planetensystem eingesetzt: TOI-150 b, einer der exzentrischsten transitierenden heißen Jupiter, der bisher bekannt ist und dessen Achsneigung gemessen werden kann; TOI-163 b, ein weiterer heißer Jupiter auf

einer kreisförmigen Umlaufbahn und mit einem aufgeblähten Radius, der ideal ist für die zukünftige atmosphärische Charakterisierung in der CVZ von *JWST*; TOI-1201 b, derzeit einer der am besten zur atmosphärischen Charakterisierung geeignetsten transistierenden Mini-Neptune, der dabei helfen kann die Herkunft dieser Planeten weiter zu untersuchen; und AD Leo, eine umfangreiche Fallstudie eines hochaktiven Sterns, die sich mit dem Rätsel beschäftigt, wie stellare Aktivität in den Radialgeschwindigkeitsmessungen Signale planetarischen Ursprungs vortäuschen kann. Diese Projekte zeigen sowohl die breite Anwendung der Software als auch die Wichtigkeit eine korrekte Methodik zu implementieren, um präzise Planetenparameter zu erhalten. Zum Abschluss der Arbeit diskutiere ich die Notwendigkeit eines besseren Verständnisses darüber wie stellare Aktivität Radialgeschwindigkeiten beeinflusst, um so den Einfluss besser korrigieren zu können. Weiterhin fordere ich dazu auf, mehr Fokus auf einen standardisierten Ansatz für die Modellierung zu legen um so irreführende Interpretationen zu vermeiden.

Contents

List of Figures

List of Tables

1 Introduction

One in 200 stars has habitable Earth-like planets surrounding it - in the galaxy, half a billion stars have Earth-like planets going around them - that's huge, half a billion. So when we look at the night sky, it makes sense that someone is looking back at us.
Michio Kaku

We are just mere observers in the vast universe trying to bring all the puzzle pieces together to make some sense out of it all. The question of, "are we alone?" is perpetual and our infinite curiosity has led us to a truly extraordinary time. A time where the (now)-so-simple question of, "do planets exist out there orbiting other stars", has evolved into even more questions left unanswered: how common are these exoplanets, what are they made up of, what do their atmospheres look like, how do they form, how many reside in the habitable zone? The list goes on. What has once seemed so far fetched has become a reality.

Along our quest for an Earth 2.0, we have unraveled that planets outside our Solar System actually don't resemble what we already know in our own neighborhood. Among the impressive amount of 4 300 and counting exoplanets found to date[1], many of them are slightly bigger than Earth or slightly smaller than Neptune. Some are the size of Jupiter but are much closer to their star on super short orbits. Or sometimes the exoplanet has not one star but actually two. We are coming across a plethora of unique configurations, and yet, our quench to find an Earth analog is still left unsatisfied.

But how can we get there? In order to find our twin, we require high precision from the instrumentation, which they have continued to deliver. In fact, most of our discoveries are largely thanks to the great leaps of improvements in the instrumentation sector. An Earth-like planet orbiting a solar-like star would cause its host to slightly wobble on the order of $\sim 10\,\mathrm{cm\,s^{-1}}$, which to put into perspective, is slower than the speed of someone crawling. Our current state of the art spectrographs are breaking the sub $1\,\mathrm{m\,s^{-1}}$ precision limit, a truly accomplishing feat, allowing smaller planetary signals to shine through in the data.

As more interesting signals start to pop up, then do the signals due to the intrinsic nature of the star as well. At this point, the instrumental noise is no longer becoming the limiting factor, but rather other "unwanted" signals that we have yet to grasp more knowledge on. In a sea of spurious signals, we need to determine which ones are truly physically there induced by a planetary companion and which ones are not. Now *that* is the ongoing challenge.

Often detecting these exoplanets by indirect methods, we can only give our best efforts to

[1] 22 April 2020, NASA exoplanet archive; `https://exoplanetarchive.ipac.caltech.edu/`

describe the data at hand. And where one method lacks, another prevails. Thus, combining data from the various methods to perform simultaneously models can provide the most optimized planetary parameters.

Without a doubt, for all the planets we do detect, there are undoubtedly many more that we won't know of their existence. But that's the beauty of it. And that's our job to find them.

1.1 Discovering new exoplanet worlds

The number of worlds revealed outside our own Solar System is substantially increasing and will continue to do so in the upcoming years with the launches of new instruments (e.g., the ongoing *TESS* space mission). To date[2], a total of 4 375 exoplanets have been identified. These planets we discover are more often than not largely thanks to indirect detection methods, namely the transit and radial velocity methods being the most successful. While other methods have not yet yielded many planets, they have promising potential in the years to come. In the following sections, I introduce and describe the various detection methods, with a focus on the transit and radial velocity technique, and their advantages and shortcomings as well as their ideal planetary targets. More attention is put not onto *how* the methods work to detect planets, but rather on the advantages as well as observational biases and shortcomings.

1.2 Transit method

The transit method immediately comes to mind when one thinks of exoplanet exploration. This is mainly due to a combination of it being the easiest to grasp, the most fruitful by number, and the one with the least limitations when carrying out large scale surveys.

The star is constantly radiating its light in all directions, and if by some lucky chance (where the stars align), there is a planet that passes by its star in the view of the observer, it produces a dip in the stellar flux. These dips in the light curves are minute, usually in the vicinity of $1/10{,}000^{\text{th}}$ of the star's overall brightness and only last for a few minutes to a few hours. The simple approximation for the probability of a transiting planet is pretty slim given by, e.g., Borucki & Summers (1984),

$$p = \frac{R_* + R_p}{a} \approx \frac{R_*}{a} \approx 0.005 \left(\frac{R_*}{R_\odot}\right) \left(\frac{a}{1AU}\right)^{-1} \tag{1.1}$$

where R_* is the radius of the star, R_p is the radius of the planet, and a is the semi-major axis of the planet orbit. The probability to observe any planet orbiting its host at 1 AU is about 0.5%. If the planet follows an orbit with eccentricity e, then the probability increases by a factor of $\frac{1}{1-e^2}$ (e.g. Barnes, 2007; Burke, 2008).

On the offset chance that a planet is indeed transiting, it turns the planet into a real world. It suddenly has the opportunity to obtain the bulk density (e.g., using a mass determination from RV follow-up), the possibility for atmospheric characterization (e.g.,

[2] 22 April 2020, NASA exoplanet archive; `https://exoplanetarchive.ipac.caltech.edu/`

via transmission spectroscopy follow-up), and even check for the spin-orbit alignment (e.g., through simultaneous transit and RV observations), all outlined in Section 1.2.3. Essentially, these planets have the potential to be the best-characterized. Currently, *TESS* (introduced in Section 1.2.2) is carrying out its extended mission fulfilling its goal of identifying promising small transiting planets ($R_p < 4\,R_\oplus$) for these mentioned follow-up studies, already finding an impressive 2 200 alluring objects (Guerrero et al., 2021).

1.2.1 Parameters obtained

The periodicity and geometry of the transit from the light curve can already lead to quickly-obtained planetary parameters such as the planetary radius, semi-major axis, and inclination, as well as the stellar mass and stellar radius (Seager & Mallén-Ornelas, 2003; Deeg & Belmonte, 2018). Figure 1.1 illustrates an idealized transit light curve presenting the observables: the transit depth δ, the total transit duration $t_\mathrm{T} \equiv t_4 - t_1$, and the transit duration inside ingress and egress $t_\mathrm{F} \equiv t_3 - t_2$.

These parameters are initially mentioned below where some are later reintroduced in Sect. 3.3.3 to discuss how they are actually incorporated into the model, oftentimes parametrized. Listed below as an overview, the equations apply to a completely edge-on system (i.e., inclination i=90°), where the planet is in a full transit rather than a grazing one (i.e., impact parameter b=0, see Section 3.3.3 for a definition) and on a circular orbit (i.e., eccentricity e=0) around a star whose intensity profile is homogeneous (i.e., limb darkening coefficients are ignored). For more detailed derivations, the reader is referred to the works of, e.g., Seager & Mallén-Ornelas (2003); Winn (2010); Perryman (2018), and references therein.

To begin, the depth of the transit δ yields a quite accurate constraint on the planetary size,

$$\delta = \frac{\Delta F}{F} \approx \left(\frac{R_p}{R_*}\right)^2 \approx 0.01 \left(\frac{R_p}{R_J}\right)^2 \left(\frac{R_*}{R_\odot}\right)^{-2} \tag{1.2}$$

where R_p and R_* are the radius of the planet and star, respectively. Larger-sized planets (e.g., Jupiter-sized) compared to their stellar hosts have the upper hand as they are more sensitive to being detected. A dip in flux of only 1% would be caused by a Jupiter-sized planet around a solar-like star, dropping even lower to 0.01% for an Earth-sized planet (Winn, 2010). The sensitivity of current space-based instruments can reach 50 parts per million (ppm; e.g., on stars with *TESS* magnitude $9-15$), which is enough to detect an Earth-sized planet around a low-mass star, i.e., M dwarf, within 100 pc. For this reason, these types of surveys can be biased towards systems with higher planet-to-star radius ratios.

The transit duration t_T ($\equiv t_{IV} - t_I$, Figure 1.1), or the time it takes the planet to pass by the star, takes the form (e.g., Winn, 2010),

$$t_\mathrm{T} = \frac{P}{\pi}\frac{R_*}{a} \tag{1.3}$$

where a is the semi-major axis of the orbit and P is the orbital period. In more useful units, the equation transforms to, e.g., Perryman (2018),

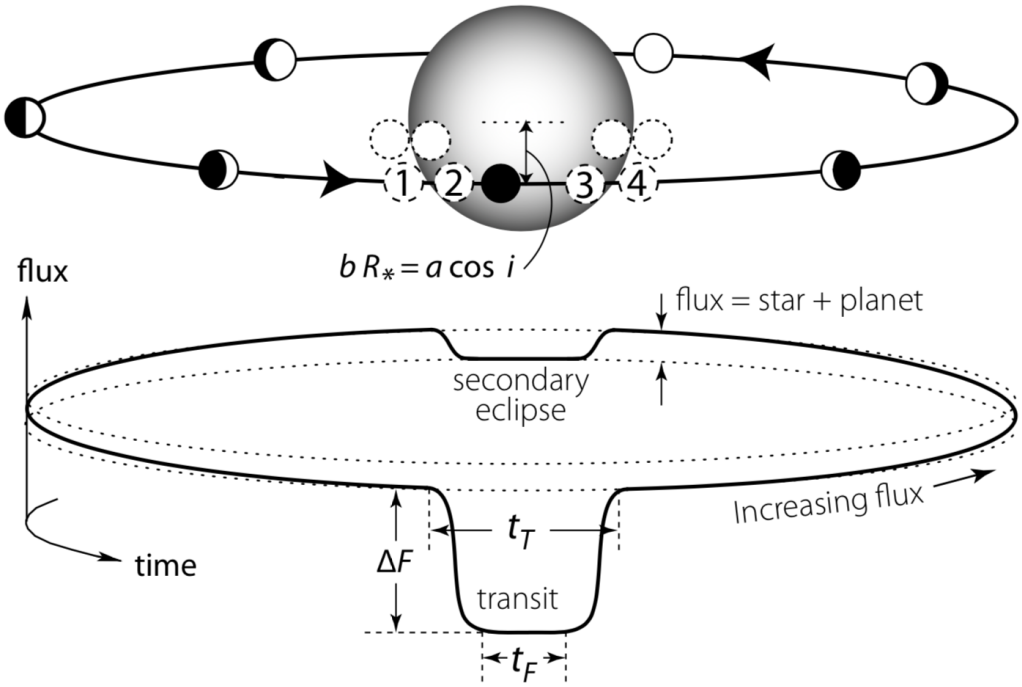

Figure 1.1: Schematic of an idealized transit light curve showcasing the observables being transit depth ($\delta \equiv \Delta F$), total transit duration ($t_{\mathrm{T}} \equiv t_4 - t_1$), and the time between ingress (t_2) and egress (t_3). During the secondary eclipse, only the stellar flux is observed; in between the flux dips, the contributing flux from the planet depends on its phase (see Section 1.2.3). After Perryman (2018, Figure 6.26).

$$t_{\mathrm{T}} \approx 13\,\mathrm{hr} \left(\frac{M_*}{M_\odot}\right)^{-1/2} \left(\frac{a}{1\,\mathrm{AU}}\right)^{1/2} \left(\frac{R_*}{R_\odot}\right) \tag{1.4}$$

where M_* and R_* are the stellar mass and radius, respectively. The duration is thus expected to be $\sim$25 h and 13 h for a Jupiter-sized planet and Earth-type planet around a solar-like star.

In addition, the semi-major axis of the orbit, a, can be acquired from observing the periodic flux dip in the light curve P, rearranging Kepler's third law,

$$a^3 = \frac{G(M_* + M_p)}{4\pi^2} P^2 \approx \frac{GM_*}{4\pi^2} P^2 \tag{1.5}$$

assuming that the mass of the planet is negligible to the mass of its host star, $M_p << M_*$. A very important by-product of obtaining transits is the ability to also constrain the stellar density (adopted from Sozzetti et al., 2007, found in this thesis as Equation 3.6). In the now current era of *Gaia*, the contrary actually holds true; highly-precise stellar parameters can return more information on the transit, and consequently on the planetary radius (Section

1.5.1).

1.2.2 The all-sky *TESS* survey

The *Transiting Exoplanet Survey Satellite*[3] (*TESS*; Ricker et al., 2015) is the first nearly all-sky space survey launched in April 2018 with the goal of discovering thousands of exoplanets around the brightest dwarf stars using the transit method. Covering roughly 75% of the sky in the close vicinity (< 200 light-years), the hope is to uncover a diverse range of planets from small, rocky worlds to giant planets that can serve as good target candidates for upcoming missions with a specific focus on atmosphere characterization using the future *James Webb Space Telescope* (*JWST*; Gardner et al., 2009). Thus far, a total of 2 645 have been detected by *TESS*, 122 of which have been confirmed via follow-up measures, e.g., mainly with spectroscopic observations.

Observing strategy

TESS was designed to observe 26 $24° \times 90°$ sections of the sky (or "sectors" — 13 in the Northern and 13 in the Southern hemisphere), for which each is roughly observed for one month (∼27 days) over the course of the primary two-year mission[4]. The two-year primary mission has already ended on July 4^{th} 2020 and has since been extended[5]. It was coordinated as such that the area in the sky where all sectors would overlap each other correspond to the *JWST* continuous viewing zone (CVZ; see Fig. 1.2). The photometric bandpass of *TESS* (600−1000 nm) is very similar to the G_{rp} band pass (630−1050 nm) for the *Gaia* survey Early Data Release 3 (EDR3; Gaia Collaboration et al., 2020), a fact that will prove to be useful when looking for possible contaminating sources in the *TESS* photometry. Additionally, the wavelength coverage extends much farther into the red wavelengths than previous photometric surveys (i.e., Howell et al., 2014), allowing for a larger sample of M dwarfs to be studied (Figure 1.2).

In the primary mission, all stars in the *TESS* Input Catalog (TIC, Stassun et al., 2018) were observed at ∼30 min cadence as Full Frame Images (FFIs), whereas around 200 000 of the brightest, most promising targets for follow-up measures were observed every ∼2 min as postage stamps. For the extended mission, the cadence for the FFIs increased to ∼10 min and a new mode adding ∼20 s cadence observations for the postage stamps was introduced. Calibrated FFIs are conveniently available for quick download via the Mikulski Archive for Space Telescopes[6] where the entire TIC is uploaded and where the archival light curve data (simple aperture photometry; `SAPFLUX`) produced by the Science Processing Operations Center pipeline reside (Jenkins et al., 2016). For publications, the systematics-corrected photometry following an adaption of the Kepler Presearch Data Conditioning algorithm (`PDCSAP` flux) is used, where possible flux contamination is also taken into account (Smith et al., 2012; Stumpe et al., 2012, 2014).

When a planet is detected, it becomes alerted as a *TESS* Target Of Interest (TOI) and

[3] `https://tess.mit.edu/`
[4] `https://tess.mit.edu/observations/`
[5] `https://heasarc.gsfc.nasa.gov/docs/tess/the-tess-extended-mission.html`
[6] `https://archive.stsci.edu/tess/`; `https://mast.stsci.edu/tesscut/`

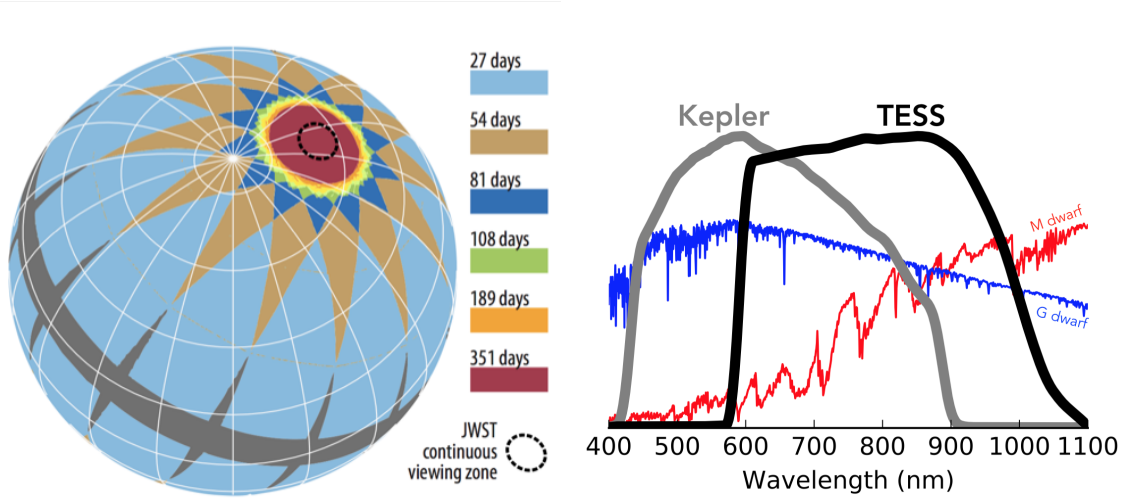

Figure 1.2: *Left.* Sky coverage map of the *TESS* overlapping observing sectors on the celestial sphere. The dashed black ring represents the *JWST* continuous viewing zone. Image credit: NASA *Right.* Bandpass image Credit: Zach Berta-Thompson with data from Sullivan et al. (2015).

gets publicized in the TOI catalog[7], where it can then be open to the community to set follow-up observations in full swing to confirm the origins of the signal.

1.2.3 Follow-up efforts

Unfortunately, transits suffer from a considerably high rate of false positives, even as high as 40% in some single-planet systems (Fressin et al., 2013), coming from sources such as eclipsing binaries or blending targets (e.g., Santerne et al., 2012; Désert et al., 2015). Especially for an instrument like *TESS* with a large 21 arcsec pixel size, ground-based follow-up photometry is absolutely imperative to confirm potential detections. Once a transiting planet is however vetted, then the world is its oyster.

Since the launch of the mission, ∼2 200 exoplanet candidates have been identified as TOIs (Guerrero et al., 2021). Listed below are some of the follow-up possibilities that can transform the planet into a key in unlocking some of the prevalent mysteries.

Mass determination Upon obtaining spectroscopic measurements, a mass estimate can promptly decipher whether the transiting object is due to a planetary companion or to a larger-mass companion, e.g., brown dwarf or stellar companion. If the former, the planet is there, we just need the mass. The true mass, rather than just the minimum mass, can then be resolved using the radial velocity method, since the transit constrains the inclination of the orbit (see Equation 1.9, Figure 1.4). The narrow constraints for the period and transit time of a transiting planet (see Section 3.3.5) also simplify the observational strategy for accordingly sampling the phase. An adequate amount of RV measurements are thus needed to provide a decent mass estimate. Additional measurements are even beneficial to constrain the eccentricity of the orbit (e.g., as for TOI-150 b in Section 4.7.2).

[7] `https://tev.mit.edu/data/collection/193/`

Atmosphere characterization A mass and radius measurement alone are unfortunately not sufficient in determining the true bulk composition. Characterizing a planet to have a rocky-core with either a gaseous atmosphere versus no atmosphere (see Section 1.5.3), relies on determining the ratio of rock, water, and hydrogen within its interior structure done via transmission spectroscopy (e.g., Rogers & Seager, 2010).

Hence, the objective is to look for suitable transiting targets for transmission spectroscopy (Batalha et al., 2019, with mass measurements with 20 % uncertainty as the the recommended precision;), where the light from the star passes through the atmosphere of the planet during a transit. In theory any planet can be characterized with transmission spectroscopy, but if there is no existing atmosphere the spectrum will be flat. For planets whose atmosphere is hot enough to emit enough detectable blackbody radiation ($\propto T^4$), then emission spectroscopy is possible. because this then gives us more insight on the planet's composition and in turn, planet formation (Kreidberg, 2018).

Spin-orbit alignment As a transiting planet passes by its host star, it also distorts the stellar spectra in a manner that can be measured via the Rossiter-McLaughlin (RM) effect (Rossiter, 1924; McLaughlin, 1924). Thanks to this effect, the alignment of the the planetary orbit with respect to the spin axis of its stellar host can be determined. This information could hint at different mechanisms responsible for planet formation. Particularly, this is especially beneficial in understanding the emergence of close-orbiting giant planets, e.g., hot Jupiters as defined in Section 1.5.2, where planets around hotter host stars are observed to have various obliquities in comparison to those around cooler stars, which are typically aligned (Gaudi & Winn, 2007; Muñoz & Perets, 2018).

Transit timing variations (TTVs) In multi-planetary systems, the planet-planet gravitational interactions can manifest themselves in the photometry as transit timing variations (TTVs), which describe the deviations of an expected transit time of a sole Keplerian orbit (Agol et al., 2005; Holman & Murray, 2005). Typically these variations accumulate on the order to a few minutes over the course of a year. From the light curve alone, and with the additional help of follow-up transit photometry in order to cover a large-enough time baseline, the full orbital state of a system could be resolved, explicitly providing the mass, period, and an eccentricity estimate for the additional planet (e.g., Hadden & Lithwick, 2017; Jontof-Hutter et al., 2016). Extremely advantageous, considering lower-mass planets with wider orbits could be detected with a higher-mass transiting planet, where this would not be as feasible with spectroscopic data.

Secondary eclipses When the transiting planet is passing behind the star, we denote this as the secondary eclipse, which can help probe further into the planet's structural and atmospheric properties (Perryman, 2018). The flux observed at this time is solely comprising that from the star itself, whereas just right before and right after, the total light is the sum of the star and of the planet (Figure 1.1). Thus, comparing the flux ratio between these two instances can probe into the flux of the planet's day-side region. With multi-wavelength secondary eclipse measurements, the low-resolution of the spectrum of the day-side emission can be constructed (Alonso, 2018), as when

doing so for transmission spectroscopy. The timing of the secondary eclipse can also aid in constraining the eccentricity of the orbit.

Phase curves Over the course of its journey around the host star, the fraction of day-side versus night-side contributions of the planet fluctuates, producing observational changes in the flux, i.e., even during the time in between the transit and secondary eclipse (Figure 1.1). While transmission spectroscopy can specify various elements found in the atmosphere, phase curves are the best in examining the 3-D structure of the exoplanet's atmosphere (Parmentier & Crossfield, 2018), hinting at the presence of clouds or hazes, as well as potentially even the heat transport and winds on the surface of the planet (e.g., HD 189733 b, Knutson et al., 2009).

1.3 Radial velocity method

For the radial velocity (RV) technique, the planet is not required to pass in front of its host star, as its presence is enough to impose a gravitational tug causing the star to move back and forth with respect to the observer. This method is based on the Doppler effect, hence why it is also known as Doppler spectroscopy, in which the stellar spectral lines are displaced in the presence of a companion, e.g., planetary. In the absence of a planet, the star is purely rotating on its axis around its own center of gravity producing a net zero signal. With the addition of a planet, both the star and the planet then orbit the common center of mass (Figure 1.3). This slight displacement causes the star to create a "wobbling" effect, moving away or towards us, such that some of its light in the spectra are either blue- or red-shifted along the line-of-sight to the observer given by,

$$\lambda = \lambda_0 \frac{1 + \frac{v_r}{c}}{\sqrt{1 - \frac{v_r^2}{c^2}}} \tag{1.6}$$

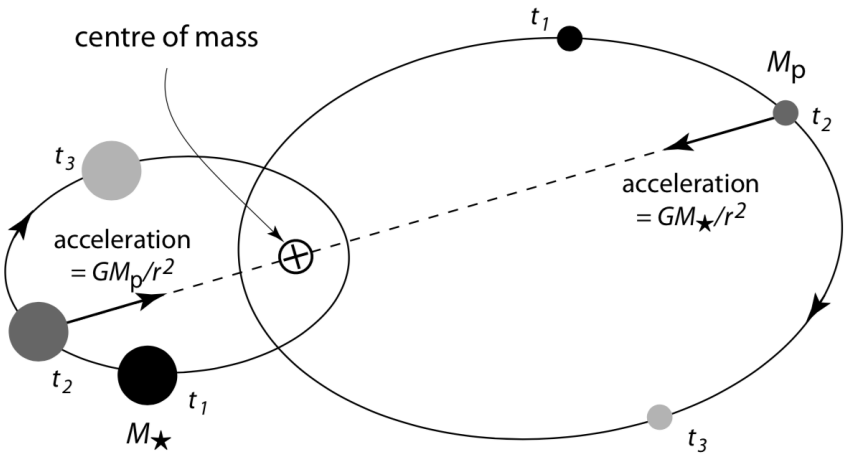

Figure 1.3: Schematic of the radial velocity method, showcasing the stellar and planetary body gravitational influence on each other. After (Perryman, 2018, Figure 2.3)

.

where λ is the wavelength of the photon measured by the observer, λ_0 is the wavelength at which the photon was emitted, v_r is the radial velocity that we measure, and c is the speed of light. Generally speaking, the obtained spectra contain various absorption and emission lines that are compared to a template spectrum in order to compute the relative shift (various approaches described in Sect. 1.3.1). We are not interested in the absolute RVs of the star but rather the relative changes over time, as it is within these tiny relative differences, on the order of a 10s of $\mathrm{cm\,s^{-1}}$ to 100s of $\mathrm{m\,s^{-1}}$, that the planetary contribution emerges.

1.3.1 Extremely precise RVs

Imagine a baby crawling...
Now imagine a baby crawling, but that baby is 100 000 000 000 000 kilometers away...

The RV community constantly talks about breaking the $1\,\mathrm{m\,s^{-1}}$ barrier. To put this figure into perspective, the most massive planet in our Solar System, Jupiter, would induce a RV signal with semi-amplitude $K = 12.5\,\mathrm{m\,s^{-1}}$, whereas the Earth only $0.09\,\mathrm{m\,s^{-1}}$ (following Equation 1.8). Thus, in order to spot an Earth-like planet, instrument-related errors, e.g., effects of mechanical and thermal stability or wavelength calibration, need to be brought to a minimum (Fischer et al., 2016). Current state-of-the-art spectrographs are breaking the frontier and reaching sub $1\,\mathrm{m\,s^{-1}}$ precision (e.g., instrumental error budget is roughly $\sim 10\,\mathrm{cm\,s^{-1}}$ with ESPRESSO; Pepe et al., 2010).

Historically speaking, the advancements have already made huge leaps of accomplishments from $\sim 1\,000\,\mathrm{m\,s^{-1}}$ around 1950 to $\sim 100\,\mathrm{m\,s^{-1}}$ in 1970 and then down to a few $\mathrm{m\,s^{-1}}$ in the 1990s (Nobel Prize, 2019). To get below $1\,\mathrm{m\,s^{-1}}$ corresponds to a Doppler shift of 10^{-5} Å in wavelength space which is just a mere $1/1\,000^{\mathrm{th}}$ of a CCD pixel (R=100 000), or just a fraction of a nanometer in physical space (assuming the typical CCD pixel size of 15 μm). Very minute effects like the variation in the index of refraction of air when the light is coming into the spectrograph, or thermal and mechanical fluctuations on the order of 0.01K can already shift the RVs by $1\,\mathrm{m\,s^{-1}}$.

RV extraction The RVs are normally extracted from the stellar spectra following a cross-correlation function (CCF) technique (Hill, 1993; Queloz, 1995), which functions quite well and is sufficient in computing high-precision RVs for G and K dwarfs. Essentially, the CCF uses a stellar binary mask as a template that is correlated with the stellar spectra to derive the RVs. However, this methodology lacks in performance for M dwarfs given that the spectra contain a forest of lines making it almost impossible to find the continuum (e.g., Merrill et al., 1962; Alonso-Floriano et al., 2015). Instead of using a binary mask as the stellar template, Anglada-Escudé & Butler (2012) proposed a different methodology of creating individual stellar templates by co-adding the same spectra that were used to compute the star's relative RVs. The RV precision for M dwarfs had then substantially improved and this approach was adopted as the standard practice for the CARMENES RV extraction pipeline, named SpEctrum Radial Velocity AnaLyser (`serval`[8]; Zechmeister et al., 2018).

[8] `https://github.com/mzechmeister/serval`

1.3.2 Parameters obtained

RVs provide the minimum mass $M_p \sin i$ of the planet (see Section 1.3.3 as to why), the period P, and can constrain the eccentricity e of its orbit. Once enough observations are taken over time, an induced sinusoidal-like signal appears in the RV data. The signal is modeled by Kepler's equations to describe the orbital motion of the planet around its star.

Behind the scenes, solving these equations requires solving the systems of equations relating the mean anomaly, eccentric anomaly, and the true anomaly ν (see the works of Wright & Howard, 2009; Fulton et al., 2018, and references therein), in order to obtain the Keplerian model $v_{\rm Kep}$ to fit against the data,

$$v_{\rm Kep} = K[\cos(\nu + \omega) + e\cos(\omega)] \tag{1.7}$$

where e and ω are the orbital eccentricity and argument of periastron of the star's orbit, respectively, and K is the RV semi-amplitude given below by Equation 1.8. Linear trends and instrumental offsets can also be included in the full RV model.

The semi-amplitude K of the periodic RV signal can be derived from Kepler's law (Equation 1.5) and can be rewritten as, e.g., Torres et al. (2008),

$$K = \frac{28.433 \text{ m s}^{-1}}{\sqrt{1-e^2}} \frac{M_p \sin i}{M_J} \left(\frac{M_p + M_*}{M_\oplus}\right)^{-1/2} \left(\frac{P}{\text{yr}}\right)^{-1/3} \tag{1.8a}$$

which with the assumption that $M_p << M_*$, can be simplified to,

$$K = \frac{28.433 \text{ m s}^{-1}}{\sqrt{1-e^2}} \frac{M_p \sin i}{M_J} \left(\frac{M_*}{M_\oplus}\right)^{-1/2} \left(\frac{P}{\text{yr}}\right)^{-1/3} \tag{1.8b}$$

Rearranging the equation in terms of the observables P and K, we get a relation for the minimum planetary mass,

$$\frac{M_p \sin i}{M_J} = 4.919 \times 10^{-3} \left(\frac{M_*}{M_\odot}\right)^{2/3} \left(\frac{K}{\text{m s}^{-1}}\right) \sqrt{1-e^2} \left(\frac{P}{\text{days}}\right)^{1/3} \tag{1.9}$$

1.3.3 RV complications

"*In life you either have time or you have money*"
In the RV world, you don't have enough time, and you don't have enough money, mostly problems...

Even after all the tedious efforts put into the instrumental operation to obtain a reliable RV measurement, the fight for planet hunting continues. Some notable complications that come with RV data are listed below. The ongoing leading challenge is the perplexing presence of stellar activity in the RVs, to which Section 1.3.4 is dedicated to.

Selection bias A huge drawback is the lack of ability to blindly survey hundreds or thousands of stars simultaneously with a single telescope. Therefore, the resources of obtaining even just one observation, i.e., spectrum, can be rather expensive. For this reason, it is oftentimes the case that RV dedicated surveys vet their projected target list to ensure a high probability of a success-driven survey (e.g., Bonfils et al., 2013). This can be problematic as it introduces a selection bias, considering the types of target stars are chosen rather than being picked at random (Teske et al., 2020). Likewise, the programs are not driven for completeness so sampling each star equally is not always possible. Especially so if the target seems to be "uninteresting", where observations are then halted.

Discontinuous sampling But even with a perfect observing strategy, nights can turn out to have bad weather, or perhaps the star is not observable, or the moon is illuminating in the sky impairing a clear and dark measurement. Such occurrences can also be reasons for unequal sampling. This discrete sampling of data can greatly affect the interpretation of the signals, i.e., two circular planets could appear as one eccentric one (e.g., Kürster et al., 2015; Trifonov et al., 2017), the aliasing between two signals makes it difficult to determine which one is the true signal (Stock et al., 2020a, discussed in Section 3.2.2), or the modeling of stellar activity becomes even more problematic (e.g., Damasso et al., 2019).

Degeneracy between mass and inclination Edge-on ($i = 90°$) systems are the most favorable since the gravitational pull of the planet can impose a greater semi-amplitude making it more accessible to detect. However, because of the mass and the inclination degeneracy, the method can greatly underestimate the planetary mass. A more massive planet not on the line-of-sight can impose the same semi-amplitude signal as a less massive planet on the line-of-sight (see Figure 1.4). However, mathematically speaking, when taking into consideration randomly orientated orbits, one finds that the probability to be uniform over $\cos i$ (Kürster et al., 2015). Therefore, it can be self-reassured that any planet exerting an RV amplitude is most likely not in a face-on configuration with respect to the observer, but rather the mass is within a factor of two or smaller.

Certainly the precise mass can be determined if the planet happens to also be transiting from which the orbital inclination is then known. If a planet transits, we can obtain RVs for a mass determination, but the other way around does not always apply, i.e., if a planet has RV measurements, it does not necessarily mean it will also transit (Equation 1.1).

1.3.4 RV variability due to stellar activity

A signal is assumed planetary until proven to be due to stellar activity
— the stellar activity equivalent to "innocent until proven guilty"

Stars are active entities with an array of classifications for intrinsic activity behavior that occur on different timescales and impose a varying degree of RV amplitudes; namely those are, oscillations (e.g., Aerts et al., 2010; Kjeldsen et al., 2005), granulations (e.g., Cegla, 2019; Dumusque et al., 2011b), magnetic cycles (e.g., Milbourne et al., 2019), active regions, and flares. Fortunately, most can be alleviated to a sub 1 $\mathrm{m\,s^{-1}}$ level through smart observing strategies such as longer exposure times or multiple exposures throughout an observing night

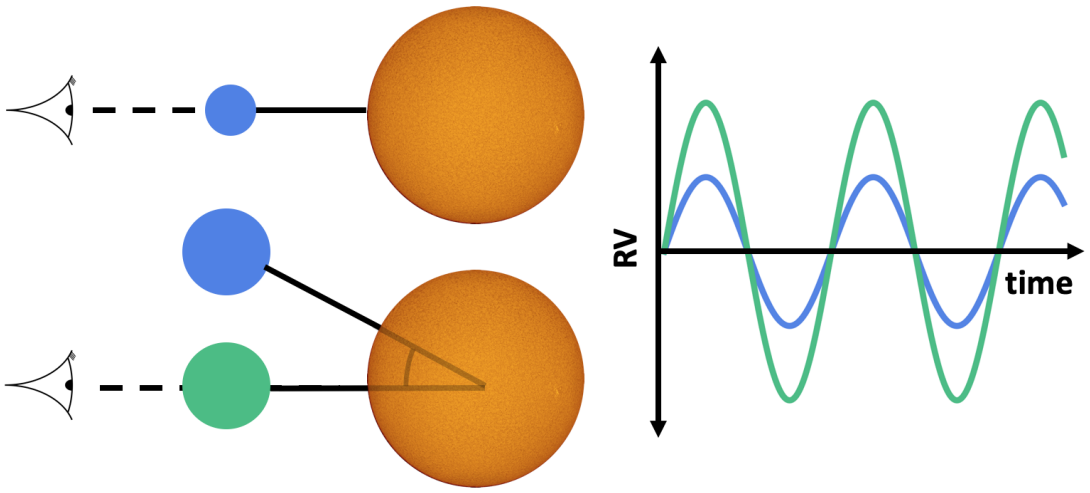

Figure 1.4: Schematic demonstrating the degeneracy of planetary mass and inclination for the RV method. A more massive planet not on the line-of-sight imposes the same RV amplitude as a less massive planet on the line-of-sight (marked as blue planets). The same massive planet on the line-of-sight would then impose a greater RV amplitude (green). Solar surface image credit: David Hajnal using the Lunt LS50THa 50 mmPressure Tuned H-alpha Telescope, 7 April 2019.

(e.g., Udry & Mayor, 2008). Others can be quite burdensome to mitigate but manageable. The current limiting challenge is, however, the RV modulations due to persistent and also fleeing active regions, made up of stellar spots that are darker compared to the photosphere, or plages, which are a little bit brighter (e.g., Queloz et al., 2001b; Lagrange et al., 2010; Haywood et al., 2014). For a complete overview of RV perturbations due to stellar physical phenomena see Dumusque et al. (2011a).

The simple fact is that these stellar spots can masquerade as planets in the RV data. When observing a star, we can split up the projection of the surface into two halves where one is constantly being blue-shifted towards the observer, and the other red-shifted away from the observer as the star rotates on its own axis (Figure 1.5). The amount of the blue-shifted region should be equal to the red-shifted region which in turn cancels out and results in a net change in RV. However, a dark spot co-rotating on the star will sometimes be blocking the blue light resulting in a red-light surplus, and vice versa. Thus, this produces a Keplerian-like RV amplitude that is periodic and spurious, oftentimes making an appearance at the stellar rotation period $P_{\rm rot}$ or its first harmonic $P_{\rm rot}/2$. However, in some cases it is possible that the stellar spot coverage is homogeneous, such that there is a net signal, yet the star is still active and covered with a myriad of spots.

A true planetary signal should be time- and wavelength-independent

The fundamental idea is that if there is a suspected signal, one should immediately check if the amplitude is consistent over time and constant over wavelength. That being said, these stars can be quite deceiving even with plenty of observations and long time-baselines. The instance of the α Tau system (Hatzes et al., 2015; Reichert et al., 2019) exhibits how the RV amplitude had decreased and the phase was shifted, even after 30 years of a plausible

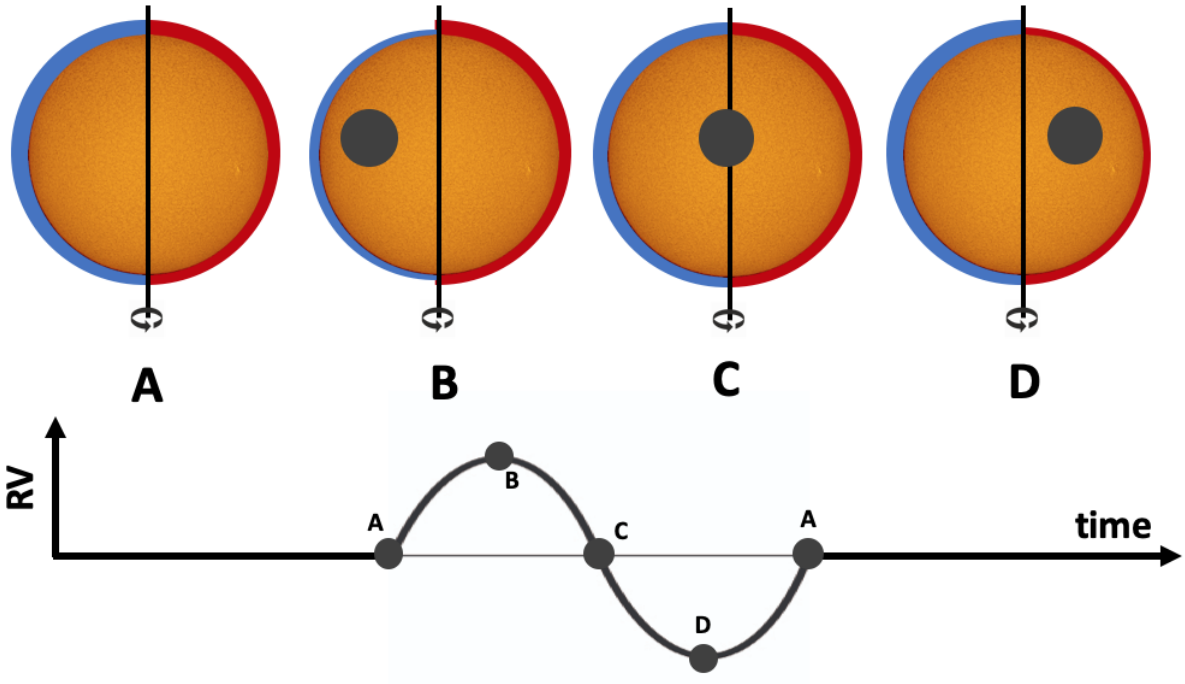

Figure 1.5: Schematic of a cool spot co-rotating on the stellar surface. There is a net zero difference in the RVs when the spot is not visible (point A) and when the spot is blocking both the blue-shifted and red-shifted light (point C). The RVs are positive and negative when the spot is blocking only the blue-shifted area (point B) or the red-shifted area (point D), respectively. Solar surface image credit: David Hajnal using the Lunt LS50THa 50 mm Pressure Tuned H-alpha Telescope, 7 April 2019.

planetary signal. The prospect of a planetaery companion was therefore disproven. In Chapter 6 of this thesis, AD Leo demonstrates the wavelength dependence of a stellar activity signal using CARMENES data as well as amplitude fluctuations over time (Figure 6.6), even though the periodicity is still persistent over the course of 19 years. The hypothesis of a planetary companion (proposed by Tuomi et al., 2018) was also, therefore, refuted.

Stellar activity indicators

Certain spectral lines can be correlated with signals found in the RVs, acting as good indicators for stellar activity behavior. Particularly, the Hα line and the Ca II IRT triplet lines have been associated with dominating signals in long-term RV data due to magnetic cycles (e.g., Kürster et al., 2003; Hatzes, 2016). Furthermore, Schöfer et al. (2019) showed that the photospheric TiO λ7050Å line was the best in recovering the correct stellar rotation period in 10% of the time, followed by the chromospheric Hα and Ca II IRT b lines, for the CARMENES M-dwarf sample.

Aside from checking the already known spectral lines as those mentioned above, new efforts have been put in motion to focus on spectral lines in general that appear to be more activity-sensitive than others (e.g. Cretignier et al., 2020; Wise et al., 2018; Dumusque, 2018). This approach is still in its early stages but seems promising for G- and K-type stars, and has been tested out on the M-dwarf AD Leo in Section 6.5.7.

Besides imposing RV modulations, as shown in Figure 1.5, co-rotating spots can also distort the shape of the absorption lines in the spectrum. True planetary signals should preserve the shape of the absorption line and not introduce any asymmetries, whereas stellar activity can impose some skewness to the lines (e.g., Queloz et al., 2001b). When employing the CCF technique, as in Section 1.3.1, the full-width half-maximum (FWHM) of the line as well as the bisector velocity span (BVS), are outputs where both act as metrics measuring how morphed the line is.

The chromatic index (CRX; Tal-Or et al., 2018) is a metric for measuring achromaticity, i.e., wavelength dependence, and has been successful for spotting stellar activity (e.g., YZ CMi, Zechmeister et al., 2018). The RV amplitude due to a star-spot temperature difference should decrease as a function of wavelength, especially into the infrared (Reiners et al., 2010); hence, this was one of the incentives for constructing the NIR-arm of the CARMENES instrument (introduced in Section 1.3.5).

Modeling Approach

How can we tackle such signals among the planetary ones? We are not able to find physical models to express these signals, yet we need to find ways of correctly modeling the stellar activity simultaneously to obtain better, more precise planetary parameters and to uncover hidden planets. Otherwise, the dependence of how the model is chosen can lead to different interpretations of a system, e.g., GJ 667 C hosting between three and seven planets (Feroz & Hobson, 2014; Anglada-Escudé et al., 2013; Anglada-Escudé & Tuomi, 2012; Gregory, 2012).

An RV fitting challenge with realistically generated RV datasets was led by Dumusque (2016) to gain a better grasp on the extent that these activity signals suppress real planetary signals, what complications are present, e.g., what is the limit of a planet's signal in the noise, and what modeling techniques reign supreme. The findings published in Dumusque et al. (2017) suggested that the most efficient methods to recover planetary signals were those using a red-noise model within a Bayesian framework, i.e., GP regression (Rajpaul et al., 2015, Section 2.4 in this thesis), moving average technique, apodized Keplerian. Such approaches were able to correctly claim planets down to a $K/N = K_{\rm pl}/{\rm RV}_{\rm rms} \times \sqrt{N_{\rm obs}} = 5$.

Yet, the problem still persists of not really understanding as to *why* these signals should be modeled as such, but more so these approaches work well enough to "model out" stellar activity behavior for our purposes. However, the stability in stellar activity over long periods of time (as in e.g., Hatzes et al., 2015; Davenport et al., 2020; Günther et al., 2020) suggests that perhaps a GP-only model would not completely correctly fit for the modulations, as presented quantitatively in the case of AD Leo in Chapter 6, where the best model to explain the persistent stellar activity signal comprised a stable component alongside a GP.

To really gain a clear understanding, however, of how stellar spots affect the RVs, tools such as SOAP 2.0 (Dumusque et al., 2014) or StarSim 2.0 (Herrero et al., 2016) can decently forward model the predicted RV modulation (and photometric variation) with an input of a spot configuration on the stellar surface, e.g., spot size, contrast, location on the stellar sphere. In doing so, different models can be applied to the generated simulations to identify the best model approach for a stellar activity signal (Stock, 2021). Particularly, comparing the best models, by efficiently calculating the Bayesian log-evidence via the Nested sampling algorithm (Chapter 2), for simulated Keplerians and GPs datasets would be beneficial in overcoming this hurdle, as discussed as a future idea in Chapter 7.

Nonetheless, techniques are evolving and continually improving with time.

1.3.5 The CARMENES survey

CARMENES[9] (**C**alar **A**lto high-**R**esolution search for **M** dwarfs with **E**xoearths with **N**ear-infrared and optical **É**chelle **S**pectrographs) is not only a spectrograph and survey, but also a consortium made up of 11 institutes from Germany and Spain working together. With the aim of finding temperate Earth-like planets, the survey is focused on collecting spectra for ∼350 nearby M dwarfs and began in January 2016 (Reiners et al., 2018) and is currently in legacy mode due to its great success. The survey has been extremely valuable in probing the area of planets orbiting M dwarfs (and even finding relatively high-mass planets around them) and shedding light on planet occurrence rates around these stars, serving as a vital player in the RV field.

The consortium provides a consistent set of stellar parameters provided by carmencita (Caballero et al., 2016a), the M-dwarf input catalog for CARMENES, for all publications. On the grounds that the stellar parameters are compatibly derived, the CARMENES discoveries are homogeneous to some extent (see Section 1.5.1 for the importance). Highlights of this survey include discoveries such as the highly eccentric and massive ($>0.46\,M_{\rm J}$) GJ 3512 b (Morales et al., 2019), two very Earth-like planets around Teegarden's star (Zechmeister et al., 2019), or the cool super-Earth around Barnard's star, our closest single star (Ribas et al., 2018), just to name a few. However, later in Section 1.4, I turn the attention more so to the impact of the CARMENES team in the realm of the *TESS* era in providing mass determinations, to emphasize both CARMENE's and my contribution in characterizing planets suitable for future studies.

The instrument

The instrument itself is located at the 3.5 m telescope at the Calar Alto Observatory in Spain. A unique attribute of CARMENES is that it is comprises of two high-resolution cross-dispersed channels: the visual (VIS) which covers the spectral range 520-960 nm (spectral resolution of $R = 94\,600$) and the near-infrared (NIR) which covers the 960-1710 nm range ($R = 80\,400$) (Quirrenbach et al., 2014, 2018). Simultaneously covering such a wide wavelength range has its advantage in aiding to mitigate for stellar activity, as discussed in Section 1.3.4. In order to fulfill the aim to search for small planets, the instrument was built for Doppler measurements with long-term stable precision on the order of a few $\mathrm{m\,s^{-1}}$ (Quirrenbach et al., 2010).

Achieving such high precision is not an easy task. As mentioned in Section 1.3.1, one pixel equates to approximately $1\,000\,\mathrm{m\,s^{-1}}$. To attain this, the temperature of each channel is kept constant to ±0.01K over 24 hours, where the VIS channel is kept at room temperature and the NIR at 140K (Quirrenbach et al., 2014). Additionally, like most spectrographs, real-time wavelength calibration is an essential aspect to account for instrumental drifts and background noise. To do so, there are two optical fibers feeding into the spectrograph: one for the target itself and one for the calibration light. For the wide wavelength range of the

[9] `http://carmenes.caha.es`

CARMENES instrument, the thorium-neon (Th-Ne), uranium-neon (U-Ne), and uranium-argon (U-Ar) lamps are used for the calibration (Quirrenbach et al., 2010, 2014). As for the wavelength solution, this is obtained by a Fabry-Pérot interferometer (Bauer et al., 2015).

Data output

Once the observations are taken, the standard first step of performing dark and bias corrections are performed by the standard reduction pipeline `caracal`, then through the guaranteed observation time data flow (Caballero et al., 2016b).

Following the approach of co-adding the same spectra proposed by Anglada-Escudé & Butler (2012) functions well for the M-dwarf sample via the `serval` pipeline (Zechmeister et al., 2018). The RVs extracted from `serval` are then corrected for barycentric motion, secular acceleration, and instrumental drift. Besides, a nightly zero-point correction is added to amend unknown causes for night-to-night fluctuations (Trifonov et al., 2020). The pipeline also provides a variety of helpful stellar activity indicators, i.e., chromatic index (CRX), differential line width (dLW), Hα index, and Ca II IRT triplet lines, as proved to be suggestive for the presence of stellar activity in Section 1.3.4.

On that same note, the CCF approach is not entirely abandoned for these M dwarfs. Following Lafarga et al. (2020), weighted binary masks, which depend on spectral type and $v \sin i$, are produced by co-adding spectra corrected for tellurics & RV shifts (Nagel, 2019), and then selecting pronounced minima. The cross-correlation function (CCF) is thus computed, providing more markers for stellar activity, i.e., its FWHM, contrast (CTR), and bisector velocity span (BVS) values.

Lastly, the pseudo-equivalent width (pEW), as defined in and provided by Schöfer et al. (2019), of the chromospheric lines such as the Hα, Ca II IRT (a, b and c), He I λ10833Å and He I D_3 lines, and of the of the photospheric lines, i.e., TiO λ7050Å, TiO λ8430Å, and TiO λ8860Å, are also derived from the CARMENES spectra.

1.4 CARMENES-*TESS* synergy

One of the strong suits of CARMENES is its role as a high-resolution spectrograph for mass determination for transiting *TESS* planets around M dwarfs. In fact, CARMENES has contributed to one third of the transiting planets discovered around these low-mass stars[10]. A few planetary discoveries that I was involved in as a co-author, particularly in regards to the modeling of the data, include those highlighted below.

GJ 357 b: The GJ 357 system (Luque et al., 2019) was a particularly good example of the benefit of large-sky transit surveys. The system had already been observed spectroscopically by many instruments, however, for each respective instrument, no signal was deemed of notable significance. Upon the transit detection of GJ 357 b, a hot, Earth-sized planet, it was made possible to combine all the various RV datasets to not only confirm the transit, but also uncover two more planetary signals hidden within the RV data, and the stellar rotation period as well. Had GJ 357 b not been detected, then these other two planets would have been kept concealed. Now, the system emerged

[10] `https://carmenes.caha.es/ext/tmp/`; last updated on 09 April 2021 (Trifonov et al., 2021)

to be one of the few multi-planetary systems known around M dwarfs (e.g., Weiss et al., 2018; Gilbert & Fabrycky, 2020), aiding in providing more information about the architecture of such systems (e.g., Lissauer, 2007). The transiting planet itself affirms the core accretion scenario as a formation channel to build terrestrial planets (e.g., Mordasini et al., 2012; Lambrechts et al., 2019), even indicating that a fourth more-massive planetary companion could reside in the system (e.g., Schlecker et al., 2020a). Additionally, this target fulfills the *TESS* aim of determining the masses of 50 planets with radii smaller than $4\,R_\oplus$ and as a very promising target for atmospheric characterization for *JWST*.

LP 714-47 b: The Neptune-like planet LP 714-47 b (Dreizler et al., 2020, also named TOI-442 b) found in the so-called "hot Neptune desert", defined to indicate the rarity of planets with masses of $\sim$0.1 M_J and periods $< 4\,\mathrm{d}$, was followed-up by multiple spectroscopic instruments with CARMENES dominating the number of data points, both in the VIS and in the NIR. The radial velocity measurements indicated of an additional signal, that if planetary, would be of Neptune-mass with a rather high eccentricity ($e = 0.26$). Including it as a Keplerian was actually favored as a model compared to using a GP, however, upon further investigation, the signal lies just at half the rotational period of the star and a few stellar activity indicators hinted that this additional signal could be of non-planetary origin. Either the stellar activity behavior shows some stable behavior, e.g., as demonstrated by modeling AD Leo in Chapter 6 in this thesis, or there happens to truly be a potential planet that needs further monitoring, e.g., similar to the long-term signal found in the TOI-1201 system showcased in Chapter 5 or TOI-1685 [c] (Bluhm et al., 2021). Nonetheless, the choice of how to model this additional signal did not drastically affect the planetary parameters of LP 714-47 b, therefore, making it among one of the best characterized planets. With such small uncertainties on its mass and radius and given that it is one of the few that populates the Neptune desert, it presents itself as an excellent target for determining the origin of this desert, with photoevaporation of the planetary atmosphere being a highly probable suspect (e.g., Owen & Wu, 2017).

GJ 3473 b: Another hot, transiting Earth-sized planet, but now on a short period orbit of $\sim 1.2\,\mathrm{d}$, GJ 3473 b is accompanied by a non-transiting planetary companion found in the RV data (Kemmer et al., 2020, also known as the TOI-488 system). Yet again, this system serves as another great example of the power of incorporating an extensive photometric and spectroscopic dataset to obtain extremely precise mass and radius measurements to less than 15% (i.e., for the transiting planet) fulfilling the objective of *TESS*, and to encounter more hidden planets in the system. Thanks to the precision, GJ 3473 b yields a rocky composition, and because the target is appealing for thermal emission spectroscopy (Kempton et al., 2018), the potentially-observed atmosphere metallicities can shed light on the planetary formation history, as well as on the stellar system.

In each of these systems, it is evident how that correct modeling approaches were put in place in order to perform simultaneous transit light curve and RV fitting, with the purpose of achieving the most precise planetary parameters.

1.5 Exoplanet demographics

Since the launch of the *Kepler*, *K2*, and *TESS* transiting missions, the demographical map of exoplanets has flourished and was quickly populated in unexpected areas (Figure 1.6). Planets we thought would never exist, and unlike those in our own Solar System, were revealed; giving rise to new research questions regarding their formation and evolution, and what kind of atmospheres they may have. The most ubiquitous planet found to date is one whose size lies between the Earth and Neptune with an orbit closer than that of Mercury to the Sun.

As we are collecting more planets, we need to prioritize those that are promising for the next step in the field: characterizing exoplanet atmospheres. But in order to get there, we first need to provide mass and radius measurements, i.e., from RVs and transit data. To obtain the most precise parameters, we need to understand the stellar host.

1.5.1 Host stars

Know thy star, know thy planet – NASA

The uncertainty in the planetary parameters is only as good as the uncertainty in the stellar parameters. Our ability in distinguishing the difference between a super-Earth and mini-Neptune (defined in Section 1.5.3), resides in how precisely we can compute the bulk density from the mass and radius measurements. In fact, with the release of *Gaia* DR2 (Gaia Collaboration et al., 2018), the community was able to refine the radius of stellar hosts to unprecedented precision which in turn tremendously improved the radii of the the planets orbiting these stellar hosts. This revealed a dearth of planets between 1.5 and 2.0 $R_\oplus$, commonly known as the radius gap (Fulton et al., 2017). Not only did the radii computed with the help of *Gaia* unveil the radius gap, but it also helps provide extremely high-precision stellar densities, which better constrains the shape of a transit (see Section 3.3.3). Aside from obtaining precise stellar mass and radius measurements, acquiring the stellar rotation period is valuable if its behavior manifests itself in the data. In that case, adding a red-noise term, e.g., with a GP (see Section 2.4.1), accommodated to this periodicity to simultaneously model the data can ensure better precision for the planetary signals.

A reoccurring theme is searching for an Earth-like planet, though such a planet around a solar-like star imposes a signal that is easily concealed. Both the transit and RV method rather benefit from a higher planet-to-mass radius and mass ratios, following Equations 1.2 and 1.8, respectively. Hence, M dwarfs, i.e., low-mass stars, are ideal target candidates. Even though these stars are the most ubiquitous in our Solar neighborhood (e.g., Henry et al., 2006), they have been challenging to observe because of the faint nature and previous transit surveys were geared towards hotter stars. Now that the *TESS* bandpass is accommodating for M dwarfs (Figure 1.2) and focusing in on the nearby neighborhood ($<$200 pc), these low-mass host stars can be easily followed-up with spectroscopic instruments.

1.5.2 Hot Jupiters

Hot Jupiters (HJs) are defined to be planets with masses larger than $\sim$0.2 M_J on orbits with periods less than $\sim$10 days. Due to their close proximity to their hosts and comparatively

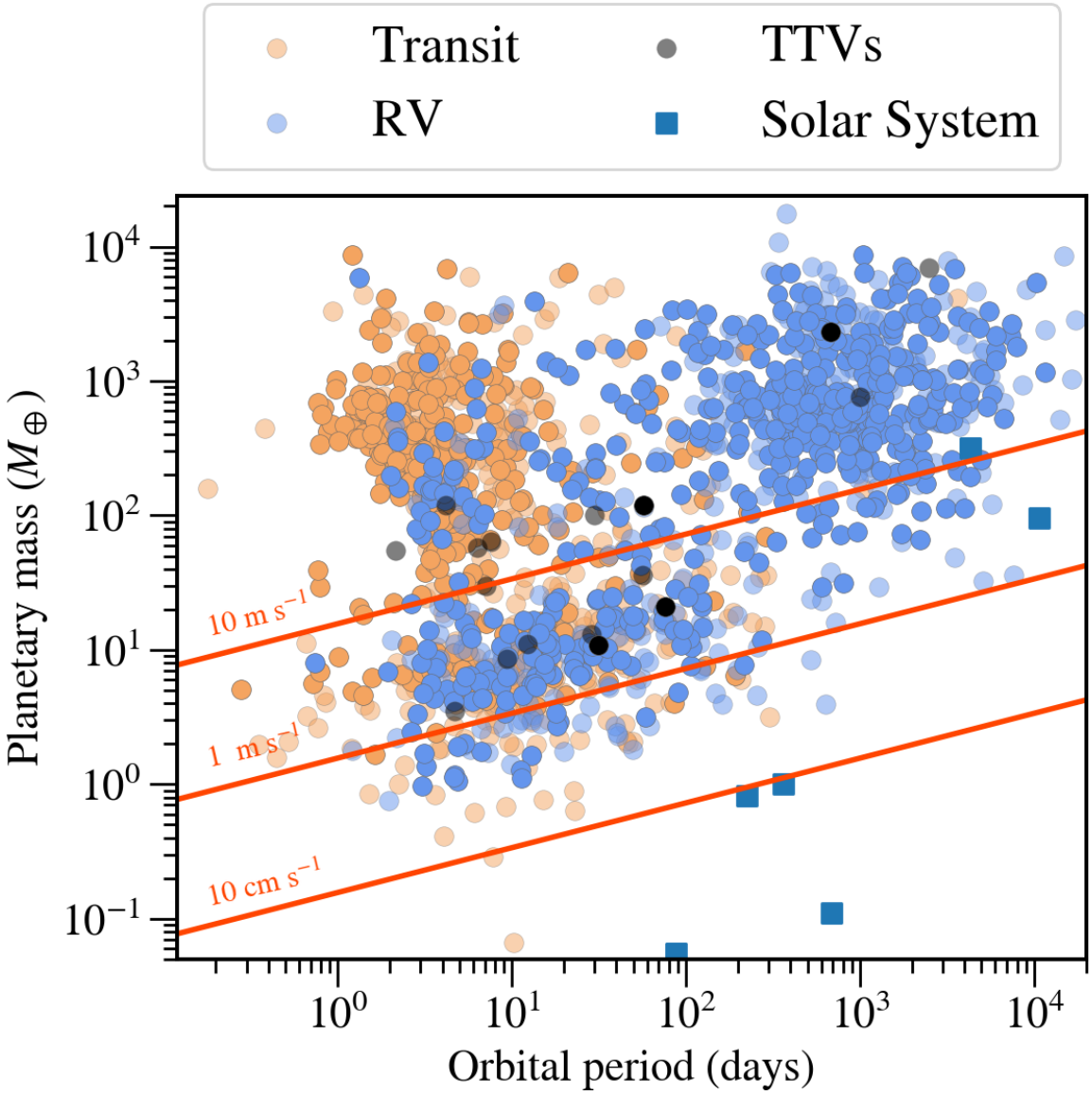

Figure 1.6: Planetary mass versus the orbital period for all the planets detected using either the transit, RV, or TTV method. Other methods are not plotted here since they are beyond the scope of this thesis. The total number amounts to 4151 (transparent points), of which 928 have mass measurements within 15 % uncertainty (opaque points). The lines represent the estimated RV signal following Equation 1.9 assuming a solar mass and zero eccentricity. The 1 m s^{-1} barrier for the RV method is visualized here as there are few mass measurements surrounding it and if so, the mass uncertainties are not reaching 15 % uncertainty. The data are taken from the NASA exoplanet archive as of 22 April 2020.

larger size, they are more accessible to detect. Despite this, they are nonetheless the least common with an occurrence rate of ∼1% (e.g., from RV surveys, Wright et al., 2012).

Interestingly, few of them have relatively significant eccentricities (∼10% have e>0.2 , Figure 4.8). Eccentricity of HJs have posed hypotheses on various migration theories. For example, an eccentric HJ, where the tidal circularization timescale is less than the age of the system, can be a good indicator of different migration histories, such as disk migration (Goldreich & Tremaine, 1980) or high-eccentricity migration due to another body, e.g., excited by planet-planet scattering (Rasio & Ford, 1996). Measuring the obliquities to look for spin-orbit (mis)alignment could aid in pinpointing the correct formation scenario out of the proposed two (Valsecchi & Rasio, 2014). Furthermore, HJs orbiting hotter stars observationally have a much broader obliquity distribution, where the cutoff is around $T_{\rm eff} \approx 6250\,{\rm K}$ (Winn et al., 2010; Triaud, 2018; Louden et al., 2021).

In Chapter 4, I present TOI-150 b, an eccentric hot Jupiter optimal for measuring its obliquity, as well as TOI-163 b, an inflated hot Jupiter that is promising for atmosphere characterization with *JWST*.

Warm/cold Jupiters

Unlike their hot Jupiter counterparts, warm/cold Jupiters are found in longer period orbits $P > 10$ days with a wide range of possible eccentricities. These are believed to be the closest analogs to Saturn and Jupiter in our Solar System. Given the longer periodicity, they are easier to detect in RVs rather than in transit data given the huge sensitivity of geometrical transit probability on the orbital distance (Equation 1.1), though there have been some recent detections with using multiple *TESS* sectors, e.g., Dong et al. (2021); Dawson et al. (2021); Hobson et al. (2021); Schlecker et al. (2020b); Brahm et al. (2019a).

1.5.3 Super-Earths and mini-Neptune

The most prevalent planets are those intermediate in size between the Earth and Neptune, called "sub-Neptune" planets. As shown in Fulton et al. (2017), the radius distribution of these small planets splits into two populations, namely "super-Earths" (1–2 $R_\oplus$), presumably with bare rocky cores, and "mini-Neptunes" (2–4 $R_\oplus$), with gas envelopes enlarging their radius. The differentiating factor between them depends on the retention or loss of a hydrogen-dominated atmosphere, which relies upon the density of the planet (Bean et al., 2021). Unfortunately, only a handful of small planets actually have precise density estimates (those with 30% precision in both mass and radius are shown in Figure 5.8). Hence, mass determination, i.e., from spectroscopic data, is absolutely crucial for transiting small planets in order to classify them, because prior to obtaining a mass, the planet can only be called a sub-Neptune.

However, even with mass and radius measurements, it is not sufficient in determining what the bulk composition of the planet is, as there are large degeneracies between the ratio of rock, water, and hydrogen (e.g., Rogers & Seager, 2010). Atmosphere characterization, i.e., with the upcoming *JWST*, can solve this and shed light on the composition, and thus on the formation of these planets (Molliere et al., in prep.). Hence, *TESS* was created with the purpose of finding and compiling a selection of promising candidates for transmission spectroscopy.

In Chapter 5, I present the transiting mini-Neptune TOI-1201 b, a highly promising candidate for atmosphere characterization using *JWST*, being just one out of just a few around an M dwarf.

1.6 Thesis overview

The focus of this thesis is to detect and characterize planets while correctly modeling all signals present in the data in order to provide the most precise planetary parameters possible for future endeavors. As instrumentation continues to break the frontier, our modeling tools and our knowledge of various astrophysical processes become the limiting factor. Given that our detection approach is indirect in nature, we need to make inferences on the data we have on hand. In particular, I have worked with RV data which often succumbs to the effects of stellar activity when searching for low-mass planets. Hence, employing modern statistical tools in order to unmask hidden planetary signals and characterize them is a must.

The first part of the thesis outlines the framework of the statistical tools including a standardized modeling approach. In the second part of the thesis, I apply these tools to present the discoveries and precise characterizations of three transiting planets, along with a star that is a great case study demonstrating the behavior of stellar activity on RV data.

The thesis is organized as follows:

The introduction above provided an overview of where the exoplanet field stands today. Emphasis was given to the transit and RV method for planet detection given that this thesis is primarily based on this type of data, specifically mainly from the space-based *TESS* mission and the CARMENES spectrograph. Obtaining the bulk density of the planet is made handily possible because the transit method yields the radii for plenty of planets, to which the RV method supplements by providing a mass, creating a powerful synergy. This information can shed light on how these planets formed and how they have evolved. To further enlighten these concepts, the next observational stage in the exoplanet field is atmospheric characterization via space-based transmission spectroscopy. For this reason, the current assignment is to identify and prioritize which targets are suitable for the upcoming *JWST*. In this thesis, I present two very promising targets that fulfill this objective: TOI-163 b and TOI-1201 b. The third planet, TOI-150 b, is not as ideal for *JWST*, however, it is nonetheless a qualified target via other follow-up observations.

In Chapter 2, I provide an overview of various statistical concepts that this thesis benefited from, particularly in the framework of Bayesian statistics. I then dive into the various techniques and approaches for identifying interesting signals in our data, as well as how we model them with the `juliet` tool, outlined in Chapter 3. The design of this chapter is intended to be a comprehensive overview of how to approach a dataset with both radial velocities and transit photometry light curves, covering common mistakes and false assumptions to avoid.

Once the whole setup is introduced, I apply this approach to a multitude of systems with various intriguing results, including promising planets for future follow-up observations as well as more insight on the RV variations inflicted by stellar activity. This versatility just highlights how widely applicable these tools are.

Chapter 4 introduces TOI-150 b and TOI-163 b, two hot Jupiters around F-type stars detected by *TESS* and followed-up spectroscopically by FEROS. The former follows a rather eccentric orbit, which for such a close-in planet challenges formation theories on how it had wound up there. Luckily, the planet is a great candidate for measuring the chances of spin-orbit misalignment, which can hint at its origin. The latter, though following a circular orbit, is nonetheless a promising inflated hot Jupiter for transmission spectroscopy considering it resides right in the *JWST* continuous viewing zone and will be steadily observable for ∼200 d.

Chapter 5 presents the mass and radius characterization of a transiting mini-Neptune in the TOI-1201 system. The stellar host is found in a wide m2.5V-m2.0V binary system where both stars fall onto the same *TESS* pixel, such that follow-up photometry was of upmost importance in determining the true stellar host. The planet's mass was determined with CARMENES follow-up radial velocities, which exhibited the stellar rotation period and an additional long-term signal that would need further monitoring. The target is one of the very few around M dwarfs to be the most promising for atmospheric characterization with not only *JWST*, but also with low-resolution transmission spectroscopy on the ground, thus having the opportunity to cover a wide wavelength range.

Lastly, the enigmatic case of AD Leo is discussed in Chapter 6. A quite controversial target, that is not shy in the community, pushes the boundaries on our understanding of how to model stellar activity in RV data. The stellar activity-induced RV signal has been stable over the course of ∼19 years, with amplitude and phase fluctuations and achromaticity. Using the most current approaches to deal with stellar activity, including modeling with a GP and recomputing the RVs based on non-active spectral lines, AD Leo still is puzzling. Hence, I explored the limitations of our modeling tools and more so, our understanding of how stellar activity manifests itself in RV data.

To finish everything off, I summarize the findings of my work in Chapter 7. Furthermore, I discuss what open-ended questions lie ahead for the next years, particularly focusing on, the importance of conducting a standardized approach to modeling in order to create a more comparable exoplanet sample, and on the significance of properly interpreting and modeling stellar activity found in the data.

2 Statistical concepts in the realm of detecting exoplanets

2.1 Motivation

The precision of instruments has improved dramatically where we are no longer limited by the uncertainty of the instrument, but rather by the data themselves. Surely the data is gifting us plenty of ground-breaking planets waiting to be found, but at the cost of picking up "unwanted" signals, primarily focusing on the ones that are dominating in RV data, which is stellar activity. To keep in mind, we consider these signals as inconveniences for planet hunters, but they can be a treasure for others. It is all about perspective.

In a field where the goal is to search for low-amplitude planetary signals in data consisting of heaps of noise, both instrumental and astrophysical, statistical methods have to be put into practice in order to unmask and correctly describe these signals with high precision.

In the recent years, the field has evolved tremendously as computational ability has advanced and statistical knowledge has progressed. Understanding how to incorporate Bayesian statistics, described in Section 2.2, became an integral part in the data analysis portion. Within the Bayesian framework, the Bayesian evidence allowed for robust model comparison. Calculating the Bayesian evidence was previously computationally demanding, however, with the emergence of the Nested Sampling (NS) algorithm, covered in Section 2.3, it became much more feasible. Lastly, with more computational power, the ability to include Gaussian Process (GP) Regression as a technique to help mitigate stellar activity behavior became feasible and is now widely used, explained in Section 2.4.

Together, these tools help gather the expertise and competence needed to choose the best model to represent the data at hand in order to unearth and characterize planetary signals.

2.2 Bayesian statistics

The ideology of Bayesian statistics has sky-rocketed in practice during the past decade, where the amount of papers including the word "Bayes" is exponentially growing (Figure 2.1). It has definitely made its way into the field of exoplanet detection, essentially becoming the standard practice, and can even be expected for a publication nowadays. In Section 2.2.1, the basics and the different aspects that make up Bayes' theorem are outlined. Section 2.2.2 addresses a common misconception regarding Bayesian inference where the belief that the prior has a large unfavorable impact on the posterior distributions of the parameters.

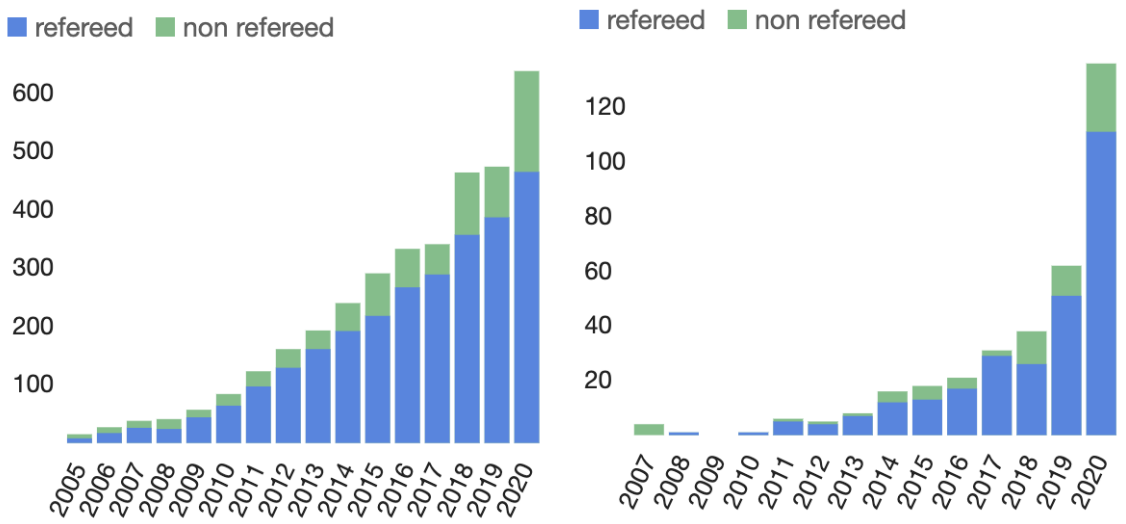

Figure 2.1: Distribution of the number of published articles with the word "Bayes" included from 2005-2020. Source: Nasa/ADS when searching `full: "bayes" full:"exoplanet"` (left) and `full: "Nested Sampling" full: "exoplanet"` (right)

Finally, Section 2.2.3 demonstrates the strengths of Bayesian inference in the realm of model comparison. For a more statistically proper and in-depth description, the reader is pointed to the works, e.g., Mackay (2003); Hogg et al. (2010); Parviainen (2017).

2.2.1 Bayes' theorem

The core of Bayesian ideology is to update the current knowledge of a problem given new experience. An initial probability is assigned to a hypothesis, which is then updated with new observations to obtain a posterior probability distribution. This then can be used as the new prior information for even more new data to again update the information on the problem. Put together, this becomes Bayes' theorem and can be qualitatively summarized as,

$$\text{posterior} \propto \text{prior} \times \text{likelihood} \tag{2.1}$$

and quantitatively, it becomes,

$$\Pr(\theta|\mathcal{D}) = \frac{\Pr(\mathcal{D}|\theta)\Pr(\theta)}{\Pr(\mathcal{D})} \tag{2.2a}$$

$$\mathcal{P}(\theta) = \frac{\mathcal{L}(\theta)\pi(\theta)}{\mathcal{Z}} \tag{2.2b}$$

where $\theta \equiv \{\theta_1, ..., \theta_d\}$ is the parameter vector, $\Pr(\theta|\mathcal{D}) \equiv \mathcal{P}(\theta)$ is the posterior probability density function, or known as the posterior representing the updated knowledge, $\Pr(D|\theta) \equiv \mathcal{L}(\theta)$ is the likelihood function, $\Pr(\theta) \equiv \pi(\theta)$ is the prior probability distribution, or simply the prior representing the current belief of the parameters, and $\Pr(\mathcal{D}) \equiv \mathcal{Z}$ is the marginal likelihood, or generally known as the Bayesian evidence, acting as a normalization factor

(Díaz, 2018).

In practice, we could have an RV dataset, i.e., denoted as $\mathcal{D}$, where we find out that there is a signal present at some periodicity either with the help of transit photometry or via a significant peak in the periodogram, or even both. Because we expect what the signal's period should be, we can impose this knowledge within the prior, i.e., $\Pr(\theta_P) = \mathcal{N}(P, \sigma_P)$, where P is the suspected period and σ_P is the uncertainty we assign to that period. We want to know how these distributions are modified once we include the RVs as additional information, which the updated values create the posterior distribution, i.e., $\Pr(\theta_P|\mathcal{D})$.

If the goal is to estimate the posterior parameters, then the normalizing Bayesian evidence term is not necessary to compute because the posterior can be marginalized (see below). This is done so with the assumption that the given model adequately explains the data. If instead model selection is the aim, then computing the evidence is absolutely crucial, further covered in Sections 2.2.3 and 2.3.

In this regard, we alter the simple version of Bayes' theorem to accommodate for when a particular model is considered. Equation 2.2 transforms into,

$$\Pr(\theta|\mathcal{D}, M) = \frac{\Pr(\mathcal{D}|\theta, M)\Pr(\theta|M)}{\Pr(\mathcal{D}|M)} \tag{2.3}$$

where the structure is fundamentally the same as previously before, but now given a particular model hypothesis, M. Hence for the same example as before, we can now start to compare whether a 2-Keplerian model is better than a 1-Keplerian model i.e., if the data supports a more complex model.

Each of the mentioned components are described further below.

Prior The prior distribution $\pi(\theta)$, is simply the assumed distribution of the parameters before taking any evidence into account,

$$\pi(\theta) = \Pr(\theta|M) \tag{2.4}$$

Incorporating prior physical or mathematical knowledge is a key feature of Bayesian inference, though is oftentimes seen as a disadvantage with the presumption that it can heavily affect the end result in a negative manner. Sect. 2.2.2 delves into more detail of why this is instead the opposite and rather the beauty of Bayesian statistics of how to correctly choose the right prior distributions to reflect the already existing knowledge. If the prior is still poorly constrained, known as the unrepresentative prior problem, then the posterior repartitioning method can address the issue by modifying the prior distribution (discussed in e.g., Skilling, 2004; Baluev, 2009; Chen et al., 2018)

Posterior Once a certain dataset is taken into account with the a priori information from the prior, the probability distribution of the parameter takes shape,

$$\mathcal{P}(\theta) = \Pr(\theta|\mathcal{D}, M) \tag{2.5}$$

and becomes the term of interest when computing parameter estimations. For parameter inference, the Bayesian evidence is not necessary since the posterior of a given

parameter, e.g., θ_1, can be marginalized over all the other parameters (e.g., Parviainen, 2017),

$$\mathcal{P}(\theta_1) = \int \Pr(\theta|\mathcal{D}, M)\mathrm{d}\theta_2 \ldots \mathrm{d}\theta_d \propto \int \mathcal{L}(\mathcal{D}|\theta, M) \cdot \pi(\theta)\mathrm{d}\theta_2, ..., \theta_d \tag{2.6}$$

To quantify the findings, it is common practice to take the mean of a given posterior along with the 1-σ confidence interval to denote the uncertainty, i.e., the 68 % confidence intervals, to provide information also on the posterior skewness.

For instances where the posterior distribution cannot be directly sampled, Markov chain Monte Carlo (MCMC) sampling is a powerful method where the sampler starts in one location in the parameter space and continually explores the area, adding the parameter vector to the chain to obtain a posterior distribution at the end (see e.g., Gregory, 2005; Gelman et al., 2013, and references therein).

Likelihood The likelihood is expressed as,

$$\mathcal{L}(\theta) = \Pr(\mathcal{D}|\theta, M) \tag{2.7}$$

and can be thought of answering the question: given this particular set of parameters and model, what are the chances of generating this exact dataset?

Imagine we assume a test model as a function of the parameters given by $m(\theta)$, where θ_i is the i-th parameter vector that produces the projected value $m_i = m(\theta_i)$ and should correspond to the observable $\mathcal{D}_i$ with known Gaussian uncertainties of $\sigma_{\mathcal{D},i}$. We assume that model m is indeed the correct model and the only argument that a data point strays from the model is because an offset from the Gaussian distribution of mean zero and variance of σ has been added, $M_i = m_i + \mathcal{N}(0, \sigma_{\mathcal{D},i})$ (Hogg et al., 2010). The given uncertainty can oftentimes be under-represented and thus requiring an additional "jitter" term, σ (see Section 3.3.2 for an explanation). Following the classical frequentist maximum likelihood approach, we want to maximize the likelihood for each individual i-th point,

$$\Pr(\mathcal{D}_i|\theta_i, M_i) = \frac{1}{\sqrt{2\pi\sigma^2_{\mathcal{D},i}}} \exp\left[\frac{-(\mathcal{D}_i - m_i)^2}{2\sigma^2_{\mathcal{D},i}}\right] \tag{2.8}$$

where the grand likelihood can be written as the product of the independent likelihoods,

$$\mathcal{L}(\theta) = \prod_i^N \frac{1}{\sqrt{2\pi\sigma^2_{\mathcal{D},i}}} \exp\left[\frac{-(\mathcal{D}_i - m_i)^2}{2\sigma^2_{\mathcal{D},i}}\right] \tag{2.9}$$

The negative natural logarithm of this equation is taken to turn the products into sums in order to spare computational efforts,

$$-\ln\mathcal{L}(\theta) = \frac{1}{2}\sum_i^N \frac{(\mathcal{D}_i - m_i)^2}{\sigma^2_{\mathcal{D},i}} + \frac{1}{2}\sum_i^N \ln\sigma^2_{\mathcal{D},i} + \frac{N}{2}\ln(2\pi) \tag{2.10}$$

where the first term $\frac{1}{2}\sum_i^N \frac{(\mathcal{D}_i - M_i)^2}{\sigma_i^2}$ is also related to the χ^2 statistic as $\chi^2/2$, the second term $\frac{1}{2}\sum_i^N \ln \sigma_{\mathcal{D},i}^2$ acts as a penalty for large likelihood values and the third term $\frac{N}{2}\ln(2\pi)$ can be simply regarded as a constant in the equation. When including an additional "jitter" term to readjust the data uncertainty (Akaike, 1998), the middle term is quite essential in ensuring that the negative log-likelihood does not simply continuously scale up, thus, favoring higher uncertainty values to the point where the conjunction between the data and model become negligible.

In the interest of pinpointing the maximum likelihood estimate (MLE), the negative log-likelihood (NLL) is the input for optimizers that minimize loss functions (e.g., Powell, 1964; Mai Anh et al., 2014). The parameter vector θ_{MLE}, corresponding to the MLE, then becomes the initial parameter vector for MCMC runs to search the parameter space and obtain posterior parameter distributions. Or in the case of `exostriker` the tool provides the parameter values corresponding to the MLE to serve as good initial information for Nested Sampling runs.

If the prior is uninformative and flat, then the highest peak in the likelihood (i.e., MLE) turns out to also be the highest peak in the posterior distribution.

Evidence The Bayesian evidence is the foundation for modal comparison (Section 2.2.3). The Bayesian evidence is the normalization constant, as the integrated posterior density given by,

$$\mathcal{Z} \equiv \Pr(\mathcal{D}|M) = \int_{\Omega_\theta} \mathcal{L}(\theta)\pi(\theta)\mathrm{d}\theta \tag{2.11}$$

Evaluating the evidence numerically proves to be an extremely challenging job since calculating the integral over a multi-dimensional parameter space requires many iterations of plugging in parameters to get the likelihood values. Nelson et al. (2020) conducted an Evidence Challenge specified for simulated RV data to better identify promising methods that not only accurately compute the evidence but also have decent computational costs. Among the most reliable approaches, Nested Sampling was one of them (Skilling, 2004), where the essence is converting the multi-dimensional evidence integral into a one-dimensional integral to ease the numerical evaluation. Nested Sampling is introduced and described in detail in Section 2.3.

2.2.2 Choosing a prior

There is no such thing as a prior with truly "no information"

To reiterate, the core of Bayesian inference stems from providing appropriate priors to derive posterior distributions (Trotta, 2008). They represent the uncertainty about the parameter before any input (i.e., data) is given. Hence, a major argument against the Bayesian approach is this subjective dependency on the prior. It is therefore of utmost importance to ensure that the correct type is chosen as well as with the correct limits applied. Even though this reliance can be seen as a disadvantage by many, it should rather be regarded as an advantageous characteristic as it can incorporate physical knowledge into

the model when fitting, e.g., applying a constrained normal prior on the period of a transiting planet for RV-only data, as in Section 3.3.5. So long as the prior is non-zero in regions where the likelihood is large then the posteriors should be unaffected and come to the same result regardless of slight modifications in the prior (Trotta, 2008). In cases where the prior is substantially remote from the true value, introducing an additional parameter to provide some flexibility on the belief of the prior is suggested in order to minimize erroneous prior choices (Simpson et al., 2017; Chen et al., 2019).

There can be thought of two sub-classes for the priors – uninformative and informative priors – ones that are very unbiased and vague, or ones that are more constrained and limiting. When the prior is uninformative, it allows the data to define the posterior (i.e., the posterior is data-driven); whereas when the prior is informative, the posterior is a mixture of both the prior and the data. If it so happens that the prior is very narrowly defined, more data would be required to "change" the established beliefs on the parameter. Likewise, an overwhelming amount of data will overpower the prior anyway and make it more obsolete. One thing to keep in mind is that no matter how "uninformative" a prior may be, it is still inherently providing some information on the prior belief of a parameter's distribution.

Listed below are the commonly used priors for our modeling purposes:

Uniform ("flat") The simplest, most common "go-to" uninformative prior is the uniform distribution, given by,

$$f(x) = \frac{1}{b-a} \text{ for } a \ \leq x \leq b \text{ else } 0 \tag{2.12}$$

It can also be called a "flat" prior since it has no preference towards any value from the given boundaries from a to b. This range does not necessarily have to be always wide, but can in principle also be narrow. The notation $\mathcal{U}(a,b)$ is used to represent the uniform prior with the set boundaries from a to b.

Jeffrey's (log-uniform) In situations where the value of the parameter is unknown and can range over multiple magnitudes, it is recommended to adopt a log-uniform prior, otherwise also known as a Jeffrey's prior (Jeffreys, 1961),

$$f(x) = \frac{1}{x \log(b/a)} \text{ for } a \ \leq x \leq b \text{ else } 0 \tag{2.13}$$

For example, if a value can fall anywhere between 1 and 10 000 and a uniform prior is used, the distribution is biased towards larger numbers whereas if the log-uniform prior is chosen, then the smaller numbers (e.g., 10-100) have as equal of an opportunity as the larger ones (e.g., 100-1 000) creating an equal playing field. The notation $\mathcal{J}(a,b)$ is used to represent the log-uniform prior with the set boundaries from a to b.

Normal (Gaussian) If prior knowledge on a parameter's distribution is available, e.g., through physical means, it is advised to use an informative prior, commonly the normal one given by,

$$f(x) = \frac{1}{\sigma\sqrt{2\pi}} \exp\left(-\frac{1}{2}\frac{(x-\mu)^2}{\sigma^2}\right) \tag{2.14}$$

The notation $\mathcal{N}(\mu,\sigma)$ is used to represent the normal prior centered on μ with an uncertainty of σ.

Fixed The prior for a given parameter can even be fixed to a particular value, simply written as,

$$f(x) = a \tag{2.15}$$

e.g., setting the eccentricity to 0 to compare circular versus eccentric orbits. The notation $\mathcal{F}(a)$ is used to represent the fixed prior to a given value of a.

To summarize, allocating the appropriate prior depends on how much knowledge lies for a given parameter. The fear of allowing the prior the dictate and negatively influence the posterior stems from the misuse of Bayesian statistics rather than the concept itself. The tool should not be blamed for the misuse of the user. In understanding what we are inputting, we are able to take advantage of the Bayesian statistics in order to obtain more precise planetary parameters.

2.2.3 Model comparison

The power of Bayesian inference is showcased for carrying out model comparison using the Bayesian evidence (Equation 2.11). In the domain of modeling for our purposes, determining the winning model plays a vital role in distinguishing the number of present planetary signals (e.g., 1 planet versus 2 planet), deducing whether the planet is on a circular or eccentric orbit, and what noise model should be used on the data (e.g., Gaussian process, extra jitter term). All of which can have an effect on the derived planetary parameters and therefore, interpretation of the planet in the scope of others.

What we are searching for is the probability of a model given the data, or the model posterior $\Pr(M_1|\mathcal{D})$. Using Bayes' Theorem, Equation 2.2, we can rewrite it as,

$$\Pr(M_1|\mathcal{D}) = \frac{\Pr(\mathcal{D}|M)\Pr(M_1)}{\Pr(\mathcal{D})} \tag{2.16}$$

where $\Pr(\mathcal{D}|M)$ is the normalizing Bayesian evidence presented as the normalizing factor in Equation 2.3, $\Pr(M_1)$ is the prior for model M_1, and $\Pr(\mathcal{D})$ is the normalizing factor. Comparing model M_1 to another model M_2 yields the ratio,

$$\frac{\Pr(M_1|\mathcal{D})}{\Pr(M_2|\mathcal{D})} = \frac{\Pr(\mathcal{D}|M_1)\Pr(M_1)}{\Pr(\mathcal{D}|M_2)\Pr(M_2)} = B_{12}\frac{\Pr(M_1)}{\Pr(M_2)} \tag{2.17}$$

where B_{12} is the ratio between the two models and is known as the Bayes factor,

$$B_{12} = \frac{\Pr(\mathcal{D}|M_1)}{\Pr(\mathcal{D}|M_2)} = \frac{\mathcal{Z}_1}{\mathcal{Z}_2} \tag{2.18}$$

Assuming that no one model is preferred over the other, i.e., $\Pr(M_1) = \Pr(M_2)$, the model comparison simplifies to the Bayes factor (though this may not always be the case Kass &

Raftery, 1995).

It is common practice to compare the Bayesian log-evidence between two models, $\ln(\frac{\mathcal{Z}_1}{\mathcal{Z}_2}) = \ln \mathcal{Z}_1 - \ln \mathcal{Z}_2 \equiv \Delta \ln \mathcal{Z}$, since this becomes then a simple subtraction computation. The basic rule of thumb that we follow here within this thesis is that if competing models are comparable (i.e., $\Delta \ln \mathcal{Z} \lesssim 2.5$), then no one model is statistically significant over the other (Trotta, 2008). In such a case, the simpler model to explain the available data is chosen following Occam's razor[11]. Indeed a prevalent worry is judging whether a model with an increased amount of parameters is justified by the data. Luckily, the complexity of the model is taken into account in the evidence (Gregory, 2005). Since the evidence, Equation 2.11 can be thought of the average of the likelihood over the prior space, increasing the model complexity by including more parameters expands the prior space and thus lowers the average, i.e., Bayesian evidence. Therefore, even though a more complex model can represent the data just as adequately as a simpler one, the difference in the Bayesian log-evidence between the two is insignificant.

When comparing log evidences,
it is of upmost importance that the data involved stays the same.

Otherwise, the comparison between Bayesian log evidences is no longer valid. An exception to this is when you add auxiliary data, e.g., a stellar activity indicator as a linear term, since this is just like adding a linear term, i.e., another new parameter to the model. Additionally, applying the same priors is strongly recommended to ensure consistency. There is some buffer here in situations where an extremely wide prior is no different from a relatively narrow prior if the prior is non-zero where the likelihood is non-zero, hence the posterior would only be non-zero where the likelihood is non-zero.

2.3 Nested Sampling

As already mentioned, computing the Bayesian evidence is extremely challenging and computationally expensive because it is an integration over the likelihood and prior space. The Nested Sampling (NS; Skilling, 2004) algorithm was introduced as an efficient Monte Carlo sampling method in estimating the Bayesian evidence, while also providing posterior distributions as a by-product. Below I give an overview and I highly recommend the works of e.g., Skilling (2004); Feroz & Hobson (2008); Feroz & Skilling (2013); Speagle (2020), for an in-depth description.

In comparison to other methods that provide posteriors for the parameters (e.g., MCMC sampling), NS does not require an initial starting vector in the parameter space; instead, it draws samples, referred to as "live" points, directly from the prior volume. This is hugely beneficial for the reason that NS is able to fully explore the entirety of the parameter space (i.e., multi-modal distributions), thus being able to reach the global maximum, given that the number of live points was sufficient enough. For other common samplers, the parameter space is frequently only explored near the initial theta vector provided by optimization

[11] Originally formulated by English Franciscan friar William of Ockham (ca. 1285-1349): "Pluralitas non est ponenda sine neccesitate".

(e.g., chi-squared fittings, least-squares, etc.) where the MLE is assumed to be the global maximum, but it instead might only be a local maximum.

Skilling (2004) introduced the concept of "prior volume" X (also referred to as prior mass) by multiplying the prior by the infinitesimal volume in the parameter space,

$$dX = \pi(\theta)\mathrm{d}\theta \tag{2.19a}$$

so that,

$$X(\lambda) = \int_{\mathcal{L}(\theta)>\lambda} \pi(\theta)\mathrm{d}\theta \tag{2.19b}$$

where $\pi(\theta)$ is the prior (Equation 2.4). The prior volume is transformed into a unit prior volume where $X_0 = 1$ corresponds to the initial prior volume. Thus, as λ increases, then $X(\lambda)$ is monotonically decreasing from 1 to 0, i.e., $0 < X_N < ... < X_1 < X_0 = 1$. The original multi-dimensional evidence integral (Equation 2.11) is then transformed into a one-dimensional integral and then approximated numerically as,

$$\mathcal{Z} = \int_0^1 \mathcal{L}(X)\mathrm{d}X \approx \sum_i^N \mathcal{L}_i w_i \tag{2.20}$$

where the weights are given by $w_1 = \frac{1}{2}(X_{i-1} - X_{i+1})$ (following the simple trapezium rule, Feroz & Hobson, 2008). Thus, each live point i contains its own likelihood value $\mathcal{L}_i$ and its own prior mass X_i.

Simply put, the NS works in the following way for each iteration in trying to constrain the unit prior space:

1. For each live point i, the likelihood value $\mathcal{L}_i$ is computed.
2. The live point with the worst likelihood value is removed from the sample, but still stored as a value for later measures.
3. A new live point with a better likelihood ($\mathcal{L} > \mathcal{L}_i$) is drawn and replaces the previous one.
4. The process repeats itself until...

the stopping criterion is met when the change in improvement for the evidence reaches a certain threshold, $\Delta\mathcal{Z}_i = L_{\max} X_i$, where $L_{\max}$. Typically, this value is 0.1 by default. Though not perfect, the mean and uncertainty in the final Bayesian evidence is achieved after just run, taking out the need to perform multiple runs (Skilling, 2004).

There are three commonly-used types of Nested Samplers, e.g., regular, importance, and dynamic. In the regular one, only the active live points are the end are considered for the final evidence calculation, quite analogous to using a burn-in for MCMC sampling. For the importance one, all the live points are considered but with a weight attached to each one, giving more importance to the ones at the end. As for the dynamic one, the amounts of live points dynamically varies with each iteration, depending on likelihood in the parameter

space, i.e., higher likelihood regions receive more live points which can help estimate the evidence better and quicker (Speagle, 2020).

Either way, choosing the right number of walkers should be adequate enough to sample the prior space sufficiently, even in regions of low likelihood. The suggested number of walkers should be at least the number of free parameters squared ($dimension^2$).

Computational times

The trick is choosing a wide enough prior without compensating the results, but narrow enough to save time. As an example, Figure 3.4 shows how a too-wide prior for the periodicity resulted in picking up aliases of the true signal, i.e., determined by transit photometry. Such a run with the wider-uniform prior including the aliases took ∼2 times longer than when using the more narrow uniform prior centered on the correct period.

For every iteration within Nested Sampling, the prior is resampled from its distribution since once one sample is drawn, it can later be discarded because it has a too-low likelihood. In comparison to other sampling methods that do not rely on a prior space, e.g., MCMC sampling, the walkers can just explore the likelihood distribution map from their initial parameter vector (unless quasi-priors are applied). Hence, the first aspect is to assess the primal computational time for prior resampling. Considering only one parameter for a typical `juliet` run that step through 30 000 iterations (the number of live points can be ignored since each iteration discards and then recomputes one likelihood value), computing the uniform prior is $\sim$ 180 times faster[12] than when computing the normal prior. This is anyhow not surprising since the uniform prior is a basic arithmetic operation whereas the normal prior requires sampling from a normal distribution. Choosing the priors' limits is irrelevant since computing the prior does not depend on the prior volume.

The key difference in minimizing computational time is thus not a result of resampling the prior space, but rather the *integration* of the prior volume. While certainly a uniform prior is computationally cheaper to simply produce values, in the end, this can be offset and can computationally cost more, depending on the prior limits.

2.4 Gaussian processes

The purpose of employing a GP in this thesis is to fulfill the necessity of modeling a behavior in the data that can not yet be described using a deterministic model. By definition, the fundamental concept of a GP is that it is a non-parametric model in nature that encapsulates an infinite amount of parameters following a Gaussian distribution.

A motivation as to why we even consider GPs in our model is discussed in Section 2.4.1, followed by a brief statistical explanation behind the inner workings of the GP in Section 2.4.2. The most important component of the GP, i.e., the kernel function, sets the rules for how data points are correlated to one another. Choosing a sensible kernel is thus outlined in Section 2.4.3.

For an extensive description of a general application to Gaussian Processes (GPs), the reader is referred to Rasmussen & Williams (2006), and for a more focused application to RVs I recommend the work of Rajpaul et al. (2015) and references therein.

[12]Using the python package `timeit`: `https://docs.python.org/3/library/timeit.html`

2.4.1 Why do we need GPs?

In general, our observed data consists of the true physical perturbations (i.e., a Keplerian model due to a planetary companion), any known instrumental effects (i.e., via a linear term), and leftover, unaccounted noise. The noise is composed of various elements, may it be photon noise or from either the instrument itself or from astrophysical means that we yet cannot explain through deterministic modeling. Sometimes adding a white-noise term, i.e., a "jitter" term (explained in Section 3.3.2), is enough to mitigate these unknown deviations and to account for all the variation in the data (e.g., Ford, 2006; Baluev, 2009). Other times, it is not if there might be an underlying correlated noise component present. This can arise given instrumental movements and drifts, or due to stellar spots on co-rotating on the star itself (e.g., Dumusque et al., 2011a).

Unfortunately, we do not know (yet) how to mitigate these effects with physical models. A deterministic model that can predict either a light curve or RV model based on the spots rotating on the stellar surface would be ideal as it could simply be included in the grand model. While such codes do exist to produce forward models, e.g., SOAP2.0 (Dumusque et al., 2014) or StarSim2.0 (Herrero et al., 2016), the downsides are that they can be extremely degenerate by nature (i.e., multiple star-spot configurations could generate the same output) and they are computationally heavy (e.g., there is a huge parameter space to explore regarding the spot's position and its lifetime). These signals, however, cannot be simply ignored if they are significantly present in the data. This can become problematic if the correlated noise is prominent enough as it will have an effect on obtaining accurate planetary parameters. While sometimes successful that these signals can be modeled as a sinsuoid (or sum of sinusoids, e.g., Dumusque et al., 2012), it makes the model quite complicated and it ignores the fundamental concept that these signals are stochastic in nature, i.e., fluctuating in amplitude and phase over time, in which a simple, definite number of sinusoids can not achieve. Therefore, a non-deterministic model approach is necessary and has become common in the field and this is where the GP makes it appearance as a non-parametric model to account for stochastic behavior to learn unknown functions.

2.4.2 GPs in a nutshell

Most of the time whenever we have data, we already have a clue of how we want to try modeling that data, e.g., maybe with a linear trend, a quadratic, or a Keplerian. This model we have on hand is denoted as the deterministic model since we consider it to be an adequate mathematical representation to describe the data. The only instances where the data divert from this model can be represented with a Gaussian distribution, $\mathcal{N}(0,\sigma)$, i.e., centered around zero with some uncertainty σ. The noisier the data are, the higher the uncertainty, and it may even be an indicator that another model could be better at describing the data. Put into an equation, it would look like,

$$y_i = f(t_i) + \mathcal{N}(0,\sigma_i) \tag{2.21}$$

where y_i is the dependent variable to t_i , $f(t_i)$ is the deterministic model acting on the data point at t_i, and the last term represents the uncertainty of the data. This is the basic concept of a simple linear regression model.

But what if we do not know the underlying model? This is where the GP can come in since it is a non-parametric model. This does not mean that it comprises of no parameters, but rather that it encompasses an infinite amount of parameters. Instead of imposing a simple, deterministic model as above, the GP replaces it and the function $f(t)$ transforms into,

$$f \sim \mathcal{GP}(\mathbf{m}, \mathbf{K}) \tag{2.22}$$

The mean function, $\mathbf{m}$ represents the deterministic model encompassing the easy-to-model elements (e.g., Keplerian model to describe a planetary signal),

$$\mathbf{m} = m(\mathbf{t}; \theta) \tag{2.23}$$

where it is a function of the input parameters, e.g., time stamps $\mathbf{t} = \{t_0, t_1, ..., t_N\}$, and of parameters needed to build the deterministic model θ. For simplicity, the mean function is usually set to zero, i.e., the GP is applied on the residuals after subtracting out the deterministic model.

The other term $\mathbf{K}$ is the covariance matrix encapsulating the kernel function that dictates how and to what extent two points (i.e., t_i and t_j) are correlated to one another,

$$\mathbf{K}_{i,j} = k(t_i, t_j; \phi) \tag{2.24}$$

where ϕ contains the hyperparameters of the GP as a means to describe the stochastic behaviors in the data that is not parametrizable, e.g., modulations due to stellar activity. Distinctive attributes to the data, e.g., the smoothness or roughness, the presence (or lack of) periodicity, can aid in selecting a sensible kernel function (see Section 2.4.3 for guidance on adopting the optimal kernel). In the case where the non-diagonal elements of the kernel matrix are zero, this simplifies back to a white-noise model.

In practice, a white-noise term is added to the kernel function transforming Equation 2.24 into,

$$\mathbf{K}'_{i,j} \equiv k'(t_i, t_j; \phi) = k(t_i, t_j; \phi) + \delta_{i,j}\sigma^2 \tag{2.25}$$

where $\delta_{i,j}$ is the Kronecker's delta and σ denotes the white-noise component. In the limit that the correlations between data points approach zero, the white-noise term if left standing. Thus, the diagonal elements of the kernel matrix denote the uncertainty for each data point whereas the non-diagonal elements represent the correlation between two data points, x_i and x_j.

Finally, to make it easy to incorporate the the GP into the modeling, we take Equation 2.10 of the log-likelihood and adapt it in the realm of the GP,

$$-\ln \mathcal{L}(\theta, \phi) = \frac{1}{2}\mathbf{r}^T \mathbf{K}^{-1} \mathbf{r} + \frac{1}{2}\ln \mathbf{K} + \frac{N}{2}\ln(2\pi) \tag{2.26}$$

where $\mathbf{r} = \mathbf{y} - \mathbf{m}$ represents the residual. In practice, we first try fitting for the deterministic model and then apply the GP onto the residuals.

The beauty of the GP is that we can relate some hyperparameters to physical interpretations, based on the kernel choice, i.e., ow smooth or rough can indicate the spot growth and decay time; the lengthscale, i.e., how closely correlated points are, can indicate the evolution times of spots; the amplitude of the GP can indicate the spot coverage on the stellar surface. Kernels that encompass both smoothness and randomness in one can thus model stellar activity's behavior.

2.4.3 Kernel choice

"But GPs can fit for anything!" - most likely someone in the room

Indeed, they are a powerful tool. They can fit anything, if you are not careful and allow them to. Choosing the right kernel is certainly an art form.

We need to ask ourselves why we are implementing a GP in the first place. Is there red-noise behavior that needs to be accounted for? Is there a stellar rotation period present in the data? Do we just want to fit a GP to make the final model look nice? Once the user understands the purpose the GP is supposed to fulfill and what intentions to continue with, then they can incorporate their expert knowledge onto the problem. Oftentimes the physical knowledge can inform the choice of the covariance function.

Below is a list of the most commonly used kernels for this thesis, as well as in the field, along with a description of when one would use them, what their hyperparameters physically represent, and how they behave in practice with included examples. In the following descriptions, the kernel function is represented as $k_{i,j}(\tau)$ which is the equivalent to what was given in Equation 2.24 where τ is now the temporal distance between two points.

Squared-exponential kernel This is the immediate classic kernel used as a GP if one wants to apply a simple red-noise model to the data. This kernel is characterized as being incredibly smooth since it is infinitely differentiable and is typically meant for situations when some underlying behavioral trend is apparent in the data but cannot be deterministically modeled (e.g., see TESS sector 31 data in Sect. 5.3). The kernel follows as such,

$$k_{i,j}(\tau) = \sigma_{\rm GP}^2 \exp\left(-\frac{\tau}{T_{\rm GP}}\right) \tag{2.27}$$

where $\sigma_{\rm GP}$ is the amplitude of the GP modulation, and $T_{\rm GP}$ is the characteristic timescale.

A large $T_{\rm GP}$ signifies that the data points continue to influence points farther away, whereas a small value suggests that the data points have very little or no influence on the other points in the dataset other than those closely neighboring them. In the limit as $T_{\rm GP}$ becomes infinitely small, the kernel approaches zero and resembles a white-noist term. $T_{\rm GP}$ is commonly equated to $1/2l^2$ where l is the length-scale that addresses the how "wiggly" the GP appears. Generally, one would not be able to extrapolate more than l units away from the given data.

Matérn-3/2 kernel The Matérn (also written as Matern) kernel is a generalization of the squared-exponential kernel where it has an additional parameter, $\rho_{\rm GP}$, to introduce a

roughness factor. Typically we use the (approximated) Matern-3/2 kernel provided by `celerite`,

$$k_{i,j}(\tau) = \sigma_{\rm GP}^2 \left(1 + \frac{\sqrt{3}\tau}{\rho_{\rm GP}}\right) \exp\left(-\frac{\sqrt{3}\tau}{\rho_{\rm GP}}\right) \tag{2.28}$$

where $\sigma_{\rm GP}$ is the amplitude of the GP, and now $\rho_{\rm GP}$ is the length scale of the GP modulations to vary the smoothness of the return functions. This kernel is preferred for data that have more of a chaotic behavior to them and are not as smooth (e.g., TESS sector 4 photometry in Sect. 5.3) since the flexibility of $\rho_{\rm GP}$ can better control the smoothness of the functions.

Exponential-sine-squared (QP-GP) kernel Here we have the de facto default kernel for quasi-periodic signals, i.e., signals that have an underlying periodic behavior but may undergo various amplitude fluctuations and phase shifts. The idea is to multiply the periodic (sine-squared) kernel with the exponential-squared kernel to account for this type of quasi-periodic behavior and presented by `george` as the quasi-periodic GP (QP-GP),

$$k_{i,j}(\tau) = \sigma_{\rm GP}^2 \exp\left(-\alpha_{\rm GP}\tau^2 - \Gamma_{\rm GP}\sin^2\left[\frac{\pi\tau}{P_{\rm GP,rot}}\right]\right) \tag{2.29}$$

where $\sigma_{\rm GP}$ is the amplitude of the GP, $\alpha_{\rm GP}$[13] is the inverse length-scale of the GP exponential component, $P_{\rm GP,rot}$ corresponds to the recurrence timescale, and $\Gamma_{\rm GP}$ is the amplitude of the GP sine-squared component.

This kernel is by the far the one put most in practice by the RV community as the hyperparameters are physically interpretable, e.g., $P_{\rm rot}$ relates to the periodicity of spots co-rotating on the stellar surface; $\sigma_{\rm GP}$ represents the amplitude of the modulations, possibly related to spot sizes; and the lengthscale l depicts the decay time of stellar spots. Thus far, it has done a relatively fine job for accounting for stellar activity (Angus et al., 2018). For these reasons, it has become the "go-to" kernel in the RV community.

Double simple harmonic oscillator (dSHO) kernel The double simple harmonic oscillator (dSHO) is the sum of two stochastically-driven, damped harmonic oscillator (SHO) terms, made possible within `juliet` by implementing a RotationTerm analogue to the one in `celerite2`[14] (Foreman-Mackey, 2018). The power spectrum of each SHO term is given by Anderson et al. (1990),

$$\mathrm{SHO}_1(\omega_{\rm GP}) = \sqrt{\frac{2}{\pi}} \frac{S_0\omega_1^4}{(\omega_{\rm GP}^2 - \omega_1^2)^2 + \omega_1^2\omega_{\rm GP}^2/Q_1^2} \tag{2.30a}$$

and

[13] $\alpha_{\rm GP} \equiv \frac{1}{2l^2}$add footnote on the mistake in the juliet paper for the lengthscale?

[14] `https://celerite2.readthedocs.io/en/latest/`

$$\mathrm{SHO}_2(\omega_{\mathrm{GP}}) = \sqrt{\frac{2}{\pi}} \frac{S_0 \omega_2^4}{(\omega_{\mathrm{GP}}^2 - \omega_2^2)^2 + \omega_2^2 \omega_{\mathrm{GP}}^2 / Q_2^2} \tag{2.30b}$$

where we applied the Rotation terms,

$$Q_1 = 0.5 + Q_0 + \delta Q \tag{2.30c}$$
$$\omega_1 = \frac{4\pi Q_1}{P_{\mathrm{rot}} \sqrt{4Q_1^2 - 1}} \tag{2.30d}$$
$$S_1 = \frac{\sigma_{\mathrm{GP}}^2}{(1+f)\omega_1 Q_1} \tag{2.30e}$$
$$Q_2 = 0.5 + Q_0 \tag{2.30f}$$
$$\omega_2 = 2\omega_1 = \frac{8\pi Q_1}{P_{\mathrm{rot}} \sqrt{4Q_1^2 - 1}} \tag{2.30g}$$
$$S_1 = \frac{f\sigma_{\mathrm{GP}}^2}{(1+f)\omega_2 Q_2} \tag{2.30h}$$

where σ_{GP} is the amplitude of the GP, P_{rot} is the primary period of the variability, Q_0 is the quality factor for the secondary oscillation, δQ is the difference between the quality factors of the first and second oscillations, and f represents the fractional amplitude of the secondary oscillation with respect to the primary one.

Such a kernel choice is well-suited to represent stellar signals modulated by the rotation period of the star for its flexible nature and it smoothly varies. For purposes with RV modeling, the dSHO is only considered because it can model two active longitudes and therefore the first harmonic better (Jeffers & Keller, 2009).

Rotation Kernel (`celerite`)* Lastly, we introduce a simple celerite covariance function that was designed and shown to be an effective, yet computationally much faster, approximation to the QP-GP kernel. However, in practice, the posteriors and results were not behaving as expected. Since then, this kernel has been urged by the author to no longer be used[15] as it was just an exercise to show the reader the possibility of kernel choosing. Provided by (Foreman-Mackey et al., 2017), it takes on the form,

$$k_{i,j}(\tau) = \frac{B}{2+C} \exp\left(\frac{-\tau}{L}\right) \left[\cos\left(\frac{2\pi\tau}{P_{\mathrm{rot}}}\right) + (1+C)\right] \tag{2.31}$$

where B and C can be thought of as the amplitude of the GP component, L as the timescale for the amplitude-modulation of the GP, and P_{rot} as the period of the modulations, all of which are kept greater than zero. Typically, P_{rot} is the hyperparameter

[15] `https://github.com/dfm/celerite/issues/151`

physically motivated, and hence the one of most interest.

Concluding remark

Modeling time series in the framework of Bayesian statistics is certainly a powerful approach in embodying prior physical meaning into the model and in distinguishing which leading model describes the data. The Nested Sampling algorithm eased the computation for Bayesian evidences, opening the door for allowing more complex concepts into the model such as GPs.

Now that these statistical concepts have been introduced, we continue on on how they are incorporated into our modeling tools in the next Chapter.

3 A toolbox for detecting and modeling signals

3.1 Motivation

In a sea of various methods and tools to detect and model planetary and non-planetary signals hidden within the data, it can be rather daunting choosing the most suitable one. Different aspects need to be considered, e.g., how easy is it to use, the flexibility of the model setup, the sampling method used, and the list goes on. As more and more data continue to flow in with higher cadence (e.g., from transit surveys) along with follow-up observations (e.g., from spectrographs), it is crucial to simultaneously fit all available data within one model in order to reap the benefits of each dataset. Doing so can be extremely complicated in terms of setting it up and time-demanding regarding the complexity of the model.

The full step-by-step process comprises first identifying a signal in the data, determining its significance (i.e., if it is noise or not), determining the nature of the signal (i.e., due to a planetary companion or stellar activity), and appropriately modeling the signal. In the case of many signals present, deciphering the winning model of whether the data supports additional signals, e.g., planetary or not, is essential as this can lead to getting a better grasp on multi-planetary systems. It is thus important that the *correct* model is chosen, since scientific interpretations are based on the results. Therefore it is important to establish a standardized modeling approach in order to ensure comparable results among the community.

The following sections are focused on the tools that this thesis benefited most from. Starting with Section 3.2, detecting the signals is made accessible with GLS periodograms and interactive plotting tools within the GUI program `exostriker` (Trifonov, 2019). Section 3.3 is the main focus and is thoroughly dedicated to the `juliet` code as I was heavily involved with understanding and becoming familiar with it as a co-author. It is a modeling package that has become the "standard" tool used within many in the CARMENES consortium and outside as well, where I was helping many get acquainted with how it works, how to correctly set it up, and how to interpret the results, oftentimes being a main-contributing co-author in various publications, e.g., GJ 357 b c d, Luque et al. (2019); GJ 3473 b, c, Kemmer et al. (2020); TOI-442 b, Dreizler et al. (2020); TIC 237913194 b, Schlecker et al. (2020b); TOI-1685 b [c] Bluhm et al. (2021). Therefore, the aim is to build an intuition for the reader on "I have this data and this tool, where do I begin and what do my results mean?".

3.2 Detecting

Before we get to modeling, we have to first find the signals. To begin, I briefly introduce how we detect signals specifically in RVs. The section is geared more towards identifying signals in the spectroscopic data seeing that the bulk of this thesis deals with this doing so for this type of data. Being part of the CARMENES-TESS working group, signals from transit photometry are usually smoothly acquired with no need to painstakingly search for potentially interesting signals, largely thanks to the help of the Science Processing Operations Center (SPOC; Jenkins et al., 2016), which provide a catalog of TOIs[16], whose periods and transit times are already specified.

Within RV data, it is surely sometimes possible that one can easily spot and recognize a signal if the amplitude is rather large compared to the measurement uncertainty and the sampling of the data is sufficient. Oftentimes, this is unfortunately not the case and we require special tools to be able to extract signals from noisy time-series data, especially if we are hunting for low-mass planets that would generate low-amplitude signals.

3.2.1 GLS periodograms

The first natural step is to make a Generalized Least Squares (GLS; Zechmeister & Kürster, 2009) periodogram, an upgrade to the Lomb-Scargle periodogram (Lomb, 1976; Scargle, 1982) where offsets and the uncertainties of each data point are taken into account. The GLS periodogram works by fitting for a sinsuoid at each test frequency and optimizing the chi-square χ^2, defined as

$$\chi^2 = \sum_i \frac{(y_i - m_i)^2}{\sigma_i^2} \tag{3.1}$$

where y_i is the data, m_i is the sinusoidal function plus a constant, and σ_i is the uncertainty for the data point. Thus the most significant peak corresponds to the most probable signal to explain the data. This works well for the most part when planets follow circular orbits, since this periodogram explicitly tests through various frequencies of sinusoids. In cases where the planet is rather on an eccentric orbit, the Blum-Kiefer-Rosenblatt periodogram (Blum et al., 1961) may perform better as it is more successful in detecting periodicities with a sawtooth behavior. Taking it even a step further is the phase-distance-correlation periodogram (Zucker, 2018), with the added benefit of generalizing the GLS to shapes beyond just the sinusoidal. However, for our purposes, the GLS periodogram fulfills our needs.

Assessing the statistical significance Even if a peak is present, we need to verify that it is meaningful among the other peaks at different frequencies. In the scenario where the data is simply noisy and poorly sampled, spurious peaks in the periodogram can appear as if they are real signals even though they are just artifacts by coincidence (Hatzes, 2002). The false alarm probability (FAP; Scargle, 1982) acts as a metric in determining the significance of a

[16] `https://tev.mit.edu/data/collection/193/`

signal in the GLS/LS periodogram, and is given as such,

$$\mathrm{FAP} = 1 - (1 - e^{-z})^{M} \tag{3.2}$$

where M is the number of independent frequencies and can be estimated by the number of peaks in the periodogram, and z is the power of the peak in the periodogram. Above serves as just an analytic estimate, but a more accurate FAP value can be calculated via a bootstrap technique of iteratively resampling a dataset, e.g., 10 000 times, without replacement to examine how frequently a certain power level (z_0) is achieved solely by chance. The most common values to compute are 10%, 1%, and 0.1%, where the threshold for a signal to be deemed certain is above 0.1%.

Pre-whitening If there is one, there are probably many. Exoplanets are commonly found in multi-planetary systems meaning that it is not surprising to find a multitude of signals in the periodogram. The process of pre-whitening is continually removing the dominant, significant peak and recomputing the periodogram until there are no interesting peaks left. For each iteration, a simultaneous sinusoidal fit is carried out, e.g., a combined two-sinusoidal model, or three-sinusoidal model, etc. The purpose of executing many GLS periodograms is to identify potentially interesting signals in order to build the priors for the later Bayesian model runs with `juliet` in order to establish the nature of the signal.

3.2.2 Aliasing

Ideally, the perfect observational schedule would consist of acquiring equally-spaced measurements continuously over a long uninterrupted amount of time. This is, however, not the world we live in. Discrete measurements and gaps in the observations can lead to aliasing. This effect due to the sampling of the data creates spurious signals that appear as real, physical signals and divert the attention from the "true" signal. The expected frequency of an alias, f_{alias}, can be computed by,

$$f_{\mathrm{alias}} = f_{\mathrm{true}} \pm m \cdot f_{\mathrm{sampling}} \tag{3.3}$$

where f_{true} is the true signal, f_{sampling} is the sampling frequency, and m is an integer value. Once the true signal is accounted for, then *all* other signals due to aliasing will also disappear. If any suspected alias signals persist, they were not related to begin with.

As expected, aliasing is an issue as it can lead to hastily assuming an incorrect period rather than the physical orbital period; as already in the case for 55 Cnc e discovered by McArthur et al. (2004) and corrected by (Dawson & Fabrycky, 2010).

One's immediate instinct says that the true signal should always have the highest power with respect to their alias counterparts. This holds almost always true for noise-free data, however, this thought quickly breaks down with noisy data (Dawson & Fabrycky, 2010), which is usually the case when searching for low mass targets in surveys (see also Figure 3.4). In an attempt to classify the correct frequency, Dawson & Fabrycky (2010) proposed the idea of generating sinusoidal simulations by assuming the "true" frequency and then comparing the phase and amplitude of the periodogram to that of the given data. If the peaks and phases of the periodogram matched relatively well within reason, then the correct

period was chosen. If not, then more potential frequencies should be tested. If the outcomes were still inconclusive, then more data would be required to break down the aliasing.

The newly-developed tool `AliasFinder`[17] (Stock & Kemmer, 2020) is a user-friendly Python 3 script that easily performs alias testing following Dawson & Fabrycky (2010). Its capability is outlined for the YZ Ceti system (Stock et al., 2020a), another case where aliasing caused the wrong periodicity to be selected (Astudillo-Defru et al., 2017). In cases where the `AliasFinder` was inconclusive in distinguishing the true signal among two periods, even comparing the log-evidences of the models with each signal being the chosen period was unsuccessful, as expected (see Sect. 5.6.2).

3.3 Modeling with `juliet`

The modeling included in this thesis is largely thanks to the python package `juliet` (Espinoza et al., 2019a). Many of the non-trivial concepts, i.e., Bayesian statistics, Nested Sampling, and GP regression, that `juliet` employs were already introduced and outlined in Chapter 2. The aim of this section is to provide the reader a solid understanding of how to build the intuition for approaching fits using `juliet`, as there are many nuances and subtleties that can be overlooked. Numerous studies, including lots of *TESS* discovery papers have benefited from using the package, e.g., Brahm et al. (2019b); Kossakowski et al. (2019); Luque et al. (2019); Jenkins et al. (2019); Bluhm et al. (2020); Espinoza et al. (2020); Bluhm et al. (2021)

3.3.1 What is `juliet`?

The fundamental goal of the python package `juliet` is to model transit photometry, radial velocities, or both, using Nested Sampling algorithms as an efficient way to obtain not only posterior distributions for the parameters, but just as importantly, the Bayesian evidences for i.e., comparison.

The tool employs a variety of already developed packages such as `batman` (Kreidberg, 2015) and `radvel` (Fulton et al., 2018) for modeling the transit photometry and RV data, respectively. Stochastic processes, e.g., due to stellar activity or instrumental effects, are modeled as GPs, for which are provided by the `celerite` (Foreman-Mackey et al., 2017) and `george` (Ambikasaran et al., 2015) packages where the most frequently applied ones are presented in Section 2.4.3. Calculating the Bayesian evidence $\ln \mathcal{Z}$ is done via Nested Sampling using either MultiNest (Feroz et al., 2009) via the `PyMultiNest` package (Buchner et al., 2014) or the `dynesty` package (Speagle & Barbary, 2018; Speagle, 2020) such that classic Nested Sampling, Importance Nested Sampling or Dynamic Nested Sampling can be selected (see Section 2.3 for the explanations on the differences).

Constructing a competent model to the data is surely achievable. This includes the ability to simultaneously fit multiple transiting and non-transiting planets, combining a variety of photometric and radial velocity datasets where each could have its own GP hyperparameters or commonly shared hyperparameters if desired, e.g., stellar rotational period signals present in both photometry and RVs, or among various RV instruments. The transit model is itself

[17] `https://github.com/JonasKemmer/AliasFinder`

with an additional dilution factor term that takes flux contamination from nearby sources into account. The radial velocity model comprises $N_{\rm RV}$ Keplerian signals (Equation 1.7) as well as a linear or quadratic trend. The huge advantage of this joint-modeling code is its versatility where we can fit a variety of parameters efficiently and explore the parameter space fully given that we are implementing a Nested Sampling algorithm.

Other similar packages include, but are not limited to, `EXOFAST` (Eastman et al., 2013), `PlanetPack3` (Baluev, 2013, 2018), `pyaneti` (Barragán et al., 2019) with each having their own advantages and disadvantages summarized in Espinoza et al. (2019a). The two competing ones that were concurrently developed and share many resemblances to `juliet` are `allesfitter` (Günther & Daylan, 2019) and `exoplanet` (Foreman-Mackey, 2019). The former is comparable though not as user-friendly, whereas the latter produces posterior distributions but not the Bayesian evidences. Within `exoplanet`, it is also possible to simultaneously model astrometric data (e.g., GJ 338 B González-Álvarez et al., 2020).

3.3.2 Instrumental jitter and offsets

Data come with "uncertainties", which are limitations of knowledge, not "mistakes" –
Matthew Sands (1919-2014), accredited by Hogg et al. (2010)

The uncertainty in the log-likelihood (Equation 2.10) corresponds to the internal standard uncertainty $\sigma_{\mathcal{D},i}$ of the data points themselves. The assumption made is that these uncertainties are considered true and accurate, which is not always the case, especially for RV data prone to various stellar astrophysical effects (Wright, 2005). To mitigate the potential under-estimation, it was suggested by Baluev (2009) to transform the total variances of the RV uncertainties by including a constant "jitter" term σ added in quadrature,

$$\sigma^2_{{\rm total},i} = \sigma^2_{\mathcal{D},i} + \sigma^2 \tag{3.4}$$

where $\sigma_{{\rm total},i}$ now replaces the previous data uncertainty $\sigma_{\mathcal{D},i}$. The coined jitter term is simply a value that is added onto the provided uncertainties for a whole dataset of a given instrument to allow a buffer for potentially more uncertainty in the data. Its composition can be a combination of instrumental effects, astrophysical processes, and outcomes from data reduction; however, regardless of its origins, it ensures the principle that the data uncertainties are not accepted as exact. Certainly if there is a quasi-periodic signal, i.e., not just white-noise, then a temporal red-noise model would be better suited (Section 2.4.1).

Each individual dataset should have its own jitter term. For photometric data sets, the amount of scatter can range from 1 to 10 000 ppm, therefore a Jeffrey's prior is recommended. For the RVs, a uniform prior is sufficient, unless the RV fluctuations are on the order of 100s of $\mathrm{m\,s^{-1}}$, then a Jeffrey's prior would also be suitable. Depending on the data quality, the jitter term might be consistent with zero, e.g., high-quality space-based photometric data from *TESS* or when a GP is also included. In this case, it is sufficient to perform intermediate runs excluding the jitter, i.e., fixing it to 0, to comprise less variable parameters in the model to speed up the process. For the final fit, however, it is advisable to keep the jitter free in order to report 95% confidence intervals.

As for the offsets, because the photometry by nature is already normalized to 1, it is expected that the offsets are slightly diverging from this base value and therefore can be

centered around 0, either with a normal or uniform prior that do not need to be substantially wide. On the other hand, there are true instrumental offsets within the RVs depending on the model that can fluctuate depending on the deterministic model. Once a rough general median value for the RVs is obtained, then a relatively wide uniform prior centered on it is sufficient.

3.3.3 Parametrizations

Rather than directly fitting certain model parameters comprised in the transit and RV model, it is standard practice to follow particular paramerizations to ensure even and efficient sampling for the execution of the model fitting. The final physical and deterministic parameters should be reported, i.e., in a posterior table.

Impact parameter and planet-to-star radius ratio – (p, b) The impact parameter $b \equiv (a/R_*)\cos i$, is defined to be the projected distance between the planet and star centers during mid-transit depending almost entirely on the transit shape and transit depth (Figures 1.1 & 3.1); where we also have the planet-to-star radius ratio $p \equiv R_p/R_*$, taken directly from the transit depth, $\delta = p^2$. Both are unitless parameters commonly used in the transit model as long as $0 < p < 1$ and $0 < b < 1 + p$ to produce meaningful physical results.

The prior choice is sometimes non-trivial and can lead to observational biases for transiting planets where the whole parameter space is simply not examined (Kipping & Sandford, 2016). Thus, instead of fitting directly for these terms, we choose to use the parametrization introduced in Espinoza (2018) in which we fit for the parameters r_1 and r_2 with uniform priors $\mathcal{U}(0, 1)$, ensuring that we explore the whole range of physically plausible values in the (p, b) plane.

In cases where b and p are unrealistically large after transforming back, this could be caused by a degeneracy in the geometry of the transit (Eylen & Albrecht, 2015). The flux dip in the lightcurve due to a relatively small planet in a full transit can also be resembled by the dip due to a large planet in a grazing transit (i.e., large b and p). Incorporating higher precision data could break the degeneracy as was the case in Schlecker et al. (2020b) where the sparse 30-min *TESS* data needed additional higher-cadence, ground-based photometry to better sample the shape of the flux dip. Alternatively, without extra data, the maximum allowed planet-to-star ratio can be set within `juliet` as an easy solution. An even better option, and the most preferred one, is if the stellar parameters are of high precision, then the stellar density should be used as a prior and included as an extra data point (see below).

Limb darkening coefficients (LDCs) – $(\mathrm{q}_1, \mathrm{q}_2)$ Stellar limb darkening is the wavelength-dependent phenomena where the star's surface appears brighter in the central part rather than on the edge. The effect behaves stronger for shorter wavelengths, causing the transit shape appear more rounded (Figure 3.1). For more in-depth descriptions of how it affects the transit light curve model, the reader is referred to the following works: Claret (2000); Mandel & Agol (2002); Kjurkchieva et al. (2013).

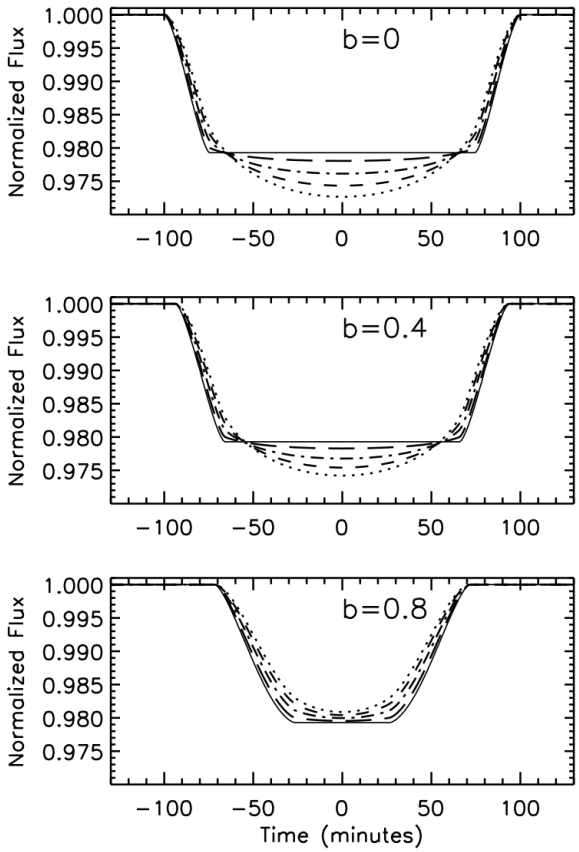

Figure 3.1: Theoretical light curves for three impact parameters b (0,0.4,0.8) representing in order a full transit to a grazing transit (solid line). The other lines illustrate the effects of limb-darkening, where the shorter the wavelength, the rounder the curve towards the bottom. Increasing b transforms the transit from a "boxy" shape into a more "rounded" shape (Figure 3.1). After Seager & Mallén-Ornelas (2003, Figure 3)

The parameters to describe this effect, known as limb darkening coefficients (LDCs), were oftentimes left fixed since it was too computationally heavy to incorporate them simultaneously into the model (Mandel & Agol, 2002; Kjurkchieva et al., 2013). This can however lead to potential biases based on limb darkening assumptions and should be avoided (investigated in e.g., Espinoza & Jordán, 2015).

High-precision, oftentimes space-based, transit data (i.e., *TESS*) can be modeled with a quadratic limb-darkening law ($\{u_1,u_2\}$), whereas the lower-precision, ground-based photometric instruments should be assigned linear limb-darkening laws ($\{u_1\}$), based on the work of Espinoza & Jordán (2016). To employ uniformative priors for the linear and quadratic limb-darkening laws, we typically adopt the parametrization with the

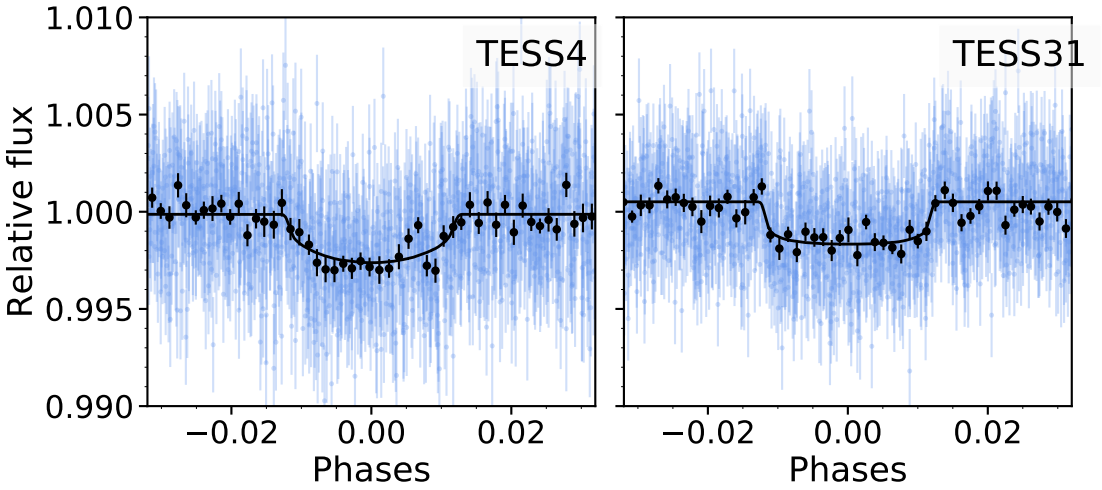

Figure 3.2: Phase-folded transits for TOI-1201 b for *TESS* sector 4 (top left) and sector 31 (top right), with the GP components subtracted out. These are comparable to those in Figure 5.5 with the exception that the LDCs are not shared among the two instruments. The shape of the flux dip is incorrect.

uniform sampling scheme from Kipping (2013a),

$$u_1 = 2\sqrt{q_1}q_2 \tag{3.5a}$$
$$u_2 = \sqrt{q_1}(1-2q_2) \tag{3.5b}$$
$$q_1 \equiv (u_1+u_2)^2 \tag{3.5c}$$
$$q_2 \equiv \frac{u_1}{2(u_1+u_2)} \tag{3.5d}$$

for which u_1 and u_2 are the coefficients for the linear and quadratic terms, respectively, and q_1 and q_2 are their parametrizations used in the model. Now, a uniform prior – $\mathcal{U}(0,1)$ – can be applied to both q_1 and q_2. We can simply quote back the true LDCs using the transformation in Equation 3.5.

It is discouraged to fix the LDCs to a particular value from stellar models, but if anything, a more informed prior could be applied because the same instrument (i.e., same wavelength) should produce the same LDCs. That being said, the LDCs do vary for a given instrument with different planets depending on the geometry of the system (Howarth, 2011). However, the discrepancy among the LDC computations are insignificant, and thus, the LDCs can be left as unique to each instrument. In the case where data quality from the same instrument is variable, one should share the limb-darkening coefficients (i.e., see Section 5.6.1 for an example on TOI-1201 b). Figure 3.2 demonstrates a particular case in which the LDCs of two *TESS* sectors were not shared leading to a discrepancy on the transit shape, even though there should not be one. This could be attributed to the larger variations during one *TESS* sector compared to the other (see Figure 5.5).

eccentricity, omega – (e,ω) The eccentricity, e, and argument of periastron, ω, can be

parametrized in three different ways, all of which are described in detail for their strengths and weaknesses in Eastman et al. (2013). The first is directly straightforward, where the prior on e is uniform from 0 to 1 and ω from $-\pi$ to π, but faces an issue of being computationally demanding. The second is faster using the reparametrization with $e\sin\omega$ and $e\cos\omega$, but runs into the complication that e favors higher eccentricities and is thus not uniform for all values as shown by Ford (2006). The third, and most recommended one, is via the transformation of $\mathcal{S}_1 = \sqrt{e}\sin\omega$ and $\mathcal{S}_2 = \sqrt{e}\cos\omega$ where $e = \mathcal{S}_1^2 + \mathcal{S}_2^2$ and $\omega = 2(\mathcal{S}_1\mathcal{S}_2)$. Here, the problem of e being uniform is fixed and the computation time is optimized. If the eccentricity is kept free, then uniform priors from -1 to 1 for both $\mathcal{S}_1$ and $\mathcal{S}_2$ are implemented, otherwise it is fixed to 0 for circular orbits.

Certainly if a circular fit is chosen, then the first direct way is likewise sufficient. One could also implement a non-uniform prior, such as the beta distribution as proposed by Kipping (2013b, 2014); however, this approach favors lower eccentricities and already assumes that the current observations are physically true (e.g., as for small planets in multi-planetary systems Van Eylen & Albrecht, 2015), which may not always be the case. On the other hand, it could allow for eccentricity to be free while preventing physically unlikely high eccentricities (i.e., the long-term signal present in the TOI-1201 system, Section 5.6.2). Additionally, Hara et al. (2019) showed that estimates may be biased towards higher eccentric values, which could be due to a combination of incorrect assignment to the data uncertainty as well as issues with the sampling frequency.

Stellar density – (ρ_*) It is beneficial to include ρ_*, the stellar density, as a prior rather than the scaled semi-major axis, a/R_*, for cases where the stellar parameters are well known and have high precision. Previously, the scaled semi-major axis deduced from the transit light curve would shed more light on the stellar density via Seager & Mallén-Ornelas (2003); Sozzetti et al. (2007),

$$\rho_* = (\frac{3\pi}{\mathrm{G}P^2})(a/R_*)^3 - \frac{M_p}{R_*^3} \tag{3.6}$$

and hence would provide a constraint on the stellar radius. However, in current times, largely due to newer and more precise data (i.e., from *Gaia* eDR3; Gaia Collaboration et al., 2020), we can now take advantage of the estimated stellar density and do the opposite. The transit light curve provides tight constraints on P from the periodicity of the transits, therefore, the stellar density can be used instead to constrain a/R_*.

This has been extremely beneficial for breaking degeneracies in transit modeling (e.g., with the impact parameter) and as well for systems with multiple transiting planets. For the former benefit, the power of incorporating ρ_* as a data point has the advantage of constraining a/R_*, which in turn constrains the impact parameter b, which can then aid in breaking the degeneracy with the eccentricity (Huber et al., 2013), but only to a certain extent (Sandford et al., 2019). For the latter mention, each planet would formerly impose its own value for the stellar density through a/R_*, even though there can only be one value for the stellar density. Hence, including the stellar density eases model fits with numerous transiting planets.

Implementing wise, the best practice is to take the mass and radius of the star along with its uncertainties and propagate them through to compute the estimated mean stellar density $\rho_* = \frac{4\pi M_*}{3R_*}$, and its Gaussian uncertainties σ_{ρ_*}. Then, this is incorporated as a normal prior $\mathcal{N}(\rho_*, \sigma_{\rho_*})$. Section 4.6.1 shows what impact a constrained versus uninformative stellar density prior entails.

As a note, when the stellar density is chosen as a prior, it is also incorporated as an additional dataset/data point to the already existing data. Therefore, one should be careful when performing i.e., comparisons ensuring that the datasets are in fact consistent, i.e., models using a/R_* as a prior should not be compared to models using ρ_* as a prior.

3.3.4 Performing transit-only, RV-only, and joint fits

We focus on how to set up various model fitting techniques to save time and to put in logic to what we are doing as a justification. Continually performing joint fits can become extremely time-intensive given the oftentimes large parameter space (>20 parameters), complexity of the model (e.g., including GPs), and large datasets making it absolutely unnecessary for every minor instance of tweaking the model. Instead, it is beneficial to perform individual transit- and RV-only model fits as "intermediate runs" when possible before combining both data sets for a final joint fit.

The reason in doing so is since both the transit photometry and radial velocity data have their own assets as an independent dataset from the other one where the other plays no significant role. For example, the transit photometry (e.g., from *TESS*) can provide extremely accurate and precise measurements for the period, P and transit time, t_0, for short-period planets. Such precision is usually not attainable with radial velocity data alone considering that the nominal uncertainty values are much higher (see Section 3.3.5 for a case study). On the other hand, the shape of the light curve lacks in constraining the eccentricity of the orbit as many correlations arise with the impact parameter (e.g., Huber et al., 2013; Eylen & Albrecht, 2015), though the RV data can come in and break the degeneracy in that regard (see Section 3.3.5 for an example).

Additionally, it is quite common that there are less planets transiting in a system than there are potential planetary signals found in the RVs. Understandably so, because the probability of catching a transiting planet decreases the farther out a planet is from its host star (Eqn. 1.1). Oftentimes it is even the case that a detection of a planet from a transit survey uncovers even more planets in the system through RV follow-up, e.g., GJ 357 c d, Luque et al. (2019); Jenkins et al. (2019); GJ 3473 c, (Kemmer et al., 2020); TOI-1685 [c], Bluhm et al. (2021). Hence, when there are multiple potential planetary signals found in the RVs, it is rather meaningless to continuously keep re-performing combined fits considering the transit photometry only provides valuable information on those planets that are indeed transiting. Therefore, it is beneficial to take advantage of the transit data to get extremely precise planetary parameters and then use the RV data to assess all the present potential planetary and non-planetary signals which would then compose the final applied, chosen model.

The following serves as a nearly step-by-step thought process of performing an analysis with a dataset that comprises both transit photometry and spectroscopy.

Transit-only fits

"Base" light curve The primary step is to identify the transiting planets in the light curve. Typically speaking, the detection comes from a space-based mission (e.g., from *Kepler*, *K2*, *TESS*) with relatively high cadence over multiple days acting as the "base" light curve and is then followed up using ground-based observations for confirmation.

The period, P, can be determined by various methods, the most popular one currently being the Box-Least Squares (BLS; Kovács et al., 2002) algorithm. Determining the transit time, t_0, can usually be done by visually inspecting the light curve to get a rough estimate, which is sufficient for the initial run; or one could attain a more precise value by performing a quick fit within `exostriker`. It is good practice to center the transit time around the last observable transit (i.e., in the "base" light curve) as it is the freshest and most up-to-date making it more accessible to propagate the uncertainties for future follow-up measures (see Section 3.3.5).

The general approach is to first focus on the base light curve to figure out all the model parameters it needs before combining all available transit photometry for the final transit-only fit. The prior on P should be a narrow, uniform to prevent potential biases with a width of 10 % of the periodicity.. As for t_0, the prior should also be uniform where the width encapsulates the times within a transit (i.e., between t_1 and t_4 in Figure 1.1). Eccentricity can be fixed to zero for the time being, since this will be explored in the RV-only fits.

If the residuals of such a run show time-correlated behavior, a GP trained on the time stamps would be adequate to detrend the light curve. With the focus on *TESS* given that the time span of one sector is just 28 days, most periodic modulation due to the stellar rotation period ($P_{\rm rot} \lesssim 14\,{\rm d}$) is averaged out. For this reason, it is more advantageous to employ either a squared-exponential or Matern-3/2 GP kernel, depending on the smoothness of the variations, as specified in Section 2.4.3. The GP is kept in the model if the log-evidence favors it.

Including additional photometry Now, additional follow-up photometry can be introduced. These data typically do not have the high precision that the base photometry has and undergo atmospheric effects and data systematics. Detrending these light curves can be done by also applying a GP, or rather more recommened, by applying a linear model onto the auxiliary data, e.g., airmass, x and y pixel centroid, background stars. If there are multiple follow-up observations, there two ways in performing the intermediate fits. Either the follow-up observations stand on their own and the priors on the P and t_0 are simply tightly constrained using the posteriors from the base light curve fitting, making this a very rapid computation. However, if the data quality is poor, this can fail and produce peculiar and undesirable results. In this case, the second approach is to perform combined runs where the follow-up observation is paired with the base light curve.

Once the nitty-gritty is sorted out and settled, the final transit-only run combining all photometric data can be executed. The posteriors on P and t_0 on this last run will serve as as guide for the priors for the final joint fit as well for the RV-only fit.

RV-only fits

Follow-up RVs for transits confirm the planetary signal, provide a mass determination (i.e., leading to a density estimate), and can even unveil additional planetary companions in the system (see Section 1.5 for why all of this is important).

In contrast to the transit-only fits where the base light curve can comprise at least roughly 20 000 exposures (i.e., 2 min cadence for 28 d from one *TESS* sector), the RV-only fits constitute substantially less on the order of 10's of data points and therefore the RV-only fits are considerably much quicker.

If a planet is detected as a transit, then it imposes a gravitational tug on its host star. Most likely, this means it is present in RV data, with the exception of some scenarios, e.g., a small planet in a wide orbit that produces signal much lower than the current detection limits. To save time and ensure accuracy, the priors for the period and transit time of a transiting planet can be fixed to the median of the posteriors values produced by the transit-only fits justified that the transit data uncertainties are much smaller than what the precision of the RV data could attain. Otherwise, one could also apply normal priors centered at the median value with inflated uncertainties, or narrow, uniform priors with a width of at least three standard deviations, to save computation time with the latter. Employing the same narrow, uniform priors as for the transit-only fits is not always advised because it some cases it can be rather erroneous due to incorrect, but closely identical, periodicities, i.e., due to aliasing, being picked up (as shown in Section 3.3.5). For non-transiting planetary signals, a wide-enough uniform prior should suffice. Because the prior is flat, the posterior will be data-driven.

For non-planetary quasi-periodic signals, a QP-GP or a dSHO-GP should be applied with a slight preference for the dSHO-GP kernel for its computational speed. A full summary of the differences between the two is demonstrated in Section 2.4.3. The hyperparameter of main interest is the period $P_{\rm rot}$ representing the modulation of the GP analogous most of the time to the stellar rotation period. Long-term photometry monitoring and stellar activity indicators found in the spectra can point to this signal. There are often two approaches to constructing the prior for the rotational period $P_{\rm rot}$; either employing a wide, uniform prior or a relatively conscious uniform prior. The former serves as an attempt to identify any unknown quasi-periodic signals whereas the latter is possible with previous knowledge of the rotation period's location (Stock, 2021).

In the case of solely possessing RV data and no transit photometry, the approach to follow is the same as for additional non-transiting potential planetary signals modeled as Keplerians. Wide-enough uniform priors should be put in place for the P and t_0.

Joint fits

The bulk of the strenuous work has been executed in the transit- and RV-only fits. Now, the process becomes smooth and effortless, only needing to combine both types of datasets to run the final joint fit. The posteriors of the RV-only fit help construct the grand picture of how many planets construct the system. The priors for the transiting planets are motivated by the final transit-only fits by adopting the posteriors and amplifying the uncertainties by at least two magnitudes, whereas the priors for the non-transiting planets are similar to those in the RV-only fits. One just needs to wait for the run to finish and then the posteriors

await!

3.3.5 Additional applications and case studies

"*Everything is easier said than done*"

Not every run is always going to be smooth sailing. It is frequently the case that either the priors were overlooked causing the posteriors to look wonky, i.e., choosing the wrong prior type (Normal instead of Uniform), the posteriors are hitting the maximum, not sharing the LDCs, etc.

Precision of eccentricity: TOI-150 b case study

Spectroscopic data can resolve eccentricities much better than transit data can. For a circular orbit, the planet is revolving around the star at a constant speed, hence, the ingress and egress duration are identical. On the contrary, a planet following an eccentric orbit will have different projected speeds such that the ingress and egress durations are slightly skewed (Ford et al., 2008; Winn, 2010), e.g., short ingress and larger egress. The distinction is already so minute that the data quality of the transit light curve requires to be of highest standard. For spectroscopic data, as long as the phase of the period is decently sampled, the shape can already provide a fairly modest constraint on the eccentricity.

As a test example, I take TOI-150 b, a hot Jupiter on an eccentric orbit, $e = 0.26$, and I perform the following runs: transit-only, RV-only, and a joint fit, where the priors are consistent among all the runs and the eccentricity is left as a free parameter (following the recommended parametrization from Section 3.3.3). For these purposes, the transit light curve comprises just one *TESS* sector and the RV dataset is composed of the FEROS and CORALIE data (Section 4.3). The posterior distributions for the eccentricity are displayed in Figure 3.3, evidently demonstrating that the transit-only run suggested of an eccentric behavior, but could not constrain it as sufficiently as the RV-only data, $e = 0.35^{+0.29}_{-0.11}$ and $e = 0.28^{+0.05}_{-0.05}$, respectively. The joint fit is then driven by the RV data but slightly diverges, $e = 0.26^{+0.04}_{-0.04}$, most likely because the transit data contributes better constraints on the period and transit time, consequently shifting the eccentricity just a pinch.

Precision of P and t_0: TOI-1201 b case study

To investigate the discrepancy in precision for planetary parameters period P and transit time t_0 between transit- and RV-only fits, I focus on a *TESS*-discovered planet, TOI-1201 b. All available photometric data is used as input for the transit-only model (i.e., *TESS* and follow-up observations), and as for the RV-only fit, I only consider the transiting planet component from the final chosen RV model (a full description can be found in Section 5.6). The following test example is valid for a short-period planet where the transit photometry would constrain these parameters better than RVs. However, in the scenario of a single-transit object in *TESS*, the RV follow-up can rather help to refine the period.

A wide, uniform prior for both P and t_0 were applied, $\mathcal{U}(2.45, 2.55)$ and $\mathcal{U}(2459167.5, 2459170.5)$, respectively. Figure 3.4 illustrates the posterior distributions, showing how multiple solutions for (P, t_0) are probable within the RV data through the

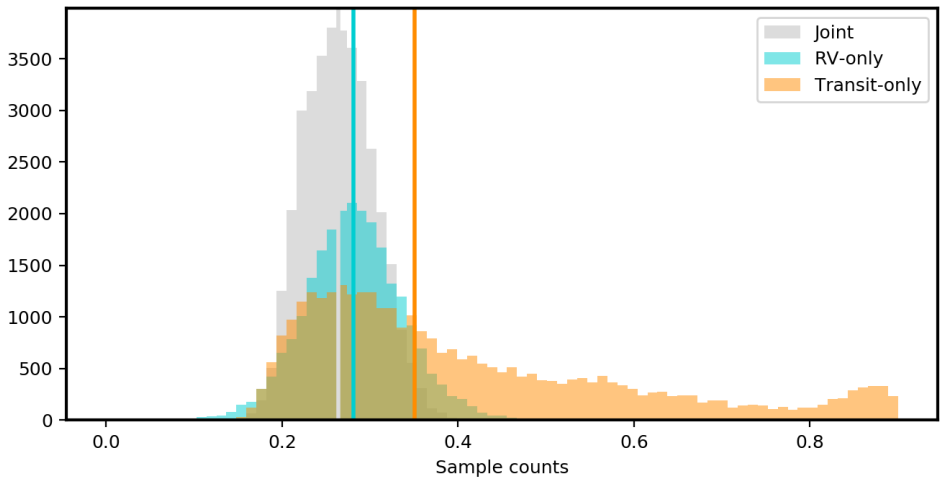

Figure 3.3: Posterior distributions of eccentricity from transit-only (orange), RV-only (teal) and joint (grey) fits for TOI-150 b, showcasing the capacity of RV data on constraining the parameter. The vertical lines represent the median values for each respective distribution.

apparent structure. In fact, without any knowledge of the transit, since the RVs suffer from aliasing (Section 3.2.2), the 1-year alias at ∼2.5 d could be falsely deemed as the "true" signal. The addition of transit data thus break the alias degeneracy.

Next, a more narrow, uniform prior is applied for the RV-only fit on P, $\mathcal{U}(2.48, 2.50)$ in order to better compare the two fits. Here, the uncertainties for P were 0.0000029 d and 0.0050 d, and for t_0 0.00049 d and 0.62 d, from transit- and RV-only fits respectively.

From this case study, it was shown that the transit data greatly constrain P and t_0 in comparison to the RV data. It is thus advisable to apply either very narrow uniform or normal priors based on the results given by the transit-only fits when performing RV-only fits to avoid detecting other more favorable signals, i.e., aliases. More so, to save on computational time, even fixing these values is recommended.

Sharing hyperparameters

GPs If both the photometry and radial velocities exhibit the stellar rotation period, it is possible to have the GP hyperparameters shared (e.g., most commonly $P_{\mathrm{rot,\,GP}}$) whereas others should be kept to the respective instrument (e.g., σ_{GP} could be in units of $\mathrm{m\,s^{-1}}$ for RVs and ppm for transit photometry). This also applies for datasets with various RV instruments each covering different wavelength ranges, since the RV amplitude induced by stellar activity is dependent on wavelength (Reiners et al., 2010). In the special case where there are two RV instruments that cover *exactly* the same wavelengths (e.g., CARMENES-VIS and HARPS-S), then in theory, the amplitude of the stellar rotation signal should be coherent among both instruments, and the only amplitude discrepancy between the two should be the instrumental jitter terms. Chapter 6 on AD Leo is a prime example of how to execute this and why it is necessary.

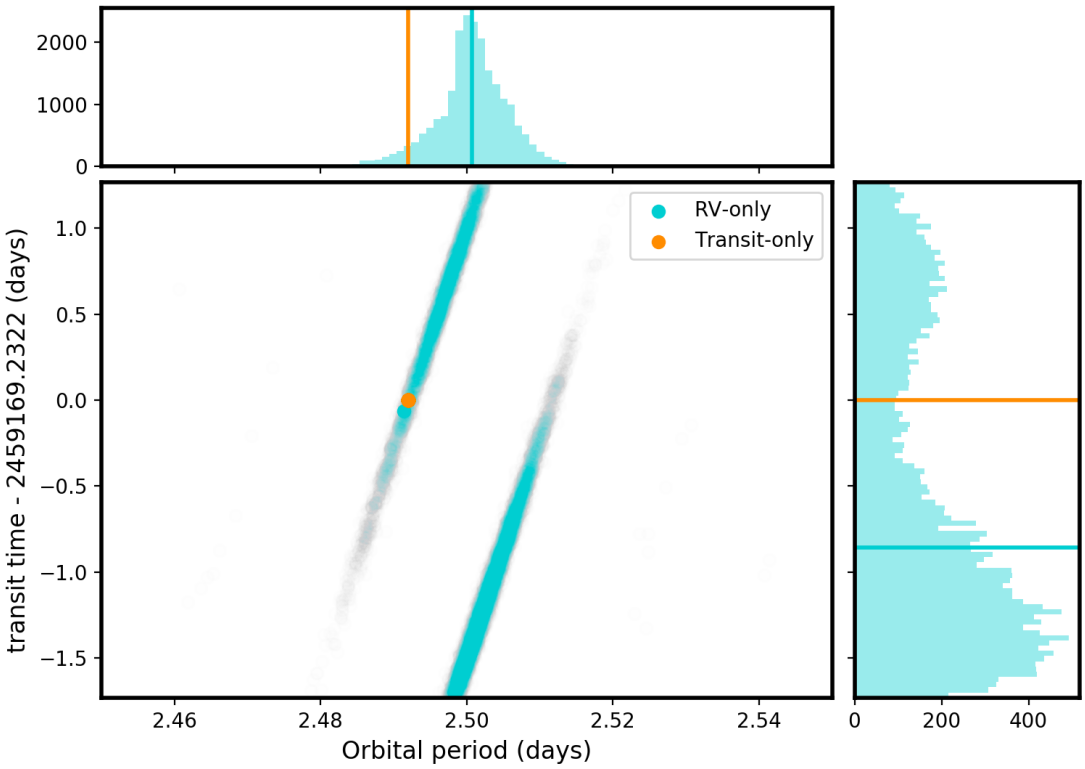

Figure 3.4: Posterior distributions of period P and transit time t_0 from a transit-only (orange) and RV-only (teal) fit on the example case of TOI-1201 b. The P and t_0 priors are consistent for both models, given by the boundaries of the plot. The axis for t_0 is centered around the final value given by the joint fit. The lines in the histogram represent the median values.

LDCs Furthermore, if different sectors of transit data were taken with the same photometric instrument, it is advised to share the limb-darkeneing coefficient parametrization q_1 (and q_2 if using a quadratic law). These coefficients depend on the star and the wavelength of the instrument, hence, if both are invariable, then the coefficient should also be the same. A case where the shape of the light curve due to different LDCs of extremely noisy data versus more behaved data from the same instrument can be shown in Figure 3.2 using *TESS* data from TOI-1201 (Section 5.3).

Masking out out-of-transit data

If access to computational means is limited and no GP is required for the base transit photometry, then for the intermediate transit-only runs, it would be sufficient to mask the out-of-transit (OOT) data since it is the shape of the flux dip that influences the model parameters. For the case of when a GP is needed, it is possible to first perform the deterministic model with the GP, subtract out the GP component to get a "flat lightcurve" and execute the same steps as above. The difference between simultaneously fitting a GP to the data versus first subtracting the GP component out from a simultaneous deterministic plus GP model is not that significant. Surely, for both scenarios, and for the final transit-only or

joint fit, the OOT data should be reincorporated.

In the end, performing a simultaneous deterministic plus GP model is key for obtaining the most precise parameters. Otherwise, if a GP-only model is performed on just the OOT flux and then subtracted out to perform the deterministic-only models, this can influence the final model parameters, e.g., limb-darkening coefficients, planet-to-star ratio, and thus the planetary ones, e.g., planetary radius.

Choosing the correct transit for t_0

Estimating an anticipated transit correctly within its uncertainty is vital for follow-up studies, both for future transiting events with ground-based instruments, and more so specifically with *JWST* for atmosphere characterization since observing time is heavily limited.

The time of a prospective transit ephemeris can be approximated with,

$$t_{0,m} = t_0(m) = t_{0,\text{base}} + m \cdot P \tag{3.7}$$

where $t_{0,m}$ is the predicted transit ephemeris after m orbits from the selected base transit time $t_{0\text{base}}$, and P is the period. Following basic error propagation, the uncertainty for $t_{0,m}$ can be calculated as such,

$$\sigma_{t_{0,m}} = \sqrt{\sigma t_{0,\text{base}}^2 + (m \cdot \sigma_P)^2} \tag{3.8}$$

For a more constrained *TESS* planet with uncertainties on the order of 10^{-4} d and 10^{-5} d for t_0 and P, respectively, on an orbit with period $P \sim 2.5$ d, the uncertainty for future transit events quickly amounts to ~ 315 s, 630 s after 1, 2 years (m=146, 292). For the same planet where σ_P is instead one or two orders of magnitude worse, then the $\sigma_{t_{0,m}}$ grows to ~ 50 min and $\sim$9 hr after 1 year. The larger m becomes, the further the uncertainty for future transits grows ($\propto |m|$).

Therefore, to minimize this, the last transit should be chosen as $t_{0,\text{base}}$ so that m is reset and starts counting from that point forward. However, it is recommended to set the $t_{0,\text{base}}$ centered on the last transit of the *base* light curve, e.g., from a continuous one like *TESS* rather than from a single, isolated transit, e.g., from follow-up observations, even if it is the last one in the entire dataset. This is motivated for the following reason that the *TESS* data acts as an anchor.

Concluding remark

Now that we have all the tools set in place, we can now apply them and look for planets!

4 TOI-150 b and TOI-163 b: two transiting hot Jupiters, one eccentric and one inflated, revealed by *TESS* residing close to the *JWST* CVZ

The content of this chapter is based on the published work in Kossakowski et al. (2019), published in *Monthly Notices of the Royal Astronomical Society (MNRAS), 490, 1094.*

Details of authorship: I am the first author of this paper and led the team effort involving 54 co-authors. I was under the supervision of Prof. Thomas Henning and Martin Kürster, and in close collaboration with Néstor Espinoza. I have done the scientific work, analysis, and reached the conclusions. The text was written by me with the contributions of Rafael Brahm in Sect. 4.4 and the plots were produced by `juliet` with some minor tweaks. Before submission and during the review process, I included suggestions brought upon by the co-authors and the reviewer. For the purpose of incorporating this paper smoothly into the thesis and avoiding redundancy, the text has either been slightly modified or removed. Since the publication, there have been slightly improved parameters from the *Gaia* eDR3 mission, however, as these parameters are slightly improved, they do not improve the final planetary parameters. Therefore, this chapter continues with *Gaia* DR2. That being said, Figs. 4.7, 4.8 & 4.9 have been updated with current exoplanet demographics as of 22 April 2021.

4.1 Motivation

We are now entering an exciting era with NASA's Transiting Exoplanet Survey Satellite (*TESS*; Ricker et al., 2015) mission, a nearly all-sky survey with the primary goal of uncovering and more so characterizing planets smaller than Neptune ($\lesssim 4\,R_\oplus$) around nearby and bright stars ($V < 13$). The expected yield for the short 2-minute cadence targets (∼200 000) is roughly 1 250 new transiting planets of various sizes (Barclay et al., 2018), adding onto the already impressive quantity of ∼4 000 transiting planets discovered[18] to date — most of which come from the *Kepler* (Borucki et al., 2010) transit survey. The quantity of new discoveries can be imagined to be even higher when we include the longer 30-minute cadence targets, potentially increasing the yield to 25,000 (Barclay et al., 2018). The opportunity for new world discoveries and classification is high considering that *TESS* is focusing on the brightest neighboring stars, making it easier for ground-based instruments to follow-up the transit planet detections allowing for further, more detailed characterization.

[18] As of 11 March 2019: `https://exoplanetarchive.ipac.caltech.edu/`

4.2 Context

Among the diversity of new worlds to be discovered by *TESS*, hot Jupiters — planets of similar mass to Jupiter ($0.3M_J \lesssim M \lesssim 2M_J$) and with periods $P < 10$ days (Dawson & Johnson, 2018) — are naturally the most accessible to detect due to their size (relatively larger flux dip in light curve) and short orbiting periods (multiple transits for a given light curve time baseline). Their massive nature also makes them ideal targets for radial velocity (RV) follow-up, as this imposes large modulations in their host star's motion. *TESS*, for this reason, will then be able to detect *most* of the transiting hot Jupiters in our stellar neighborhood; HD 202772A b (Wang et al., 2019) and HD2685 b (Jones et al., 2019) are thus just the first of many to be detected by the mission.

Hot Jupiters are interesting objects on their own right, as they are objects that are still not well understood. For example, it is known that their radii are larger than expected from models of irradiated exoplanets (see, e.g., Thorngren & Fortney, 2018a, and references therein) — however, the mechanism of this so-called "radius inflation" is still not known. Their formation is also a mystery — how giant exoplanets like these end up in short period orbits around their stars is still an open question in the field (see Dawson & Johnson, 2018, for a review). A larger sample of exoplanets might help resolve these issues or help find new predictions for models to make — for example, using the current sample of hot Jupiters, Sestovic et al. (2018) recently showed that the radius inflation might depend on mass. Using a similar sample, Thorngren & Fortney (2018a) suggested that the efficiency with which energy is deposited in the interior of hot Jupiters to make them look inflated might depend on equilibrium temperature. Bailey & Batygin (2018) recently showed that the period-mass distribution of hot Jupiters could be explained by in-situ formation of hot Jupiters. It is clear from studies like these that enlarging the sample of known, well-characterized hot Jupiters can aid in understanding their nature and evolution, and thus is an important endeavor to undertake.

In this Chapter, we introduce the discovery and characterization of two new hot Jupiters, TOI-150 b and TOI-163 b, whose signals were initially detected by *TESS* long-cadence photometry and then thoroughly followed up by other photometric (CHAT, Hazelwood, LCO/CTIO, El Sauce, TRAPPIST-S) and spectroscopic ones (FEROS, CORALIE) ground-based facilities.

The Chapter is structured as follows. In Section 4.3, we present all of the photometric, spectroscopic, and speckle image observations gathered for both targets. The characterization of the stellar hosts are presented in Section 4.4. The joint fit analysis of the data, combining transit photometry and radial velocities is presented in Section 4.5. A further analysis investigating the stellar density and searching for secondary eclipses in Section 4.6. Lastly, Sections 4.7 and 4.8 cover a discussion on these targets and their qualifications as follow-up candidates for atmospheric characterization and spin-orbit alignment.

During the writing of this manuscript, another paper (Cañas et al., 2019) introduced the discovery of TOI-150 b. Though the paper delivered the planetary detection, we provide and present a more complete and thorough analysis with 4 photometric follow-up instruments and a total of 23 radial velocities (20 from FEROS and 3 from CORALIE), which in turn provides a precise constraint on the planetary and orbital parameters of the system. The inclusion of these extra radial velocity measurements, allow us to find a strong signal of an

eccentric orbit for this exoplanet — this is further discussed in Section 4.7.2. Cañas et al. (2019) were not able to constrain the eccentricity.

4.3 Data

The photometric and high-resolution imaging observations were obtained as part of the *TESS* Follow-up Program (TFOP)[19]. All follow-up photometric data along with the speckle images were acquired via Exoplanet Follow-up Observing Program for *TESS* (ExoFOP-*TESS*). The radial velocities are presented in Table 4.5. We used the ***TESS*** `Transit Finder`, which is a customized version of the `Tapir` software package (Jensen, 2013), to schedule photometric time-series follow-up observations. In addition, we worked with the AstroImageJ software package (Collins et al., 2017) to perform aperture photometry for most of these follow-up photometric observations, excluding CHAT which uses a separate pipeline (Jordan et al. in prep.). For TOI-150, we have 5 photometric datasets, i.e., *TESS*, LCO z and i bands, El Sauce, and TRAPPIST-S, and two radial velocity instruments, i.e., FEROS, CORALIE. The data alongside with the best model fits are plotted in Figs. 4.1 and 4.4. For TOI-163 we also have 5 photometric datasets, i.e., *TESS*, CHAT, Hazelwood, LCO i band, and El Sauce; and one radial velocity instrument, i.e., FEROS. The data and model fits can be found in Figs. 4.2 and 4.5 — these are detailed below.

4.3.1 *TESS* transit photometry

A detailed overview of the *TESS* instrument and its purpose can be found in Sect. 1.2.2. Both targets, TYC 9191-519-1 (TIC 271893367, TOI-150, *Gaia* DR2 5262709709389254528) and HD 271181 (TIC 179317684, TOI-163, *Gaia* DR2 5136625920246310 4), were observed in Sector 1 (from 2018 July 25 – August 22) with the 30-minute cadence full-frame images (FFIs). Calibrated FFIs are conveniently available for quick download via the Mikulski Archive for Space Telescopes (MAST)[20] where the entire *TESS* Input Catalog (TIC) is uploaded and where the archival light curve data produced by the Science Processing Operations Center (SPOC; Jenkins et al., 2016) pipeline reside. The light curves used for this work were taken from the *TESS* alerts page, from which we extracted the Simple Aperture Photometry fluxes (`SAPFLUX`).

Outliers that were flagged were removed as well as the same data points mentioned in (Huang et al., 2018) which were taken out due to the increased spacecraft pointing jitter. In order to search for possible additional signals to the ones detected by the *TESS* team, we analyzed the light curves using the Box-least-squares algorithm (BLS; Kovács et al., 2002). Using the whole dataset we recovered the prominent signals of TOI-150 b and TOI-163 b of 5.87 d and 4.23 d, respectively. After masking these signals, no more signals are found in the photometry. In order to mitigate stellar and/or instrumental long-term trends in the photometry, we masked the in-transit data and performed a Gaussian Process (GP) regression using the quasi-periodic kernel as presented in `celerite` (Foreman-Mackey et al., 2017), which we use to detrend the light curves of our target stars. The detrended and flattened

[19] `https://tess.mit.edu/followup/`

[20] `https://archive.stsci.edu/tess/;https://mast.stsci.edu/tesscut/`

TESS light curves of both targets are shown in Figs. 4.1 and 4.2, for TOI-150 and TOI-163 respectively, alongside with the phase-folded plots of all photometry instruments where any GP components are already subtracted. We point out that both targets exhibit photometrically quiet behavior, and therefore the pre-conditioned light curves look practically identical to the post-conditioned ones.

4.3.2 Transit photometric follow-up

We obtained multiple transit photometric follow-up observations as outlined below. These systematic trends within the light curves were detrended accordingly and incorporated into our final joint model fit (see Sect. 4.5).

CHAT We acquired photometric data in the i band on the night of 21 September 2018 for TOI-163 from the Chilean-Hungarian Automated Telescope (CHAT; Jordan et al., in prep.) 0.7 m telescope located at Las Campanas Observatory (LCO) in Chile. The primary objective of CHAT is to serve for photometric follow-up for exoplanet candidates; the telescope has achieved 1 mmag RMS precision for stars with V magnitude 12-14. The photometry was reduced with a standard pipeline which performs bias, dark and flat-field corrected images, and these were used to extract aperture photometry for various apertures. The optimal aperture was chosen as the one that, after correcting for atmospheric effects using comparison stars of similar brightness and colors, produced the light curve with the smallest root-mean-square residuals after filtering with a median filter. The resulting light curve showed an evident ingress event at the predicted time from the *TESS* observations on the target.

Hazelwood Photometric follow-up data for TOI-163 was also gathered within the *TESS* Follow-up Observing Program (TFOP) Working Group; specifically, within Sub Group 1 "Seeing-limited Photometry". The data was gathered using a 0.32 m Planewave CDK telescope from Hazelwood Observatory, a backyard observatory, located in Victoria, Australia and operated by Chris Stockdale. The observed data in the Rc filter taken on 13 October 2018 included pre-transit baseline, ingress, and after-transit baseline with some missing observations around the egress. The photometry, although with large systematic trends, showed an evident ingress of the target at the expected *TESS* time predicted by the *TESS* observations. The aperture radius is 5.5 arcsec and there were no stars within 3' of the target with a delta magnitude less than 5.5. One should also note that additional Hazelwood photometry for TOI-163 was taken in the g' band on 14 January 2019, but due to cirrus cloud interference, several data points had been discarded and the quality of the remaining data would not benefit the final fit, so therefore, these data points were not incorporated.

LCO-CTIO Additional photometric data for TOI-150 were taken on 9 November 2018 with the 1 m telescope at Cerro Tololo Inter-American Observatory (CTIO) located near La Serena in Chile via the Las Cumbres Observatory Global Telescope (LCOGT) program (Brown et al., 2013). The photometry was taken in two bands: z and i band, where both covered the egress of the transit. The aperture radius for the z band was 5.84 arcsec and showed no possible contamination from neighboring objects; whereas the aperture radius for the i band was 19.5 arcsec and showed *potential* contamination. This contamination

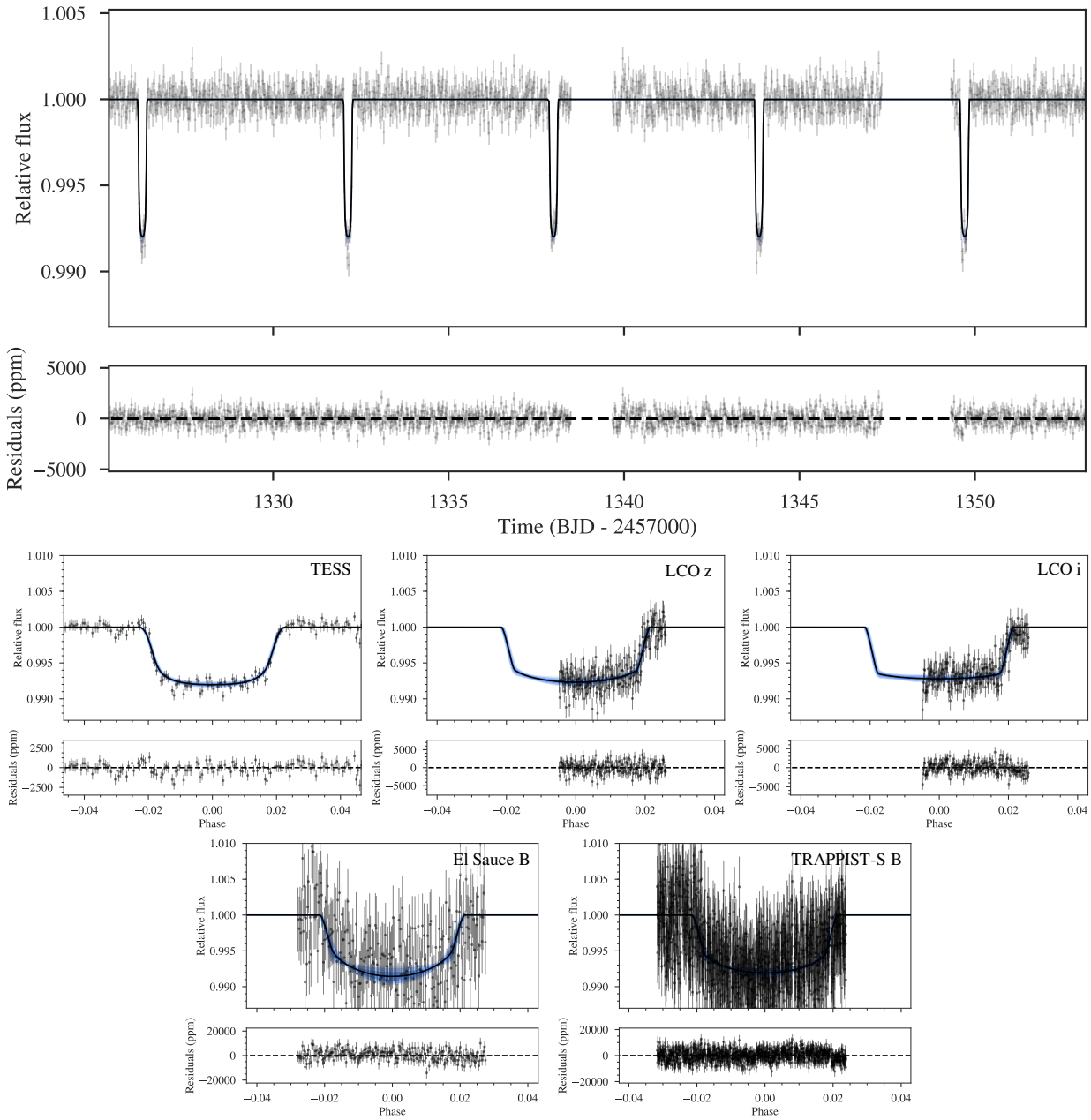

Figure 4.1: *Top.* Above is the full *TESS* light curve for TOI-150 taken from Sector 1, where the best-fit model from `juliet` is overplotted (black line) along with the 68%, 95%, and 99% posterior bands (blue shaded regions) taken from 5 000 samples. *Bottom.* Phase-folded transits for TOI-150 b for all available photometric instruments: *TESS* (top left), LCO z band (top middle), LCO i band (top right), El Sauce (bottom left), and TRAPPIST-S (bottom right). Any GP components have been subtracted out in the phase-folded curves, and to mention specifically for the TRAPPIST-S photometry, the meridian flip had also been corrected for.

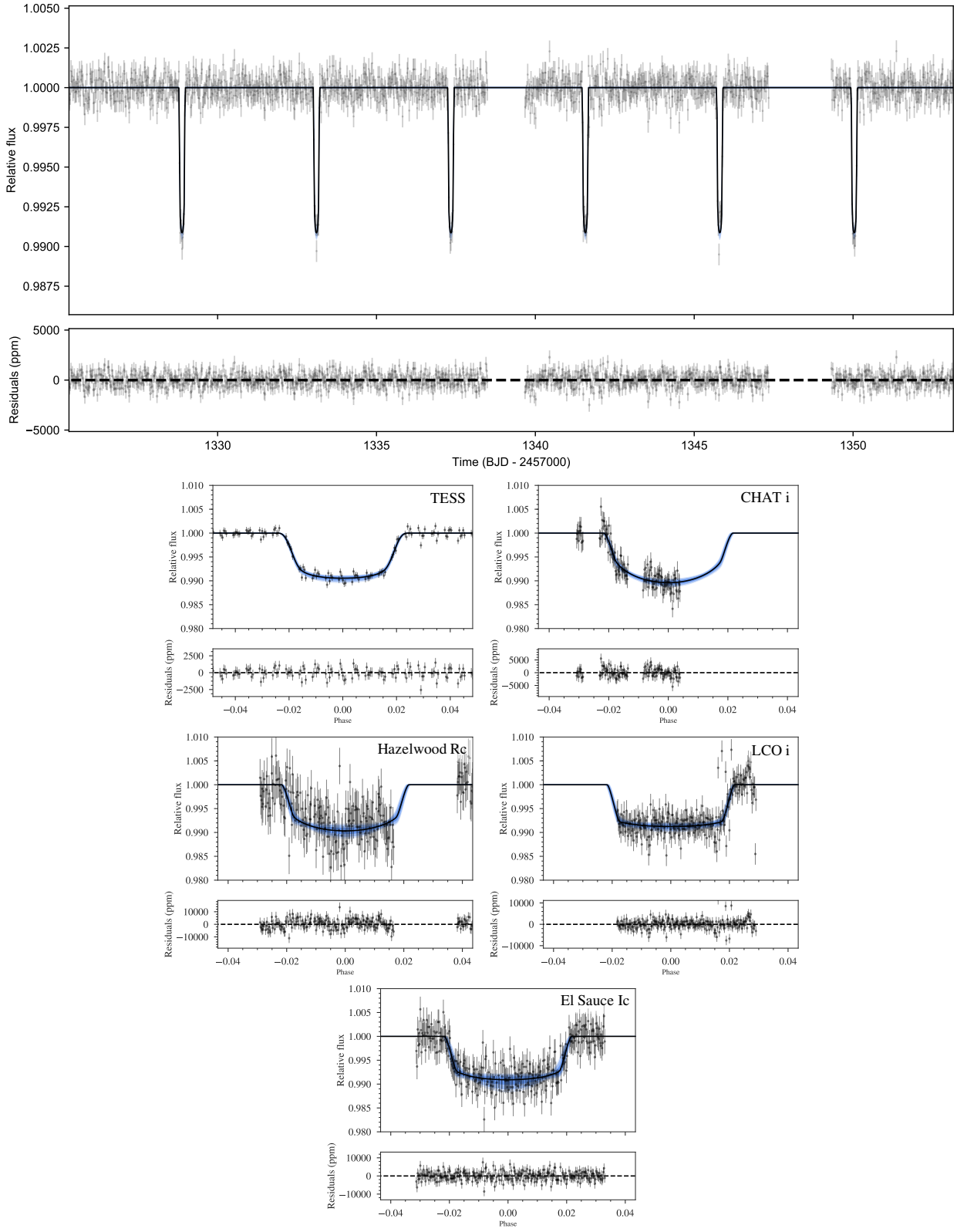

Figure 4.2: *Top.* Above is the full *TESS* light curve for TOI-163 taken from Sector 1, where the best-fit model from `juliet` is overplotted (black line) along with the 68%, 95%, and 99% posterior bands (blue shaded regions). 5 000 samples from the posterior were considered for the confidence intervals. *Bottom.* Phase-folded transits for TOI-163 b for all available photometric instruments: *TESS* (top left), CHAT (top middle), Hazelwood (top right), LCO i band (bottom left), and El Sauce (bottom right). The phase-folded curves have been fixed by subtracting out any GP components. Gaps present in the CHAT and Hazelwood photometry can be attributed to weather and instrumental failures.

possibility was taken into consideration as a dilution factor for the fit, but it was found that the contamination is insignificant (Sect. 4.5.1).

Photometric follow-up was also taken for TOI-150 on 12 November 2018 in the i band, where the aperture radius was 13.2 arcsec and there were no apparent objects near the target with a magnitude difference less than 5.97 mag. However, there were systematics that were dealt with via Gaussian Process regression, as explained in Sect. 4.5.2.

El Sauce Data for both TOI-150 and TOI-163 were obtained from the Observatorio El Sauce located in the Río Hurtado Valley, in the south of the Atacama desert. TOI-150 was observed in the B filter on 30 January 2019 and TOI-163 in the Ic filter on 6 January 2019, both covering a full transit with an aperture radius of 7.4 arcsec and using a 0.36 m telescope.

TRAPPIST-South Lastly, we obtained photometry for a full transit for TOI-150 on 19 December 2018 using the 0.6 m TRAnsiting Planets and PlanetesImals Small Telescope−South (TRAPPIST-South) located in La Silla, Chile. Observations were carried out with good weather conditions in the B filter with an aperture radius of 5.76 arcsec and all possible candidates within 2' had been cleared.

4.3.3 Spectroscopic follow-up

FEROS In order to identify if the transit signals are truly due to planetary companions and to also measure the mass of the planetary companions, we obtained radial velocities (R $\approx$ 48 000) from the FEROS spectrograph (Kaufer & Pasquini, 1998), which is mounted on the MPG 2.2 m telescope located at La Silla Observatory in Chile. To calibrate the measurements, a simultaneous method was imposed where a ThAr calibration lamp is observed in a comparison fiber next to the science fiber, so that instrumental RV drifts can be correctly accounted for. Exposure times were on average 400-600 seconds long for these bright F-type stars. The data was reduced using the CERES pipeline (Brahm et al., 2017a).

For TOI-150, 20 data points were taken over the course of 49 days (19 September 2018 - 7 November 2018). The data showed radial velocities that evidently phased up with the photometric ephemerides with a semi-amplitude of 200 $\mathrm{m\,s^{-1}}$; additionally, the stellar spectrum hinted towards a 6000 K, $\log g = 4.0$ stellar host. Similarly, 20 data points were obtained for TOI-163 over the course of 47 days (17 September 2018 - 3 November 2018). The radial velocities also phased up with the photometric ephemerides, with a semi-amplitude of 100 $\mathrm{m\,s^{-1}}$ for the target; the stellar spectrum indicated the host star to be a 6500 K, $\log g = 4.0$ star. No correlation was observed with the bisector spans (BIS) for any of the targets (Fig. 4.3) and the data can be found in Table 4.5.

CORALIE Three high-resolution spectra were obtained for TOI-150 with CORALIE on the Swiss 1.2 m Euler telescope at La Silla Observatory, Chile (Mayor et al., 2003) over a timespan of 32 days (6 October 2018 - 7 November 2018). CORALIE has resolution $R = 60000$ and uses simultaneous Fabry-Pérot wavelength calibration during science exposures. The science-fibre is 2 arcsec on sky. For each epoch we compute the RVs by cross-correlation with a binary G2 mask using the standard CORALIE pipeline. Line-profile diagnostics such as bisector span and FWHM are produced as well, to check for correlations with RV of which none were

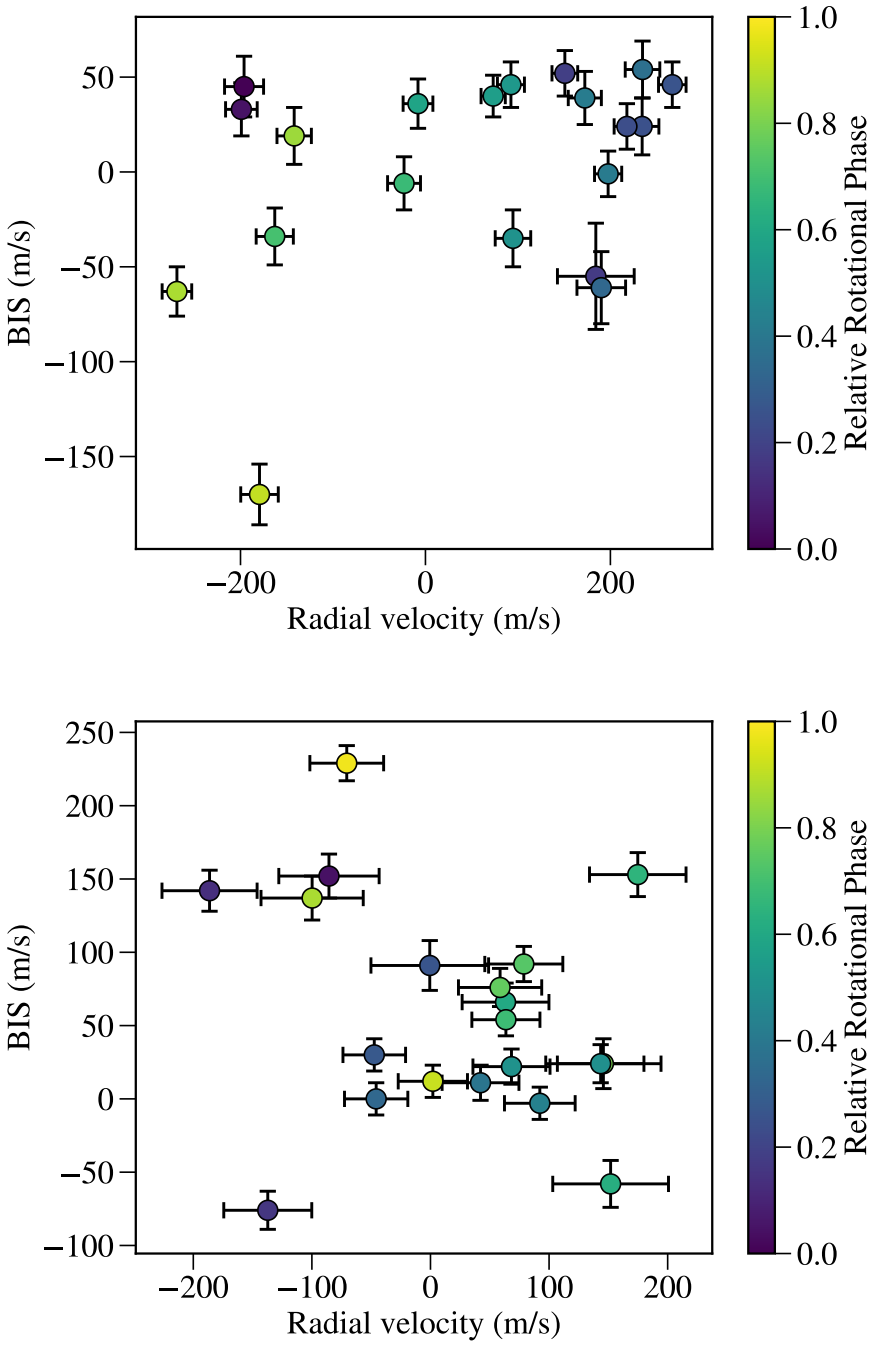

Figure 4.3: The radial velocity and BIS are plotted against each other for TOI-150 (left) and TOI-163 (right) using just the FEROS data and they show no correlation. The radial velocity was offset by μ_{FEROS} ($5938.91\,\mathrm{m\,s^{-1}}$) and the color represents the phase of the period (5.8575d), both of which where taken from the posterior, see Table 4.3 for TOI-150. Likewise, the radial velocity was offset by μ_{FEROS} ($21393.73\,\mathrm{m\,s^{-1}}$) and phase-folded with the period (4.231306d) given by the same posterior tables. The phase is defined to be 0 when the first data point was taken.

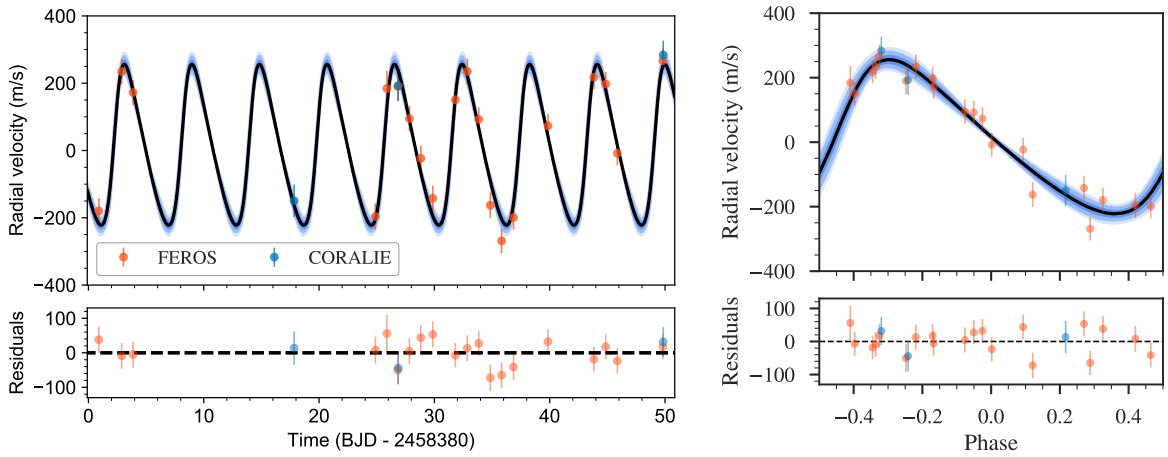

Figure 4.4: *Left.* The radial velocity measurements for TOI-150 are illustrated, along with the best model (black line) and the 68%, 95%, and 99% posterior bands (blue bands) using 5 000 samples from the posteriors. FEROS and CORALIE data points are shown in orange and blue, respectively. Below are then the residuals after subtracting the best model fit. *Right.* The phased radial velocity measurements for TOI-150 b, where one can see the eccentric behavior of the signal's orbit.

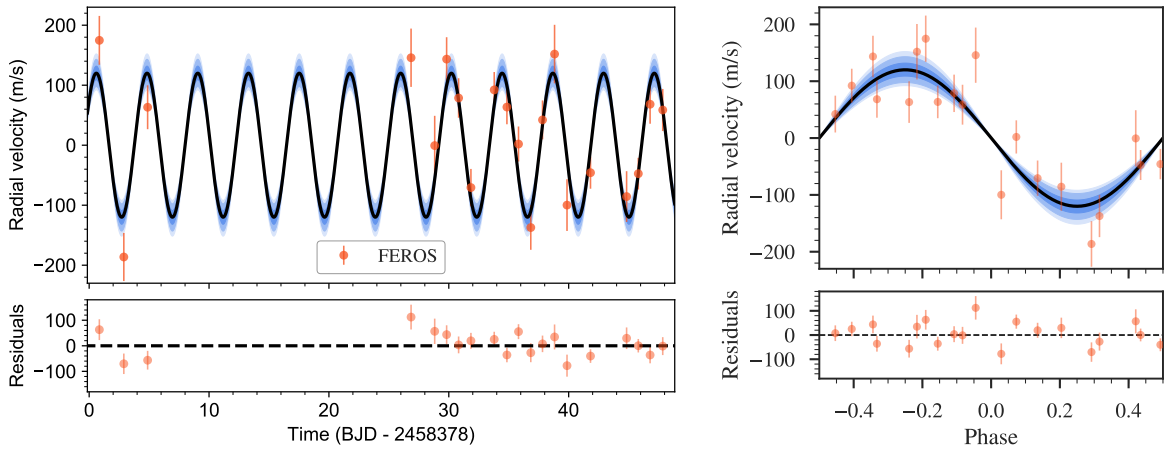

Figure 4.5: *Left.* The FEROS radial velocity measurements for TOI-163 are presented, along with the best model (black line) and the 68%, 95%, and 99% posterior bands (blue bands) based on 5 000 samples. Below are then the residuals after subtracting the best model fit. *Right.* The phased radial velocity measurements for TOI-163 b.

found. We also compute RVs using other binary masks ranging from A0 to M4, to check for a mask-dependent signal indication a blend. The CORALIE RVs confirm the planetary nature of the *TESS* detetction and is in phase with the transit ephemerides.

4.3.4 Gemini/DSSI speckle images

Speckle imaging for TOI-163 was obtained on 28 October 2018, using the Differential Speckle Survey Instrument (DSSI) (Horch et al., 2009, 2012; Howell et al., 2016) located at the 8 m

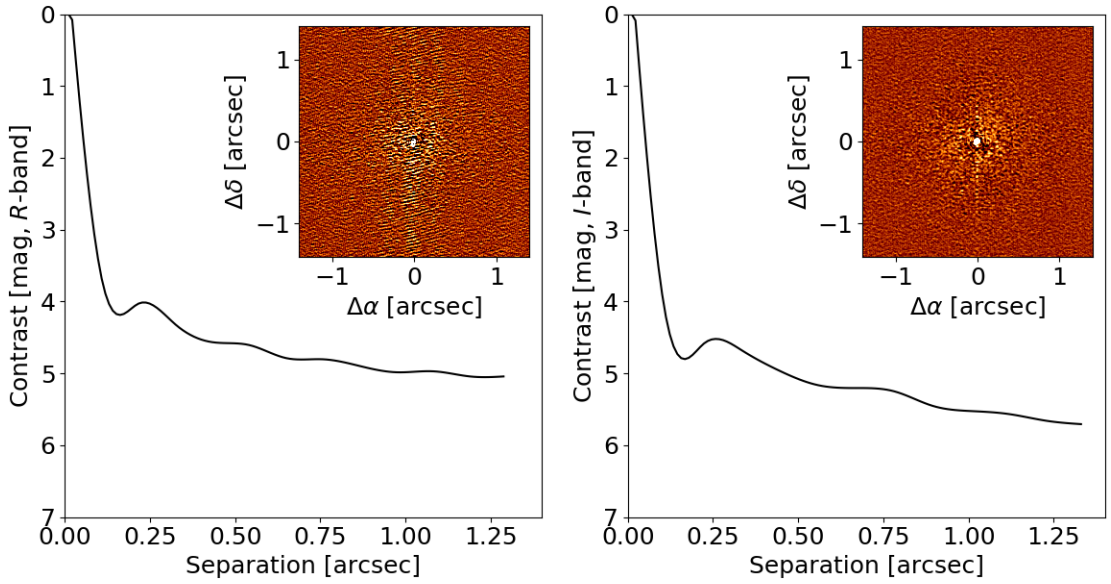

Figure 4.6: Presented here are the Gemini speckle interferometric observation contrast curves for the R (692 nm) and I (880 nm) band for TOI-163, along with the reconstructed images to show that there are no close stellar companions that could affect the light curve.

Gemini South Telescope at Cerro Pachon, Chile. The DSSI obtains simultaneous speckle images of targets as faint as V magnitude 16 - 17, in 2 channels: R (692 nm) and I (880 nm), where the spatial resolution reached is ∼0.017 arcsec and ∼0.028 arcsec, respectively. The 692-nm and 880-nm filters are labeled as the R and I bands, respectively, since their wavelength centers align, however, the true filter is considerably narrower with a $\Delta\lambda$ of 40 nm and 50 nm for the respective wavelengths. The contrast curves (Fig. 4.6) show that there are no stellar companions to a depth of 3.7 magnitudes for the R band and 3.9 magnitudes for the I band at 0.1 arcsec; and >4.6 and >5.1 magnitudes outside a radius of 0.5 arcsec for the two wavelengths, respectively.

4.4 Stellar parameters

To derive the stellar parameters for the host stars of these two targets, we analyzed the co-added FEROS spectra via the Zonal Atmospheric Stellar Parameters Estimator algorithm (ZASPE, Brahm et al., 2015, 2017b). This code computes the atmospheric parameters (T_{eff}, log$g$, [Fe/H]) and the projected rotational velocity ($v \sin i$) by comparing the observed spectra to a grid of synthetic models generated from the ATLAS9 model atmospheres (Castelli & Kurucz, 2003). Only spectral regions that are significantly sensitive to changes in the atmospheric parameters are used for comparison. This process is then executed in an iterative method, where the uncertainties are obtained through Monte Carlo simulations. With this procedure we find that TOI-150 has an effective temperature of $T_{\rm eff} = 6\,255.0 \pm 90.0$ K, a surface gravity of $\log g = 4.20 \pm 0.0090$ dex, a metallicity of $[{\rm Fe/H}] = 0.28 \pm 0.036$ dex, and a projected rotational velocity of $v \sin i = 7.96 \pm 0.28$ m s^{-1}. As for TOI-163, we find an effective temperature of $T_{\rm eff} = 6\,495.0 \pm 90.0$ K, a surface gravity of $\log g = 4.187 \pm 0.011$ dex,

a metallicity of $[\mathrm{Fe/H}] = 0.220 \pm 0.041$ dex, and a projected rotational velocity of $v \sin i = 14.08 \pm 0.27$ m s^{-1}.

We then followed the two step procedure adopted in Brahm et al. (2018, 2019c) to infer the physical parameters and evolutionary stage of the host stars. First, we are able to derive a very precise stellar radius of each star by combining the parallax measurement provided by *Gaia* DR2 with public broad band photometric measurements (taken from Tycho-2 or 2MASS). Then we use the Yonsei-Yale isochrones (Yi et al., 2001) to estimate the stellar mass and age of each host star by comparing the obtained effective temperature and stellar radius to those predicted by the isochrones. In the end, we obtain radius values of $R = 1.526 \pm 0.012$ for TOI-150 and $R = 1.648^{+0.023}_{-0.025}$ for TOI-163; and then mass values of $M = 1.351^{+0.038}_{-0.026}$ and $M = 1.4352^{+0.029}_{-0.028}$ for the stars, respectively. From there, we can compute the stellar density, ρ_*, for which we will be using as a prior for the fits. The derived stellar parameters can be found in Table 4.1.

Table 4.1: Stellar parameters of TOI-150 and TOI-163.

Parameter	TOI-150 Value	TOI-163 Value	Source
Identifying Information			
TIC ID	271893367	179317684	TIC[a]
GAIA ID	5262709709389254528	4651366259202463104	*Gaia* DR2[b]
2MASS ID	J07315176-7336220	J05190435-7153441	2MASS[c]
R.A. (J2015.5, h:m:s)	$7^h31^m51.7^s$	$5^h19^m4.3^s$	*Gaia* DR2[b]
DEC (J2015.5, d:m:s)	$-73°36'21.73''$	$-71°53'43.9''$	*Gaia* DR2[b]
Proper motion and parallax			
$\mu_\alpha \cos\delta$ (mas yr^{-1})	27.14 ± 0.03	7.14 ± 0.07	*Gaia* DR2[b]
μ_δ (mas yr^{-1})	-15.21 ± 0.03	16.37 ± 0.08	*Gaia* DR2[b]
Parallax (mas)	2.94 ± 0.02	2.40 ± 0.05	*Gaia* DR2[b]
Spectroscopic properties			
$T_{\rm eff}$ (K)	6255 ± 90	6495 ± 90	ZASPE[d]
Spectral Type	F	F	ZASPE[d]
[Fe/H] (dex)	0.28 ± 0.036	0.22 ± 0.041	ZASPE[d]
$\log g_*$ (cgs)	4.13 ± 0.009	4.187 ± 0.011	ZASPE[d]
$v \sin(i_*)$ (km s^{-1})	7.96 ± 0.279	14.08 ± 0.266	ZASPE[d]
Photometric properties			
T (mag)	10.865 ± 0.019	10.843 ± 0.018	TIC[a]
G (mag)	11.34 ± 0.015	11.22 ± 0.015	*Gaia* DR2[b]
B (mag)	12.173 ± 0.212	11.852 ± 0.204	Tycho-2[e]
V (mag)	11.39 ± 0.0015	11.467 ± 0.0014	Tycho-2[e]
J (mag)	10.324 ± 0.028	10.404 ± 0.021	2MASS[c]
H (mag)	10.045 ± 0.022	10.153 ± 0.024	2MASS[c]
Ks (mag)	9.94 ± 0.019	10.124 ± 0.023	2MASS[c]
Derived properties			
M_* ($M_\odot$)	$1.351^{+0.038}_{-0.026}$	$1.4352^{+0.029}_{-0.028}$	YY*
R_* ($R_\odot$)	$1.526^{+0.012}_{-0.012}$	$1.648^{+0.023}_{-0.025}$	YY*
L_* ($L_\odot$)	$3.137^{+0.340}_{-0.270}$	$4.330^{+0.250}_{-0.256}$	YY*
M_V	$3.507^{+0.107}_{-0.153}$	$3.125^{+0.069}_{-0.072}$	YY*
Age (Gyr)	$2.346^{+0.425}_{-0.901}$	$1.823^{+0.300}_{-0.331}$	YY*
ρ_* (kg m^{-3})	$533.2^{+14.4}_{-16.5}$	$451.8^{+18.9}_{-19.4}$	YY*

Note. Logarithms given in base 10.

(a) *TESS* Input Catalog (Stassun et al., 2018); (b) *Gaia* Data Release 2 (Gaia Collaboration et al., 2018); (c) Two-micron All Sky Survey (Cutri et al., 2003); (d) Zonal Atmospheric Stellar Parameters Estimator (Brahm et al., 2015, 2017b); (e) Tycho-2 Catalog (Høg & Murdin, 2000)

*: Yonsei-Yale isochrones (Yi et al., 2001); using stellar parameters obtained from ZASPE.

4.5 Analysis and results for TOI-150 and TOI-163

For both *TESS* targets, a simultaneous analysis of the photometry, radial velocity, and stellar density was efficiently preformed using `juliet` (Espinoza et al., 2019a). An extensive overview of the package is provided in Sect. 3.3.

The specific details of the analysis for each target, TOI-150 b and TOI-163 b, are outlined within this section. In general, the same steps were more or less taken with some minor differences regarding eccentricities, instrument jitter terms σ, and instrument dilution factors D. The treatment of the *TESS* light curves for both targets was identical in the sense that they are long-cadence observations, so therefore, we applied a resampling technique (outlined in Kipping, 2010), where we resampled $N = 20$ points per given data point.

We do the following parametrizations (see Sect. 3.3.3 for the outlined suggestions and their detailed justifications). The *TESS* photometry was modeled with a quadratic limb-darkening law, whereas the other photometric instruments were assigned linear limb-darkening laws. We fit for the parameters r_1 and r_2 instead of fitting directly for the planet-to-star radius ratio ($p = R_p/R_*$) and the impact parameter of the orbit (b). Our final fits include ρ_*, the stellar density as taken from Table 4.1, as a prior The impact that a stellar density prior may have on various parameters is discussed in Sect. 4.6.1.

The process of first performing transit-only fits and then RV-only fits before embarking on the final joint fit is thoroughly outlined in Sect. 3.3.4, along with the justifications for various prior choices. We follow this methodology of initially setting up uniform priors for the period, P, and transit time, t_0 for the transit-only fit where we then take the posterior and use this as the prior for the RV-only fits. For the final fit, we inflated the priors for P and t_0 and slightly constrained the semi-amplitude, K.

As a recollection of what data was collected for TOI-150, we have transit photometry (Fig. 4.1) from *TESS*, LCOGT z band (egress), LCOGT i band (egress), El Sauce (full), and TRAPPIST-S (full), as well as radial velocities (Fig. 4.4) from FEROS (20 points) and CORALIE (3 points). As for TOI-163, we have transit photometry (see Fig. 4.2) from *TESS*, CHAT (ingress), Hazelwood (ingress), LCO i band (full), and El Sauce (full), along with radial velocities from FEROS (Fig. 4.5).

The full model posterior distributions from the final fits for both objects can be found in Table 4.3 where the derived planetary posteriors are in Table 4.4 and the priors are located in Table 4.2.

Table 4.2: Below are the priors used for TOI-150 and TOI-163 for the *final* joint analysis fit using `juliet`. As a recollection, $p = R_p/R_*$ and $b = (a/R_*)\cos(i_p)$, where R_p is the planetary radius, R_* the stellar radius, a the semi-major axis of the orbit and i_p the inclination of the planetary orbit with respect to the plane of the sky. e and ω are the eccentricity and argument of periastron of the orbits. The prior labels of $\mathcal{N}$, $\mathcal{U}$, and $\mathcal{J}$ represent normal, uniform, and Jeffrey's distributions. Reasons for why some parameters are fixed to a value are better explained in detail in Sect. 4.5.2. The parametrization for (p, b) using (r_1, r_2) (Espinoza & Jordán, 2015, 2016) and the linear (q_1) and quadratic (q_1, q_2) limb-darkening parametrization (Kipping, 2013a) are both described in Sect. 4.5.

	Prior			
Parameter name	TOI-150 b	TOI-163 b	Unit	Description
Stellar parameters				
ρ_*	$\mathcal{N}(535.76, 17.48^2)$	$\mathcal{N}(451.406, 29.5^2)$	kg/m^3	Stellar density.
Planetary parameters				
P_b	$\mathcal{N}(5.87, 0.01^2)$	$\mathcal{N}(4.23, 0.001^2)$	days	Period.
$t_{0,b} - 2458320$	$\mathcal{N}(6.32, 0.01^2)$	$\mathcal{N}(8.88, 0.01^2)$	days	Time of transit-center.
$r_{1,b}$	$\mathcal{U}(0,1)$	$\mathcal{U}(0,1)$	—	Parametrization for p and b.
$r_{2,b}$	$\mathcal{U}(0,1)$	$\mathcal{U}(0,1)$	—	Parametrization for p and b.
K_b	$\mathcal{U}(150, 300)$	$\mathcal{U}(80, 170)$	m s^{-1}	Radial velocity semi-amplitude.
$\mathcal{S}_{1,b} = \sqrt{e_b}\sin\omega_b$	$\mathcal{U}(-1,1)$	0.0 (fixed)	—	Parametrization for e and ω.
$\mathcal{S}_{2,b} = \sqrt{e_b}\cos\omega_b$	$\mathcal{U}(-1,1)$	0.0 (fixed)	—	Parametrization for e and ω.
Parameters for *TESS*				
$D_{\rm TESS}$	$\mathcal{U}(0.5,1)$	$\mathcal{U}(0,1)$	—	Dilution factor for *TESS*.
$M_{\rm TESS}$	$\mathcal{N}(0.0.1^2)$	$\mathcal{N}(0.0.1^2)$	ppm	Relative flux offset for *TESS*.
$\sigma_{\rm TESS}$	$\mathcal{J}(0.1, 600^2)$	0.0 (fixed)	ppm	Extra jitter term for *TESS*
$q_{1,\rm TESS}$	$\mathcal{U}(0,1)$	$\mathcal{U}(0,1)$	—	Quadratic limb-darkening parametrization.
$q_{2,\rm TESS}$	$\mathcal{U}(0,1)$	$\mathcal{U}(0,1)$	—	Quadratic limb-darkening parametrization.
Parameters for CHAT				
$D_{\rm CHAT}$	—	1.0 (fixed)	—	Dilution factor for CHAT.
$M_{\rm CHAT}$	—	$\mathcal{N}(0.0.1^2)$	ppm	Relative flux offset for CHAT.
$\sigma_{\rm CHAT}$	—	0.0 (fixed)	ppm	Extra jitter term for CHAT
$q_{1,\rm CHAT}$	—	$\mathcal{U}(0,1)$	—	Linear limb-darkening parametrization.
Parameters for Hazelwood				
$D_{\rm Hazwelwood}$	—	1.0 (fixed)	—	Dilution factor for Hazwelwood.
$M_{\rm Hazwelwood}$	—	$\mathcal{N}(0, 0.1^2)$	ppm	Relative flux offset for Hazwelwood.
$\sigma_{\rm Hazwelwood}$	—	$\mathcal{J}(0.1, 5000^2)$	ppm	Extra jitter term for Hazwelwood
$q_{1,\rm Hazwelwood}$	—	$\mathcal{U}(0,1)$	—	Linear limb-darkening parametrization.
$\rm GP_{\sigma,Hazwelwood}$	—	$\mathcal{J}(0.1, 12000^2)$	—	Amplitude of GP component.
$\rm GP_{y,Hazwelwood}$	—	$\mathcal{J}(0.01, 50^2)$	—	Pixel y-centroid GP component.
Parameters for LCO z band				
$D_{\rm LCO\text{-}z}$	1.0 (fixed)	—	—	Dilution factor for LCO z band.
$M_{\rm LCO\text{-}z}$	$\mathcal{N}(0, 0.1^2)$	—	ppm	Relative flux offset for LCO z band.
$\sigma_{\rm LCO\text{-}z}$	$\mathcal{J}(0.1, 10000^2)$	—	ppm	Extra jitter term for LCO z band
$q_{1,\rm LCO\text{-}z}$	$\mathcal{U}(0,1)$	—	—	Linear limb-darkening parametrization.
Parameters for LCO i band				
$D_{\rm LCO\text{-}i}$	1.0 (fixed)	1.0 (fixed)	—	Dilution factor for LCO i band.
$M_{\rm LCO\text{-}i}$	$\mathcal{N}(0, 0.1^2)$	$\mathcal{N}(0, 0.1^2)$	ppm	Relative flux offset for LCO i band.
$\sigma_{\rm LCO\text{-}i}$	$\mathcal{J}(0.1, 10000^2)$	$\mathcal{J}(0.1, 5000^2)$	ppm	Extra jitter term for LCO i band

Parameter name	Prior TOI-150 b	Prior TOI-163 b	Unit	Description
$q_{1,\text{LCO-}i}$	$\mathcal{U}(0,1)$	$\mathcal{U}(0,1)$	—	Linear limb-darkening parametrization.
$\text{GP}_{\sigma,\text{LCO-}i}$	$\mathcal{J}(0.1,10000^2)$	$\mathcal{J}(0.1,10000^2)$	—	Amplitude of GP component.
$\text{GP}_{\text{t, LCO-}i}$	$\mathcal{J}(0.01,10^2)$	—	—	Time GP component.
$\text{GP}_{\text{FWHM, LCO-}i}$	—	$\mathcal{J}(0.01,100^2)$	—	FWHM GP component.
$\text{GP}_{\text{sky flux, LCO-}i}$	—	$\mathcal{J}(0.01,100^2)$	—	Sky Flux GP component.
Parameters for El Sauce				
$D_{\text{El Sauce}}$	1.0 (fixed)	1.0 (fixed)	—	Dilution factor for El Sauce.
$M_{\text{El Sauce}}$	$\mathcal{N}(0,0.1^2)$	$\mathcal{N}(0,0.1^2)$	ppm	Relative flux offset for El Sauce.
$\sigma_{\text{El Sauce}}$	$\mathcal{J}(0.1,10000^2)$	$\mathcal{J}(0.1,5000^2)$	ppm	Extra jitter term for El Sauce
$q_{1,\text{El Sauce}}$	$\mathcal{U}(0,1)$	$\mathcal{U}(0,1)$	—	Linear limb-darkening parametrization.
$\text{GP}_{\sigma,\text{El Sauce}}$	$\mathcal{J}(0.1,10000^2)$	$\mathcal{J}(0.1,150^2)$	—	Amplitude of GP component.
$\text{GP}_{\rho,\text{El Sauce}}$	—	$\mathcal{J}(0.001,30^2)$	—	Rho for Matern GP component.
$\text{GP}_{T,\text{El Sauce}}$	—	$\mathcal{J}(0.001,30^2)$	—	Timescale for Matern GP component.
Parameters for TRAPPIST-S				
D_{TRAPPIST}	1.0 (fixed)	—	—	Dilution factor for TRAPPIST-S.
M_{TRAPPIST}	$\mathcal{N}(0,0.1^2)$	—	ppm	Relative flux offset for TRAPPIST-S.
σ_{TRAPPIST}	$\mathcal{J}(0.1,10000^2)$	—	ppm	Extra jitter term for TRAPPIST-S
$q_{1,\text{TRAPPIST}}$	$\mathcal{U}(0,1)$	—	—	Linear limb-darkening parametrization.
$\theta_{0,\text{TRAPPIST}}$	$\mathcal{U}(-0.5,0.5)$	—	ppm	Offset value for meridian flip.
RV parameters				
μ_{FEROS}	$\mathcal{N}(5939.0783,.5^2)$	$\mathcal{N}(21392.22,15^2)$	m s^{-1}	Systemic velocity for FEROS.
σ_{FEROS}	$\mathcal{J}(0.1,100^2)$	0.0 (fixed)	m s^{-1}	Extra jitter term for FEROS.
μ_{CORALIE}	$\mathcal{N}(5885.6659,15^2)$	—	m s^{-1}	Systemic velocity for CORALIE.
σ_{CORALIE}	0.0 (fixed)	—	m s^{-1}	Extra jitter term for CORALIE.

4.5.1 Flux contamination possibility

Because *TESS* has a large pixel size of 21 arcsec it is particularly important to search for nearby sources which could pollute the aperture requiring dilution factors (D) to be taken into account (see Sections 2.1 and 3.1.2 in Espinoza et al., 2019a).

TOI-150 TOI-150 (*Gaia* DR2 5262709709389254528, G_{rp} magnitude of 10.85) may face some obstacles with nearby neighbors, where there are two that have relatively low magnitudes (14.20, *Gaia* DR2 5262709881187945344, ∼41 arcsec ≈ 2 *TESS* pixels; 11.98, *Gaia* DR2 5262706681434867968, ∼62 arcsec ≈ 3 *TESS* pixels), and the other nearby targets are not significantly bright enough.

Because the *Gaia* G_{rp}-band and the *TESS* band are quite similar, we can approximate what the dilution factor for *TESS* (D_{TESS}) would be using equation 2 in Espinoza et al. (2019a) to get $D \approx 0.71$ (assuming that the two bright objects are within the same *TESS* pixel). We therefore allow the *TESS* dilution factor to vary uniformly with the conservative lower bound of 0.5 to 1.0, with the idea in mind that the other targets are probably not impacting the flux significantly. Indeed, we do find that D_{TESS} is consistent with 1 (0.9699; Table 4.3). As for the other photometric instruments, the dilution factors are fixed to 1.0 as there is no indications of flux contamination.

TOI-163 Fortunately, TOI-163 (*Gaia* DR2 4651366259202463104, G_{rp} magnitude of 10.82) doesn't have any neighboring *Gaia* DR2 targets with a large enough flux to impact the light curve, however, there are plenty of faint objects that *might* have some influence, and therefore we let the dilution factor ($D_{\rm TESS}$) be free for just the *TESS* photometry. In fact, if we perform a rough estimation, there are about 20 objects within one *TESS* pixel with magnitudes >18, so if we assume 20 objects with worse-case scenario magnitudes of 18, this translates to a D of ∼0.9626. This actually corresponds quite well with the dilution value we get from the final fit of 0.96996 (see Table 4.3).

In addition to no bright nearby *Gaia* objects, speckle data from Gemini/DSSI in both the R (692 nm) and I (880 nm) wavelengths show that there are no significant sources of light nearby (Fig. 4.6). Therefore, this further confirms the planetary nature of the signal found in the light curve and radial velocities and allows us to fix the dilution factors of the other photometric instruments to 1.0.

4.5.2 Intstrumental detrending & jitter terms

TOI-150 The *TESS* photometric data appears clean and well-behaved whereas the LCO z and i band, the El Sauce, and TRAPPIST-S data might have some dependencies on other potential factors. To see which additional factors are necessary to take into account, photometry-only fits first were made with each photometric instrument, and the posterior log-evidences were compared between fits without any detrending parameters and fits accounting for possible systematic trends using a Gaussian Process (GP) regression with a multi-dimensional squared-exponential kernel combining multiple components in time, airmass, centroid position, full-width half maximum (FWHM) and/or sky flux, if available. It was found that for the LCO z and i band photometry no additional terms are needed to correct the photometry from systematics other than a flux offset. For El Sauce photometry, we found that airmass was an important regressor to take into account with a GP. Finally, for the TRAPPIST-S photometry, we found that no additional GP was needed — however, the meridian flip offset flux has to be modelled. For this, we simply added an extra parameter (θ_0) that accounts for an additive flux offset at the (known) time of the meridian flip.

Aside from the GP components, we also allowed jitter terms (see Sect. 3.3.2) for both the photometry and the radial velocities. Some were found to be consistent with 0, namely $\sigma_{\rm TESS}$ and $\sigma_{\rm CORALIE}$, and therefore these parameters are set to 0 for the final fits; whereas the others ($\sigma_{\rm LCO\text{-}z}$, $\sigma_{\rm LCO\text{-}i}$, and $\sigma_{\rm FEROS}$) are left to be free.

TOI-163 While the *TESS* and CHAT data are relatively well-behaved, the Hazelwood, LCO i band, and El Sauce data show clear signs of systematic effects, therefore, we performed additional model fits with and without GP components, in the same manner as for TOI-150. We decided to consider 1 GP component (y pixel centroid) for the Hazelwood photometry, 2 GP components (FWHM, sky flux) for the LCO i band photometry, and an exponential and Matern GP kernel (time) for the El Sauce photometry.

As for the jitter terms, we encounter that $\sigma_{\rm TESS}$, $\sigma_{\rm CHAT}$, and $\sigma_{\rm FEROS}$ can be fixed to 0, whereas $\sigma_{\rm Hazelwood}$, $\sigma_{\rm LCO\text{-}i}$, and $\sigma_{\rm El\ Sauce}$ will be allowed to be free in the fit.

4.5.3 Final model parameters

With the whole set up complete, we perform two main runs for a circular and eccentric model by keeping every parameter prior identical except for $\sqrt{e_b}\sin\omega_b$ and $\sqrt{e_b}\cos\omega_b$, which were fixed for the circular model and free for the eccentric model.

TOI-150 Interestingly enough, this hot Jupiter prefers an eccentric orbit ($e = 0.26$) rather than a circular one ($\Delta \ln \mathcal{Z} > 700$).

TOI-163 TOI-163 b follows a rather circular model, ever so slightly preferred ($\Delta \ln \mathcal{Z} < 2$).

4.5.4 Signals in the residuals

After performing a 1-planet model fit, the radial velocity residuals were checked for additional potential signals.

TOI-150 By eye and by the generalized Lomb-Scargle periodogram (GLS; Zechmeister & Kürster, 2009), no signals suggestive of being above the significance level of the False Alarm Probability (FAP) were seen (Eq. 24 in Zechmeister & Kürster, 2009). That being said, there is *some* hint of power around $\sim$ 10 days. To further investigate if it is possible that there is evidence for a 2-planet model, supplementary fits were carried out on *just* the RVs from FEROS and CORALIE. Using wide uniform priors for the period and semi-amplitude of a second signal with `juliet`, we found that indeed the posterior period for an additional, non-zero amplitude signal in the data peaks at about 10 days. However, when the log-evidences of the 1-planet and 2-planet models are compared, the difference is not significant ($\Delta \ln \mathcal{Z} \lesssim 2$) and thus the simpler, 1-planet model is favored by the current data and for this reason, we do not continue to investigate the secondary signal further at this point.

TOI-163 FWe found suggestions in the RV residuals for an extra periodic signal (Fig. 4.5). Looking at the GLS periodogram of the radial velocity residuals, a bump around 34 days is present — it is, however, not above any significance level. 2-planet models fits on solely the RVs from FEROS were performed, again trying wide uniform priors in the period and semi-amplitude of a possible signal. The posterior period of this additional possible signal was 37 days — however, the log-evidence of this 2-planet fit was also not significantly better than the 1-planet fit ($\Delta \ln \mathcal{Z} \lesssim 2$), and thus the 1-planet fit model is preferred and the potential signal is not further explored.

Table 4.3: Presented below are the posterior parameters obtained for TOI-150 b TOI-163 b using `juliet`. Priors can be found in Table 4.2. $^{(a)}$ Error bars denote the 68% posterior credibility intervals. $^{(b)}$ Upper limits denote the 95% upper credibility interval of fits.

	Posterior estimate^a	
Parameter name	TOI-150 b	TOI-163 b
P_b (days)	$5.857487^{+0.000089}_{-0.000097}$	$4.231306^{+0.000063}_{-0.000057}$
$t_{0,b}$ (BJD UTC)	$2458326.27730^{+0.00086}_{-0.00089}$	$2458328.8797^{+0.00062}_{-0.00063}$
ρ_* (kg/m^3)	538^{+15}_{-16}	459^{+24}_{-25}

Parameter name	Posterior estimate[a] TOI-150 b	TOI-163 b
$r_{1,b}$	$0.552^{+0.077}_{-0.115}$	$0.577^{+0.035}_{-0.038}$
$r_{2,b}$	$0.0826^{+0.0012}_{-0.0011}$	$0.091^{+0.0016}_{-0.0015}$
K_b (m/s)	240^{+11}_{-11}	120^{+12}_{-11}
e_b	$0.262^{+0.045}_{-0.037}$	0 (fixed[b], < 0.091)
Posterior parameters for *TESS*		
D_{TESS}	$0.9959^{+0.0028}_{-0.0053}$	$0.970^{+0.012}_{-0.030}$
M_{TESS} (ppm)	7^{+20}_{-20}	-1^{+20}_{-21}
σ_{TESS} (ppm)	0 (fixed[b], < 87)	0 (fixed[b], < 90.3)
$q_{1,\mathrm{TESS}}$	$0.68^{+0.19}_{-0.22}$	$0.45^{+0.27}_{-0.21}$
$q_{2,\mathrm{TESS}}$	$0.076^{+0.092}_{-0.050}$	$0.14^{+0.19}_{-0.09}$
Posterior parameters for CHAT		
M_{CHAT} (ppm)	—	7^{+248}_{-265}
σ_{CHAT} (ppm)	—	0 (fixed[b], < 361)
$q_{1,\mathrm{CHAT}}$	—	$0.75^{+0.09}_{-0.09}$
Posterior parameters for Hazelwood		
$M_{\mathrm{Hazelwood}}$ (ppm)	—	3904^{+1917}_{-2355}
$\sigma_{\mathrm{Hazelwood}}$ (ppm)	—	3154^{+220}_{-206}
$q_{1,\mathrm{Hazelwood}}$	—	$0.54^{+0.17}_{-0.18}$
$\mathrm{GP}_{\sigma,\mathrm{Hazelwood}}$ (ppm)	—	3591^{+2342}_{-1259}
$\mathrm{GP}_{\mathrm{y,Hazelwood}}$	—	$6.97^{+11.45}_{-3.65}$
Posterior parameters for LCO z band		
$M_{\mathrm{LCO}\text{-}z}$ (ppm)	-258^{+169}_{-163}	—
$\sigma_{\mathrm{LCO}\text{-}z}$ (ppm)	1096^{+110}_{-100}	—
$q_{1,\mathrm{LCO}\text{-}z}$	$0.404^{+0.083}_{-0.050}$	—
Posterior parameters for LCO i band		
$M_{\mathrm{LCO}\text{-}i}$ (ppm)	-1317^{+172}_{-182}	-7744^{+1174}_{-1145}
$\sigma_{\mathrm{LCO}\text{-}i}$ (ppm)	1366^{+79}_{-74}	22515^{+170}_{-144}
$q_{1,\mathrm{LCO}\text{-}i}$	$0.179^{+0.089}_{-0.085}$	$0.21^{+0.14}_{-0.12}$
$\mathrm{GP}_{\sigma,\mathrm{LCO}\text{-}i}$	—	4725^{+762}_{-593}
$\mathrm{GP}_{\mathrm{FWHM,LCO}\text{-}i}$	—	$13.1^{+14.3}_{-6.3}$
$\mathrm{GP}_{\mathrm{sky\ flux,LCO}\text{-}i}$	—	27^{+34}_{-12}
Posterior parameters for El Sauce		
$M_{\mathrm{El\ Sauce}}$ (ppm)	-6374^{+1675}_{-1392}	-1772^{+18632}_{-12903}
$\sigma_{\mathrm{El\ Sauce}}$ (ppm)	4449^{+242}_{-228}	2457^{+144}_{-145}
$q_{1,\mathrm{El\ Sauce}}$	$0.73^{+0.15}_{-0.19}$	$0.34^{+0.29}_{-0.22}$
$\mathrm{GP}_{\sigma,\mathrm{El\ Sauce}}$	3608^{+1442}_{-1021}	$16.2^{+26.2}_{-8.9}$
$\mathrm{GP}_{airmass,\mathrm{El\ Sauce}}$	18^{+17}_{-14}	—
$\mathrm{GP}_{\rho,\mathrm{El\ Sauce}}$	—	$2.4^{+9.3}_{-2.0}$

Parameter name	Posterior estimate[a] TOI-150 b	TOI-163 b
$\mathrm{GP}_{T,\text{El Sauce}}$	—	$0.79^{+4.52}_{-0.65}$
Posterior parameters for TRAPPIST-S		
$M_{\text{TRAPPIST-S}}$ (ppm)	-6673^{+207}_{-215}	—
$\sigma_{\text{TRAPPIST-S}}$ (ppm)	4122^{+99}_{-95}	—
$q_{1,\text{TRAPPIST-S}}$	$0.54^{+0.12}_{-0.12}$	—
$\theta_{0,\text{TRAPPIST-S}}$	$-0.00500^{+0.00041}_{-0.00043}$	—
Posterior RV parameters		
μ_{FEROS} (m/s)	$5939.0^{+7.3}_{-7.2}$	$21393.7^{+6.7}_{-6.6}$
σ_{FEROS} (m/s)	$32.8^{+7.9}_{-6.6}$	0 (fixed[b], < 43)
μ_{CORALIE} (m/s)	5887^{+12}_{-13}	—
σ_{CORALIE} (m/s)	0 (fixed[b], < 36)	—

Table 4.4: Presented below are the derived planetary parameters obtained for TOI-150 b and TOI-163 b using the posterior values from Table 4.3.

Parameter name	Posterior estimate[a] TOI-150 b	TOI-163 b
Derived transit parameters for		
R_p/R_*	$0.0826^{+0.0012}_{-0.0011}$	$0.09082^{+0.0016}_{-0.0015}$
$b = (a/R_*)\cos(i_p)$	$0.33^{+0.12}_{-0.17}$	$0.365^{+0.053}_{-0.057}$
a_b/R_*	$9.917^{+0.092}_{-0.099}$	$7.57^{+0.13}_{-0.14}$
i_p (deg)	$88.09^{+0.98}_{-0.68}$	$87.24^{+0.47}_{-0.45}$
u_1	$0.124^{+0.131}_{-0.082}$	$0.19^{+0.16}_{-0.12}$
u_2	$0.69^{+0.15}_{-0.21}$	$0.48^{+0.25}_{-0.32}$
t_T (hours)	$5.12^{+0.21}_{-0.18}$	$4.93^{+0.17}_{-0.15}$
Derived physical parameters		
M_p (M_J)	$2.51^{+0.12}_{-0.12}$	$1.22^{+0.12}_{-0.12}$
R_p (R_J)	$1.255^{+0.021}_{-0.019}$	$1.489^{+0.034}_{-0.034}$
ρ_p (g cm^{-3})	$1.68^{+0.12}_{-0.12}$	$0.49^{+0.059}_{-0.055}$
g_p (m s^{-2})	$41.3^{+2.5}_{-2.4}$	$14.2^{+1.5}_{-1.5}$
a (AU)	$0.07037^{+0.00087}_{-0.00088}$	$0.0580^{+0.0014}_{-0.0014}$
T_{eq} (K)[c]	$1404.5^{+7.1}_{-6.5}$	1669^{+16}_{-14}

[a] Error bars denote the 68% posterior credibility intervals.

[c] Equilibrium temperatures calculated assuming 0 Bond Albedo.

4.6 Further analysis

4.6.1 Stellar density prior

We also experimented with the impact that a stellar density prior[21], ρ_*, may have on eccentricity as well as on the stellar density itself by allowing the stellar density prior to be an uninformative Jeffrey's prior, $\mathcal{J}(1,10000)$, rather than a normal prior (as provided by Table 4.2). Focusing just on the TOI-150 data since this target has a planet with eccentric behavior, we found that the eccentricities agree with each other regardless of whether ρ_* was given as a normal ($e = 0.26 \pm 0.04$) or Jeffrey's prior ($e = 0.27 \pm 0.05$). Both obtained stellar densities from the eccentric fits agreed with the expected density where the distribution was accurate ($\rho_* = 537^{+15}_{-16}$) but much more uncertain when ρ_* was given as a Jeffrey's prior ($\rho_* = 523^{+129}_{-120}$). As for the circular fits, both obtained density distributions deviated from the expected value yet showed narrow precision; when ρ_* was given as a normal prior, the deviation was mild ($\rho_* = 451^{+10}_{-11}$), where the deviation was huge for when ρ_* was given as a Jeffrey's prior ($\rho_* = 25^{+3}_{-4}$), for which both the photometry and radial velocity visually exhibited larger residuals from the fit. This demonstrated disagreement of stellar density distributions among the circular fits is due to the fact that the evidence for TOI-150 favors a non-circular model over a circular model ($\Delta \ln Z > 700$).

4.6.2 Search for secondary eclipses

A search for secondary eclipses was performed on the *TESS* photometry. The expected secondary eclipse depth, assuming reflected light is the main component (i.e., a depth equal to $A_g(a/R_p)^2$, where A_g is the geometric albedo) was smaller than 69±2 ppm for TOI-150 b, and 144±7 ppm for TOI-163 b (assuming $A_g < 1$, which seems to be the case for hot Jupiters; see, e.g., Heng & Demory, 2013). Given the *TESS* data as of now solely from Sector 1, there is no significant dip at the anticipated times. They might be detectable, however, once data from future sectors is released — see Sect. 4.7.3 for a more in-depth discussion. Detecting phase variations (as described in Shporer, 2017) with the current data is not possible given the large amount of systematics present.

4.7 Discussion

4.7.1 The two systems

With the help of multiple photometric and spectroscopic instruments (which highlights the enormous contribution that a program such as TFOP can deliver to exoplanetary science) we were able to obtain tight constraints on the period and time of periastron, and thanks to precise parallax measurements from *Gaia* we constrain the stellar radius, and therefore the planetary radius and semimajor-axis very well, in comparison to other known hot Jupiters[22]

[21] When ρ_* is given as a prior, then a, the scaled semi-major axis, is no longer a model parameter.

[22] using the NASA Exoplanet Archive; `exoplanetarchive.ipac.caltech.edu`, accessed on 11 March 2019

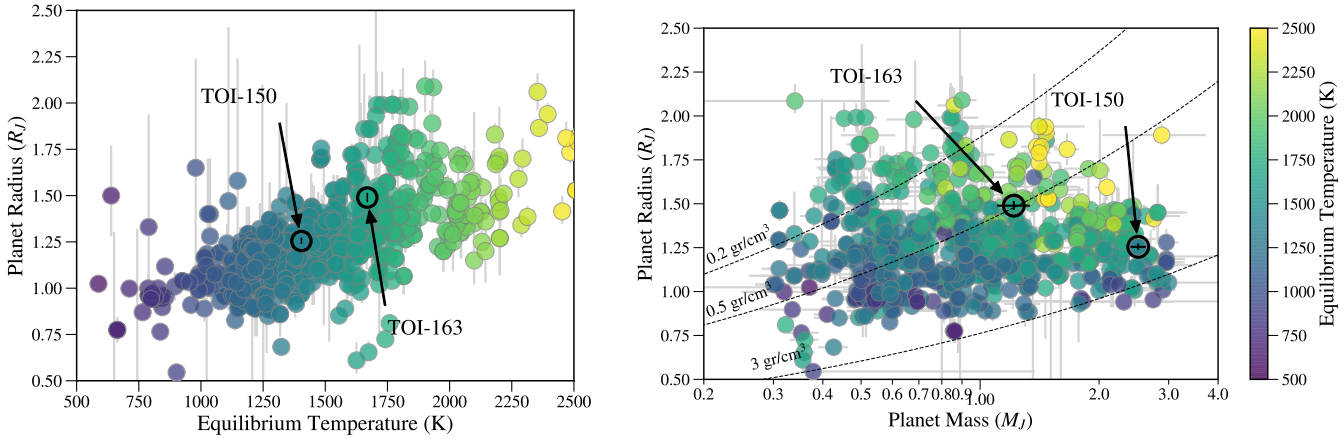

Figure 4.7: Radius versus equilibrium temperature (left) and a radius versus mass (right) plot of the known hot Jupiters ($0.7 \leq P$ (days) ≤ 10, $0.3 \leq M_p$ (M_J) ≤ 3.0) where TOI-150 b and TOI-163 b are annotated and their error bars are plotted on top. Note the small error for the targets characterized in this work in comparison with previously characterized systems.

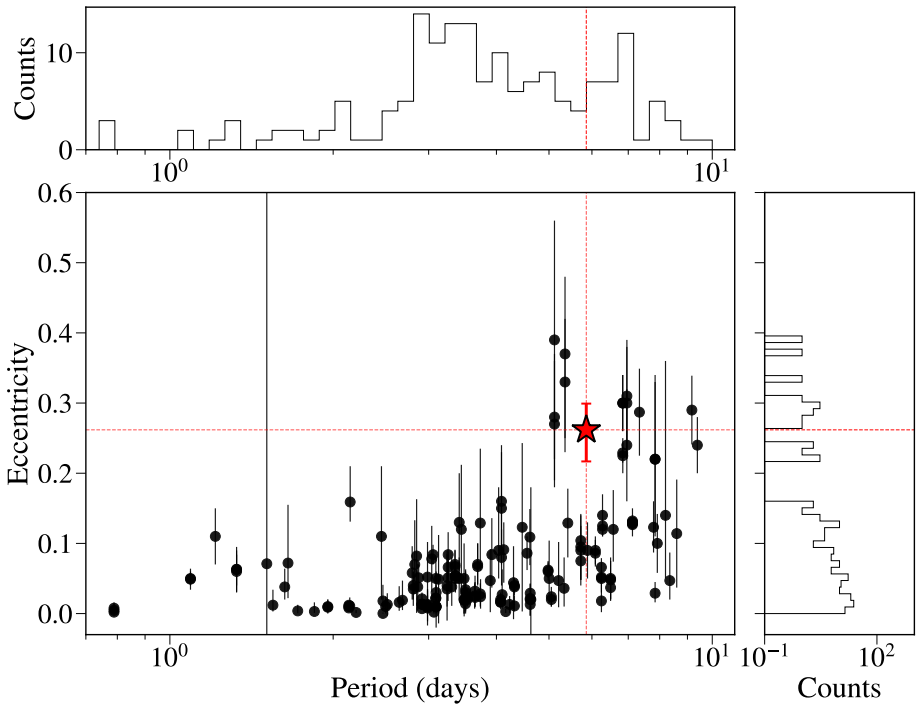

Figure 4.8: Eccentricities as a function of planetary period for known hot Jupiters ($0.7 \leq P$ (days) ≤ 10, $0.3 \leq M_p$ (M_J) ≤ 2.0) where TOI-150 b is denoted as a red star. There are a total of 168 planets with non-zero eccentricity. Note that non-zero eccentricity planets without proper error bars were ignored given that the provided eccentricity values most likely were representing the upper eccentricity value rather than the true eccentricity.

(Fig. 4.7). TOI-150 b is a $1.254 \pm 0.016 R_J$ massive ($2.61^{+0.19}_{-0.12}$ M_J) hot Jupiter in a 5.857-day orbit with a peculiarly high eccentricity ($e = 0.262^{+0.045}_{-0.037}$) — discussed more in Sect. 4.7.2 — and density larger than Jupiter's ($\rho_p = 1.7 \pm 0.1$ g cm^{-3}). On the other hand, TOI-163 b is an inflated hot Jupiter ($R_P = 1.478^{+0.022}_{-0.029} R_J$, $M_P = 1.22 \pm 0.11 M_J$) on a $P = 4.231$-day circular orbit, with a density less than that of Saturn ($\rho_p = 0.49 \pm 0.05$ g cm^{-3}). Though TOI-163 b does not appear to be an outlier in Fig. 4.7 relative to the other planets, targets of such equilibrium temperatures are not expected to have such high radii, but rather radii of $1 R_J$ (Sestovic et al., 2018) These two targets are quite exciting given that both of them should be observed in at least 12 sectors with *TESS*. Moreover, TOI-150 and TOI-163 are only 10.4° and 6.4°, respectively, away from the center of the Continuous Viewing Zone (CVZ)[23] of the future *James Webb Space Telescope* (*JWST*; Gardner et al., 2009). Note that the CVZ has a relatively small radius of 5°, meaning that TOI-163 is sitting right on the edge. In fact, both targets should be observable for more than ∼200 days[24] with this future exciting space-based observatory. Though both targets are not particularly suitable for transmission spectroscopy with *JWST*, they both show promise for secondary eclipse observations — further discussed in Sect. 4.7.3. Both targets are moreover ideal for the Rossiter-McLaughlin (RM) effect, where an ample number of observations during the transits could be taken, allowing us to resolve the effect well and thus, gain a better grasp for the spin-orbit alignment of the system — also explained more in Sect. 4.7.3.

4.7.2 Eccentricity of TOI-150 b

When we look at all the known hot Jupiters and their eccentricities (Fig. 4.8), we notice that most of them have zero eccentricities. For a hot Jupiter to have a non-zero eccentricity, it either has to be currently migrating towards a circular orbit through tidal decay or it has to be excited into an eccentric orbit by, e.g., a stellar or planetary companion. For this reason, exoplanets with higher eccentricities are intriguing to follow and explore — TOI-150 b is alluring for this reason.

We calculate the circularization time-scale (Eq. 2 in Adams & Laughlin, 2006) to be 3.46 ± 0.68 Gyr using a Q-factor of 10^6 (Penev et al., 2012), or 2 magnitudes larger if we adopt a Q-factor of $\sim 10^8$ (Collier Cameron & Jardine, 2018) since the time-scale scales linearly with Q. This time-scale is then on the same order of magnitude as the age of the star or larger ($\gtrsim 2.46$ Gyr, Table 4.1). If the time-scale were shorter than the age of the star, then we would expect to see an already circular orbit, unless there were other companions involved that could have excited the planet into an eccentric orbit. Our calculation serves as just a rough order of magnitude estimate, as the Q-factor is not so well defined for F-type stars — work similar to that of Penev et al. (2016); Hoyer et al. (2016b,a) have constrained this factor for solar-type stars to be 6.5−7 using massive ultra-short period giant exoplanets. Such a study is needed for F-type stars to understand whether our selected Q-factor is reasonable and, thus, if the observed circularization time-scale truly agrees with our estimated age of the system.

[23] `https://jwst-docs.stsci.edu/display/JTI/\JWST+Observatory+Coordinate+System+and+Field+of+Regard`

[24] Fig. 2, `https://jwst-docs.stsci.edu/display/JTI/\JWST+Target+Viewing+Constraints`

4.7.3 Secondary eclipses, transmission spectroscopy, and RM effect

As mentioned before, both targets are very close to the *JWST* CVZ, particularly TOI-163 being just on the edge. This makes these targets interesting in their own right as scheduling for these targets would be easier, which would open the window for several exciting possibilities of atmospheric characterization. For transmission spectroscopy in particular, TOI-163 b is a decent target (with an expected atmospheric signal in transmission of ∼70 ppm, assuming one scale-height of variation; see, e.g., Wakeford et al., 2019) whereas TOI-150 b is not particularly good since the expected atmospheric signal in transmission (∼20 ppm) is just hitting the noise floor of 20 ppm for *JWST* (Greene et al., 2016).

In general, the expected atmospheric signal alone does not tell us how good actual observations with observatories like *JWST* will be for the targets, as this has to be weighted against, e.g., the apparent magnitude of the targets. We thus use the figure of merit (FOM) introduced by Zellem et al. (2017) in order to calculate how good our targets are for transmission spectroscopy studies and compare this to the known hot Jupiters. This FOM is given by

$$\mathrm{FOM}_{transspec} = \frac{\delta_{transpec}}{10^{0.2H-mag}},$$

where

$$\delta_{transpec} = \frac{2R_pH}{R_*^2}.$$

Here, R_p is the planetary radius, R_* is the stellar radius, and $H = k_bT_p/mg_p$ is the planetary scale-height. For calculating the scale height, the different parameters include the Boltzmann's constant, k_b, the planetary equilibrium temperature, T_p, the mean mass, m, that makes up the planet's atmosphere (assumed $2.3\,m_{\mathrm{proton}}$ for a hot Jupiter resembling a composition consisting mostly of H_2), and the gravity on the planet's surface, g_p. $H-mag$ in the FOM is the magnitude of the host star in the H band. We present the FOM for transmission spectroscopy for all known transiting hot Jupiters in the top panel of 4.9. As can be seen, TOI-163 is the best of the two here presented exoplanets for transmission spectroscopy, but it has a rather average FOM in comparison to other known hot Jupiters (Fig. 4.9).

We repeat this exercise for our targets, but now for secondary eclipses following the FOM introduced in Zellem et al. (2018), which is given by

$$\mathrm{FOM}_{eclipse} = \frac{F_pR_p^2F_*^{-1}R_*^{-1}}{10^{0.2H-mag}}$$

where F is the flux of either the planet or star and which here, for simplicity, we approximate with blackbody radiation. We find that the secondary eclipses of both targets should be observed with *JWST* (Fig. 4.9).

Both targets are deemed as highly suitable targets for follow-up Rossiter-McLaughlin (RM) observations, which can aid in determining the spin-orbit alignment between the hot Jupiter and the host star. Many hot Jupiters have been found to have large misalignments (Crida & Batygin, 2014) and the degree of misalignment can help in distinguishing between different migration theories. In addition, both targets lie just above the cutoff ($T_{eff} = 6090^{+150}_{-110}$K)

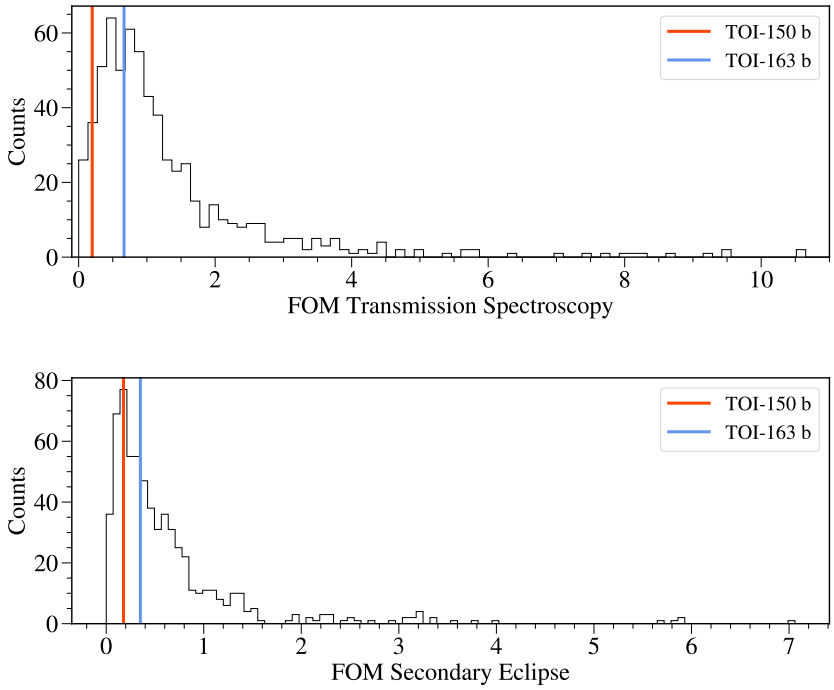

Figure 4.9: Distributions of the figure of merit (FOM) for both transmission spectroscopy (top) and secondary eclipses (bottom) for all known transiting hot Jupiters ($0.7 \leq P$ (days) ≤ 10, $0.3 \leq M_p$ (M_J) ≤ 2.0) are shown. The two targets are not the top candidates for transmission spectroscopy with *JWST*, but will be good follow-up candidates for secondary eclipses. Note that those with all required parameters in calculating the FOM were kept (646 in total).

where we expect to see co-planar and misaligned planets (Triaud, 2018), which is even more so intriguing for TOI-150 b given its eccentric nature. Using equation 6 of Gaudi & Winn (2007),

$$K_R = 52.8 \text{ m s}^{-1} \left(\frac{V_S \sin I_S}{5 \text{ km s}^{-1}}\right) \left(\frac{r}{R_J}\right)^2 \left(\frac{R}{R_\odot}\right)^{-2}$$

where $V_S \sin I_S$ is 7.96 and 14.08 km s^{-1} for TOI-150 and TOI-163 (Table 4.1), respectively, r is the radius of the planet, and R is the radius of the star; we obtain K_R values of $56.9^{+2.6}_{-2.5}$ and $121.4^{+4.9}_{-4.7}$ ms^{-1} for TOI-150 b and TOI-163 b, respectively. Given that the average spectrum exposure time is roughly 400∼600 seconds with an average uncertainty of 15ms^{-1} (for an instrument like FEROS) and that the transit duration is $5.12^{+0.21}_{-0.18}$ and $4.93^{+0.17}_{-0.15}$ hours for TOI-150 b and TOI-163 b, respectively, then we would be able to obtain at least 30 and 29 observations during the transit, which is more than adequate to resolve the RM effect, making both targets optimal for these observations.

4.8 Summary and conclusions

We have presented the 30-minute cadence *TESS* discovery of two hot Jupiters, TOI-150 b and TOI-163 b, supported by follow-up photometric and spectroscopic measurements, in which a joint fit of the transit photometry and radial velocity data was performed using the new tool `juliet` in order to thoroughly constrain the planet parameters with truly high precision. The radial velocity and speckle imaging all favor and provide evidence of the planetary nature of these detected signals. Both targets exhibit promising outcomes for investigating spin-orbit alignment using the RM effect and they both will serve as great secondary eclipse candidates considering they are very close to the *JWST* CVZ. TOI-150 b is on its own an appealing exoplanet to investigate given its high, non-zero eccentricity of 0.26, a very uncommon value among already known hot Jupiters.

4.9 RV data

Table 4.5: RV data for TOI-150 and TOI-163

BJD	RV (m/s)	σ_{RV} (m/s)	BIS (m/s)	σ_{BIS} (m/s)	Instrument
TOI-150 b					
2458380.90067285	5759.5	20.3	—	—	FEROS
2458382.88380768	6173.3	18.1	—	—	FEROS
2458383.87194905	6111.3	17.9	—	—	FEROS
2458404.88308931	5742.8	21.1	—	—	FEROS
2458405.88147085	6123.2	41.5	—	—	FEROS
2458406.83142053	6129.1	26.3	—	—	FEROS
2458407.83470737	6033.6	19.2	—	—	FEROS
2458408.82604035	5915.8	17.8	—	—	FEROS
2458409.86509756	5797.0	18.6	—	—	FEROS
2458411.81545717	6089.7	13.9	—	—	FEROS
2458412.85573438	6173.7	18.7	—	—	FEROS
2458413.84420872	6031.4	14.6	—	—	FEROS
2458414.84889668	5776.0	20.1	—	—	FEROS
2458415.82757009	5670.2	16.0	—	—	FEROS
2458416.86018291	5739.9	17.1	—	—	FEROS
2458419.8486401	6012.2	13.1	—	—	FEROS
2458423.83362607	6156.8	13.8	—	—	FEROS
2458424.85709901	6136.5	14.7	—	—	FEROS
2458425.86485223	5930.9	16.1	—	—	FEROS
2458429.80863718	6205.9	14.9	—	—	FEROS
2458380.90067285	5759.5	20.3	-170.0	16.0	FEROS
2458382.88380768	6173.3	18.1	24.0	15.0	FEROS
2458383.87194905	6111.3	17.9	39.0	14.0	FEROS
2458404.88308931	5742.8	21.1	45.0	16.0	FEROS
2458405.88147085	6123.2	41.5	-55.0	28.0	FEROS

2458406.83142053	6129.1	26.3	-61.0	19.0	FEROS
2458407.83470737	6033.6	19.2	-35.0	15.0	FEROS
2458408.82604035	5915.8	17.8	-6.0	14.0	FEROS
2458409.86509756	5797.0	18.6	19.0	15.0	FEROS
2458411.81545717	6089.7	13.9	52.0	12.0	FEROS
2458412.85573438	6173.7	18.7	54.0	15.0	FEROS
2458413.84420872	6031.4	14.6	46.0	12.0	FEROS
2458414.84889668	5776.0	20.1	-34.0	15.0	FEROS
2458415.82757009	5670.2	16.0	-63.0	13.0	FEROS
2458416.86018291	5739.9	17.1	33.0	14.0	FEROS
2458419.8486401	6012.2	13.1	40.0	11.0	FEROS
2458423.83362607	6156.8	13.8	24.0	12.0	FEROS
2458424.85709901	6136.5	14.7	-1.0	12.0	FEROS
2458425.86485223	5930.9	16.1	36.0	13.0	FEROS
2458429.80863718	6205.9	14.9	46.0	12.0	FEROS
2458397.83712	5736.999031	48.658679	31.324024	—	CORALIE
2458406.86688	6079.387336	46.069359	-93.379215	—	CORALIE
2458429.84056	6170.489484	42.783046	94.843539	—	CORALIE
TOI-163 b					
2458378.85013241	21568.5	40.7	—	—	FEROS
2458380.89084693	21207.4	40.1	—	—	FEROS
2458382.87693218	21457.0	36.6	—	—	FEROS
2458404.85311362	21539.5	48.6	—	—	FEROS
2458406.82378293	21393.1	49.6	—	—	FEROS
2458407.81941527	21537.2	36.5	—	—	FEROS
2458408.8185913	21472.4	32.9	—	—	FEROS
2458409.84656667	21323.1	31.1	—	—	FEROS
2458411.78963728	21485.9	29.8	—	—	FEROS
2458412.84865563	21457.3	28.7	—	—	FEROS
2458413.81576425	21395.7	29.2	—	—	FEROS
2458414.84005922	21256.5	37.1	—	—	FEROS
2458415.81862245	21435.9	32.4	—	—	FEROS
2458416.82361037	21545.6	48.8	—	—	FEROS
2458417.86201875	21293.9	43.1	—	—	FEROS
2458419.82121021	21347.9	26.7	—	—	FEROS
2458422.83279187	21308.1	42.3	—	—	FEROS
2458423.80890101	21346.3	26.4	—	—	FEROS
2458424.79374323	21462.0	32.5	—	—	FEROS
2458425.84750539	21452.4	35.1	—	—	FEROS
2458378.85013241	21568.5	40.7	153.0	15.0	FEROS
2458380.89084693	21207.4	40.1	142.0	14.0	FEROS
2458382.87693218	21457.0	36.6	66.0	13.0	FEROS
2458404.85311362	21539.5	48.6	24.0	17.0	FEROS
2458406.82378293	21393.1	49.6	91.0	17.0	FEROS
2458407.81941527	21537.2	36.5	24.0	13.0	FEROS
2458408.8185913	21472.4	32.9	92.0	12.0	FEROS
2458409.84656667	21323.1	31.1	229.0	12.0	FEROS
2458411.78963728	21485.9	29.8	-3.0	11.0	FEROS

2458412.84865563	21457.3	28.7	54.0	11.0	FEROS
2458413.81576425	21395.7	29.2	12.0	11.0	FEROS
2458414.84005922	21256.5	37.1	-76.0	13.0	FEROS
2458415.81862245	21435.9	32.4	11.0	12.0	FEROS
2458416.82361037	21545.6	48.8	-58.0	16.0	FEROS
2458417.86201875	21293.9	43.1	137.0	15.0	FEROS
2458419.82121021	21347.9	26.7	0.0	11.0	FEROS
2458422.83279187	21308.1	42.3	152.0	15.0	FEROS
2458423.80890101	21346.3	26.4	30.0	11.0	FEROS
2458424.79374323	21462.0	32.5	22.0	12.0	FEROS
2458425.84750539	21452.4	35.1	76.0	13.0	FEROS

5 TOI-1201 b: a mini-Neptune transiting a bright and relatively young M dwarf

The content of this Chapter is based on the soon-to-be submitted work to the journal A&A.

Details of authorship: I am the first author of this paper and led the team effort involving 36+ co-authors. I was under the supervision of Prof. Thomas Henning and Martin Kürster, with collaboration with Jonas Kemmer. I have done the scientific work, analysis, and reached the conclusions. The stellar parameters were computed by Andreas Schweitzer. The text was written by me with the contributions of Jose Caballero in Sect. 5.5. All figures were done by me, unless otherwise stated in the caption.

5.1 Motivation

We present the discovery of a transiting mini-Neptune around TOI-1201, a relatively bright and young early M dwarf ($J \approx 9.5$ mag, ~600 Myr) in an equal-mass ~8 arcsec-wide binary system, using data from the *Transiting Exoplanet Survey Satellite* (*TESS*), along with follow-up transit observations. With an orbital period of 2.49 d, TOI-1201 b is a mini-Neptune with a radius of $R_b = 2.415 \pm 0.090\,R_\oplus$. This signal is also present in the precise radial velocity measurements from CARMENES, confirming the existence of the planet and providing a planetary mass of $M_b = 6.28 \pm 0.88\,M_\oplus$. The spectroscopic observations additionally show evidence of stellar activity at 19 d and an undetermined long periodic variation. In combination with ground-based photometric monitoring from WASP-South and ASAS-SN, we attribute the 19 d signal to the stellar rotation period ($P_{\rm rot}$ = 19–23 d), although we cannot rule out that the variation seen in photometry belongs to the visually close binary companion. We spectroscopically resolve TOI-1201 and its companion and calculate precise stellar parameters for both objects. The transiting planet is an excellent target for transmission spectroscopy (TSM = 128^{+35}_{-27}) with the upcoming *James Webb Space Telescope*. Its spin-orbit alignment is also feasible to measure via the Rossiter-McLaughlin effect with current state-of-the-art spectrographs (e.g., ESPRESSO).

5.2 Context

Results from the *Kepler* (Borucki et al., 2010; Mathur et al., 2017) and *K2* (Howell et al., 2014) missions have revealed M dwarfs ($T_{\rm eff} \lesssim 4000$ K) host on average ~2.5 planets with

radii below 4 $R_\oplus$ and with periods less than 200 d (e.g. Dressing & Charbonneau, 2013, 2015). The distribution of radii of small, close-in planets exhibits a bimodal distribution producing a radius gap that separates them into "super-Earths" with radii slightly larger than Earth (1–2 $R_\oplus$) and "mini-Neptunes" slightly smaller than Neptune (2–4 $R_\oplus$). For solar-like stars, this radius gap occurs between 1.7 $R_\oplus$ and 2.0 $R_\oplus$ (Fulton et al., 2017; Fulton & Petigura, 2018; Van Eylen et al., 2018) and it resides a bit lower for low-mass stars, between 1.4 $R_\oplus$ and 1.7 $R_\oplus$ (Cloutier & Menou, 2020; Van Eylen et al., 2021). This bimodality suggests that mini-Neptunes are mostly rocky planets that were born with primary atmospheres and were able to retain them, whereas planets below the radius gap lost their atmospheres and were stripped to their cores (Bean et al., 2021).

Determining the mechanism that drives atmospheric loss for these planets remains ambiguous, with the prime candidates being core-powered mass loss (Ginzburg et al., 2016, 2018; Gupta & Schlichting, 2019, 2021), and photo-evaporation (e.g., Owen & Wu, 2013, 2017; Lehmer & Catling, 2017; Van Eylen et al., 2018; Mordasini, 2020). In both models, the heating of the planet's upper atmosphere drives a hydrodynamic outflow. In the case of core-powered mass loss, the planet's heating originates from infrared (IR) radiation coming from the cooling planetary interior, while photo-evaporation is due to extreme ultraviolet photons from the host star. However, is not clear which heating mechanism dominates the mass loss observed for mini-Neptune-sized planets. Thus, determining accurate masses of these worlds is critical in constraining the mass loss rate to learn how they evolve over time in hopes to better explain the origin of the radius gap. Precise mass and radius measurements alone are however not sufficient in establishing the bulk composition, as there are large degeneracies when figuring out the ratio of rock, water, and hydrogen for the interior structure (Rogers & Seager, 2010; Lopez & Fortney, 2014). Mini-Neptunes (Barnes et al., 2009; Rogers et al., 2011; Marcy et al., 2014; Rogers, 2015) are one of the most commonly detected outcomes of planet formation, and understanding the composition of their atmospheres can help to reveal the nature, origins, and evolution of these objects (Miller-Ricci & Fortney, 2010; Benneke & Seager, 2013; Crossfield & Kreidberg, 2017). Luckily, we find ourselves in an era in which the ongoing *Transiting Exoplanet Survey Satellite* (*TESS*; Ricker et al., 2015) mission is set out to find such targets suitable for transmission spectroscopy using the future *James Webb Space Telescope* (*JWST*; Gardner et al., 2009). Thus far, only a handful of Neptune-like planets around M dwarfs show promising potential based on their transmission spectroscopy metric (TSM; Kempton et al., 2018). Namely, these are: GJ 436 b (Butler et al., 2004), GJ 3470 b (Bonfils et al., 2012), GJ 1214 b (Charbonneau et al., 2009), LTT 3780 c (Nowak et al., 2020; Cloutier et al., 2020), TOI-1728 b (Kanodia et al., 2020), and LP 714-47 b (Dreizler et al., 2020).

Observations of planets in multiple-star systems can shed light on stellar and planet formation (see e.g., Goodwin et al., 2007, 2008). To date, planet discoveries in binary systems where the primary is an M dwarf are scarce even though they are the most abundant stars in our Galaxy (Henry et al., 2006; Winters et al., 2015). In less than 10% of the known binary systems with planet detections, is an M dwarf the primary[25]. Such a low count is not surprising since close M-dwarf systems were typically discarded from dedicated detection surveys due to the lack of high-resolution near-infrared spectrographs and the high risk of potential light contamination in transits (e.g., Cortés-Contreras et al., 2017).

[25] `https://exoplanetarchive.ipac.caltech.edu/`, accessed on 29 March 2021

Nearly half of the solar-like stars in our solar neighborhood are members of binaries or multiple systems (Duquennoy & Mayor, 1991; Raghavan et al., 2010), and 25 % of them are found in wide binaries ($s > 100$ AU). It has been shown that the planet occurrence rate for these wide binary systems is comparable to that around single stars presumably because the influence of the stellar companion is negligible on the formation of the planet (Raghavan et al., 2010; Wang et al., 2014; Deacon et al., 2016). Turning our focus back to M dwarfs, the stellar multiplicity rate is believed to be ∼16–27 % (Janson et al., 2012, 2014; Cortés-Contreras et al., 2017; Winters et al., 2019). However, the planet occurrence rate in low-mass binaries is still uncertain because these stellar targets have not been a major focus and were rather strongly biased against.

This number of detected planets around M dwarfs has however been rising. Many of the recent discoveries of wide binary systems have been made by the CARMENES team: HD 180617 (Kaminski et al., 2018), Gl 49 (Perger et al., 2019), LTT 3780 (Nowak et al., 2020; Cloutier et al., 2020), HD 79211 (GJ 338 B, González-Álvarez et al., 2020), GJ 3473 (TOI-488, Kemmer et al., 2020), and HD 238090 (GJ 458 A, Stock et al., 2020b). Precise stellar properties, as well as radial velocities, are commonly computed solely for the host, oftentimes missing the details for the companion with some exceptions, such as GJ 338 B (González-Álvarez et al., 2020) or GJ 15 A and B (Howard et al., 2014; Pinamonti et al., 2018; Trifonov et al., 2018). Studying these properties, such as metallicity and age, can shed light on which environments favor planet formation (Johnson & Li, 2012; Hobson et al., 2018; Montes et al., 2018). Observing more systems would allow for a better grasp on how stellar multiplicity in M-dwarf systems plays a role in the planet formation process and in the types of planets that can exist.

In this paper, we present the discovery and mass determination of the transiting mini-Neptune, TOI-1201 b. The planet orbits one companion of the M-dwarf wide binary system PM J02489–1432. We calculate precise stellar parameters and present radial velocity (RV) measurements for both the host and the companion. The mini-Neptune, with a period of 2.5 d, was initially discovered as a transiting planet candidate in *TESS* data and is confirmed here using ground-based photometry and RV measurements. Future observations with *JWST* will be able to precisely constrain the atmospheric compositions of this and other similar planets and, thus, provide important constraints on mini-Neptune formation.

The paper is organized as follows. The *TESS* photometry is introduced in Sect. 5.3 followed by the various ground-based photometric and spectroscopic observations in Sect. 5.4. The stellar properties of both TOI-1201 and its companion are discussed in Sect. 5.5. The modeling analysis combining all the available data to produce the final planetary parameters is presented in Sect. 5.6. Finally, in Sect. 5.7, we unveil the future prospects for TOI-1201 b. We give our final conclusions in Sect. 5.8.

5.3 *TESS* photometry

TOI-1201 (TIC 29960110) was observed by *TESS* with the short cadence (2-min integrations) during cycle 1, sector 4 (camera #1, CCD #1) between 18 October and 15 November 2018, and also during the first year of the extended mission during cycle 3, sector 31 (camera #1, CCD #1, 20-s and 2-min integrations) between 21 October 2020 and 19 November 2020. For the analysis, we used only the 2-min integrations. The target was not initially announced

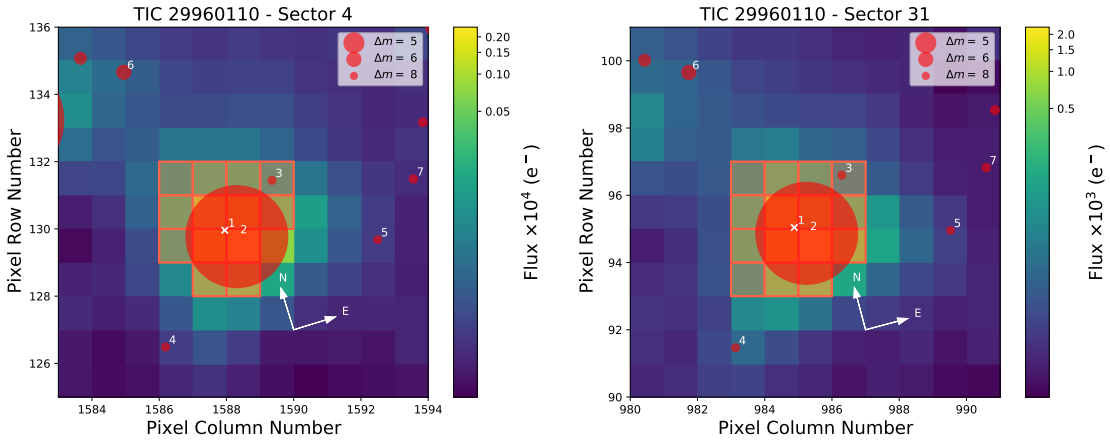

Figure 5.1: *TESS* TPF plot for TOI-1201 for sectors 4 and 31. The SAP was computed using the flux counts coming in from the red bordered pixels (mask). The red circles represent neighboring sources listed from *Gaia* DR2 where the size corresponds to the brightness difference with respect to TOI-1201. The close companion to TOI-1201 is indicated as source # 2.

as a *TESS* object of interest (TOI) along with the other TOIs from sector 4, but rather its companion (TOI-393, TIC 29960109) that fell on the same pixel was (Sect. 5.5.2). Fig. 5.1 displays a plot of the target pixel file (TPF) and the aperture mask used to produce the simple aperture photometry (`SAP`), created using `tpfplotter`[26] (Aller et al., 2020).

Within the *TESS* follow-up program (TFOP) "Seeing-limited Photometry" SG1 subgroup[27], the first follow-up transit photometric data immediately indicated that TOI-1201 was the correct stellar host and not TOI-393 (see Sect. 5.4.1). We downloaded the *TESS* data from the Mikulski Archive for Space Telescopes [28]. The *TESS* photometric light curve is corrected for systematics (`PDCSAP` flux) (Smith et al., 2012; Stumpe et al., 2012, 2014) and is presented in Fig. 5.5 with the best-fit model (explained in detail in Sect. 5.6.3).

TOI-1201 and its equally bright (0.26 mag fainter in G_{BP} fainter) companion are just 8 arcsec away from one another (see Sect. 5.5.2) and, therefore, fall on the same *TESS* pixel (21 arcsec). This raises the issue of ensuring that the radius ratio is correct. This problem is solved since the `PDCSAP` flux is corrected for possible nearby flux contamination. Therefore, the preliminary parameters provided by the Science Processing Operations Center (Jenkins et al., 2016) presented in the TOI catalog[29] are valid. The transit signal was thus detected to have a period of 2.49198±0.00032 d and a depth of 2128±160 parts per million (ppm), corresponding to an approximate planetary radius of 2.2±1.3 $R_\oplus$ and equilibrium temperature of 640 K.

[26] `https://github.com/jlillo/tpfplotter`
[27] `https://tess.mit.edu/followup/`
[28] `https://mast.stsci.edu`
[29] `https://tev.mit.edu/data/collection/193/`

Table 5.1: Log of ground-based transit follow-up observations taken for TOI-1201.

Instrument	Country	Date	Filter	Coverage$^{(a)}$ [%]	Exposure [s]	Duration [min]	Pixel scale [arcsec]	N_{obs}
LCOGT-SSO	Australia	2019-08-27	z_s	100	60	331	0.389	306
LCOGT-SAAO	South Africa	2019-09-23	g_p	100	75	215	0.389	170
OAA	Spain	2019-09-29	V	100	240	234.1	1.44	56

aThe coverage represents how much of the transit was observed.

5.4 Ground-based observations

5.4.1 Follow-up seeing-limited transit photometry

We considered the photometric data where TOI-1201 was not the intended target (see Sect. 5.3), as well as two additional datasets where TOI-1201 was the focus. The transit data are summarized in Table 5.1, where technical details, e.g., filter, duration, are included. Not shown, we also observed a transit with MKO, but the observations were hampered due to observational systematics separating the two stars that would limit its usefulness in an analysis.

LCOGT. We obtained two transits for TOI-1201 using the 1.0 m telescopes in the Las Cumbres Observatory Global Telescope (LCOGT) network (Brown et al., 2013). All of the LCO 1.0 m telescopes are equipped with the 4096×4096 pix SINISTRO camera, having an image scale of 0.389 arcsec/pixel, and the aperture radius was set to 7 arcsec, which could potentially be susceptible to flux contamination from the companion. We took this into consideration as a dilution factor for the fit, but it was found that the contamination was insignificant (see Sect. 5.6.1).

We first acquired full-transit photometric data in the z_s band on the night of 27 August 2019 at the Siding Spring Observatory[30] (SSO) in Australia. The full transit of TOI-1201 b was also observed in the g_p filter at the South African Astronomical Observatory[31] (SAAO) located in Sutherland, South Africa on 14 October 2019.

OAA. We observed another full transit on 29 September 2019 with the main 0.4 m telescope at the Observatori Astronòmic Albanyà[32] (OAA) in Girona, Spain with stable observing conditions allowing for deep exposures. We used a Moravian G4-9000 camera with a Johnson V-band filter using 13 arcsec aperture with a field of view of 36 arcmin $\times$ 36 arcmin and a scale of 1.44 arcsec pixel^{-1}. The sequence consisted of 56 images with 240 s exposure times. The `AstroImageJ` pipeline was used to reduce the data.

[30] `https://www.sidingspringobservatory.com.au/`
[31] `https://www.saao.ac.za/`
[32] `https://www.observatorialbanya.com/`

5.4.2 Long-term photometric monitoring

We assembled a list of archival long-time baseline data, namely from the WASP-South and ASAS-SN surveys.

WASP-South. TOI-1201 was observed with the Wide Angle Search for Planets (WASP) array of eight cameras at the South African Astronomical Observatory in Sutherland, (WASP-South Pollacco et al., 2006) over the course six years from 2008 to 2014, amounting to about 64 000 acquired data points. From 2008 to 2009, the 200 mm lenses were used (camera 222), and from 2012 to 2014, the data were taken with the 85 mm lenses (camera 281). Since the extraction aperture included both stars and the pixel-scale was 13.7 arcsec/pixel, it was not possible to use these data to determine which star is producing the modulation.

ASAS-SN. The All-Sky Automated Survey for Supernovae (ASAS-SN) is comprised of 24 14 cm aperture Nikon telephoto lenses, each equipped with a 2048×2048 ProLine CCD camera, at locations distributed worldwide (Shappee et al., 2014; Kochanek et al., 2017). We input the stellar coordinates for TOI-1201 as provided in Table 5.2 to search the ASAS-SN database[33]. Two sources associated to these coordinates with a separation of $\sim$3.2 arcsec popped up, so both light curves are surely contaminating each other (assuming that the source APJ024859.45-143214.2 corresponds to TOI-1201 and the other source AP37838964 to the companion). This is true since the pixel-scale is 8 arcsec/pixel and the aperture is around 15 arcsec, therefore blending is an issue. The extracted data consists of a total of 619 points spanning roughly 1600 d from March 2012 to January 2019 in four cameras (ba, bb, be, bf), all in the V band.

5.4.3 High resolution spectroscopy with CARMENES

We obtained 35 high-resolution spectra from November 2019 to February 2020 for the transit host TOI-1201 with the CARMENES[34] instrument located at the 3.5 m telescope at the Calar Alto Observatory in Almería, Spain. We used only the data collected with the VIS channel, which covers the spectral range 520–960 nm with a spectral resolution of $R = 94\,600$ (Quirrenbach et al., 2014, 2018). One of the measurements was missing a drift correction and was, therefore, discarded and additionally, another data point that was a huge outlier (RV$\sim 100\,\mathrm{m\,s^{-1}}$; $\sigma \gtrsim 10$) was removed, which resulted in 33 observations that were used for the analysis. The companion at 8.2 arcsec (see Sect. 5.5.2) was also observed by CARMENES 23 times from November 2019 to January 2020.

The RVs were measured using `serval`[35] (Zechmeister et al., 2018). They were corrected for barycentric motion, secular acceleration, instrumental drift, and nightly zero-points using our standard approach (Zechmeister et al., 2018; Trifonov et al., 2020). Additionally, `serval` provides a list of stellar activity indicators, namely the chromatic index –CRX–, the differential line width –dLW–, the Hα line, and the Ca II IRT triplet lines). Following Lafarga

[33] `https://asas-sn.osu.edu/`

[34] Calar Alto high-Resolution search for M dwarfs with Exo-earths with Near-infrared and optical Échelle Spectrographs, `http://carmenes.caha.es`

[35] `https://github.com/mzechmeister/serval`

et al. (2020), we applied binary masks to the spectra and computed the cross-correlation function (CCF) and its FWHM, contrast (CTR), and bisector velocity span (BVS) values. The pseudo-equivalent width (pEW), as defined in and provided by Schöfer et al. (2019), of the photospheric lines TiO λ7050 Å, TiO λ8430 Å, and TiO λ8860 Å were also derived from the CARMENES spectra. The RVs for TOI-1201 are shown in Fig. 5.6.

5.5 Stellar properties

5.5.1 Basic astrophysical parameters

Table 5.2 summarizes the stellar parameters of TOI-1201 and its companion. Both stars are poorly investigated late-type dwarfs (e.g., Lépine & Gaidos, 2011; Frith et al., 2013) For building the table, we first got equatorial coordinates, parallaxes, and proper motions of the two stars from *Gaia* EDR3 (Gaia Collaboration et al., 2020) and blue-optical to mid-infrared photometry already compiled by Cifuentes et al. (2020). Next, we integrated the spectral energy distributions as the latter authors for computing the bolometric luminosities, L_*. Following the χ^2 stellar synthesis of Passegger et al. (2019) and using only the CARMENES VIS channel spectra, we derived the photospheric parameters $T_{\rm eff}$, $\log g$, and [Fe/H]. From them, with the Stefan-Boltzman law and the mass-radius relation of Schweitzer et al. (2019), we obtained the stellar masses and radii, from which we determined the stellar bulk density.

Also on the CARMENES spectra, we used the same cross-correlation function methodology with weighted binary masks of Lafarga et al. (2020) for computing the stellar radial velocities[36], V_r. With them and the *Gaia* astrometry, we calculated Galactocentric space velocities UVW and assigned the stars to the Galactic kinematic population of the young disk, and young stellar kinematic group following Montes et al. (2001). Its hypothetical membership in the Hyades Supercluster (Eggen, 1958, 1984) would translate into an age of around 0.6 Gyr (cf. Montes et al., 2001, – see also, e.g., Perryman et al. 1998 and Martín et al. 2018 for Hyades cluster age determinations), but additional non-kinematical information would be needed to confirm this approximate age.

We also computed projected rotation velocities, $v \sin i$, on the CARMENES spectra as Reiners et al. (2018) and estimated spectral types m2.0 and m2.5 for the primary and secondary, respectively, from absolute magnitudes and colours as Cifuentes et al. (2020), consistent with the effective temperatures (lower-case 'm' indicates that the estimated spectral types are not measured from low-resolution spectra as in, e.g., Alonso-Floriano et al. 2015). The tabulated rotation period for the primary host star is discussed in Sect. 5.5.3.

5.5.2 The stellar host and its companion

The earliest name in the literature of TOI-1201 is PM J02489–1432W. At only about 8.2 arcsec to the east, Lépine & Gaidos (2011) tabulated a second star, PM J02489–1432E,

[36]RAVE DR4 Kordopatis et al. (2013) tabulated $\gamma = +6.6 \pm 6.1\,{\rm km s^{-1}}$ and $T_{\rm eff} = 3600 \pm 310$ K for the primary and $\gamma = +31.7 \pm 1.4\,{\rm km s^{-1}}$ and $T_{\rm eff} = 3840 \pm 70$ K for the secondary. The RAVE spectrum of the primary had a very poor signal-to-noise ratio (S/N = 4.2), which led to wrong V_r and stellar parameter determination (e.g., $\log g = 1.5 \pm 1.0$, inconsistent with the star's main-sequence nature).

Table 5.2: Stellar parameters of TOI-1201 and its 8.2 arcsec-wide companion.

Parameter	Primary	Secondary	Reference
	Names and identifiers		
Name	PM J02489–1432W	PM J02489–1432E	LP2011
Karmn	J02489–145W	J02489–145E	Cab2016
Gaia EDR3 ID	5157183324996790272	5157183324996789760	*Gaia* EDR3
TOI	1201	393	ExoFOP-*TESS*
TIC	29960110	29960109	Sta18
	Coordinates and spectral types		
α (J2000)	02:48:59.27	02:48:59.83	*Gaia* EDR3
δ (J2000)	–14:32:14.9	–14:32:16.2	*Gaia* EDR3
Sp. type[a]	m2.0 ± 0.5 V	m2.5 ± 0.5 V	This work
	Magnitudes		
NUV (mag)	21.664 ± 0.337	21.923 ± 0.491	*GALEX*
B (mag)	...	14.111 ± 0.030	UCAC4
g' (mag)	13.7285 ± 0.0028	13.334 ± 0.020	Pan-STARRS1/UCAC4
G_{BP} (mag)	13.344 ± 0.025	13.694± 0.014	*Gaia* EDR3
V (mag)	...	12.706 ± 0.020	UCAC4
r' (mag)	12.5537 ± 0.0010	12.110 ± 0.080	Pan-STARRS1/UCAC4
G (mag)	12.0888 ± 0.0072	12.3710 ± 0.0052	*Gaia* EDR3
i' (mag)	11.4326 ± 0.038	10.900 ± 0.010	Pan-STARRS1/UCAC4
G_{RP} (mag)	10.9748 ± 0.0092	11.2333 ± 0.0061	*Gaia* EDR3
J (mag)	9.528 ± 0.042	9.733 ± 0.024	2MASS
H (mag)	8.876 ± 0.057	9.125 ± 0.027	2MASS
K_s (mag)	8.646 ± 0.029	8.875 ± 0.021	2MASS
$W1$ (mag)	7.721 ± 0.014	7.731 ± 0.011	AllWISE/WISE
$W2$ (mag)	7.693 ± 0.013	7.670 ± 0.012	AllWISE/WISE
$W3$ (mag)	7.918 ± 0.020	8.063 ± 0.019	AllWISE/WISE
$W4$ (mag)	7.709 ± 0.129	7.794 ± 0.120	AllWISE/WISE
	Parallax and kinematics		
π (mas)	26.571 ± 0.022	26.539 ± 0.023	*Gaia* EDR3
d (pc)	37.636 ± 0.032	37.680 ± 0.033	*Gaia* EDR3
$\mu_\alpha \cos\delta$ (mas yr^{-1})	+164.069 ± 0.025	+174.433 ± 0.033	*Gaia* EDR3
μ_δ (mas yr^{-1})	+46.549 ± 0.027	+45.465 ± 0.029	*Gaia* EDR3
V_r (km s^{-1})	+31.771 ± 0.018	+31.868 ± 0.018	This work
U (km s^{-1})	–38.495 ± 0.018	–39.577 ± 0.020	This work
V (km s^{-1})	–17.125 ± 0.018	–18.521 ± 0.019	This work
W (km s^{-1})	–12.652 ± 0.019	–11.956 ± 0.020	This work
Galactic population	Young disk		This work
Stellar kinematic group	Hyades Supercluster		This work
	Photospheric parameters		
$T_{\rm eff}$ (K)	3476 ± 51	3437 ± 51	This work
$\log g_*$ (cgs)	4.80 ± 0.04	4.80 ± 0.04	This work
[Fe/H] (dex)	0.05 ± 0.16	0.05 ± 0.16	This work
$v \sin i$ (km s^{-1})	<2	<2	This work
$P_{\rm rot}$ (d)	19–23	...	This work
	Physical parameters		
L_* ($10^{-4} L_\odot$)	340.0 ± 5.7	268.3 ± 2.5	Cif20
R_* ($R_\odot$)	0.508 ± 0.016	0.462 ± 0.014	This work
M_* ($M_\odot$)	0.512 ± 0.020	0.463 ± 0.018	This work
ρ_* (kg m^{-3})	5500^{+580}_{-490}	6400^{+750}_{-680}	This work

aPhotometrically derived spectral types. Cab2016: Caballero et al. (2016b); *Gaia* EDR3: Gaia Collaboration et al. (2020); *GALEX*: Bianchi et al. (2011); Sta18: Stassun et al. (2018); UCAC4: Zacharias et al. (2013); 2MASS: Cutri et al. (2003); Cif2020: Cifuentes et al. (2020); LG2011: Lépine & Gaidos (2011); Pan-STARRS1: Kaiser et al. (2010).

slightly fainter (by 0.28 mag and 0.20 mag in the G and J bands, respectively) and redder (by 0.08 mag in $G-J$ colour). The brighter primary is TOI-1201 and the fainter secondary is the companion. While they are located at the same *Gaia* parallactic distance ($\Delta\pi = 0.032 \pm 0.032$ mas) and have the same radial velocities ($\Delta V_r = 0.097 \pm 0.025\,\mathrm{km\,s^{-1}}$ – see Lafarga et al. 2020 for the error underestimation), their proper motions are similar but not identical ($\Delta\mu_\alpha \cos\delta = 10.34 \pm 0.041\,\mathrm{mas^{-1}}$, $\Delta\mu_\delta = 1.084 \pm 0.040\,\mathrm{mas^{-1}}$). Although in spite of the total proper motion difference of only 6 % the pair would pass any kinematic and astrometric binarity criterion (e.g., Montes et al., 2018), such a difference may be indicative of a relative orbital motion as shown by, e.g., Makarov & Kaplan (2005).

The Washington Double Star catalog (WDS; Mason et al., 2001) tabulates the pair as WDS J02490–1432 (KPP 2871). Although first reported by Lépine & Gaidos (2011) and next tabulated by El-Badry & Rix (2018), they were Knapp & Nanson (2019) who made the first multi-epoch astrometric analysis and gave the WDS discovery designation (KPP 2871). However, as of 19 April 2021, WDS listed only five independent epochs between 1998.6 and 2015.5. For complementing those data, we retrieved SuperCOSMOS (Hambly et al., 2001) digitizations of First Palomar Observatory Sky Survey (POSS-I) and United Kingdom Schmidt Telescope (UKST) photographic plates taken between December 1955 and September 1989, and measured angular separation ρ and position angle θ between the primary and secondary as in Caballero (2010). Besides, we recomputed the angular separation ρ and position angle θ for the 2MASS (Cutri et al., 2003), DENIS (Epchtein et al., 1997), and *Gaia* DR1, DR2, and EDR3 (Gaia Collaboration et al., 2016, 2018, 2020) observations. The 11 resulting astrometric epochs, which cover 61.97 yr, are displayed in Table 5.3. The pair was not resolved, though, by a number of all-sky surveys: GSC2.3/USNO-A2/USNO-B1, SDSS, UKIDSS LAS, WISE (e.g. Monet et al., 2003; Lawrence et al., 2007; Alam et al., 2015; Marocco et al., 2020).

In the six decades of astrometric observations of the binary, there has been an appreciable increase in ρ from 7.2 arcsec to 8.4 arcsec. Unfortunately, any variation in θ has been masked by the uncertainty of the individual observations, typically larger than 1 deg. Assuming the *Gaia* EDR3 value as the minimum angular separation of the pair, and at the stars heliocentric distance, the minimum projected physical separation s is 316.4±1.3 AU, which is also the minimum semimajor axis a of the binary. Together with the individual masses of the primary and secondary in Table 5.2 and Kepler's Third Law, the minimum orbital period $P_{\rm orb}$ of the binary is 5709±86 yr. The astrometric monitoring of 61.57 yr represents only 1 % of the orbit in time but, for certain geometries (e.g., near periastron), the monitoring could represent as much of 10 % and be consistent with the observations. Certainly, a prohibitively long astrometric and radial-velocity follow-up will be needed to dynamically characterise the system in detail, but at least the minimum physical separation of about 320 AU between the two nearly identical stars (mass ratio 0.09043 ± 0.027) may impose restrictions on the original protoplanetary disk size and planet stability in our system.

5.5.3 Rotation period

We considered the available photometric data in the archive (i.e., WASP, ASAS-SN) to determine the stellar rotation period as well as various stellar activity indicators provided by the spectra.

Table 5.3: Astrometric data of the binary WDS J02490–1432 (KPP 2871).

Epoch	ρ (arcsec)	θ (deg)	Origin
1953.927	7.17 ± 0.30	100.7	POSS-I Red
1986.935	7.76 ± 0.20	97.7	UKST Infrared
1988.838	7.90 ± 0.20	96.4	UKST Blue
1989.742	7.81 ± 0.20	100.0	UKST Red
1998.582	8.19 ± 0.13	98.3	2MASS[a]
1999.782	8.184	99.0 ± 0.2	UCAC4[b]
2000.775	8.23 ± 0.10	98.7	DENIS
2012.110	8.39542	98.788	KPP[c]
2015.000	8.4 ± 1.0	98.96	*Gaia* DR1[d]
2015.500	8.391 ± 0.061	98.96	*Gaia* DR2[e]
2016.000	8.408 ± 0.034	98.94	*Gaia* EDR3

aWDS tabulates $\rho = 8.15$ arcsec and $\theta = 98.3$ deg (Thurgood Marshall High School, priv. comm.). bFrom Zacharias et al. (2013). cFrom Knapp & Nanson (2019). dWDS tabulates $\rho = 8.34363$ arcsec and $\theta = 99.001$ deg (Knapp & Nanson, 2019). eWDS tabulates $\rho = 8.34896 \pm 0.00004$ arcsec and $\theta = 98.999$ deg (El-Badry & Rix, 2018)

Long-term photometry. Solely focusing on the WASP data first, we find a signal of 21 days in the periodogram. We confirm this periodicity by implementing into `juliet` (Sect. 5.6.1) a RotationTerm analogue to the one in `celerite2`[37] (Foreman-Mackey, 2018), which is the sum of two stochastically-driven, damped harmonic oscillator (SHO) terms. The power spectrum of each SHO term is given by Anderson et al. (1990),

$$\mathrm{SHO}_1(\omega_{\mathrm{GP}}) = \sqrt{\frac{2}{\pi}} \frac{S_0 \omega_1^4}{(\omega_{\mathrm{GP}}^2 - \omega_1^2)^2 + \omega_1^2 \omega_{\mathrm{GP}}^2 / Q_1^2} \tag{5.1a}$$

and

$$\mathrm{SHO}_2(\omega_{\mathrm{GP}}) = \sqrt{\frac{2}{\pi}} \frac{S_0 \omega_2^4}{(\omega_{\mathrm{GP}}^2 - \omega_2^2)^2 + \omega_2^2 \omega_{\mathrm{GP}}^2 / Q_2^2} \tag{5.1b}$$

where we applied the Rotation terms,

[37] `https://celerite2.readthedocs.io/en/latest/`

$$Q_1 = 0.5 + Q_0 + \delta Q \tag{5.1c}$$

$$\omega_1 = \frac{4\pi Q_1}{P_{\rm rot}\sqrt{4Q_1^2 - 1}} \tag{5.1d}$$

$$S_1 = \frac{\sigma_{\rm GP}^2}{(1+f)\omega_1 Q_1} \tag{5.1e}$$

$$Q_2 = 0.5 + Q_0 \tag{5.1f}$$

$$\omega_2 = 2\omega_1 = \frac{8\pi Q_1}{P_{\rm rot}\sqrt{4Q_1^2 - 1}} \tag{5.1g}$$

$$S_1 = \frac{f\sigma_{\rm GP}^2}{(1+f)\omega_2 Q_2} \tag{5.1h}$$

and where $\sigma_{\rm GP}$ is the amplitude of the GP, $P_{\rm rot}$ is the primary period of the variability, Q_0 is the quality factor for the secondary oscillation, δQ is the difference between the quality factors of the first and second oscillations, and f represents the fractional amplitude of the secondary oscillation with respect to the primary one. Such a kernel choice is well-suited to represent stellar signals modulated by the rotation period of the star for its flexible nature and it smoothly varies. We go for the double SHO (dSHO) because the SHO alone lacks to modulate the presence of more than one stellar spot (Jeffers & Keller, 2009).

The WASP dataset consists of 11 epochs of data, where each was considered to be an independent instrument with its own instrumental offset and jitter term. The data of each instrument were nightly binned in order to cut down on computational time, but is also valid since we are searching for signals on the order of a few days. From the posterior results (Fig. 5.2), we obtain a photometric stellar rotation period of $P_{\rm rot} = 21.37 \pm 0.46$ d. However, as already mentioned in Sect. 5.4.2, the pixel-scale is 13.7 arcsec/pixel making it difficult to distinguish whether the signal belongs to TOI-1201 or its companion.

Moving on, we consider the ASAS-SN data and follow the same analysis as on the WASP dataset. There were four different cameras (ba,bb,be,bf) for which we assigned each individual instruments with their own offsets and jitter terms, and the GP hyperparameters were kept shared. The fit produces a GP rotational period of $P_{\rm rot} = 20.951 \pm 0.025$ d. Like before, the data supports a signal at 21 d but can't be resolved between the two objects. In addition, the periodogram showed a sharp bump at $\sim$400 d which might be attributed to some magnetic cycle of the star, though this was not further investigated.

We also consider the *TESS* light curve before being corrected for systematics (`SAP` flux) and simply divided the light curve into three chunks and shifted them using a sinusoidal signal with a period of 20.5 d and amplitude variations of $\sim$6.7 ppt (Fig. 5.9). These data also support the 21 d signal, though yet again, the *TESS* pixel (21 arcsec) contains both objects.

Spectroscopy. We additionally inspect the various activity indicators from the spectroscopic observations to further affirm the stellar activity presence. TOI-1201 is a rather active star with a measured median Hα pseudo-equivalent width (pEW) of -0.425 ± 0.062Å (Jeffers et al., 2018; Schöfer et al., 2019).

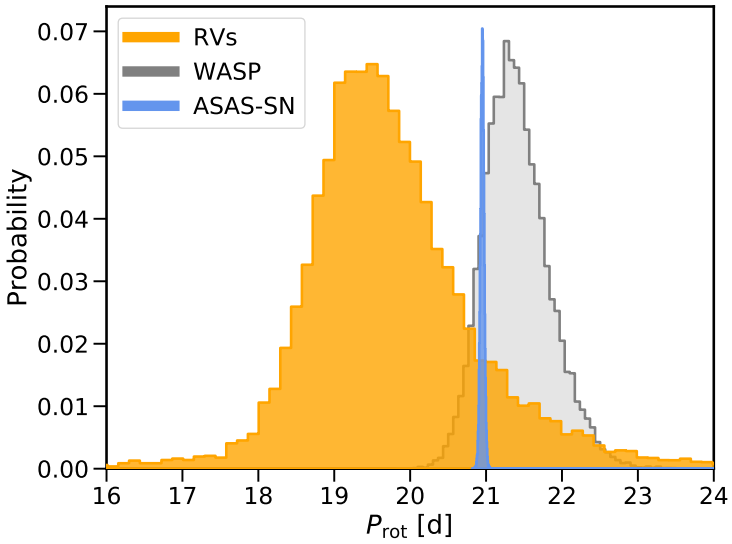

Figure 5.2: Probability density of the posterior samples for the estimated rotational period of the star ($P_{\rm rot}$) when using a dSHO-GP to fit the WASP data (gray) and to ASAS-SN data (blue). The posterior distributions for the RVs (orange) come from the dSHO-GP component in the final joint fit (Sect. 5.6.3).

While there are no significantly strong correlations between the RVs and any of the activity indicators, the GLS periodograms (Fig. 5.3) do hint towards the 21 d signal found in the photometry. The CRX, dLW, Hα index, Ca II IRT triplet lines, FWHM, TiO λ7050 Å and TiO λ8430 Å all indicate some power between 19-23 d with power sometimes >1% FAP, or broadly around ∼35-40 d, corresponding to an alias of the 21 d due to the sampling frequency of 41 d found in the window function. The others (e.g., He I λ10833Å, He I D_3, BIS) do not show any peaks of interests.

Additionally, the RVs themselves exhibit a peak at around 19 d (Fig. 5.4). When constructing our final model in Sect. 5.6.2, we take all the mentioned evidence above into consideration to assume this signal to have quasi-periodic behavior. This produces a periodicity of $P_{\rm rot,\ RV} = 19.62^{+1.10}_{-0.81}$ d and is plotted in comparison to the long-term photometric results in Fig. 5.2.

To summarize, we see a clear 21 d signal in the photometry, a strong 19 d signal in RVs, and a number of activity indicators peaking at these quoted periodicities between 19-23 d. We therefore establish the rotational period of TOI-1201 to be 19-23 d. If TOI-1201 is indeed relatively young (∼600 Myr) belonging to the Hyades star cluster, then a stellar rotation period of 21 d is inline with a star with an effective temperature of ∼3 500 K (Curtis et al., 2019), which matches our observations.

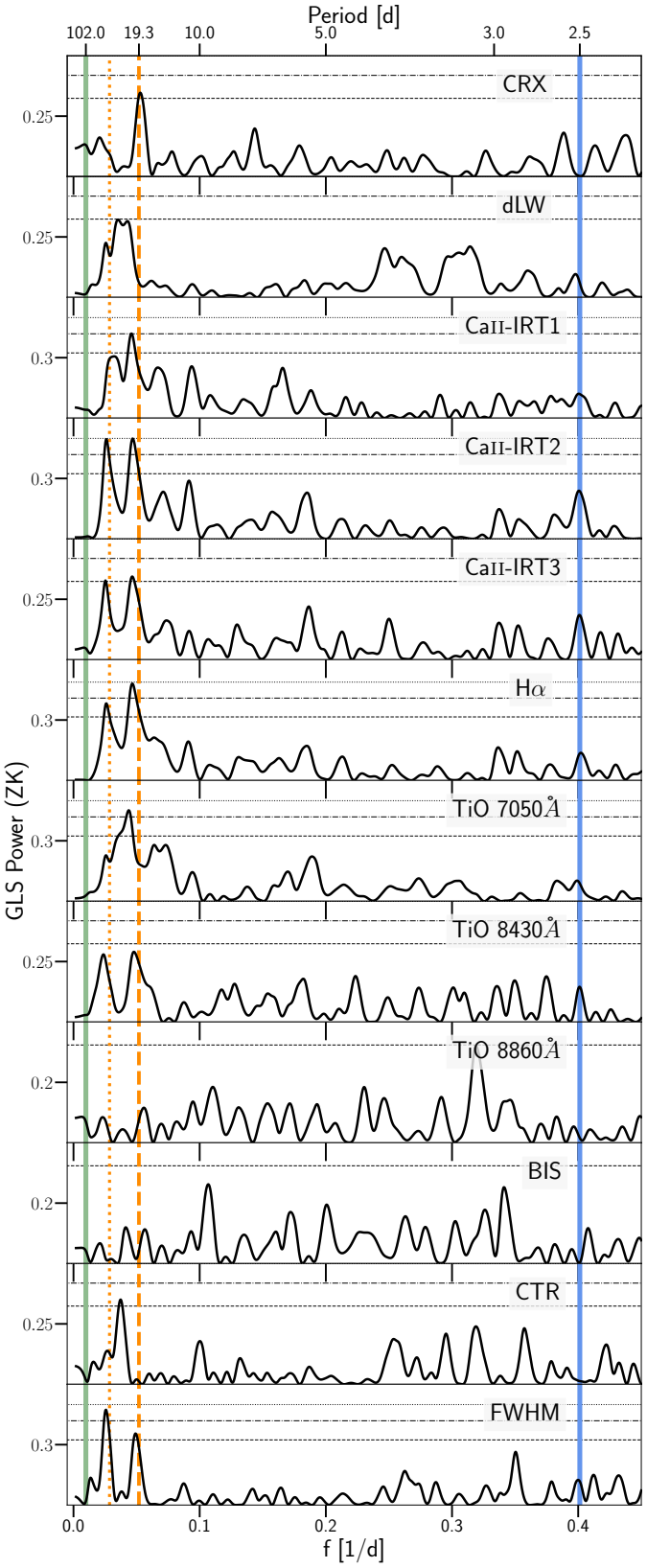

Figure 5.3: GLS periodograms of the various stellar activity indicators from the CARMENES spectroscopic data for TOI-1201. The solid vertical blue lines correspond to the transiting planet (2.49 d) and the green one to the long-term signal (∼102 d). The dashed and dotted vertical orange lines correspond to the rotational period picked up in the RVs (∼19 d) and its alias (∼35 d), respectively. The horizontal dotted, dot-dashed, and dashed lines represent the 10%, 1%, and 0.1% FAP lines.

5.6 Analysis and results

5.6.1 Transit-only modeling

To first obtain refined values for the orbital period and transit time for the transiting planet, we perform fits on just the given transit photometry. This includes the photometry from the two *TESS* sectors and the transits from the three other ground-based instruments (i.e., LCO-SAAO, OAA, and LCO-SSO).

All modeling fits for this paper are done using `juliet`[38] (Espinoza et al., 2019a), a python fitting package for joint-modeling (transit and RV) that uses Nested Samplers to explore the prior volume in order to efficiently compute the Bayesian model log-evidence, $\ln \mathcal{Z}$. Though there are a variety of Nested Samplers, we employ `dynesty`[39] (Speagle & Barbary, 2018; Speagle, 2020) due to the large parameter space of our models. Section 3.3.1 covers a complete description of the code. For model comparison, we follow the general rule that if $\Delta \ln \mathcal{Z} \lesssim 3$ (Trotta, 2008), then the two models are indistinguishable and neither is preferred so the simpler model would then be chosen. For any $\Delta \ln \mathcal{Z}$ that is greater than 3, the model with the larger Bayesian log-evidence is favored.

For the transit model, we apply the following parameter transformations, as suggested in Sect. 3.3.3. We fit for the parameters r_1 and r_2 instead of fitting directly for the planet-to-star radius ratio, $p = R_p/R_*$, and the impact parameter of the orbit, b. We take advantage of our high-precision derived stellar parameters (Table 5.2) and include the stellar density, ρ_*, into the model rather than the scaled semi-major axis, a/R_*. The *TESS* data is modeled jointly with a quadratic limb-darkening law (i.e., the q_1 and q_2 parameters are shared among both *TESS* sectors), while the ground-based instruments are assigned linear limb-darkening laws (both parametrized with the uniform sampling scheme of Kipping, 2013a). Instrumental offsets are considered as well as instrumental jitter terms which are added in quadrature to the given instrumental measurement uncertainty. The dilution factor, or the amount that a light curve is diluted due to neighboring light pollution, is fixed for all instruments. The *TESS* instrument already takes this factor into account and the aperture of the ground-based instruments were not affected enough by the neighboring bright companion. We performed fits with a free dilution factor to verify this (since $\Delta \ln \mathcal{Z} = \ln \mathcal{Z}_{D=1.0} - \ln \mathcal{Z}_{D \neq 1.0} > 6$).

To detrend time-correlated noise in the *TESS* sector 31 data, we adopted the squared-exponential GP kernel,

$$k_{i,j}(\tau) = \sigma_{\rm GP}^2 \exp\left(-\frac{\tau}{T_{\rm GP}}\right)$$

where $\tau = |t_i - t_j|$ is the temporal distance between two points, $\sigma_{\rm GP}$ is the amplitude of the GP modulation, and $T_{\rm GP}$ is the characteristic timescale. This kernel is characterized as being smooth since it is infinitely differentiable, which is sufficient for the *TESS* sector 31 data but not for the data from *TESS* sector 4. To account for the roughness in the *TESS*

[38] `https://juliet.readthedocs.io/en/latest/`
[39] `https://github.com/joshspeagle/dynesty`

sector 4 data, we applied the (approximated) Matern-3/2 kernel provided by `celerite`,

$$k_{i,j}(\tau) = \sigma_{\rm GP}^2 \left(1 + \frac{\sqrt{3}\tau}{\rho_{\rm GP}}\right) \exp\left(-\frac{\sqrt{3}\tau}{\rho_{\rm GP}}\right)$$

where $\tau = |t_i - t_j|$ is again the temporal distance between two points and $\sigma_{\rm GP}$ is the amplitude of the GP, but now $\rho_{\rm GP}$ is the length scale of the GP modulations to vary the smoothness of the return functions. Both sectors of *TESS* had their own respective GP amplitude ($\sigma_{\rm GP}$). As for the ground-based transit photometry, we detrend the LCO-SAAO and LCO-SSO light curves with airmass using a linear term. Based on the TLS, we setup the prior on the period to be uniform, $\mathcal{U}(2.45, 2.55)$, and the ephemeris to be focused on the last transit in the data, $\mathcal{U}(2459169.2, 2459169.3)$. When combining all the transit observations, we determine $P = 2.49198582 \pm 0.0000029$ d and t_0 (BJD-TDB) $= 2459169.23219^{+0.00049}_{-0.00047}$. These posterior values then serve as a guide for the priors for the final joint fit in Sect. 5.6.3.

5.6.2 RV-only modeling

To search for signals within the RV data, we first calculated the generalized Lomb-Scargle (GLS) periodograms (Zechmeister & Kürster, 2009), approaching the data as if we had no prior information on the transiting planet. We first employed the `exostriker`[40] (Trifonov, 2019) to identify potential combinations of the signals present in the GLS that describe the data appropriately. We use this information to build the priors for our RV-only `juliet` runs. Fig. 5.4 shows a sequence of these GLS periodograms after subtracting an increasing number of sinusoidal signals. The theoretical false alarm probability (FAP) levels are computed following the theoretical levels (Eqn. 24 in Zechmeister & Kürster, 2009)

The 2.5 d transiting signal only significantly appears after subtracting out the dominating long-term signal at around ∼100 d (Fig. 5.4 b). The residuals from simultaneously fitting two sinusoids for the 2.5 d and 100 d signals then show two prominent, however insignificant, peaks at 19 d and 35 d, which are aliases of one another (induced by a peak at 41 d found in the window function). We attempted to figure out which one of the two is the true signal using the `AliasFinder`[41] (Stock & Kemmer, 2020; Stock et al., 2020a), however, it was not conclusive which one was the correct signal. Additionally, we performed some `juliet` runs using either 19 d or 35 d as the period but these were also inconclusive, as expected. Though, as was already presented in Sect. 5.5.3, the 19 d signal is consistent with the rotational period of the star based on ground-based photometry, as well as other stellar activity indicators. After removing this 19 d signal with an initial sinusoid fit, the resulting residuals show nothing further in the GLS periodogram that would indicate more present signals (Fig. 5.4 d).

Therefore, the CARMENES RV data show three significant signals: the transiting planet (2.5 d), a long-term signal (∼100 d), and the stellar rotation period (∼19 d). The next step was to compare various models to test whether circular or eccentric Keplerian orbits were preferred, if the stellar activity indicators (e.g., CRX, dLW) should be included as linear terms or not, and checking what kind of impact a GP kernel may have. A table summarizing

[40] `https://github.com/3fon3fonov/exostriker`
[41] `https://github.com/JonasKemmer/AliasFinder`

the runs are listed in Table 5.4 and the priors in Table 5.8.

Transiting mini-Neptune For the transiting planet, we fixed the priors for the period and the time of periastron to the median values based on the posteriors from the transit-only fits (Sect. 5.6.1) since the transit data provide us with very constrained values such that the precision of the RV data would not be able to.

Stellar rotation period For the stellar rotation period signal at 19 d, we tested out fitting it with a sinusoid, a quasi-periodic GP kernel (QP-GP) as presented in `george`, and a double SHO (dSHO-GP) kernel. The kernel for the QP-GP is as such,

$$k_{i,j}(\tau) = \sigma_{\rm GP}^2 \exp\left(-\alpha\tau^2 - \Gamma \sin^2\left(\frac{\pi\tau}{P_{\rm rot}}\right)\right)$$

where $\tau = |t_i - t_j|$ is temporal distance between two points, $\sigma_{\rm GP}$ is the amplitude of the GP modulation, α is the inverse length-scale of the GP exponential component, Γ is the amplitude of the GP sine-squared component, and $P_{\rm rot}$ is the rotational modulation of the GP quasi-periodic component. We followed the prior set up as discussed in Stock et al. (2020a), where α is log-uniform from 10^{-8} to 10^{-4} corresponding to length-scales[42] of 100 to 10 000 days and Γ is log-uniform from 10^{-2} to 10^{1}. These constraints ensure that truly rotational-like signals are picked up by the GP, rather than allowing the exponentially decaying component to be the dominant term. The dSHO-GP kernel we used is the same one used to determine the stellar rotation period (Sect. 5.5.3) and was already introduced in Eqn. 5.1. For both GP kernels, we implemented a narrow prior for the period, $\mathcal{U}(15, 25)$, which we name $\rm GP_{19d}$. The motivation for the narrow prior centered around the 19 d is to avoid picking up periods (i.e., the alias at 35 d) not associated with the stellar rotation period signal.

The models between using a Keplerian and a GP (either with a QP-GP or a dSHO-GP) were indistinguishable (i.e., $\Delta \ln \mathcal{Z} < 2$), therefore, we decided to use the GP to describe the nature of the 19 d signal. Given our prior knowledge that this signal is physically produced by the stellar rotation period, the quasi-periodic behavior of the GP better explains the inherent inconsistent behavior of a stellar activity signal that may not be exhibited with the current data given the relatively short time span. Even if we choose to model the stellar rotation period with a sinusoid, the transiting planetary parameters are unaffected (Fig. 5.11, specifically focusing on 2 Kep + GP versus 3 Kep).

Long-term signal To account for the 100 d signal, we experimented with a quadratic trend, a Keplerian model, and a GP. We used a wide, uniform prior for the period and time of periastron, $\mathcal{U}(60, 150)$ and $\mathcal{U}(2458730, 2458840)$, respectively. When compared to a quadratic model, a circular Keplerian was preferred ($\Delta \ln \mathcal{Z} = \ln \mathcal{Z}_{\text{circular Keplerian}} - \ln \mathcal{Z}_{\text{quadratic}} \sim 18$). If we set the eccentricity parameter free, the posteriors favored a periodicity at ∼80 d with a relatively high eccentricity of ∼0.5-0.6. The eccentric Keplerian model has a slightly better log-evidence, however, the difference in log-evidence compared to the circular Keplerian

[42] $\alpha = 1/l^2$ where l is the timescale for the GP variations. In the original `juliet` paper (Espinoza et al., 2019a), α was defined as $\alpha = 1/2l^2$. However, this has since been corrected.

models is indistinguishable ($\Delta \ln \mathcal{Z} = \ln \mathcal{Z}_{\text{eccentric Keplerian}} - \ln \mathcal{Z}_{\text{circular Keplerian}} < 3$). Therefore, we continue to model this signal with a circular orbit if modeling it with a Keplerian.

Lastly, we experimented with two GP kernels, the QP-GP and dSHO-GP, as previously explained above for the stellar rotation period but this time with a wider prior for the period, $\mathcal{U}(10, 150)$. We denote this with GP_{wide}. The motive for the wider period prior is to evaluate whether the GP can pick up the longer-term signal and how the log-evidence compares to when using a circular Keplerian. The GP_{wide} often picked up signals at 80 d, 35 d (the alias of the stellar rotation period), and also 100 d, but the 19 d signal seemed to be overdominated by the others. The 1 Keplerian (2.5 d) + GP_{wide} model was actually comparable to the 2 Keplerian and 2 Keplerian + GP_{wide} models ($\Delta \ln \mathcal{Z} < 3$). Based on the log-evidences alone, we would claim the winning model to be the 1 Keplerian (2.5 d) + GP_{wide}. However, in the end, we favor the 2 Keplerian + dSHO-GP_{19d} and justify this choice with the reasons listed in the following paragraphs.

Final model choice We have the prior physical knowledge that there is a transiting planet at 2.5 d and a stellar rotation signal at ∼19 d, therefore we expect for these two signals to appear in the RVs for which we can model them with a Keplerian and a GP, respectively. The most prominent signal apparent in the data is however the 100 d signal, which we cannot ignore. Modeling it with a Keplerian and GP yields comparable log-evidences. Since we only observed roughly one period, this is not unexpected. That means, even if the signal would be of a quasi-periodic nature, it is justified to model it as a stable component in the meantime. In doing so, we also ensure that the model is restricted to the signals that we anticipated.

Since both GP kernels are indistinguishable in their evidences, we choose the dSHO-GP, as it serves our purpose to fit the quasi-periodic stellar activity signal very well and at the same, it is computationally much faster compared to the QP-GP. In the case of multiple undetermined signals, the QP-GP may be beneficial (see 1 Kep + QP-GP_{19d} vs 1 Kep + dSHO-GP_{19d}) since the QP-GP was able to still account for the longer-term signal with the help of the exponential-squared term, whereas the dSHO-GP could not. However, the dSHO-GP accomplishes our current purposes.

To ensure that the planetary parameters of the transiting planet are not drastically affected by our model choice, we examined the minimum mass derived from the RV only fits (see Fig. 5.11). All considered models agree within their uncertainties. Furthermore, nothing in the stellar activity indicators is significant in power at the frequencies of the transiting planet (∼2.5 d) or of the 100 d signal (Fig. 5.3). Based on these results, we continue the analysis with the 2 Keplerian + dSHO-GP_{19d} as the favored model. The transiting planet follows a circular Keplerian model, the stellar rotation period is represented with a dSHO-GP centered around the period of interest, and the most significant signal at ∼100 d is modeled with a circular Keplerian. We want to emphasize that our decision to model the long-term signal with a circular Keplerian is not driven by the assumption that this could be a planet candidate. Since we only observed one period, we cannot elaborate on the nature of this signal and further monitoring is needed in order to determine its origin.

Table 5.4: RV-only model comparison using the Bayesian log-evidences for TOI-1201.

Model	Periods [d]	$\ln \mathcal{Z}$	$\Delta \ln \mathcal{Z}$
Flat	...	-116.70	-1.06
Quadratic	...	-126.46	-10.82
1 Kep	2.5	-115.64	0.0
1 Kep	2.5*	-116.02	-0.39
1 Kep	106	-108.13	7.51
1 Kep	91*	-107.53	8.10
1 Kep + QP-GP$_{\mathrm{19d}}$	2.5	-113.95	1.69
1 Kep + QP-GP$_{\mathrm{wide}}$	2.5	-97.99	17.65
1 Kep + dSHO-GP$_{\mathrm{19d}}$	2.5	-105.33	10.31
1 Kep + dSHO-GP$_{\mathrm{wide}}$	2.5	-100.24	15.40
2 Kep	2.5, 100	-103.39	12.25
2 Kep	2.5*, 101	-103.31	12.33
2 Kep	2.5, 81*	-101.44	14.20
2 Kep + QP-GP$_{\mathrm{19d}}$	2.5, 95	-99.04	16.60
2 Kep + QP-GP$_{\mathrm{19d}}$	2.5, 81*	-98.51	17.13
2 Kep + QP-GP$_{\mathrm{wide}}$	2.5, 109	-98.09	17.55
2 Kep + QP-GP$_{\mathrm{wide}}$	2.5, 89*	-98.30	17.34
2 Kep + dSHO-GP$_{\mathrm{19d}}$	**2.5, 102**	**-98.39**	**17.25**
2 Kep + dSHO-GP$_{\mathrm{19d}}$	2.5, 78*	-97.52	18.12
2 Kep + dSHO-GP$_{\mathrm{wide}}$	2.5, 113	-97.94	17.70
2 Kep + dSHO-GP$_{\mathrm{wide}}$	2.5, 94*	-97.77	17.86
3 Kep	2.5, 19, 104	-100.24	15.40

The model we use for the final joint fit is the 2 Kep (2.5 d,101 d) + dSHO-GP$_{\mathrm{19d}}$ indicated by the bold-faced row. A larger $\Delta \ln \mathcal{Z}$ indicates a better model. If the GP had a wide period prior, it is expressed as GP$_{\mathrm{wide}}$, and if the GP was centered around the 19 d stellar rotation period, it is marked as GP$_{\mathrm{19d}}$. As expected, the period values may vary slightly depending on the model where the median value of the period posteriors is listed under the Periods column. The model names correspond to those in Fig. 5.11. *An eccentric orbit was used.

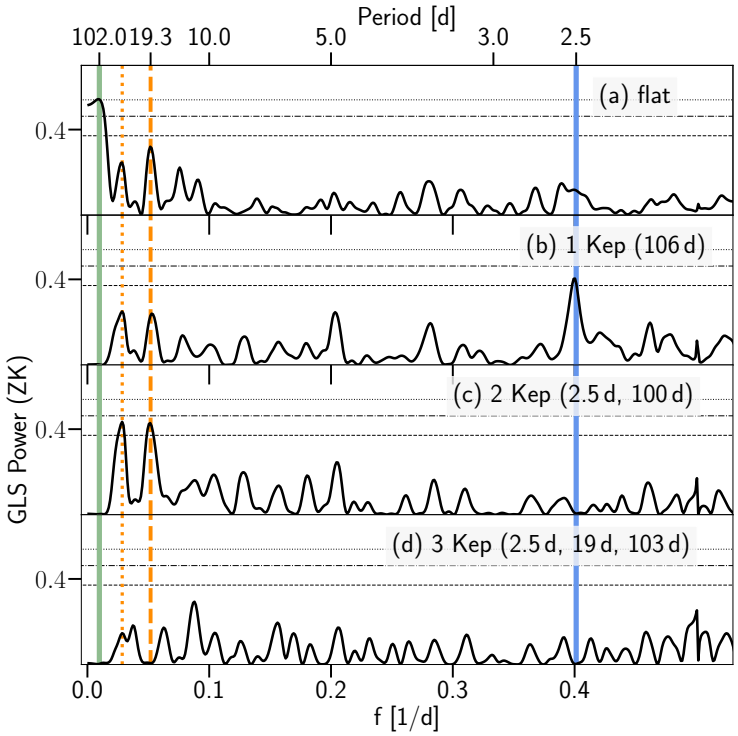

Figure 5.4: GLS periodograms of the RV residuals after subtracting different models for TOI-1201. The solid vertical blue line corresponds to the transiting planet (2.49 d) and the green one to the long-term signal (∼102 d). The dashed and dotted vertical orange lines correspond to the rotational period picked up in the RVs (∼19 d) and its alias (∼35 d), respectively. Panel (a): no signal fitted, just the given RVs. Panel (b): residuals after subtracting the long-term signal at P∼100 d. Panel (c): residuals after subtracting a simultaneous model fit of two signals at 100 d and 2.5 d. Panel (d): residuals after subtracting a simultaneous model fit of three signals at 100 d, 2.5 d, and 19 d. The dashed, grey, horizontal lines represent the FAP levels of 10%, 1%, and 0.1% (from bottom to top).

5.6.3 Joint modeling

We finally combine all the data from the *TESS* observations, the ground-based transit follow-ups, and the CARMENES RV data to produce the most precise planetary parameters. Our final model consists of the 2.5 d transiting planet, a long-term 100 d signal, and a stellar rotational period component at 19 d. The first two are modeled by a circular Keplerian whereas the last one is modeled using a dSHO-GP centered on 19 d, for reasons described in Sect. 5.6.2. We use the results from the posteriors of the transit-only and RV-only fits to set up the priors for the final joint fit, as discussed in detail and justified in Kemmer et al. (2020). The reason for doing this is because each individual dataset provides precise constraints on certain planetary parameters that is independent from the other dataset. For planetary parameters that are shared, such as the period and the time of periastron, the transit-only fits already provide such high precision values that the RVs would not achieve. Therefore, the RV only fits would have these parameters fixed to the median value from the posteriors of the transit only fits. The priors on the joint fits, on the other hand, are Gaussians based on the posteriors of the transit only fits with sigma values slightly inflated.

Table 5.5: RV model comparison using the Bayesian log-evidences for the companion of TOI-1201.

Model	$\ln \mathcal{Z}$	$\Delta \ln \mathcal{Z}$
Flat	-63.40	-4.13
Linear	-71.38	-12.11
1 Kep (28.5 d)	-59.27	**0.0**

These priors can be found in Table 5.9.

Our findings from the joint fit, including the derived planetary parameters, are presented in Table 5.6. The best model fits for the transit photometry and the RVs are shown in Figs. 5.5 and 5.6, respectively. Table 5.10 is a comprehensive posterior table including all of the model parameters such as the instrumental parameters.

5.6.4 Radial velocities of the companion

Observations for the companion of TOI-1201 were acquired on the same nights as for the host star. With the high-resolution spectra from CARMENES, we were able to compute very precise stellar parameters for both objects in the binary system (Sect. 5.5).

We then perform a complementary analysis on the RVs and various stellar activity indicators of the companion to search for potentially interesting signals. The GLS periodogram of the RVs (top panel of Fig. 5.10) shows a significant peak at 27 d (above 10% FAP level). Doing `juliet` runs, we compared the Bayesian log-evidences of a flat model, linear model, and a sinusoidal (i.e., circular Keplerian) model. We found the best one to be the one circular Keplerian model at 28.5 d with a semi-amplitude of K=3.42±0.89 m s^{-1} (see Table 5.5 for the results). To investigate the nature of the signal, we considered the same stellar activity indicators as mentioned in Sect. 5.5.3. While no signals seem rather significant, some at ∼16 d and ∼30 d, which are the 41 d aliases of one another, hint that the 28.5 d in the RVs might be somehow related to stellar activity (Fig. 5.10). However, given the low number of data points, it remains inconclusive. Thus given the current data at hand, we cannot claim anything and additional RV data would be necessary for the companion of TOI-1201 to determine the origin of this signal.

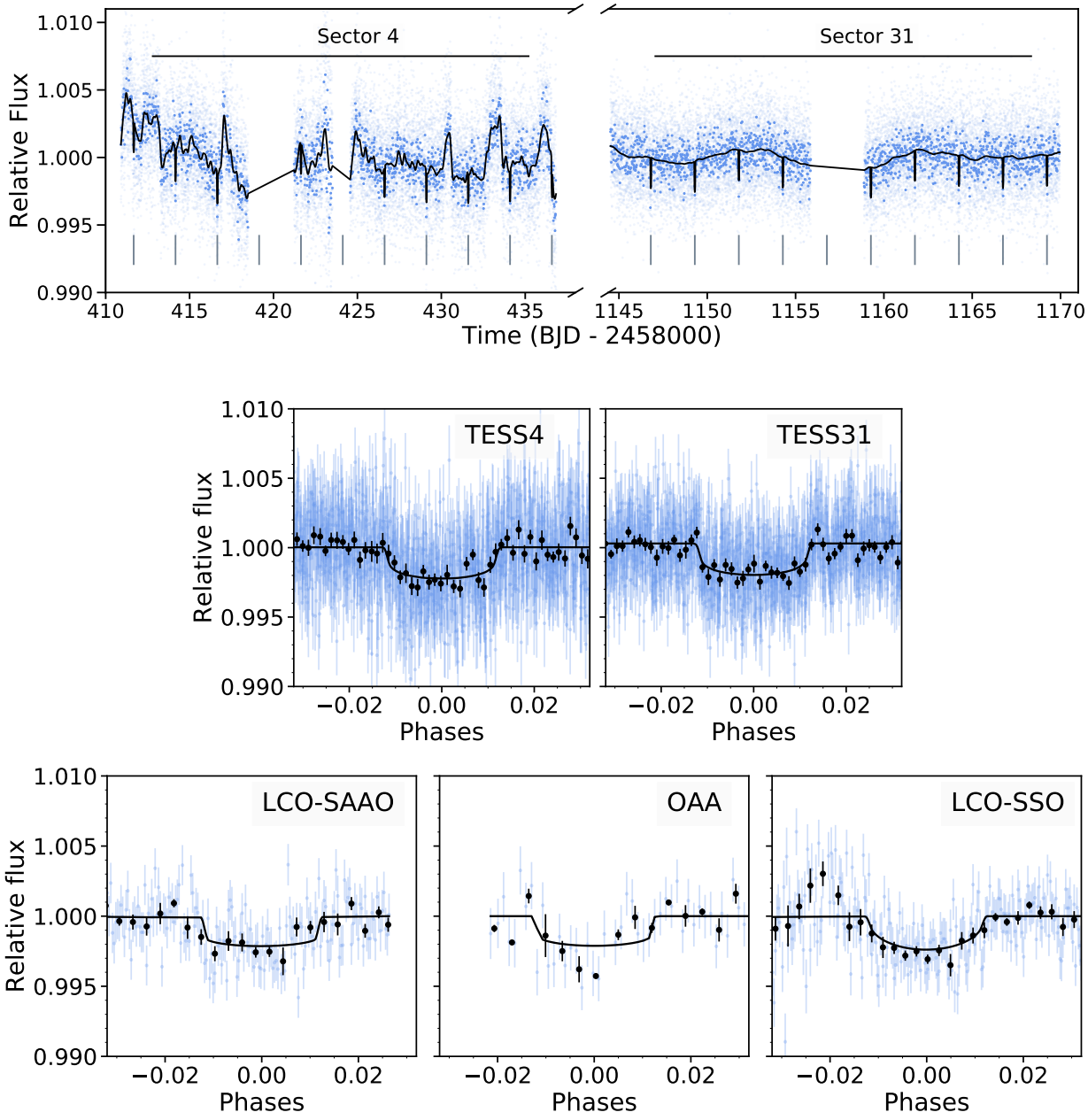

Figure 5.5: *Top.* Above is the full *TESS* light curve for TOI-1201 taken from sector 4 and sector 31. The fainter dots are the data and the opaque dots are the data binned to 20 minutes. The vertical, grey lines represent the locations of the transit, where the black line is the `juliet` best-fit model from the joint fit. *Middle/Bottom.* Phase-folded transits for TOI-1201 b for all available photometric instruments: *TESS* sector 4 (middle left) and sector 31 (middle right), LCO-SAAO *gp* band (bottom left), OAA V band (bottom middle), and LCO-SSO z_s band (bottom right). Any GP components and linear trends have been subtracted out in the phase-folded curves.

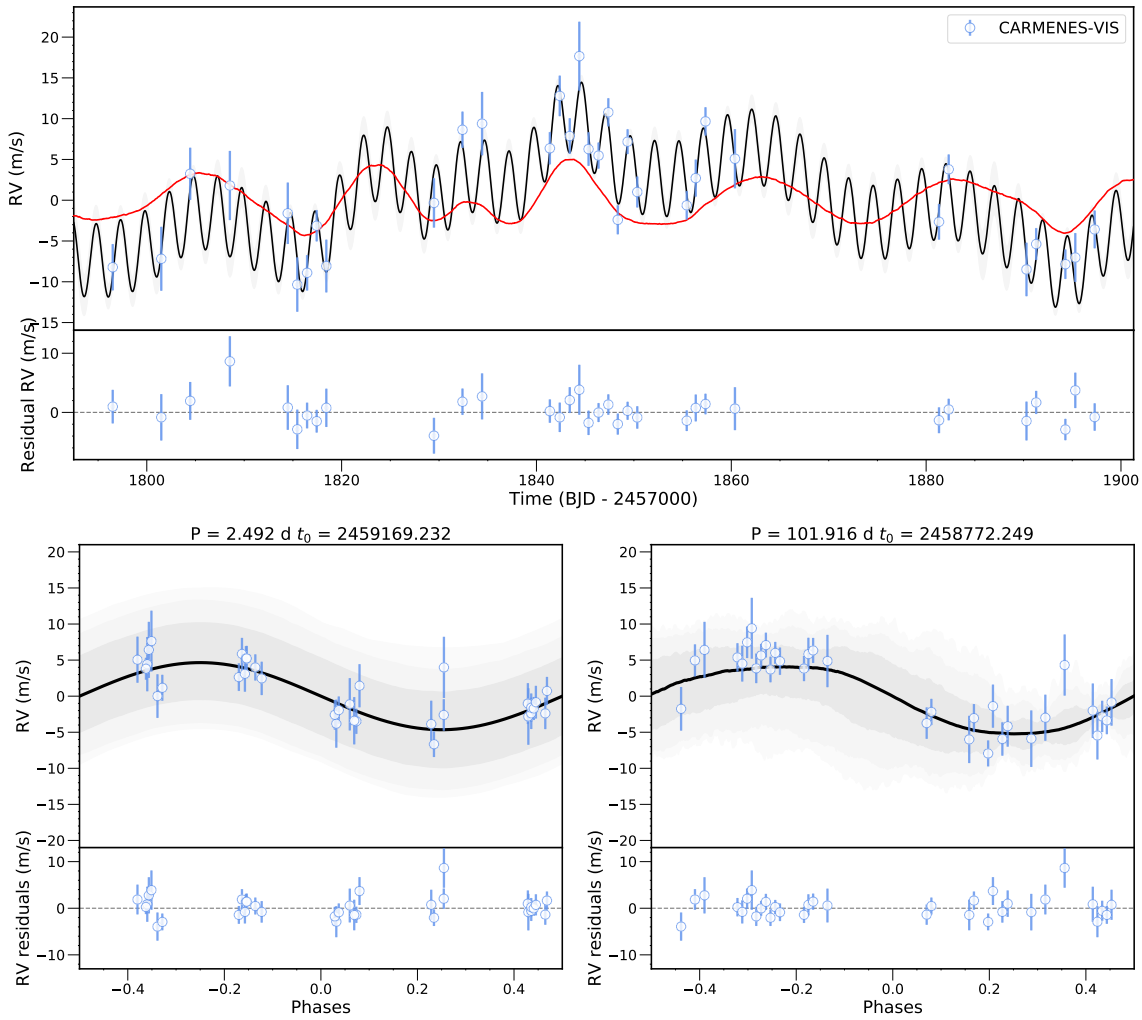

Figure 5.6: The CARMENES RV data with the best fit model from the joint fit over plotted (black) and the dSHO-GP component (red). *Top panel:* RVs over time. *Bottom panels:* RVs phase-folded to the periods of the transiting planet and the long-term signal, on the left and right respectively. The bottom panel of each plot show the residuals after the model is subtracted out. The grey bands represent the 68%, 95%, and 99% credibility intervals.

Table 5.6: Derived planetary parameters for TOI-1201 b.

Parameter	Posterior TOI-1201 b	Unit
P_p	$2.4919863^{+0.0000030}_{-0.0000031}$	d
$t_{0,p}$	$2459169.23222^{+0.00052}_{-0.00054}$	d
$r_{1,p}$	$0.603^{+0.048}_{-0.055}$	...
$r_{2,p}$	$0.04383^{+0.00096}_{-0.00110}$	...
K_p	$4.65^{+0.60}_{-0.64}$	$\mathrm{m\,s^{-1}}$
e_p	0.0 (fixed)	...
ω_p	90.0 (fixed)	...
$p = R_p/R_*$	$0.04383^{+0.00096}_{-0.00110}$	...
$b = (a_p/R_*)\cos(i_p)$	$0.404^{+0.071}_{-0.082}$	...
a_p/R_*	$12.23^{+0.36}_{-0.36}$	...
i_p	$88.11^{+0.42}_{-0.40}$	deg
t_T	$1.747^{+0.096}_{-0.091}$	h
M_p	$6.28^{+0.84}_{-0.88}$	$M_\oplus$
$M \sin i_p$	$6.28^{+0.84}_{-0.88}$	$M_\oplus$
R_p	$2.415^{+0.091}_{-0.090}$	$R_\oplus$
ρ_p	$2.45^{+0.48}_{-0.42}$	$\mathrm{g\ cm^{-3}}$
g_p	$10.5^{+1.8}_{-1.6}$	$\mathrm{m\ s^{-2}}$
a_p	$0.0287^{+0.0012}_{-0.0012}$	AU
T_{eq}	703^{+15}_{-14}	K
S_p	$40.6^{+3.6}_{-3.2}$	$S_\oplus$

5.7 Discussion and future prospects

Following our analysis, we report the confirmation of TOI-1201 b. The relatively hot mini-Neptune orbits its host star every 2.49 d, has a radius of $2.415 \pm 0.090\,R_\oplus$, a mass of $6.28 \pm 0.88\,M_\oplus$, and a bulk density of 2.45 ± 0.48 g cm^{-3}. A summary of all derived planetary parameters can be found in Table 5.6. An additional signal at 102 d is revealed in the RV data where its origins are still unknown. If we were to assume it has planetary origins, we would then obtain a period of $P = 102^{+21}_{-15}$ d and a semi-amplitude of $K = 5.84^{+0.91}_{-0.87}\,\mathrm{m\,s^{-1}}$ such that the minimum mass is $27.0^{+5.6}_{-4.5}\,M_\oplus$. This potential multi-planetary system is probable (see Appendix 5.9.1) making further monitoring quite appealing. Additionally, the RV data show a 19 d signal corresponding to the ∼21 d rotational period of the star given by photometry. Below we discuss the plentiful potential TOI-1201 b has for future follow-up observations and characterizations of the system.

Spin-orbit alignment Following Boué et al. (2013), we compute the expected Rossiter-McLaughlin (RM; Rossiter, 1924; McLaughlin, 1924) amplitude to be in the range $K_{RM} \sim 1.5 - 3\,\mathrm{m\,s^{-1}}$, since the $v_* \sin i$ of the star and the spin-orbit angle are not exactly defined. Collecting roughly 10 data points within the transit (duration of 1.8 ± 0.1 hours) to achieve precision better than the RM amplitude is well within reach for the current state-of-the-art spectrographs with sub $\mathrm{m\,s^{-1}}$ precision (e.g., ESPRESSO, MAROON-X).

For this reason, the mini-Neptune TOI-1201 b presents itself as a promising candidate for measuring the spin-orbit angle between the stellar spin axis and orbit of the transiting planet, which can be determined by the RM effect. Studying this effect can shed light on orbital architectures of planetary systems specifically around low-mass stars, where it is expected that close-orbiting giant planets around such stars are aligned (Gaudi & Winn, 2007; Winn et al., 2010; Muñoz & Perets, 2018) because of strong tidal interactions with the stellar convective envelope. To date, there are only 6 other planets around M dwarfs with measured obliquities: namely, GJ 436 b (Bourrier et al., 2018), TRAPPIST-1 b, e, f (Hirano et al., 2020a), AU Mic b (Addison et al., 2020; Hirano et al., 2020b; Palle et al., 2020), and K2-25 b (Stefansson et al., 2020). Determining the spin-orbit angle of this particular planet =is especially interesting in the context of the companion (320 AU away), because it could hint possible interaction. As was the case for the highly eccentric orbit ($e = 0.93$) of HD 80606b, where it was proposed that Kozai cycles are at play due to the stellar host's companion 1200 AU away. The predictions then brought by Fabrycky & Tremaine (2007) of a large spin-orbit misalignment were proven true (Hébrard et al., 2010).

Transmission spectroscopy TOI-1201 b falls in the realm of Neptune-sized planets above the M-dwarf radius valley (Fig. 7 in Van Eylen et al., 2021). In this regard, the density of TOI-1201 b suggests that its composition is inline with a Earth-like rocky core with an H-He envelope of 0.3% (Fig. 5.8), following the theoretical composition models from Zeng et al. (2019)[43].

Following Kempton et al. (2018), the transmission spectroscopy metric (TSM) turns out to be 128^{+35}_{-27}, which is well above the cutoff of 92 with the *JWST*/NIRISS bandpass (for planet

[43] https://www.cfa.harvard.edu/~lzeng/planetmodels.html#mrrelation

radii of $1.5\,R_\oplus < R_p < 2.75\,R_\oplus$). Among other transiting planets with measured masses via RVs or TTVs around M dwarfs[44], TOI-1201 b is ranked high and one of just a few optimal targets known thus far (Fig. 5.7).

TOI-1201 b is therefore a very viable and compelling candidate for atmospheric characterization using transmission spectroscopy. Thus far, not many planets with radii less than of $10\,R_\oplus$ are suitable for such an atmospheric study. Determining the atmospheric compositions will allow for a better understanding of the formation histories of these planets, and aid in figuring out whether the atmospheres of mini-Neptunes are metal-rich or cloudy (Benneke & Seager, 2013).

Our transit ephemeris from the joint fit (see Table 5.6) results in an uncertainty of $\sim$60 s towards the beginning of 2022, just right after the presumed launch of *JWST* in October 2021. The uncertainty then increases to $\sim$100 s and $\sim$140 s for the beginning of 2023 and 2024, respectively.

Likewise, TOI-1201 b is ideal for low-to-mid-resolution ground-based transit spectroscopy covering the optical regime, serving as a great complement to the expected near- and mid-IR wavelength range measurements from *JWST*. These ground-based observations are typically challenging due to strong atmospheric and instrumental variations (e.g., Nikolov et al., 2016; Huitson et al., 2017; Diamond-Lowe et al., 2018; Espinoza et al., 2019b; Wilson et al., 2021; Chen et al., 2021). Companion stars that are closest in brightness and space to the target star help mitigate these effects since both stars experience a similar path both through the Earth's atmosphere and the instrument, allowing to monitor and remove those from the target star. In this regard, TOI-1201 is accompanied by a close-by companion (8.2 arcsec) with very similar stellar properties (see Table 5.2) which makes it a perfect star to detrend atmospheric and instrumental effects from TOI-1201's light curve.

Planet occurrence rates around M-dwarf binary systems Observational surveys were strongly biased against stars in known binary or multiple systems, introducing a selection bias against them. As already listed in Sect. 5.2, many planets discovered around M-dwarf binary systems are in systems with a wide separation. Like these, TOI-1201 is also in the same situation ($s \sim 300$ AU). Therefore, the TOI-1201 system most likely does not face significant gravitational interactions with its companion to hinder planet formation. It is essentially identical to a system with planets around a single star (Desidera & Barbieri, 2007; Roell et al., 2012). Interestingly enough, in all of these systems, the stars are quite different in spectral type with the exception of GJ 338 ABb (M0/M0; González-Álvarez et al., 2020) and TOI-1201 (M2.0/2.5). Where it is more prevalent that only the host stars are provided with precise stellar parameters and spectroscopic measurements, both are present for the primary and companion in the TOI-1201 system. Though unfortunately, nothing was clearly suggestive of a planetary signal for the companion (Sect. 5.6.4).

[44]Using the continuously updated table: `https://carmenes.caha.es/ext/tmp/`; last updated on 09 April 2021 (Trifonov et al., 2021)

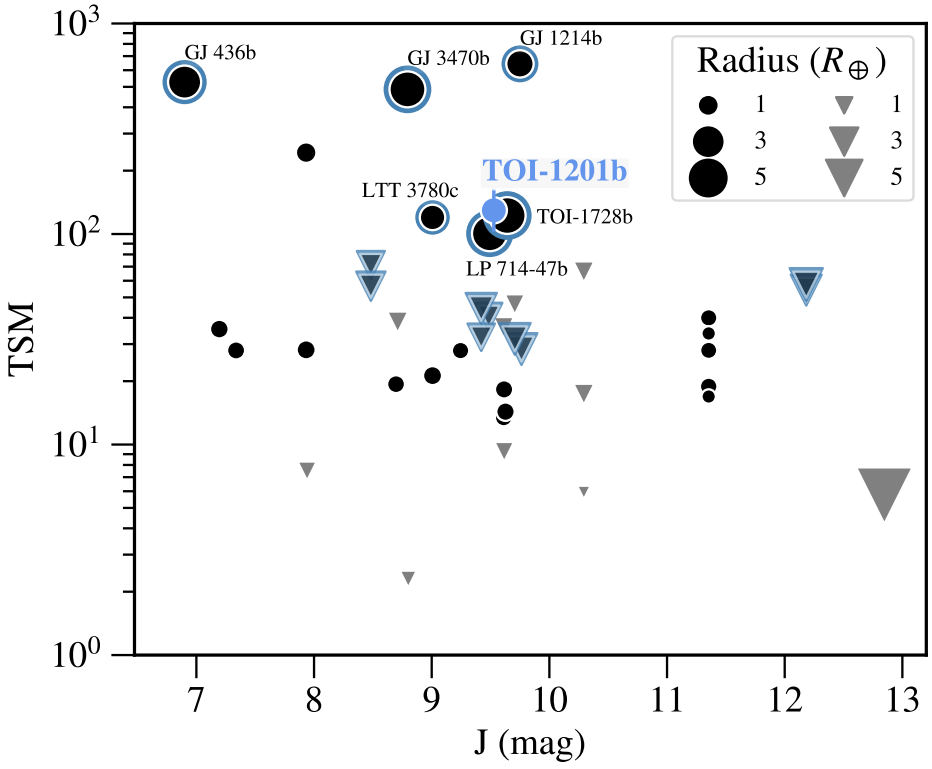

Figure 5.7: Transmission spectroscopy metric (TSM) as a function of J magnitude for currently known transiting exoplanets around M dwarfs with a measured mass. The size of each point is related to the size of the planet. Neptune-like planets ($1.7R_\oplus < R_p < 6R_\oplus$) are outlined in blue and those who meet the respective criteria are labeled. The uncertainties are only computed for TOI-1201 b. TSM: TOI-1201 b is ranked as one of the more promising targets with a TSM of 128^{+35}_{-27}, well above the threshold of 92 for its radius bin. Other promising targets that are above the cutoff are marked with a black circle, whereas those below the cutoff are represented with upside-down grey triangles.

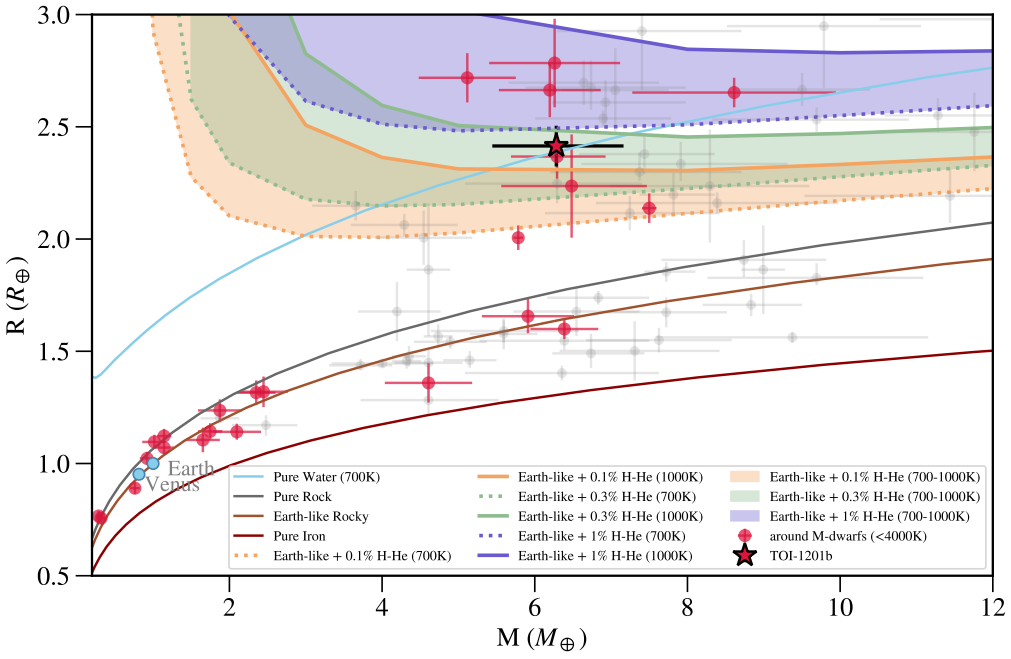

Figure 5.8: Mass-radius diagram. TOI-1201 b is indicated as a red star outlined in black. The grey points represent the other planets ($R < 3\,R_\oplus$ and $M < 12\,M_\oplus$) with measured masses and radii to precision better than 20%. The red points are those planets around M dwarfs ($T_{\rm eff} < 4000$K). All theoretical composition models are taken from Zeng et al. (2019). The lines represent models for cores composed of pure Iron (100% Fe), Earth-like rocky (32.5% Fe+67.5% $MgSiO_3$), pure Rock (100% $MgSiO_3$), and pure water (100% H_2O for 700K). Above, the solid and dotted lines represent the theoretical composition models for Earth-like rocky cores with varying sizes of H-He envelopes (0.1%, 0.3%, 1%) for equilibrium temperatures of 700K and 1000K, respectively. Plot inspired by Van Eylen et al. (2021).

5.8 Conclusions

In this paper, we presented *TESS* and ground-based photometric observations, together with CARMENES spectroscopic measurements, of the M dwarf TOI-1201. We confirmed the transiting planet at 2.5 d and provided a mass determination using RV follow-up to obtain the following derived planetary parameters: $2.415^{+0.091}_{-0.090}\,R_\oplus$ for the radius and $6.28^{+0.84}_{-0.88}\,M_\oplus$ for the mass. This transiting planet then carries a density of $2.45^{+0.48}_{-0.42}\,\mathrm{g\,cm^{-3}}$, classifying it as a mini-Neptune. The planet is an optimal target for further studies, namely for spin-orbit alignment using the Rossiter-McLaughlin effect achievable with the current spectroscopic instruments, and for atmospheric studies using transmission and emission spectroscopy with upcoming space-based facilities such as *JWST*.

The RVs also exhibited a longer-term signal at ∼102 d that cannot be ignored as it has the highest semi-amplitude. It is too premature to claim that this signal has potential planetary origins. However, if the signal is suggestive of an additional planet in the system, then its minimum mass would be $27.0^{+5.6}_{-4.5}\,M_\oplus$, which would be in agreement with current core accretion models of planet formation. Further RV measurements are, however, necessary to falsify or to proof a planetary origin of the signal.

We were able to narrow down the stellar rotation period for TOI-1201 to be 19–23 d using archival long-term photometry and stellar activity indicators provided by the spectral information. The stellar rotation period also presents itself in the RVs, for which we take into account in our final model. The stellar host is the primary of a wide ($s \sim 320$ AU) binary system of two nearly identical M2.0–2.5 dwarfs. We were able to obtain RV measurements for the companion as well, providing precise stellar parameters. We analyzed CARMENES spectroscopic data to find one significant signal at around 27 d. However, we find the results inconclusive as this signal may be related to the stellar rotation period and more RV data would be required.

5.9 Appendix

5.9.1 Two-planet model

As discussed in Sect. 5.6.2, a ∼102 d signal found in the RVs appears as the dominating signal. It is favored in the model when included as an additional planetary component (Table 5.4; 2 Kep + dSHO-$\mathrm{GP_{19d}}$ vs 1 Kep + dSHO-$\mathrm{GP_{19d}}$), however, a GP could also model it well (Table 5.4; 2 Kep + dSHO-$\mathrm{GP_{19d}}$ vs 1 Kep + dSHO-$\mathrm{GP_{wide}}$). If considered to be a planet, it would then have a minimum mass of $27.0^{+5.6}_{-4.5}$ (Table 5.7, Fig. 5.14). Thus far, we cannot immediately rule out a possible planet candidate, however, given that the orbital period is on the order of the time baseline, we do not have sufficient evidence to unequivocally prove the origin of the signal to be planetary. Additional ground-based data over a longer coverage would be necessary for determining the origins of this signal.

From a dynamical point of view, it would be an unproblematic configuration, since both planets maintain a sufficient spatial separation to preserve long term stability. In addition, the longer-period planet candidate, whose expected bulk mass would require a significant gaseous envelope, is far enough from the star to avoid significant atmospheric losses due to

Table 5.7: Same derived posterior table as Table 5.6 but including the second signal to be of planetary origin.

Parameter	Posterior		Unit
	b	c	
P_p	$2.4919863^{+0.0000030}_{-0.0000031}$	102^{+21}_{-15}	d
$t_{0,p}$	$2459169.23222^{+0.00052}_{-0.00054}$	2458772^{+12}_{-16}	d
$r_{1,p}$	$0.603^{+0.048}_{-0.055}$	...	...
$r_{2,p}$	$0.04383^{+0.00096}_{-0.00110}$	...	...
K_p	$4.65^{+0.60}_{-0.64}$	$5.84^{+0.91}_{-0.87}$	$\mathrm{m\,s^{-1}}$
e_p	0.0 (fixed)	0.0 (fixed)	...
ω_p	90.0 (fixed)	90.0 (fixed)	...
$p = R_p/R_*$	$0.04383^{+0.00096}_{-0.00110}$	...	...
$b = (a_p/R_*)\cos i_p$	$0.404^{+0.071}_{-0.082}$	...	...
a_p/R_*	$12.23^{+0.36}_{-0.36}$	...	...
i_p	$88.11^{+0.42}_{-0.40}$	...	deg
t_T	$1.747^{+0.096}_{-0.091}$	...	h
M_p	$6.28^{+0.84}_{-0.88}$	$> 27.0^{+5.6}_{-4.5}$	$M_\oplus$
R_p	$2.415^{+0.091}_{-0.090}$	...	$R_\oplus$
ρ_p	$2.45^{+0.48}_{-0.42}$	...	$\mathrm{g\ cm^{-3}}$
g_p	$10.5^{+1.8}_{-1.6}$	...	$\mathrm{m\ s^{-2}}$
a_p	$0.0287^{+0.0012}_{-0.0012}$	$0.341^{+0.046}_{-0.034}$	AU
T_{eq}	703^{+15}_{-14}	204^{+12}_{-13}	K
S_p	$40.6^{+3.6}_{-3.2}$	$0.287^{+0.072}_{-0.065}$	$S_\oplus$

photoevaporation (Owen & Jackson, 2012). A Neptunian-mass planet at this orbit is thus not unexpected.

In fact, core accretion theory, which is considered the most promising path of planet formation, routinely predicts planets like those found in TOI-1201. Global formation models of multi-planet systems find the configuration we suggest to be a rather typical outcome (e.g., Schlecker et al., 2020b, their Fig. D.3). New planetary population syntheses specifically tailored to M-dwarf systems also propose the regular formation of planets in the mass range of TOI-1201 b and c (Burn et al., subm.). Therefore, we believe that TOI-1201 c is a promising candidate planetary companion, and further observations, especially ground-based longer coverage of a single instrument, will be necessary to unequivocally determine the nature of the signal.

5.9.2 Additional figures

5.9.3 Priors and posteriors

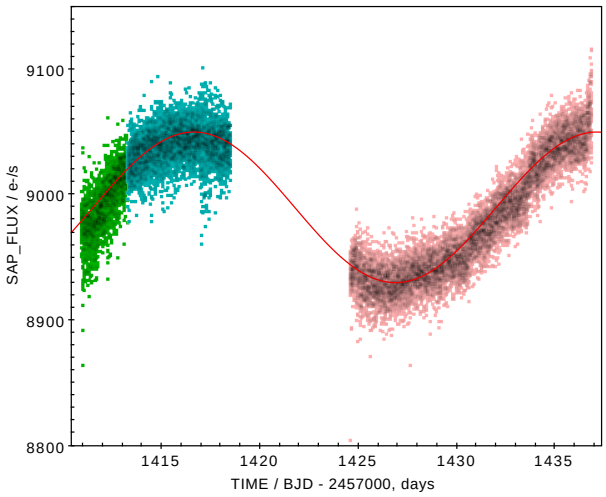

Figure 5.9: Phase-folded *TESS* light curve from sector 4 exhibiting the stellar rotation period at 20.5 d for TOI-1201.

Table 5.8: Priors for the RV-only fits for TOI-1201 with `juliet` in Sect. 5.6.2.

Parameter	Prior	Unit	Description
	Parameters for transiting planet b		
P_b	$\mathcal{F}(2.4919858227\hat{A}\ )$	d	Period
$t_{0,b}$	$\mathcal{F}(2459169.2321864809)$	d	Time of transit center
K_b	$\mathcal{U}(0.0, 20)$	$\mathrm{m\,s^{-1}}$	RV semi-amplitude
$S_{1,b} = \sqrt{e_c}\sin\omega_c$	$\mathcal{F}(0.0)$ (circular)	...	Parametrization for e and ω
	$\mathcal{U}(-1, 1)$ (eccentric)	...	Parametrization for e and ω
$S_{2,b} = \sqrt{e_b}\cos\omega_b$	$\mathcal{F}(0.0)$ (circular)	...	Parametrization for e and ω
	$\mathcal{U}(-1, 1)$ (eccentric)	...	Parametrization for e and ω
	Parameters for long-term signal in RVs		
P_c	$\mathcal{U}(60.0, 150.0)$	d	Period
$t_{0,c}$	$\mathcal{U}(2458730.0, 2458840.0)$	d	Time of transit center
K_c	$\mathcal{U}(0.0, 20.0)$	$\mathrm{m\,s^{-1}}$	RV semi-amplitude
$S_{1,c} = \sqrt{e_c}\sin\omega_c$	$\mathcal{F}(0.0)$ (circular)	...	Parametrization for e and ω
	$\mathcal{U}(-1, 1)$ (eccentric)	...	Parametrization for e and ω
$S_{2,c} = \sqrt{e_b}\cos\omega_b$	$\mathcal{F}(0.0)$ (circular)	...	Parametrization for e and ω
	$\mathcal{U}(-1, 1)$ (eccentric)	...	Parametrization for e and ω
	RV instrumental parameters		
$\mu_{\text{CARMENES-VIS}}$	$\mathcal{U}(-10.0, 10.0)$	$\mathrm{m\,s^{-1}}$	Systemic velocity for CARMENES-VIS
$\sigma_{\text{CARMENES-VIS}}$	$\mathcal{J}(0.01, 100.0^2)$	$\mathrm{m\,s^{-1}}$	Extra jitter term for CARMENES-VIS
	dSHO-GP parameters		
$\sigma_{\text{GP, CARMENES-VIS}}$	$\mathcal{U}(0.0, 10.0)$	$\mathrm{m\,s^{-1}}$	Amplitude of the dSHO-GP
$Q_{0\ \text{GP, CARMENES-VIS}}$	$\mathcal{J}(1.0, 100000.0^2)$	...	Quality factor for the secondary oscillation of the dSHO-GP
$f_{\text{GP, CARMENES-VIS}}$	$\mathcal{U}(0.1, 1.0)$	...	Fractional amplitude of the secondary oscillation of the dSHO-GP
$\delta Q_{\text{GP, CARMENES-VIS}}$	$\mathcal{J}(1.0, 100000.0^2)$	...	Quality factor difference between the first and second oscillations of the dSHO-GP
$P_{\text{rot, GP, CARMENES-VIS}}$	$\mathcal{U}(15.0, 25.0)$	d	Primary period of the dSHO-GP
	$\mathcal{U}(10.0, 150.0)$ (wide)	d	Primary period of the dSHO-GP
	QP-GP parameters		
$\sigma_{\text{GP, CARMENES-VIS}}$	$\mathcal{U}(0.0, 10.0)$	$\mathrm{m\,s^{-1}}$	Amplitude of the QP-GP
$\Gamma_{\text{GP, CARMENES-VIS}}$	$\mathcal{J}(0.01, 10.0)$	...	Amplitude of the sine-squared component of the QP-GP
$\alpha_{\text{GP, CARMENES-VIS}}$	$\mathcal{J}(10^{-8}, 0.001^2)$	$\mathrm{d^{-2}}$	Inverse length-scale of the exponential component of the QP-GP
$P_{\text{rot, GP, CARMENES-VIS}}$	$\mathcal{U}(15.0, 25.0)$	d	Rotational period of the quasi-periodic component of the QP-GP
	$\mathcal{U}(10.0, 150.0)$ (wide)	d	Rotational period of the quasi-periodic component of the QP-GP

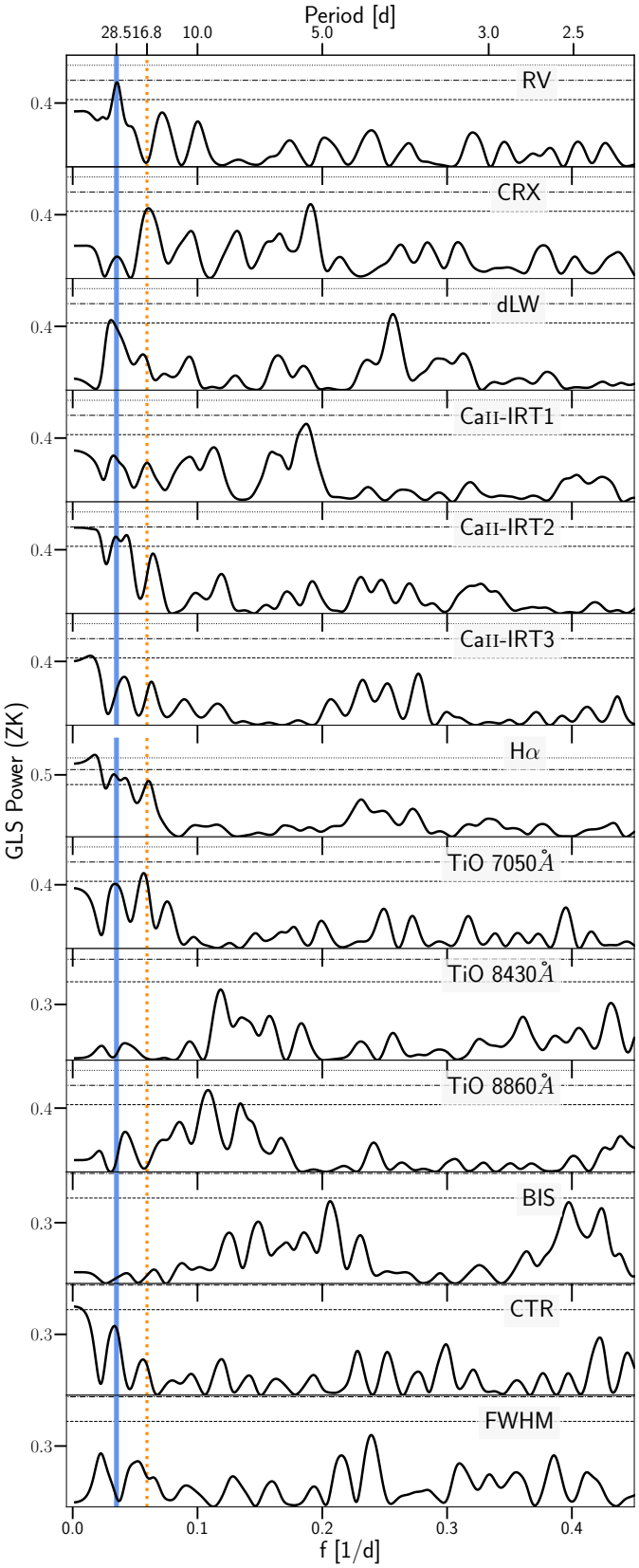

Figure 5.10: GLS periodograms of the RVs and various stellar activity indicators from the CARMENES spectroscopic data for the companion of TOI-1201. The solid vertical blue line corresponds to the main signal found in the RVs (28.5 d). The dotted vertical orange line corresponds to the 41 d alias (∼16.8 d). The horizontal dotted, dot-dashed, and dashed lines represent the 10 %, 1 %, and 0.1 % FAP lines, respectively.

Table 5.9: Priors for the final joint transit and RV fit for TOI-1201 with `juliet` in Sect. 5.6.3.

Parameter	Prior	Unit	Description
	Stellar parameters		
ρ_*	$\mathcal{N}(5400.0, 600.0^2)$	kg m^{-3}	Stellar density
	Parameters for transiting planet b		
P_b	$\mathcal{N}(2.4919858227, 0.0001^2)$	d	Period.
$t_{0,b}$	$\mathcal{N}(2459169.232186481, 0.05^2)$	d	Time of transit center.
$r_{1,b}$	$\mathcal{U}(0.0, 1.0)$	...	Parametrization for p and b
$r_{2,b}$	$\mathcal{U}(0.0, 1.0)$	...	Parametrization for p and b
K_b	$\mathcal{U}(0.0, 20)$	m s^{-1}	RV semi-amplitude
$S_{1,b} = \sqrt{e_b}\sin\omega_b$	0.0 (fixed)	...	Parametrization for e and ω
$S_{2,b} = \sqrt{e_b}\cos\omega_b$	0.0 (fixed)	...	Parametrization for e and ω
	Parameters for long-term RV signal		
P_c	$\mathcal{U}(60.0, 150.0)$	d	Period
$t_{0,c}$	$\mathcal{U}(2458730.0, 2458840.0)$	d	Time of transit center
K_c	$\mathcal{U}(0.0, 20.0)$	m s^{-1}	RV semi-amplitude
$S_{1,c} = \sqrt{e_c}\sin\omega_c$	0.0 (fixed)	...	Parametrization for e and ω
$S_{2,c} = \sqrt{e_c}\cos\omega_c$	0.0 (fixed)	...	Parametrization for e and ω
	RV instrumental parameters		
$\mu_{\text{CARMENES-VIS}}$	$\mathcal{U}(-10.0, 10.0)$	m s^{-1}	Systemic velocity for CARMENES-VIS
$\sigma_{\text{CARMENES-VIS}}$	$\mathcal{J}(0.01, 100.0^2)$	m s^{-1}	Extra jitter term for CARMENES-VIS
$\sigma_{\text{GP, CARMENES-VIS}}$	$\mathcal{U}(0.0, 10.0)$	m s^{-1}	Amplitude of the dSHO-GP
$Q_{0\text{ GP, CARMENES-VIS}}$	$\mathcal{J}(1.0, 100000.0^2)$	...	Quality factor for the secondary oscillation of the dSHO-GP
$f_{\text{GP, CARMENES-VIS}}$	$\mathcal{U}(0.1, 1.0)$	...	Fractional amplitude of the secondary oscillation of the dSHO-GP
$\delta Q_{\text{GP, CARMENES-VIS}}$	$\mathcal{J}(1.0, 100000.0^2)$	...	Quality factor difference between the first and second oscillations of the dSHO-GP
$P_{\text{rot, GP, CARMENES-VIS}}$	$\mathcal{U}(15.0, 25.0)$	d	Primary period of the dSHO-GP
	Photometry instrumental parameters		
D_{TESS4}	1.0 (fixed)	...	Dilution factor for TESS4
M_{TESS4}	$\mathcal{U}(-0.1, 0.1)$	ppm	Relative flux offset for TESS4
σ_{TESS4}	$\mathcal{J}(10^{-7}, 100000.0^2)$	ppm	Extra jitter term for TESS4
$\sigma_{\text{GP, TESS4}}$	$\mathcal{J}(10^{-5}, 100.0^2)$	ppm	Amplitude of the Matern-3/2-GP for TESS4
$\rho_{\text{GP, TESS4}}$	$\mathcal{J}(0.001, 100.0^2)$	d	Length scale of the Matern-3/2-GP for TESS4
D_{TESS31}	1.0 (fixed)	...	Dilution factor for TESS31
M_{TESS31}	$\mathcal{U}(-0.1, 0.1)$	ppm	Relative flux offset for TESS31
σ_{TESS31}	$\mathcal{J}(10^{-7}, 100000.0^2)$	ppm	Extra jitter term for TESS31
$\sigma_{\text{GP, TESS31}}$	$\mathcal{J}(10^{-8}, 0.0001^2)$	ppm	Amplitude of the exp-GP for TESS31
$T_{\text{GP,TESS31}}$	$\mathcal{J}(10^{-5}, 100.0^2)$	d	Characteristic timescale of the exp-GP for TESS31
$q_{1,\text{TESS4+TESS31}}$	$\mathcal{U}(0.0, 1.0)$	...	Quadratic limb-darkening parametrization for TESS4 and TESS31
$q_{2,\text{TESS4+TESS31}}$	$\mathcal{U}(0.0, 1.0)$	...	Quadratic limb-darkening parametrization for TESS4 and TESS31
D_{OAA}	1.0 (fixed)	...	Dilution factor for OAA
M_{OAA}	$\mathcal{U}(-0.1, 0.1)$	ppm	Relative flux offset for OAA
σ_{OAA}	$\mathcal{J}(10^{-7}, 100000.0^2)$	ppm	Extra jitter term for OAA
$q_{1,\text{OAA}}$	$\mathcal{U}(0.0, 1.0)$	...	Linear limb-darkening parametrization for OAA
$D_{\text{LCO-SSO}}$	1.0 (fixed)	...	Dilution factor for LCO-SSO
$M_{\text{LCO-SSO}}$	$\mathcal{U}(-0.1, 0.1)$	ppm	Relative flux offset for LCO-SSO
$\sigma_{\text{LCO-SSO}}$	$\mathcal{J}(10^{-7}, 100000.0^2)$	ppm	Extra jitter term for LCO-SSO
$q_{1,\text{LCO-SSO}}$	$\mathcal{U}(0.0, 1.0)$	...	Linear limb-darkening parametrization for LCO-SSO
$\theta_{0,\text{LCO-SSO}}$	$\mathcal{U}(-0.1, 0.1)$		Linear term applied to the airmass for LCO-SSO
$D_{\text{LCO-SAAO}}$	1.0 (fixed)	...	Dilution factor for LCO-SAAO
$M_{\text{LCO-SAAO}}$	$\mathcal{U}(-0.1, 0.1)$	ppm	Relative flux offset for LCO-SAAO
$\sigma_{\text{LCO-SAAO}}$	$\mathcal{J}(10^{-7}, 100000.0^2)$	ppm	Extra jitter term for LCO-SAAO
$q_{1,\text{LCO-SAAO}}$	$\mathcal{U}(0.0, 1.0)$	...	Linear limb-darkening parametrization for LCO-SAAO
$\theta_{0,\text{LCO-SAAO}}$	$\mathcal{U}(-0.1, 0.1)$		Linear term applied to the airmass for LCO-SAAO

Table 5.10: Full set of posterior parameters used in the model for TOI-1201 described in Sect. 5.6.3

Parameter	Posterior
Stellar parameters	
ρ_* (kg m^{-3})	5566^{+510}_{-480}
Posterior parameters for transiting planet b	
P_b (d)	$2.4919863^{+0.0000030}_{-0.0000031}$
$t_{0,b}$ (d)	$2459169.23222^{+0.00052}_{-0.00054}$
$r_{1,b}$	$0.603^{+0.048}_{-0.055}$
$r_{2,b}$	$0.04383^{+0.00096}_{-0.00110}$
K_b (m s^{-1})	$4.65^{+0.60}_{-0.64}$
Parameters for long-term signal in RVs	
P_c (d)	102^{+21}_{-15}
$t_{0,c}$ (d)	2458772^{+12}_{-16}
K_c (m s^{-1})	$5.84^{+0.91}_{-0.87}$
RV instrumental parameters	
$\mu_{\text{CARMENES-VIS}}$ (m s^{-1})	$-2.91^{+0.74}_{-0.97}$
$\sigma_{\text{CARMENES-VIS}}$ (m s^{-1})	$0.36^{+0.78}_{-0.29}$
$\sigma_{\text{GP, CARMENES-VIS}}$ (m s^{-1})	$3.7^{+1.7}_{-1.1}$
$Q_{0\ \text{GP, CARMENES-VIS}}$	$5.6^{+41.0}_{-3.8}$
$f_{\text{GP, CARMENES-VIS}}$	$0.57^{+0.25}_{-0.28}$
$\delta Q_{\text{GP, CARMENES-VIS}}$	179^{+5600}_{-170}
$P_{\text{rot, GP, CARMENES-VIS}}$ (d)	$19.62^{+1.10}_{-0.81}$
Photometry instrumental parameters	
M_{TESS4} (ppm)	$-0.00003^{+0.00020}_{-0.00021}$
σ_{TESS4} (ppm)	810^{+44}_{-45}
$\sigma_{\text{GP, TESS4}}$ (ppm)	$0.001455^{+0.000110}_{-0.000098}$
$\rho_{\text{GP, TESS4}}$ (d)	$0.255^{+0.027}_{-0.022}$
M_{TESS31} (ppm)	$-0.0003^{+0.0011}_{-0.0018}$
σ_{TESS31} (ppm)	$0.0075^{+3.7000}_{-0.0074}$
$\sigma_{\text{GP, TESS31}}$ (ppm)	$0.0000023^{+0.0000170}_{-0.0000019}$
$T_{\text{GP, TESS31}}$ (d)	$0.027^{+0.130}_{-0.024}$
$q_{1,\text{TESS4+TESS31}}$	$0.47^{+0.25}_{-0.22}$
$q_{2,\text{TESS4+TESS31}}$	$0.33^{+0.28}_{-0.20}$
M_{OAA} (ppm)	$-0.00002^{+0.00019}_{-0.00019}$
σ_{OAA} (ppm)	$0.072^{+32.000}_{-0.072}$
$q_{1,\text{OAA}}$	$0.46^{+0.30}_{-0.27}$
$M_{\text{LCO-SSO}}$ (ppm)	$0.03181^{+0.00041}_{-0.00041}$
$\sigma_{\text{LCO-SSO}}$ (ppm)	926^{+140}_{-150}
$q_{1,\text{LCO-SSO}}$	$0.69^{+0.18}_{-0.23}$
$\theta_{0,\text{LCO-SSO}}$	$0.0007^{+0.0003}_{-0.0003}$
$M_{\text{LCO-SAAO}}$ (ppm)	$0.0383^{+0.0030}_{-0.0031}$
$\sigma_{\text{LCO-SAAO}}$ (ppm)	112^{+860}_{-110}
$q_{1,\text{LCO-SAAO}}$	$0.47^{+0.24}_{-0.24}$
$\theta_{0,\text{LCO-SAAO}}$	$0.0333^{+0.0026}_{-0.0026}$

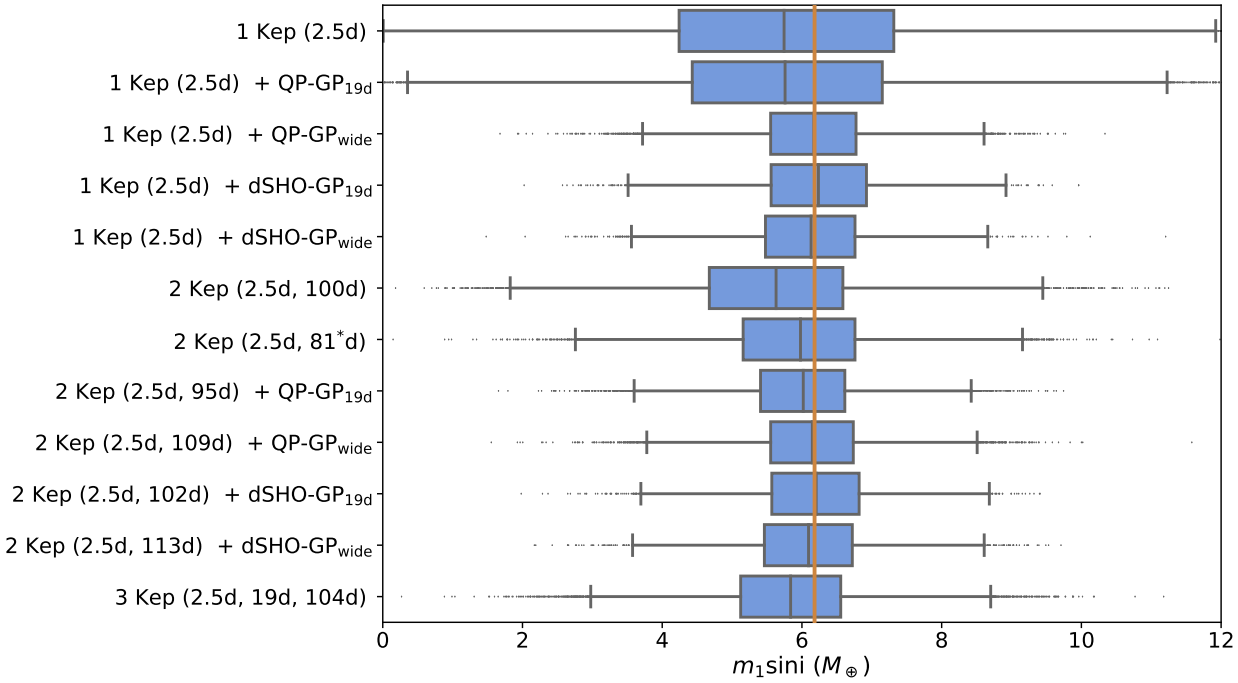

Figure 5.11: The posteriors of the minimum mass of the 2.5 d transiting planet depending on the model choice for the RV-only fits. The orange vertical line is the median value corresponding to the 2 Kep (2.5 d, 02 d) + dSHO-GP_{19d}. The 25% and 75% quartiles are represent as the blue box, whereas the extending black line show the rest of the distribution and the dots are considered as "outliers". The model names correspond to those in Table 5.4.

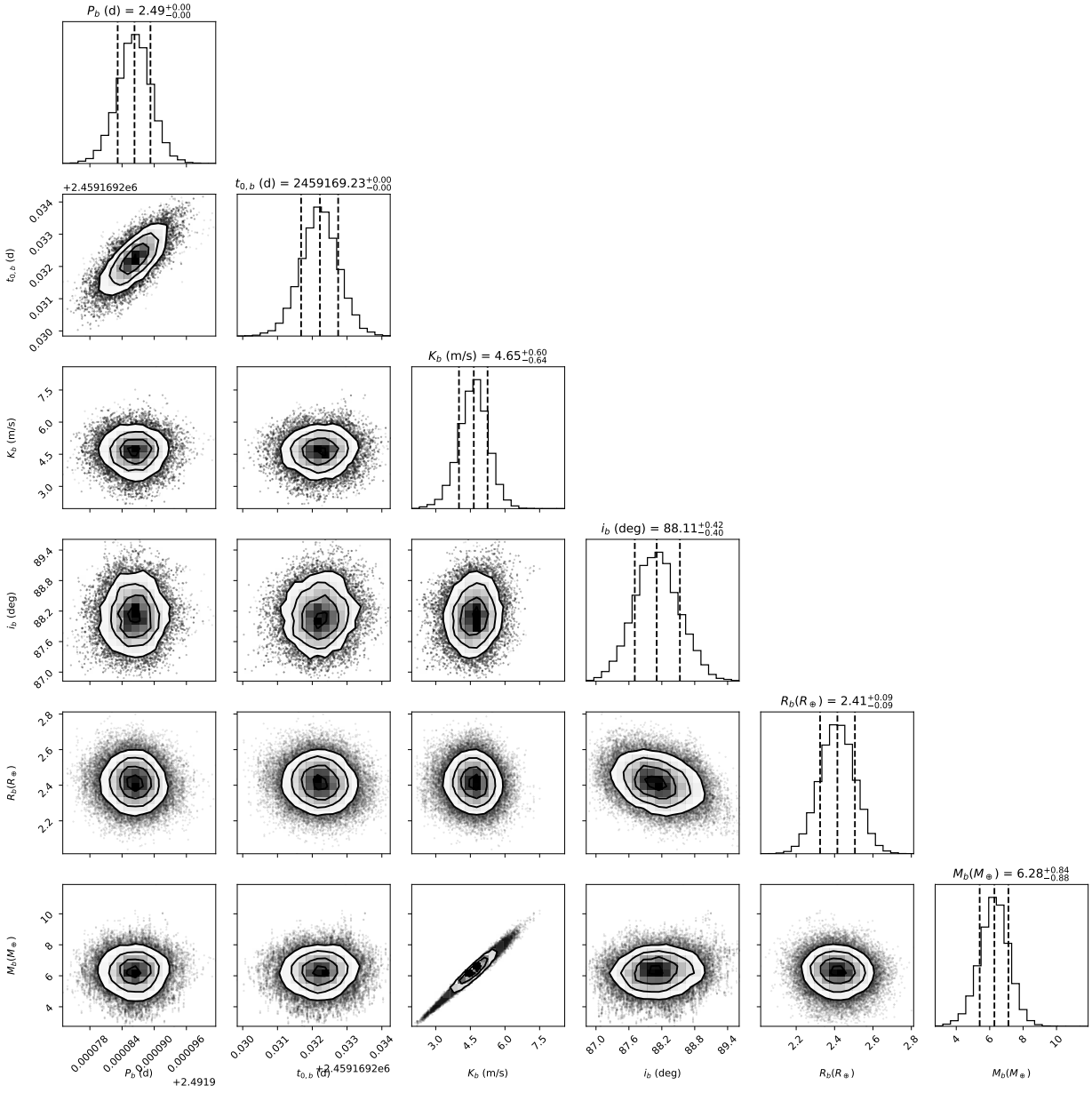

Figure 5.12: Posterior distributions for the transiting planet from the joint fit described in Sect. 5.6.3.

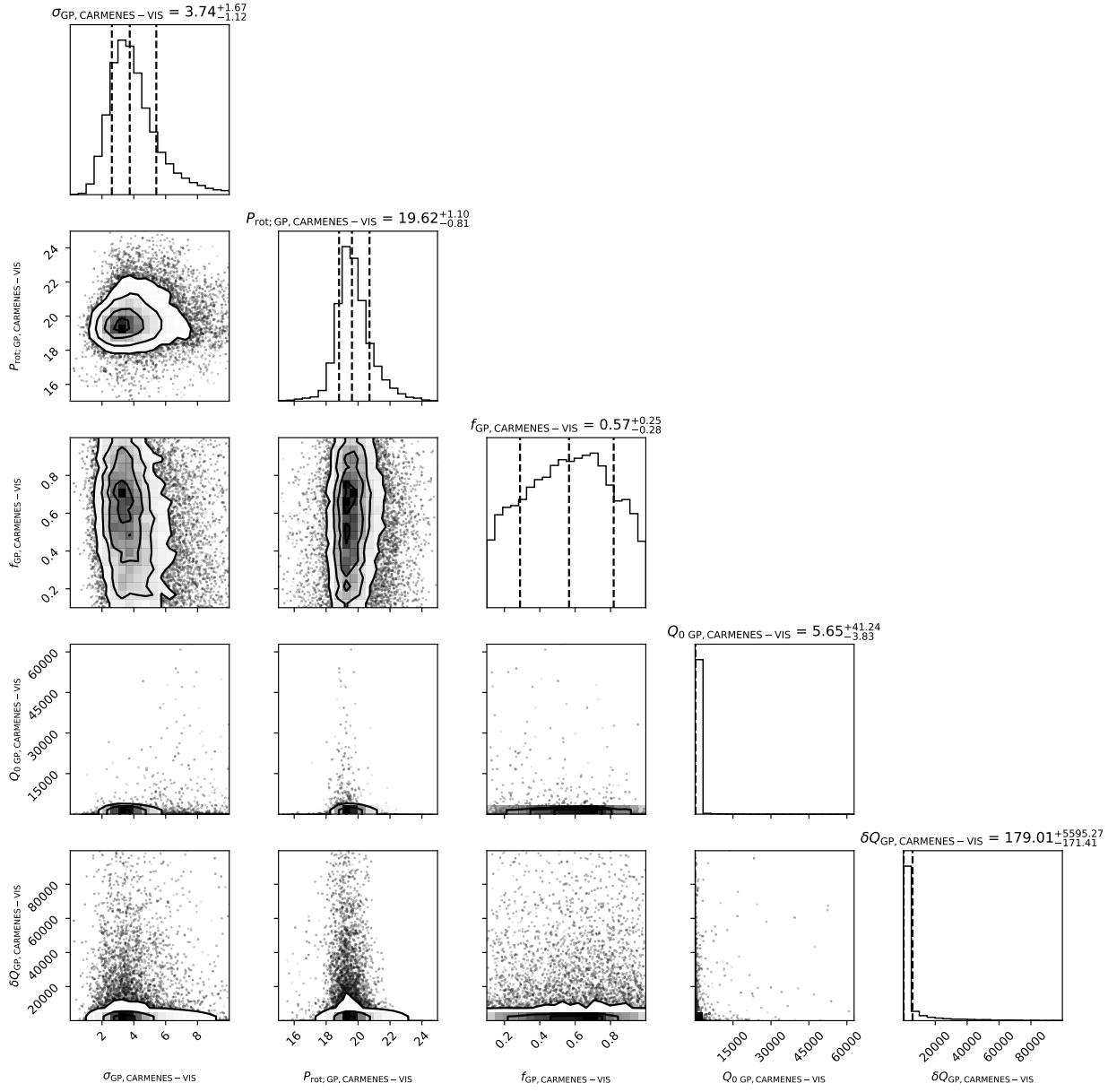

Figure 5.13: Posterior distributions for the dSHO-GP on the CARMENES RVs from the joint fit described in Sect. 5.6.3.

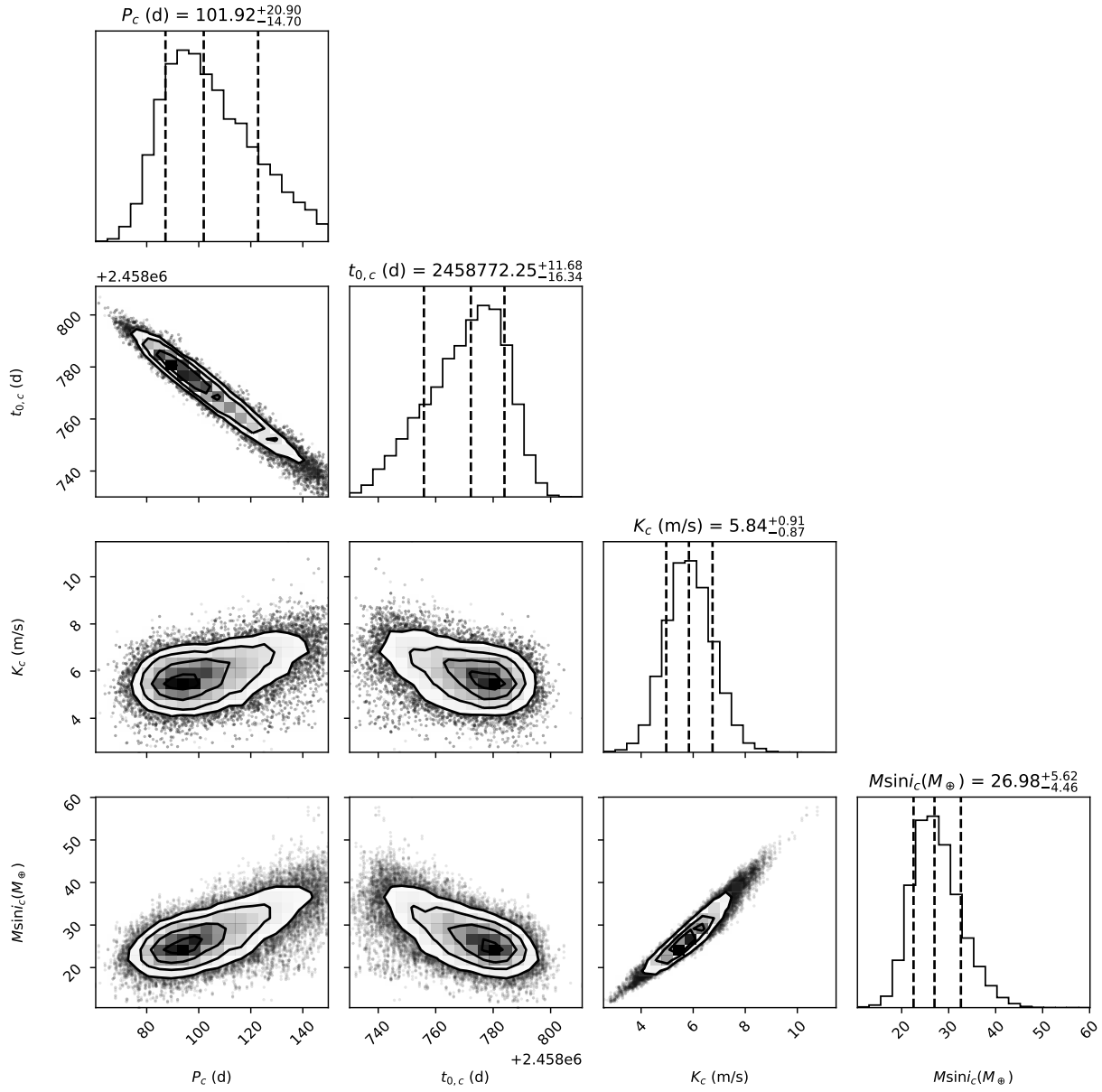

Figure 5.14: Posterior distributions for the long-term signal from the joint fit described in Sect. 5.6.3.

6 AD Leonis: stable radial-velocity variations at the stellar rotation period

The content of this Chapter is based on the soon-to-be submitted work to the A&A journal.

Details of authorship: I am the first author of this paper and led the team effort involving 31 co-authors. I was under the supervision of Prof. Thomas Henning and Martin Kürster. I have done the scientific work, analysis, and reached the conclusions. The stellar parameters were deduced by Andreas Schweitzer. The text was written by me with the contributions of Marina Lafarga in Sect. 6.5.7, José Caballero and Miriam Cortés-Contreras in Sect. 6.1. All figures were produced by me except for Fig. 6.4 by Stephan Stock and Fig. 6.8 by Marina Lafarga. I have circulated the manuscript to all co-authors and received their comments and I incorporated them.

6.1 Motivation

A challenge with radial velocity (RV) data is disentangling the origin of signals between a planetary companion or of stellar activity. Obtaining data over a large time span and wavelength range is crucial but can oftentimes be difficult to achieve. The existence of a planetary companion has been proposed, as well as contested, around the relatively bright, nearby M3.0 V AD Leo at the same period as the stellar rotation of 2.23 d. We further investigate the nature of this signal for the flaring star. We introduce new CARMENES RV data and an analysis in combination with archival data taken by HIRES and HARPS-S, along with newer released data taken by HARPS-N, GIANO-B, and HPF. Additionally, we look into the binarity of AD Leo. We consider all possible correlations that the RVs may have with the stellar activity indicators. We additionally perform a variety of modeling techniques considering all RV data using the Bayesian log-evidence to determine whether a Keplerian planetary model, a red-noise quasi-periodic stellar activity model using a Gaussian Process, or a mixed model would explain the observed data best. In addition, we take a closer look at spectral lines potentially associated with stellar activity. The CARMENES data agree with the expected periodicity of 2.23 d. We conclude however that the signal is attributed solely to stellar activity due to the strong evidence that the RV amplitude decreases with wavelength and there are strong correlations with some of the stellar activity indicators. When considering the RV dataset as a whole, we find that a mixed model composed of a stable and a variable component performs best. Moreover, when recomputing the RVs using only inactive spectral lines, there appears to be some residual power at the period of interest.

We therefore conclude that RVs induced by stellar activity can comprise a stable component. In addition, we disprove a binary companion around AD Leo.

6.2 Context

Representing 75 % of the stars in the solar neighborhood (Henry et al., 2006; Winters et al., 2015), M dwarfs are good targets for radial velocity (RV) surveys given that their star-to-planet mass ratios are lower than for other more massive stars, making it easier to find planetary detections of a given mass. In addition, early- to mid-type M dwarfs are thought to host at least 2.5 planets per star on average (Dressing & Charbonneau, 2015; Hardegree-Ullman et al., 2019), which make them excellent targets for discovering exoplanets. There are a few drawbacks to these promising stars: they can be difficult to observe, considering that they are typically faint objects, and most are known to be quite active, which can introduce additional stellar-activity induced signals to the data.

Modern spectrographs are capable of reaching $\mathrm{m\,s^{-1}}$ level precision or even tens of $\mathrm{cm\,s^{-1}}$ (e.g., ESPRESSO), which is needed in the search for Earth-like planets, but their measurements can then be affected by unwanted signals. Intrinsic stellar variablitiy in the form of dark spots, bright plages, flares, etc., can produce RV variations that mimic planetary signals. These can conceal true planetary signals, or masquerade as a fake planet, which also can be modeled with a Keplerian orbit. To help mitigate these stellar activity induced RV signals, statistical techniques such as Gaussian Process Regression (GP) have been used by treating these effects as a quasi-periodic signal (Haywood et al., 2014; Rajpaul et al., 2015; Jones et al., 2017; Stock et al., 2020a). These signals can be wavelength-dependent, usually with the amplitude decreasing in the redder regime of the spectrum, but still containing some residual effect depending on the star-spot configuration and temperature (Reiners et al., 2010, and references therein).

Focusing on certain spectral lines as activity indicators sensitive to chromospheric (e.g., Hα, Ca II infrared triplet) or photospheric (e.g., TiO) effects on active M dwarfs, proves to be quite successful for determining the star's rotational period (see Fig. 11 in Schöfer et al., 2019). Moreover, efforts for identifying which spectral lines in general (i.e., not focusing on already-known specific lines) seem to be more activity-sensitive than others have been fruitful for a selection of G–K dwarfs (e.g., Dumusque, 2018; Cretignier et al., 2020). Such an approach proves to be rather challenging for M dwarfs, where the spectra contain a forest of lines making it almost impossible to find the continuum (Merrill et al., 1962; Boeshaar, 1976; Kirkpatrick et al., 1991; Alonso-Floriano et al., 2015). This approach, however, seems to have been successful for stars that show a clear variation of RVs with wavelength (e.g., EV Lac).

We turn our attention specifically to the mid-type M dwarf AD Leo, a star whose stellar rotation period of 2.23 d presents itself both in photometry and RVs (Morin et al., 2008; Tuomi et al., 2018; Carleo et al., 2020; Robertson et al., 2020). Despite its strong flaring activity manifest at many wavelengths (Buccino et al., 2007; Rauer et al., 2011; Tofflemire et al., 2012; Vidotto et al., 2013), AD Leo has been included in a number of studies addressing the existence of planets orbiting this star.

Tuomi et al. (2018), referred to as T18 hereinafter, first suggested that a planet may be orbiting AD Leo in a 1:1 spin-orbit resonance since it proved to be difficult to explain

both the photometry and RV measurements simultaneously using a variety of star-spot scenarios. Furthermore, they claimed that the RV measurements were time- and wavelength-independent, and the putative planet exhibited a semi-amplitude of $\sim$19 m s^{-1}. Despite what would normally serve as definite evidence for solely stellar activity behavior, T18 concluded that AD Leo is an active M dwarf hosting a hot Jupiter ($\geq 0.2 M_{Jup}$) in a 1:1 spin-orbit resonance.

This notion of such a hot Jupiter around an M dwarf is unique. Many studies addressing the correlation between the orbital period ($P_{\rm orb}$) and the stellar rotation period ($P_{\rm rot}$) have thus far been focused on more solar-like transiting host stars rather than M dwarfs, using *Kepler* data (Borucki et al., 2010). Findings from McQuillan et al. (2013); Walkowicz & Basri (2013) suggest a clear absence of close-in planets ($P_{\rm orb} \lesssim 3$ days) around rapidly rotating stars ($P_{\rm rot} \lesssim 10$ days), where planets with shorter periods were nearly synchronous ($P_{\rm orb} \sim P_{\rm rot}$). Teitler & Königl (2014) proposed that the cause was tidal ingestion of close-in planets by their host stars. With regards to M dwarfs, Newton et al. (2016) showed that typical stellar rotation periods would often match the periods of planets in their habitable zone. Therefore, finding the key methods to successfully disentangling a hypothetical planetary signal on top of the stellar activity signal could help uncover future planets around M dwarfs in the habitable zone as well as ensure the correct derived planetary parameters.

However, the existence of a hot Jupiter around AD Leo has been challenged. Carleo et al. (2020, referred to as C20 hereinafter) recently investigated the 2.23 d signal and obtained observations with GIARPS at the 3.56 m Telescopio Nazionale Galileo (Claudi et al., 2017). Even though the 2.23 d signal was persistent, the amplitude heavily diminished as a function of wavelength and of time. Simultaneous photometric data from STELLA showed a shift of $\sim$0.25 in phase ($\sim$0.6 d) in comparison to the HARPS-N RV curves. Therefore, C20 disputed the argument posed by T18, concluding that the RV modulation is not compatible with a planetary companion. Shortly after, the conclusions by Robertson et al. (2020), referred to as R20 hereinafter, were also in line with C20, as they likewise observed a decrease in amplitude between the two observing seasons using HPF data.

In this chapter, we first present an independent analysis of CARMENES RV data along with stellar activity indicators. We then combine all available datasets to apply various RV models. In addition, we implement a method to infer stellar activity from an analysis of spectral lines. Aside from the planet debate, the potential binarity of the target is addressed for the first time. We organize the paper as follows. In Sect. 6.3, we introduce the active M dwarf AD Leo. The binarity of AD Leo is discussed and disproven in Sects. 6.3.3 and 6.5.1. Sect. 6.4 presents all available RV data that will be analyzed. In Sect. 6.5, we investigate the data for spectroscopic variability in terms of the time- and wavelength-dependence of the 2.23 d signal as well as correlations with known stellar activity indicators. Finally, in Sects. 6.6 and 6.7, we present a discussion and summary of our results.

6.3 AD Leo

6.3.1 Stellar parameters

AD Leo (GJ 388), an M3.0 V star at a distance of slightly less than 5 pc and with $V \sim$ 9.5 mag, is one of the closest and brightest M dwarfs. Already tabulated in the Bonner

Table 6.1: Stellar parameters of AD Leo.

Parameter	Value	Reference
	Identifiers	
BD	+20 2465	Arg1861
Ci	18 1244	Por1915
GJ	388	Gli1957
Karmn	J10196+198	Cab2016
	Astrometry and kinematics	
α (epoch J2015.5)	10:19:35.72	*Gaia* EDR3
δ (epoch J2015.5)	19:52:11.32	*Gaia* EDR3
$\mu_\alpha \cos\delta$ (mas a^{-1})	–498.62 ± 0.03	*Gaia* EDR3
μ_δ (mas yr^{-1})	–43.43 ± 0.03	*Gaia* EDR3
π (mas)	201.41 ± 0.03	*Gaia* EDR3
d (pc)	4.964 ± 0.001	*Gaia* EDR3
γ (km s^{-1})	12.286 ± 0.021	Laf2020
U (km s^{-1})	-14.929 ± 0.010	This work
V (km s^{-1})	-7.444 ± 0.007	This work
W (km s^{-1})	$+3.391 \pm 0.017$	This work
Galactic population	Young disk	Mon2001
Stellar kinematic group	Castor	LS2010
	Key photometry	2MASS: Cutri et al. (2003); AF2015:
G (mag)	8.2041 ± 0.0015	*Gaia* EDR3
J (mag)	5.449 ± 0.027	2MASS
	Photospheric parameters	
Spectral type	M3.0 V	AF2015
$T_{\rm eff}$ (K)	3308 ± 64	Pas2019
$\log g$ (cgs)	4.93 ± 0.07	Pas2019
[Fe/H] (dex)	-0.13 ± 0.19	Pas2019
	Activity	
$v \sin i$ (km s^{-1})	2.4 ± 1.5	This work
$P_{\rm rot}$ (d)	2.2399 ± 0.0008	Mor2008
pEW(Hα) (Å)	–4.52±0.04	Sch2019
$\log {\rm H}\alpha / L_{\rm bol}$	–3.614±0.003	Sch2019
$\log R'_{\rm HK}$	–4.33±0.01	Hoj2019
$\log L_{\rm X} / L_{\rm bol}$	–3.18	Mor2008
	Physical parameters	
$L_\star$ ($10^{-5}\,L_\odot$)	2341 ± 35	Cif2020
$R_\star$ ($R_\odot$)	0.466 ± 0.018	This work
$M_\star$ ($M_\odot$)	0.467 ± 0.022	This work
i (deg)	$12.9^{+8.4}_{-8.1}$	This work

Alonso-Floriano et al. (2015); Arg1861: Argelander (1860); Cab2016: Caballero et al. (2016b); Cif2020: Cifuentes et al. (2020); *Gaia* EDR3: Gaia Collaboration et al. (2020); Gli1957: Gliese (1957); Hoj2019: Hojjatpanah et al. (2019); Laf2020: Lafarga et al. (2020); LS2010: López-Santiago et al. (2010); Mon2001: Montes et al. (2001); Mor2008: Morin et al. (2008); Pas2019: Passegger et al. (2019); Por1915: Porter et al. (1915); Sch2019: Schöfer et al. (2019).

Sternverzeichnis by Argelander (1860), AD Leo has been the subject of numerous investigations in the last century (e.g., Abell, 1959; Engelkemeir, 1959; Lang et al., 1983; Saar & Linsky, 1985; Hawley & Pettersen, 1991; Hawley et al., 2003; Osten & Bastian, 2008; Hunt-Walker et al., 2012).

In Table 6.1, we list the most recent, and believed to be most precise, parameters of AD Leo. In particular, we tabulate equatorial coordinates, proper motions, and parallax from the *Gaia* Early Data Release 3 (Gaia Collaboration et al., 2020) and absolute RV from Lafarga et al. (2020, uncorrected of gravitational redshift for consistency with the previous literature), from which we re-compute Galactocentric space velocities as in Cortés-Contreras (2016). The spectral type of Alonso-Floriano et al. (2015) superseded previous determinations (e.g., Johnson & Morgan, 1953; Bidelman, 1985; Stephenson, 1986; Keenan & McNeil, 1989), while the photosphere parameters of Passegger et al. (2019) match previous CARMENES publications and are similar, but not identical, to those of Rojas-Ayala et al. (2012), Lépine et al. (2013), Gaidos et al. (2014), or Mann et al. (2015). With the effective temperature of Passegger et al. (2019), the bolometric luminosity of Cifuentes et al. (2020), and the Stefan-Boltzmann law we derived the stellar radius and, with the radius-mass relation of Schweitzer et al. (2019), the stellar mass. For compiling the most precise parameters of the activity indicators, we used the `SVO Discovery Tool`[45]. The rotational velocity was computed by us exactly as in Reiners et al. (2018), but on the newest CARMENES template spectra (Sect. 6.4).

As first reported by Montes et al. (2001), the Galactocentric space velocity of AD Leo is consistent with it belonging to the Galactic young disk (Leggett, 1992). Later, López-Santiago et al. (2010) and Klutsch et al. (2014) proposed AD Leo as a candidate member of the Castor moving group, in agreement with our latest kinematic data. The age of the Castor moving group, of about 300–500 Ma (Barrado y Navascués, 1998; Mamajek et al., 2013), is consistent with age determinations for AD Leo by Shkolnik et al. (2009), Brandt et al. (2014), and Meshkat et al. (2017).

Such a young age partly explains the flares frequently observed in AD Leo. The star has been known to exhibit activity ever since the first observed optical flare event in 1949 (Gordon & Kron, 1949), followed by many others (e.g., Liller, 1952; MacConnell, 1968; Pettersen et al., 1984; Crespo-Chacón et al., 2006)[46]. Later on, emission in the X-ray and radio regimes has also been observed (Gurzadyan, 1971; Robinson et al., 1976). Muheki et al. (2020) and Namekata et al. (2020) have presented the most recent analyses on high-resolution optical spectroscopy and X-ray observations of flares and coronal mass ejections on AD Leo.

The young age of AD Leo also explains the moderately large rotational velocity and short rotational period, of 2.24 d, as well as X-ray, Ca II H&K, and Hα emission (see references in Table 6.1). In addition, this star presents large RV variations: it shows a standard deviation larger than $20\,\mathrm{m\,s^{-1}}$, ($\sim 1.5\times$ median absolute deviation RV as in Tal-Or et al. (2019) and Grandjean et al. (2020)), which can be connected to stellar activity, the presence of a planetary companion, or both. We compute the stellar inclination, i, to be $\sim 13°$ from 10^6 MCMC realizations using $v \sin i$, R, and P_{rot} as provided in the stellar parameters table.

[45] `http://sdc.cab.inta-csic.es/SVODiscoveryTool/`

[46] Of the 70 reports of the IAU Information Bulletin on Variable Stars citing AD Leo, only 18 did not have the star name in the title.

Previous papers quoted values of $\sim 20°$ (Morin et al., 2008) and $\sim 15°$ (Tuomi et al., 2018).

6.3.2 Photometry

T18 took a closer look at the available photometry from ASAS-North and ASAS-South, as well as from short-cadence *MOST* observations (see T18 for photometry references). As a recap, the ASAS photometry shows a long-term periodicity of around 4,070 d, most likely due to a long-term stellar activity cycle. During the brightness minimum of this cycle, the signal at the rotation period of 2.23 d seems to disappear turning up only during the brightness maximum, in which the *MOST* observations were taken. These short-cadence *MOST* data, taken over the course of 9 d (Hunt-Walker et al., 2012), showed fluctuations with periodicity 2.23 d, but also demonstrated behavior of slight phase shifts and amplitude and period variations, indicating that the stellar surface should be experiencing rapid evolution. Other observations taken with different instruments are in agreement with the 2.23 d period (2.2399 d and 2.237 d provided by Morin et al., 2008; Carleo et al., 2020, respectively).

AD Leo has not been and will not be observed in any of the currently planned *TESS* sectors[47]

6.3.3 Hypothetical binary

There is some confusion in the literature regarding the hypothetical multiplicity of AD Leo. First of all, in spite of being listed as "γ Leo C" in some astronomical databases (e.g., SIMBAD), AD Leo is not a wide ($\rho \sim 5.7$ arcmin) physical companion to Algieba, which is a binary system of two G- and K-type giant stars visible to the naked-eye located eight times further (γ^{01} Leo + γ^{02} Leo; van Leeuwen, 2007; Gaia Collaboration et al., 2020).

Next, the Washington Double Star catalogue (WDS; Mason et al., 2001) tabulates AD Leo as a close binary candidate. The presence of a hypothetical companion around AD Leo was first inferred by Reuyl (1943) from measurements of photographic plate images. He suggested an eccentric ($e = 0.6$) and close-in ($a \sim 0.54$ AU, projected angular separation of $\rho \sim 0.11$ arcsec) orbit with an orbital period of 26.5 years, making the companion a brown dwarf ($M \approx 0.032 M_{\odot}$). Later, van de Kamp & Lippincott (1949) found indications of an astrometric trend from photographic plates that did not fit those orbital elements. Following up two decades later, Lippincott (1969) found an ambiguous deviation from linear proper motion, thus deciding that it was inconclusive to determine whether there could be a variable proper motion due to a companion.

With speckle imaging at 7800 Å at the 3.6 m Canada-France-Hawai'i Telescope, Balega et al. (1984) resolved a companion candidate to AD Leo at $\rho = 0.078 \pm 0.010$ arcsec ($r \approx 0.39$ AU) and position angle of $\theta = 39 \pm 4$ deg in 1981, which received the WDS name 10200+1950 and discoverer code BAG 32. Two additional measurements in 1983 were provided by Balega & Balega (1985) at $\rho \sim 0.11$ arcsec, but with $\theta \sim 330$ deg. Afterwards, with lucky imaging in the I band at the 1.5 m Telescopio Carlos Sánchez, Cortés-Contreras et al. (2017) resolved a candidate source, about 2.0 mag fainter than AD Leo, at $\rho = 0.195 \pm 0.061$ arcsec ($r \approx 0.97$ AU) and $\theta = 23.8 \pm 3.7$ deg in 2012. However, it fell on the

[47] *TESS* Web Viewing Tool: `https://heasarc.gsfc.nasa.gov/cgi-bin/tess/webtess/wtv.py` Accessed 4 August 2020.

first Airy disk, and they were not able to detect it again in observations in 2015 with the same instrument setup. From $\Delta I \approx 2.0$ mag and the projected physical separation of about 0.97 AU, Cortés-Contreras et al. (2017) estimated an m5 V spectral type for the companion candidate and an orbital period of $P \sim 1.5$ a, which might be the source discovered by Balega et al. (1984). Because of this hypothetical companion, AD Leo was initially discarded from the CARMENES guaranteed time observation target list (Caballero et al., 2016b; Reiners et al., 2018), but it was added later.

Further attempts at resolving the companion proved to be unsuccessful, such as *Hubble Space Telescope* imaging taken in 2005, or additional speckle imaging by Docobo et al. (2006). With adaptive optics at 8 m-class telescopes, Daemgen et al. (2007) and Brandt et al. (2014) imposed very strict upper limits to the presence of companions, of $\Delta K_s \sim 7.8$ mag at $\rho \geq 0.5$ arcsec and $\Delta H \sim 10.9$ mag at $\rho \geq 1.5$ arcsec, respectively. From Fig. 7 in Daemgen et al. (2007), their Altair/Gemini North observations discarded any companion of $\Delta Ks \sim 2.0$ mag at $\rho \geq 0.1$ arcsec and, therefore, refuted the findings of Balega et al. (1984), Balega & Balega (1985), and Cortés-Contreras et al. (2017). The absence of any close companion to AD Leo is further addressed with our spectroscopic data in Sect. 6.5.1. The binary issue was not addressed in T18, C20, or R20.

6.4 Spectroscopic data

The Doppler data that are used in our analysis are described below. All data and spectrograph descriptions are summarized in Table 6.2. Fig. 6.1 displays all RVs used in this analysis, along with the GLS periodograms (Zechmeister & Kürster, 2009) of the data in Fig. 6.2.

Table 6.2: Summary of spectroscopic data for AD Leo[a].

Instrument	Subsets	$\Delta\lambda$ (nm)	R	# of spectra	Obs. start–Obs. end
CARMENES VIS	VIS1+VIS2	520–960	94 600	46 (26+20)	March – April 2018, Feb 2020
CARMENES NIR	NIR1+NIR2	960–1710	80 400	46 (26+20)	March – April 2018, Feb 2020
HIRES	...	500-620	60 000	43	Jun 2001 – Dec 2013
HARPS-S	...	380–690	115 000	47	Dec 2003 – May 2014
HARPS-N	HT1+HT2	390–680	115 000	63 (42+21)	April – June 2018, Nov 2018 – Jan 2019
GIANO-B	G1+G2	970–2450	50 000	25 (12+13)	April – May 2018, May – June 2018
HPF	HPF1+HPF2	810–1280	55 000	35 (5+30)	April 2018, Dec 2018 – Feb 2020

aAll instruments used for the analysis along with their wavelength range, spectral resolution, and number of spectra.
The information in parentheses is in accordance to the subset e.g., VIS1 has 26 spectra, whereas VIS2 has 20.

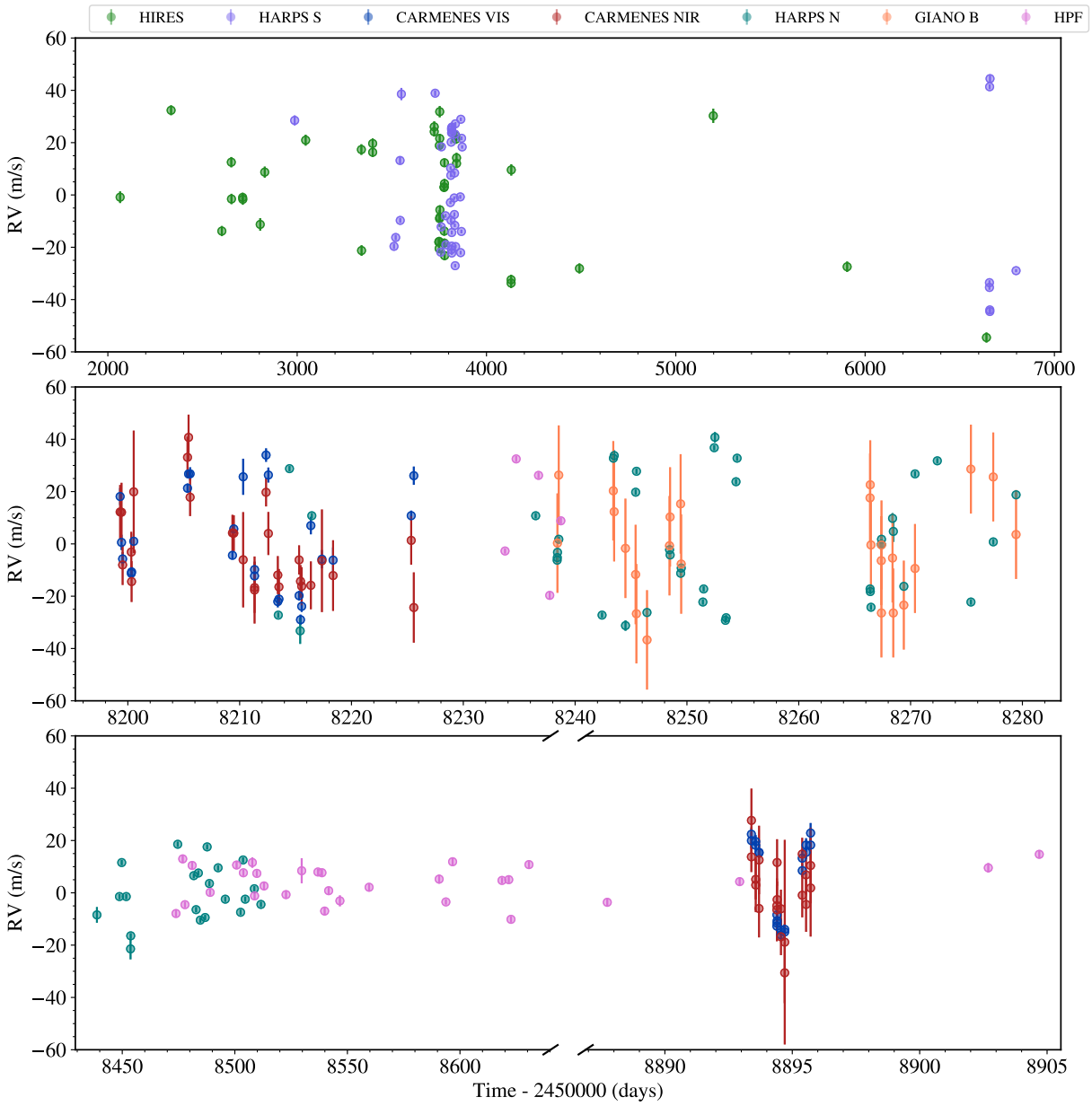

Figure 6.1: Time series of all RVs with instrumental offsets accounted for. The HIRES and HARPS-S data span a large time range and the rest of the data come in ∼12 years later after the time when the majority of the previous data were taken. The time axis is interrupted in several places, and stretched differently between the individiual sections. Additionally, the majority of HIRES and HARPS-S time series are overlapping each other. Four of the HARPS-N data overlap with CARMENES data; and the GIANO-B data are taken all within the first observing run for HARPS-N. The first season of HPF data overlaps with the HARPS-N and GIANO-B datasets whereas the HPF second season overlaps with the HARPS-N and CARMENES second season.

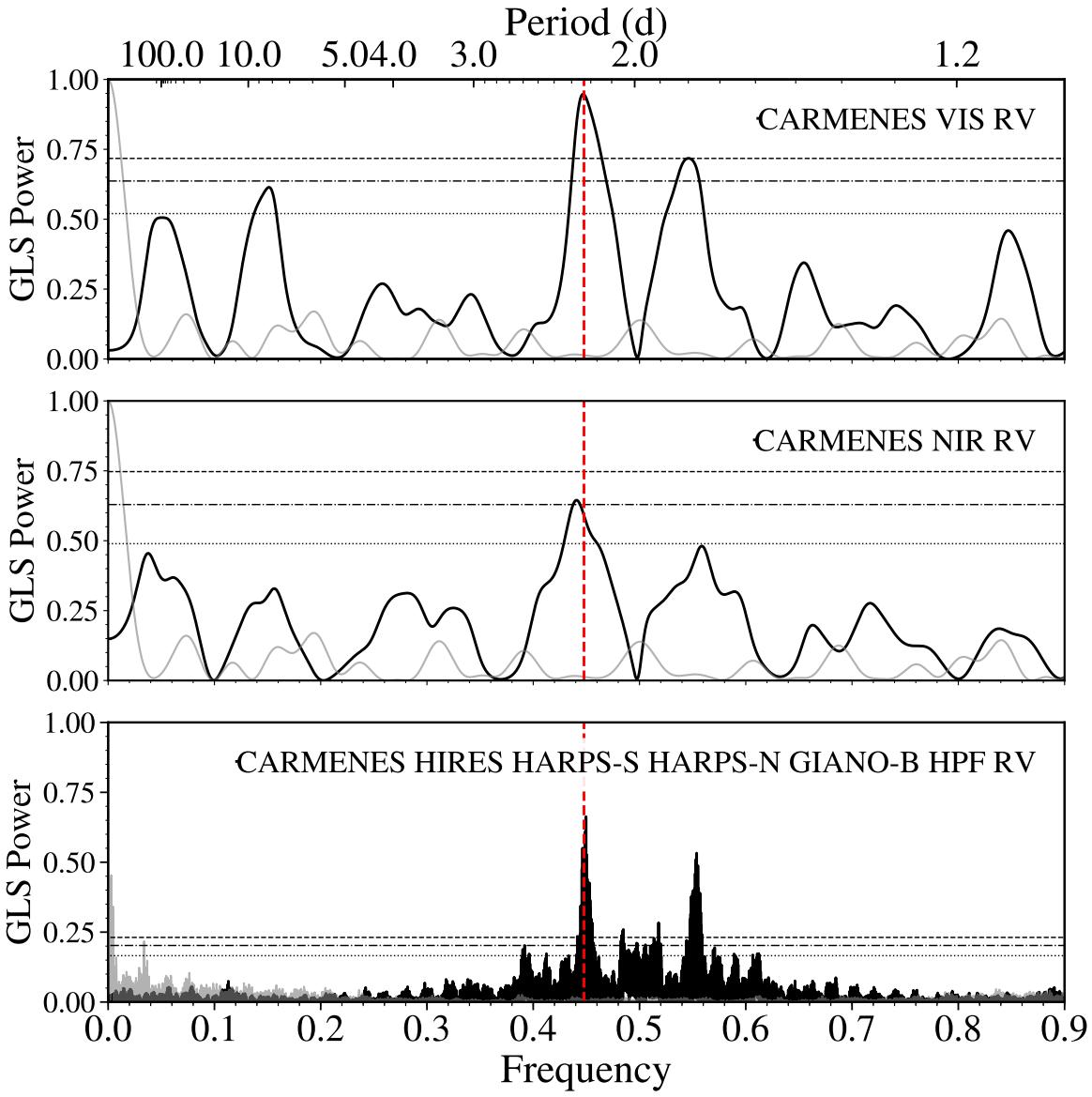

Figure 6.2: GLS periodograms for the CARMENES VIS and NIR RV datasets from season 1 only (top and middle). We then consider all data points from all instruments (CARMENES VIS, CARMENES NIR, HARPS-S, HIRES, HARPS-N, GIANO-B, and HPF) together where the offsets are accounted for (bottom panel). The red vertical dashed line corresponds to a period of 2.23 d and the grey lines correspond to the window function, i.e., the sampling of data points. The horizontal lines correspond to FAP levels of 10% (dotted), 1% (dash-dotted), and 0.1% (dashed). These are computed by using the randomization technique for 10 000 samples.

6.4.1 CARMENES

The CARMENES[48] instrument is located at the 3.5 m telescope at the Calar Alto Observatory in Spain. It is a dual arm instrument to produce RV measurements at optical (VIS) and near-infrared (NIR) wavelengths (Quirrenbach et al., 2014, 2018, see Table 6.2 for the instrument specifications).

We obtained 26 spectra for AD Leo (Karmn J10196+198) over the time span of 25 days from 21 March 2018 to 16 April 2018, notably 12 years after the majority of the HIRES and HARPS-S data were taken. On some nights, we observed AD Leo multiple times for sampling better the short period of 2.23 d. We call this subset of data VIS1 and NIR1 since AD Leo was observed again later in February 2020 as part of a DDT program, for which 20 data points were obtained over ∼3 d, which we call subset VIS2 and NIR2. The RVs from both subsets were first extracted with `serval` (Zechmeister et al., 2018), so that they are corrected for barycentric motion, secular acceleration, and instrumental drift. The final RVs we use had nightly zero-points applied (Tal-Or et al., 2019; Trifonov et al., 2020). Fig. 6.3 displays a closer look at solely the first subset CARMENES data and the best respective models (a more in-depth description is provided in the modeling Sect. 6.5.6).

6.4.2 HARPS-South

Spectroscopic data for AD Leo are in the public archive from the High-Accuracy Radial velocity Planet Searcher (HARPS, Mayor et al., 2003), a high-resolution échelle spectrograph located at the ESO 3.6 m telescope at La Silla Observatory in Chile. We found a total of 52 spectra that were taken over a span of ∼4 500 d (from 12 December 2003 to 4 April 2016). Due to a fiber-upgrade intervention (Lo Curto et al., 2015), we considered the HARPS-S data as coming from two separate instruments, before and after this upgrade. After the intervention, only five data points were taken close to one another (within 2 d); there data have a very low root-mean-square (RMS) deviation from their mean. We did not consider them for the further analysis since they could fit anywhere in a model with a large offset and therefore do not provide new insight. Thus, for the rest of the analysis, we used the 47 HARPS-S spectra from before the intervention. Additionally, the majority of data (i.e., 33 points) were taken over the course of ∼115 d (January–May 2006). The spectra were first processed using `serval` (Zechmeister et al., 2018) to obtain helpful stellar activity indicators (e.g., CRX, dLW, Hα, see Zechmeister et al., 2018, for more explanation). We then analyzed the nightly zero point corrected RVs provided by Trifonov et al. (2020).

6.4.3 HIRES

We have 43 spectra from the high-resolution spectrograph HIRES (Vogt et al., 1994) mounted on the 10 m Keck-I telescope located at the Mauna Kea Observatory in Hawai'i, which has been in service since 1994. The data were taken over the course of 4 500 days (from June 2001 to December 2013). A majority of them (i.e., 22 points) were taken in 2005/2006 over 120 d and, moreover, overlap with the higher cadence HARPS-S data (see Fig. 6.1). Butler et al.

[48]Calar Alto high-Resolution search for M dwarfs with Exo-earths with Near-infrared and optical Échelle Spectrographs, `http://carmenes.caha.es`

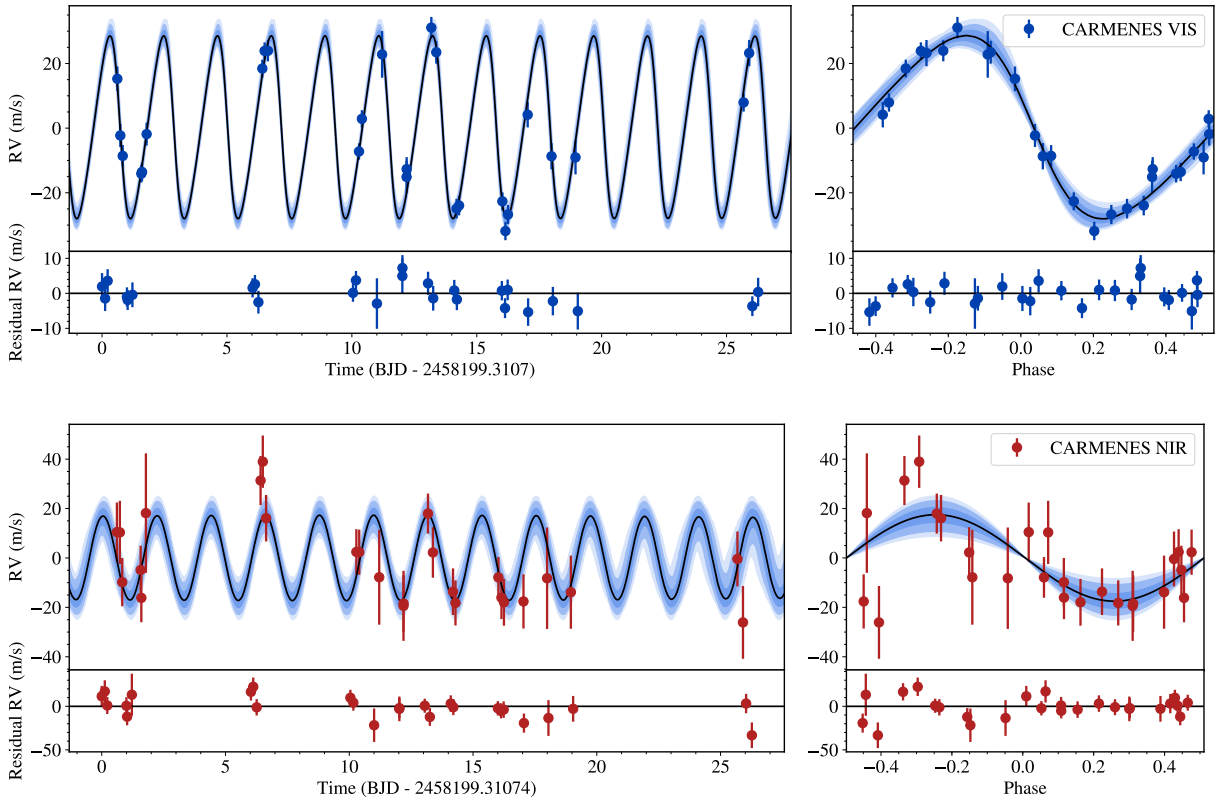

Figure 6.3: Radial velocity times series along with phase-folded plots for the CARMENES data (*top*: VIS, *bottom*: NIR) with residuals from the best-fit model. The best-fit models are overplotted (black line) along with the 68%, 95%, and 99% posterior bands (blue shaded regions). The jitter terms of $2.1\,\mathrm{m\,s^{-1}}$ and $6.0\,\mathrm{m\,s^{-1}}$ for VIS and NIR, respectively, are added in quadrature to the formal errors. We note the difference in the RV y-axis ranges as well as the amplitude difference, $28.3\,\mathrm{m\,s^{-1}}$ and $17.5\,\mathrm{m\,s^{-1}}$ for VIS and NIR, respectively.

(2017) released a large RV database of 64 480 observations for a sample of 1 699 stars, which was later re-analyzed by Tal-Or et al. (2019) for minor though significant systematic effects such as an RV offset due to the CCD upgrade in 2004, long-term drifts, and slight intra-night drifts. Therefore, we continued with the corrected HIRES RVs provided by Tal-Or et al. (2019). Data from HIRES are also specifically addressed further under Sect. 6.5.5.

6.4.4 Additional data from the literature

GIARPS. For our analysis, we directly take the data provided by Carleo et al. (2020), hereafter C20. These spectroscopic data are taken in GIARPS mode (Claudi et al., 2017), where high resolution spectroscopic measurements are taken simultaneously with HARPS-N (Cosentino et al., 2012, extracted with the TERRA pipeline) and with GIANO-B (Oliva et al., 2006) reduced with the on-line DRS pipeline and the off-line GOFIO pipeline. Both instruments are located at the 3.58 m Telescopio Nazionale Galileo (TNG) at the Roque de los Muchachos Observatory in La Palma, Spain. The GIARPS mode is similar to CARMENES in the sense it also addresses potential variations of a signal amplitude over a wide wavelength

range. There were two runs of HARPS-N, with only the first run having simultaneous GIANO-B data; four of the HARPS-N data overlap with the CARMENES data. To stay consistent with C20, we also consider two separate runs for HARPS-N and GIANO-B, and designate them as HT1, HT2, G1, and G2 for our analysis.

HPF. Our last dataset comes from the Habitable-zone Planet Finder (HPF), a stable NIR Doppler spectrograph that is designed to reach $1-3\,\mathrm{m\,s^{-1}}$ RV precision for M dwarfs with the help of wavelength calibration via a custom NIR laser frequency comb (Mahadevan et al., 2012, 2014). The spectrograph is installed at the 10 m Hobby-Eberly Telescope at McDonald Observatory in Texas. The HPF data are of high quality providing an RV precision of $1.5\,\mathrm{m\,s^{-1}}$ on AD Leo. A total of 35 HPF RVs were obtained, 5 of which during HPF commissioning and 30 afterwards, namely HPF1 and HPF2. The HPF data in this paper are tabulated in Robertson et al. (2020), hereafter R20. These data overlap with optical RV data from HARPS-N and show also an amplitude decrease between observing seasons.

6.5 Analysis and results

6.5.1 Stellar binarity

As a first approach to search to address the potential stellar binarity and look for traces of it, we combined all the RV data to look for long-term trends. However, this method presents its challenges as there is no temporal overlap between the various datasets and each has its own, unknown zero-point offset. We nonetheless attempted a grid search for a Keplerian signal for which we stepped through the period, amplitude, eccentricity and omega parameter space, where each instrument also had its own offset and jitter term (see Sect. 3.3.2). One then adapts the values with the best log likelihood. Unfortunately, the lack of temporal overlap led to strong ambiguities and degeneracies. We therefore did not find any conclusive periodicity in this RV analysis.

We continued to investigate whether there is evidence for the presence of a companion within our CARMENES spectra that could affect the analysis presented later in this work. We computed a 1D cross-correlation function (CCF) with a binary mask over a large RV range and did not find any hint of a clear secondary peak, neither in the VIS nor the NIR data. To be certain, we also ran `todcor` (Zucker & Mazeh, 1994), which computes a 2D CCF to get the RVs of the two components simultaneously, and the results showed no evidence for a companion as well. The 2D CCF method with `todcor` is the appropriate approach to follow in the case of double-lined binaries, but since the secondary signal seems to be either too weak if expected to be $\sim$10 $\mathrm{km\,s^{-1}}$ away from the primary, or too hidden if expected to be very close to the primary, we concluded that no secondary heavily distorts the CCF profile and, therefore, would not cause any noticeable effects on the CCF parameter values (see Sect. 6.5.4). We therefore conclude that there is no evidence for a stellar binary companion of AD Leo.

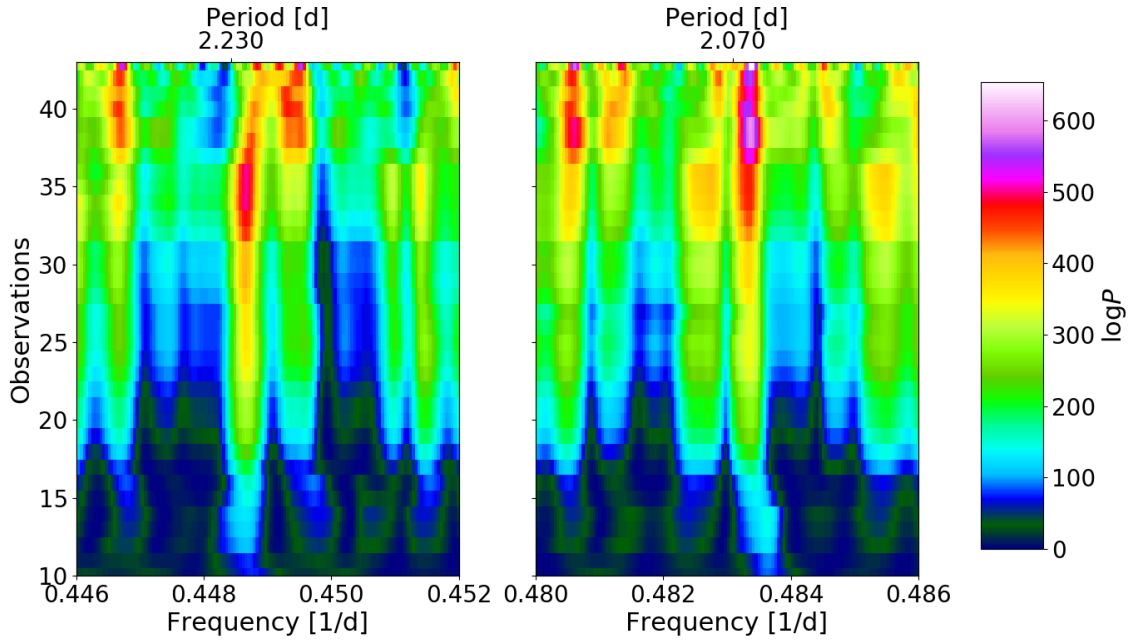

Figure 6.4: S-BGLS periodograms of the HIRES data of AD Leo, zoomed into two frequency ranges (left, 2.23 d, and right, 2.07 d) for the HIRES data. The nominal value $\log P$ does not carry significance, rather the relative values of $\log P$ are of importance.

6.5.2 Aliasing in HIRES data

The periodogram of the HIRES dataset as a whole exhibits the strongest peak at 2.07 d. instead of at 2.23 d (see Fig. 6.4). This can be understood as the window function has a peak at 1 month, i.e., 29.53 d; 2.07 d and 2.23 d are thus an alias pair with respect to this period. As in Dawson & Fabrycky (2010); Stock et al. (2020a), a de-aliasing approach using the `AliasFinder` (Stock & Kemmer, 2020) was performed. However, probably due to the underlying signal may not be a simple sinusoid, but rather a quasi-periodic signal with varying amplitudes and phase-shifts, the results were not fully conclusive. To further investigate, we performed a stacked Bayesian GLS (s-BGLS) periodogram (see Fig. 6.4) where the stacking enables us to determine the coherence of a signal with increasing number of observations (Mortier et al., 2015; Mortier & Collier Cameron, 2017). As Mortier & Collier Cameron (2017), we normalized all s-BGLS periodograms to their respective minimum values, with the minimum probability set to 1. We found that until about 35 data points, which corresponds to the start of the sparse data, the 2.23 d signal seems to be the most prominent. Afterwards, the alias at 2.07 d gains significance. This behavior is in accordance to what we expect from an unstable, incoherent signal: when one signal loses significance, another one gains it (as also demonstrated Mortier & Collier Cameron, 2017, with the Sun as an example). We conclude that the HIRES data are fully consistent with an RV modulation with a 2.23 d period.

6.5.3 Spectroscopic variability

A true planetary signal should have an amplitude and phase that are constant both in time and as a function of wavelength. Unfortunately, they can be mimicked and mistaken by spots co-rotating on the stellar surface.

To aid in disentangling the origin of the signal, stellar activity indicators, such as photometric variability, bisector inverse slope (BIS, the measurement of asymmetry of the CCF), CaII IRT (8498, 8542, 8662 Å), Hα (6562.8 Å), log$R^{'}_{HK}$, chromatic index (CRX), differential line width (dLW), have been shown to be successful in identifying and indicating a non-planetary signal. In addition, we also consider the pseudo-equivalent widths (pEW) of various potential stellar activity lines (such as CaII IRT, Hα, NaD lines (5897.56 Å and 5891.58 Å), Fe I 8691 Å, and HeD3 (5877.25 Å)) as described in Schöfer et al. (2019), where correlations and periodograms can be found in Appendix 6.8.2. In the literature, periodic RV signals are often considered planetary in nature if the same signal is not found in activity indicators. However, it is possible that the RV signal is found in some indicators, but not others. Therefore it is important to examine as many activity indicators as possible.

Covering a wider and redder wavelength range is an advantage of the CARMENES instrument, because it has been found that signals in RV measurements induced by stellar activity are expected to be more pronounced in the bluer wavelength regime (e.g., Desort et al., 2007; Reiners et al., 2010; Mahmud et al., 2011; Sarkis et al., 2018).

6.5.4 Wavelength dependence of RV signal

Chromatic index. A planetary signal should be wavelength-independent. The chromatic index (CRX), calculated by `serval`, is a photospheric activity indicator that measures the RV-log λ correlation where a straight line is fit to the values computed from individual échelle orders) as a function of log λ (Zechmeister et al., 2018; Tal-Or et al., 2018). The CRX acts as a measure of wavelength dependence as predicted by cool spots on the surface of M dwarfs. However, without further modeling, it does not provide any insight as to how large the spot coverage fraction is or what the star-spot temperature contrast may be. Fig. 6.5 presents the RV-CRX correlation for HARPS-S, CARMENES VIS, and CARMENES NIR; in which the CARMENES VIS shows a clear anti-correlation indicating chromatic dependency and HARPS-S surprisingly demonstrates a positive correlation. Given these strong correlations, stellar activity is unquestionably affecting the RVs.

Wavelength chunks. The CARMENES VIS channel has 55 RV orders, 42 of which are considered when computing the RV measurement via a weighted mean (Zechmeister et al., 2018). Likewise, these orders can be separated into four wavelength chunks, where each chunk consists of 10 (or 11) orders in order to preserve some precision, and the RVs are then recomputed for each respective wavelength coverage. Similarly, the CARMENES NIR channel has 28 RV orders over the Y, J, and H photometric bands. Due to telluric contamination, especially in the J band, only a selected few orders are considered (Bauer et al., 2020). We then use two wavelength chunks, one for the Y and another for the H band, consisting of 12 and 7 individual orders, respectively.

Each wavelength chunk is treated as an individual dataset. We fit a simple sinusoid (i.e., circular Keplerian model) to obtain K, the semi-amplitude of the signal and 1-σ errors.

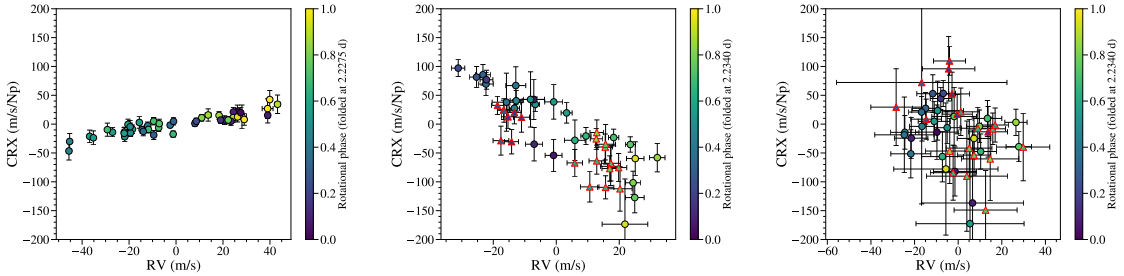

Figure 6.5: RV-CRX correlation plots for HARPS-S, CARMENES VIS, and CARMENES NIR from left to right. The RV are corrected for respective instrumental offsets and the colors indicate the rotational phase where 0.0 indicates the time of highest RV value and the phase-folded period is obtained individually for each instrument from the best Keplerian model fit. The CARMENES season two data are identified as triangles with red outlines.

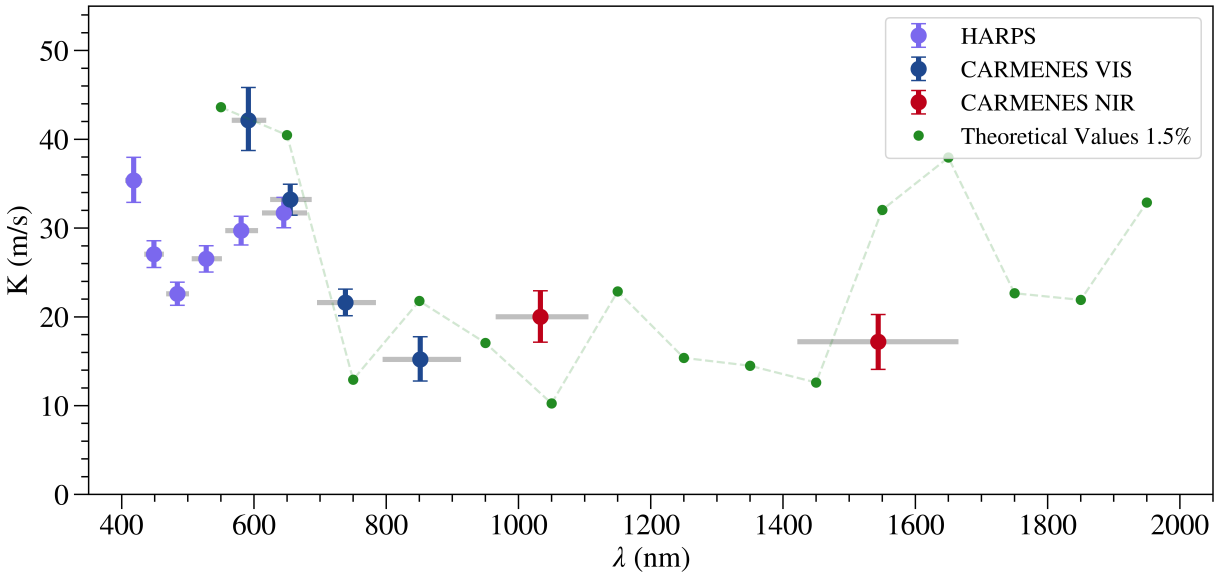

Figure 6.6: Plot of RV semi-amplitudes as a function of wavelength for the wavelength chunks from HARPS and the CARMENES VIS and NIR spectographs. The gray horizontal lines for each data point correspond to the wavelength coverage considered when computing the RV for the wavelength chunk. The green dots connected by a dashed line represent the theoretical values of a 1.5% spot coverage on a 3700 K, $v \sin i$ of $5\,\mathrm{km\,s^{-1}}$ star with a temperature difference of 200 K taken from Reiners et al. (2010). The theoretical values are binned in 2 to serve as a better comparison to the wavelength bins provided by the real data.

When doing this, the semi-amplitude clearly decreases with increasing wavelength in the VIS, but then reaches a plateau when continuing in the NIR (Fig. 6.6). This behavior of decreasing but then constant RV semi-amplitude is in agreement with Reiners et al. (2010) for a spot on the surface of an M dwarf; specifically, a spot covering 1.5% of the projected surface, with a temperature 200 K cooler than the star (assumed $T_{\mathrm{eff}} = 3700$ K), and a stellar $v \sin i$ of $5\,\mathrm{km\,s^{-1}}$, in line with AD Leo's stellar parameters (Table 6.1). Simulations show a linear relation between spot coverage and RV semi-amplitude for low spot coverage values.

A large spot-star temperature difference ($T_{spot} = \frac{2}{3}T_{\rm eff}$), in comparison, would not cause a notable semi-amplitude dependency as a function of wavelength; however, it is not likely for cooler stars, such as AD Leo, to have large spot-star temperature differences (Bauer et al., 2018).

Likewise, the HARPS-S instrument covers 72 spectral orders, of which 61 produce reliable RVs after being processed by `serval` (signal-to-noise is too low for the others). Similarly, we computed 6 wavelength chunks with 10 spectral orders each (11 for the reddest chunk) and followed the same methodology as for the CARMENES wavelength chunks. Reiners et al. (2013) and T18 performed similar analyses but differed in interpretation, where T18 suggested there is no dependence on wavelength, whereas Reiners et al. (2013) claimed otherwise and mentioned that this is the first case of a known active star with increasing amplitude with wavelength. Here, we find a slight positive incline, which is plotted for comparison to the CARMENES data in Fig. 6.6. The positive slope can be interpreted as being due to the Zeeman effect, which has the opposite effect compared to a spot-temperature difference where the RV amplitude is predicted to increase for redder wavelengths (Reiners et al., 2013).

For the overlapping wavelengths, the amplitudes of the wavelength chunks do not particularly agree which can simply be an artifact that HARPS-S data were were not taken contemporaneously to our our data and the signal underwent some amplitude variations.

6.5.5 Other activity indicators

Other activity indicators at our disposal include BIS and various emission lines. The BIS, taken from the CCF, acts as a measurement of the spectral line asymmetry where an anti-correlation demonstrates activity-induced RV modulations. Queloz et al. (2001a) first investigated this anti-correlation in-depth for which the RV signal created is due to a photospheric spot.

For calculating the CCF parameters within CARMENES, weighted binary masks, which depend on spectral type and $v \sin i$, are produced by coadding spectra corrected for tellurics & RV shifts and then selecting pronounced minima (Lafarga et al., 2020). From there, the CCF parameters, BIS, Contrast, and full-width half-maximum (FWHM), are obtained for both the VIS and NIR channel. Fig. 6.10 shows the various correlations with the RVs. The BIS-RV anti-correlation for the VIS channel is in line with the same anti-correlation found by C20 in the HARPS-N data.

Additionally, we look at the dLW (we refer to Zechmeister et al., 2018, for a more in-depth description). However, in our case, there seems to be no correlation (see Fig. 6.11). Along with the dLW, other expected stellar activity indicators such as the emission of Hα (Kürster et al., 2003; Hatzes et al., 2015; Hatzes, 2016; Jeffers et al., 2018; Barnes et al., 2014) and the CaII IRT (Gomes da Silva et al., 2011; Martin et al., 2017; Robertson et al., 2015, 2016) seem to not show peaks at 2.23 d in periodograms (Fig. 6.9).

6.5.6 Time dependence of the RV signal

We are limited by the sampling of our observations as it is difficult to take continuous ground-based RVs over the course of a long time baseline (and sometimes even with years of data

a phase-shift may suddenly appear as demonstrated in example of evolved K giants, Hatzes et al., 2018; Reichert et al., 2019). We subsequently suffer from missing key information as to what occurs in large data gaps — as is the case between the majority of the HIRES, HARPS-S data and CARMENES, GIARPS, HPF data for AD Leo being 12 years apart. Remarkably, the 2.23 d signal persisted over all this time and the semi-amplitudes of the signal between the older archival data (i.e., HARPS-S and HIRES) and CARMENES VIS channel data are within one sigma of each other. However, it is evident that amplitude changes and phase-shifts occurred.

Modeling: Keplerian versus stellar activity. The RV data can be modeled by two components: a stable component (in amplitude, period, and phase) and a variable component. The former is described by a deterministic model, e.g., a circular or eccentric Keplerian orbit. We would like to emphasize that when we use a Keplerian model, we consider it more as a "stable model". Therefore, parameters that are typically called $P_{\rm planet}$ and $K_{\rm planet}$ to represent the period and semi-amplitude of the Keplerian signal will be rather named $P_{\rm stable}$ and $K_{\rm stable}$ to indicate that we are considering a "stable mode"[49] that appears persistent. We use a non-parametric GP model to describe the quasi-periodic behavior of the RV signals due to the star. The kernel we employ is an exponential-squared-sine-squared kernel, i.e., quasi-periodic (QP-GP) kernel, provided by `george` (Ambikasaran et al., 2015),

$$k_{i,j}(\tau) = \sigma_{\rm GP}^2 \exp\left(-\alpha_{\rm GP}\tau^2 - \Gamma_{\rm GP}\sin^2\left(\frac{\pi\tau}{P_{\rm GP,rot}}\right)\right) \tag{6.1}$$

where $\tau = |t_i - t_j|$ is temporal distance between two points, $\sigma_{\rm GP}$ is the amplitude of the GP modulation, $\alpha_{\rm GP}$ is the inverse length-scale of the GP exponential component, $P_{\rm GP,rot}$ corresponds to the recurrence timescale, and $\Gamma_{\rm GP}$ is the smoothing parameter. The former term is an exponential that can model the decorrelation due to the changes in phase and amplitude as active regions grow and decay over time, whereas the latter term accounts for the reoccuring periodicity.

We use the model-fitting python package, `juliet` (Espinoza et al., 2019a) in order to compare a Keplerian versus a GP model on the various RV datasets. For our purposes, the RVs are modeled by `radvel` (Fulton et al., 2018) and the GP models with the help of `george` (Ambikasaran et al., 2015) where we use the `dynesty` package (Speagle & Barbary, 2018; Speagle, 2020) to execute the Nested Sampling algorithm in order to efficiently computes the Bayesian model log-evidence, $\ln \mathcal{Z}$.

The main motivation for calculating the Bayesian log-evidence ($\ln \mathcal{Z}$) is to perform model comparisons. Outlined by Trotta (2008), we follow the rule of thumb that a $\Delta \ln \mathcal{Z}$ greater than 5 between two models indicates strong evidence in favor for the model with the larger Bayesian log-evidence (odds are $\sim$150 to 1), whereas a $\Delta \ln \mathcal{Z}$ less than 2.5 indicates moderate evidence, and anything less than 1 is inconclusive.

We investigate multiple models to see which one is preferred for each individual dataset as well as combined datasets. The models being tested are:

[49] From here on, we will be using the terms Keplerian model and stable model interchangeably, though we are *not* claiming that this component is solely due to a planetary companion.

1. Keplerian-only models, i.e, both circular and eccentric;
2. GP-only model, as a proxy to describe stellar activity with spots appearing and disappearing
3. Mixed (Keplerian + GP) models, to describe stable components with variable ones

The RV periodograms (Fig. 6.2) indicate the interesting signal to be around 2.23 d. Thus, for all models with a Keplerian, the prior of the period of the planet, $P_{\rm stable}$, was kept uniform but narrow to avoid picking up aliases (i.e., at 1.8 d or 2.4 d), $\mathcal{U}(2.2, 2.25)$, and similarly for the time of periastron, t_0, $\mathcal{U}(2458404, 2458406)$, in order to avoid picking up other plausible modes, . The semi-amplitude prior was simply uniform as well, $\mathcal{U}(0, 50)$. As for the GP models, the rotational period, $P_{\rm GP,rot}$ follows the same prior as $P_{\rm stable}$ for consistency. Then, we consider wide log-uniform priors[50] for the $\sigma_{\rm GP}$ (between 0.1 and 70 m s^{-1}), as well as for $\Gamma_{\rm GP}$ (between 10^{-5} and 10^{2}) and $\alpha_{\rm GP}$ (between 10^{-8} and 10^{-1}, corresponding to timescales[51] of $\sim$3 d - 10 000 d). Additional jitter terms (log-uniform from 10^{-2} to 30 m s^{-1}) and offsets were considered as well and were kept consistent for all model runs.

The resulting posteriors on the $P_{\rm stable}$ ($P_{\rm GP,rot}$ if using a GP), semi-amplitude $K_{\rm stable}$ ($\sigma_{\rm GP}$ if GP), added instrumental jitter terms ($\sigma_{\rm inst}$) and eccentricity along with the differences in Bayesian log-evidence can be found in Table 6.3.

CARMENES only. Focusing on just the CARMENES subset 1 data, an eccentric ($e \sim 0.19$) Keplerian model is preferred over a circular model for the VIS channel ($\Delta \ln \mathcal{Z} \sim 6$). This is in agreement with the optical HARPS-N data where C20 also found a similar eccentricity when applying a Keplerian model only. As for the NIR channel, a circular model performs best. Moreover, the NIR data does not actually have a clear model preference, simply attributed to the lower precision. Phase-folded plots using the best model fits (Fig. 6.3) appear reasonable, showing a uniformly distributed scatter. When introducing combined Keplerian + GP models, the Keplerian component dominates and the GP component is not needed, i.e., $\sigma_{\rm GP}$ goes to zero. This finding is understandable given that the time span of the data is roughly $\sim$10 cycles of the periodicity, which is too short for noticeable changes of the stellar spot pattern.

Whole dataset. We then consider the whole AD Leo RV dataset. We expect the Keplerian-only models, where the amplitude for all given instruments is shared, to perform poorly given that the amplitude is clearly decreasing as a function of wavelength (shown in Sect. 6.5.4), When incorporating the GP, each instrument is allowed to have its own GP amplitude, $\sigma_{\rm GP,\ inst}$ (following Eqn. 6.1), because each instrument has its own noise level, zero point offset, wavelength range, jitter, etc. The other GP hyperparameters are shared.

The idea of combining all available datasets covering a wide wavelength range is that the dataset with the smallest amplitude, i.e., NIR data, will act as an upper limit for any stable

[50] The choice for the log-uniform priors as they are is to enable any value that we think is suitable to be considered.

[51] defined as $\frac{1}{l^2}$ where l is the timescale of variations. The original relation in Espinoza et al. (2019a) incorrectly defined $\alpha = 1/2l^2$. This has since been corrected.

signal. Within the framework of `juliet`, the data is first attempted to fit the deterministic model as best as possible, where the GP is then applied to the residuals.

Likewise, we expect that the added jitter terms and GP amplitude parameters for the redder instruments will be consistent with zero in the mixed model because the stable model will most likely saturate for the redder instruments. The role of the GP is to account for the excess amplitude observed with the bluer instruments.

The winning model by far is the mixed circular Keplerian + GP model, i.e., $\ln \mathcal{Z}_{\text{mixed}} - \ln \mathcal{Z}_{\text{GP-only}} = 15$ and $\ln \mathcal{Z}_{\text{mixed}} - \ln \mathcal{Z}_{\text{Keplerian-only}} = 151$. As anticipated, the Keplerian-only models fail to explain the data in the sense that finding a common amplitude is not feasible such that the jitter values become too high, and likewise, the phase shifts are quite strong that a simple sinusoid can not describe this behavior. Surprisingly, even though the GP-only model is flexible and could model the data well, the evidence suggests that a model containing an additional stable periodic component is favored and necessary. Tests on simulated RV data based on StarSim (Herrero et al., 2016) indicate that a Keplerian signal is in rare cases more efficient than the quasi-periodic GP in modeling a coherent activity signal (Stock priv. comm.). We find that the stable signal amplitude K_{stable} is $12.8 \pm 1.8\,\text{m}\,\text{s}^{-1}$, where the P_{stable} is rounded to 2.23 d and the P_{GP} is rounded to 2.22 d. All posteriors for the different models can be found in Table 6.3 and the phase-folded plots for the best model, i.e., the mixed model, are shown in Fig. 6.7.

To summarize all of our findings, we have the following take-away points:

- The CARMENES-VIS data alone prefer an eccentric Keplerian ($e \sim 0.19$). This is in agreement with the HARPS-N data from C20.
- The CARMENES-NIR data alone prefer a circular Keplerian, i.e., a sinusoid.
- Combining all datasets, the mixed circular Keplerian + GP model provides the best fit. This signifies that there is a stable and variable component in the stellar activity. The circular Keplerian has a K_{stable} of $12.8 \pm 1.8\,\text{m}\,\text{s}^{-1}$.
- We find that the GIANO-B data are not very helpful in constraining the amplitude, due to the larger measurement errors.

6.5.7 Spectral lines affected by stellar activity

Aside from wavelength- and time-dependence checks, we investigate the possible effect of stellar activity on spectral lines. We follow a similar approach as Dumusque (2018), which has proven to be fruitful for a selection of G-K dwarfs whose RV is dominated by activity. Essentially, we use the CCF technique, where we obtain a binary mask that contains all available, reliable lines for a spectrum (following Lafarga et al., 2020). We then compute individual RVs of the few thousands of spectral lines we have identified, and obtain an RV time series for each line. To classify the lines according to their sensitivity to activity, we compare their RVs to an activity indicator obtained from the same spectra (such as the CRX, BIS, or the total RV, in the case of stars where the RV modulation is solely due to stellar origins). We then select a sub-sample of spectral lines that are least affected by stellar activity (those that do not show a strong correlation) and recompute the RVs using

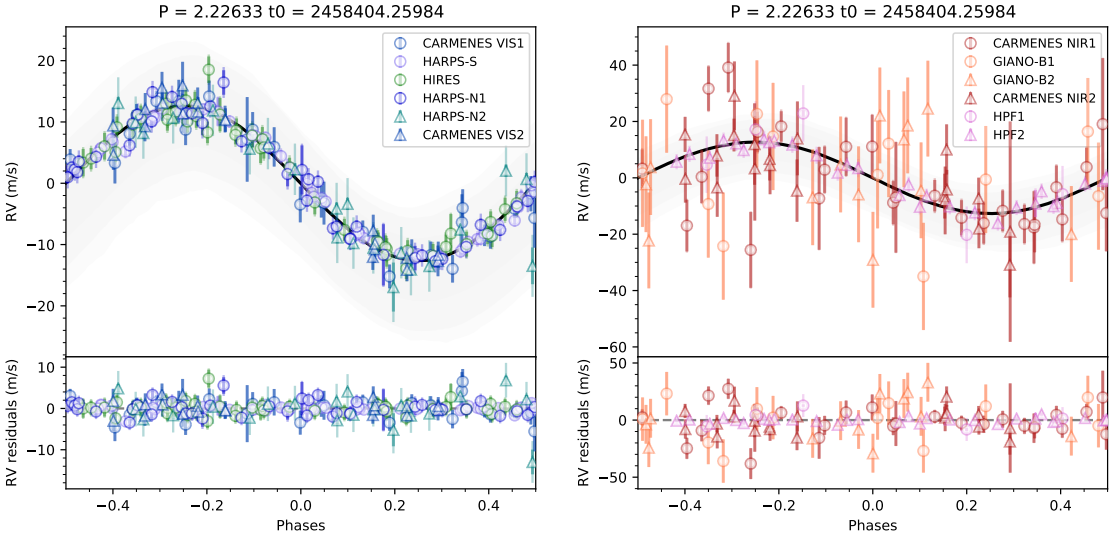

Figure 6.7: Phase-folded plots for the optical (left) and near-infrared (right) instruments using the circular Keplerian + GP model. The GP component is subtracted out and the grey bands represent the 67%, 95%, and 99% confidence intervals. The first subset of any given instrument is represented with a circle, whereas the second subset by a triangle, when applicable. The added jitter is plotted (fainter) along with the true errorbars (thicker). The y-axis ranges differ between the two plots.

this sub-sample to mitigate stellar activity. The recomputed RVs then have a smaller scatter and the modulation due to stellar rotation decreases.

This technique has been tested for other M dwarfs similar to AD Leo (spectral types 3.0 to 4.5 V, relatively low rotational velocities and high activity levels) that are well-known to exhibit *strong* stellar activity signals (e.g., YZ CMi, EV Lac) and appears to perform well and as expected (Lafarga priv. comm.). We found similar results regardless of the activity indicator (total RV, CRX or BIS) used to compute the correlations with the individual line RVs, with the total RV yielding slightly smaller RV scatters.

Specifically for AD Leo[52], we compare the computed individual line RVs to the CRX or the BIS and estimate the strength of stellar activity based on these correlations. To quantify the correlation strength, we used the Pearson correlation coefficient r. We considered as 'inactive' those lines with r close to 0. We also discarded lines that had time series scatter larger than 400 $\mathrm{m\,s^{-1}}$, as measured from their weighted standard deviation (wstd) RV; these are weak lines that mostly add noise to the recomputed RVs. Our results for the correlation with the CRX are shown in Fig. 6.8, where we generated three line sub-samples: (1) all spectral lines – black, (2) where $r \leq 0.30$ – orange , and (3) where $r \leq 0.20$ – blue. We obtained similar values using the correlation with the BIS. We recomputed the RVs from both the orange and blue sub-samples, thus using the least activity-affected lines. We then would expect a decrease in the time series RV scatter, which we do not observe. Regarding the modulation, the periodograms of these two datasets show a decrease in the power of the 2.23 d peak compared to the all-lines dataset, but there is still some power left.

[52]We focus on just the first season in 2018 since the second season only covers a bit more than one periodic cycle and this then introduces too much scatter due to the photon noise being too high.

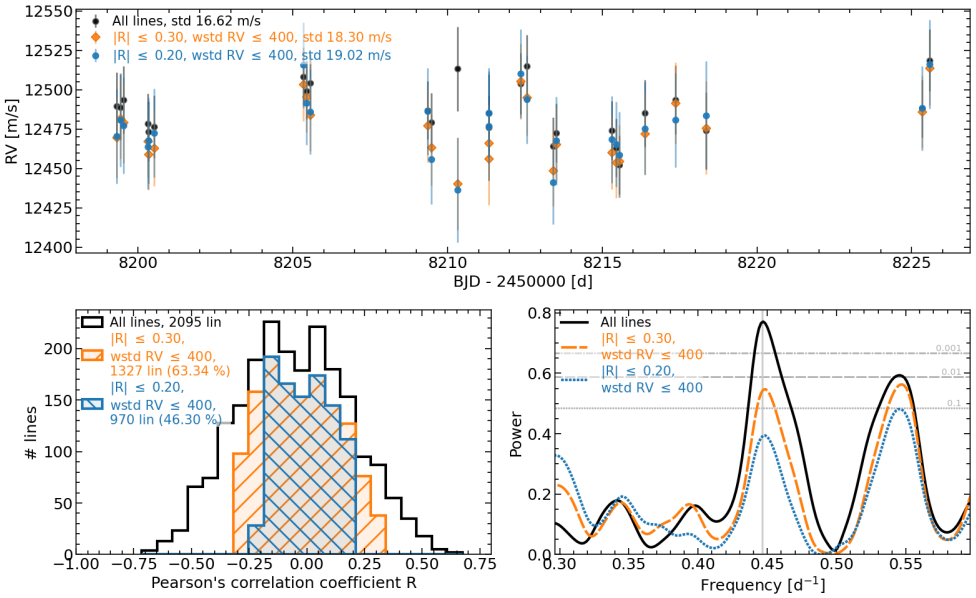

Figure 6.8: The three various sub-samples of the spectral lines: black – all, orange – $r \leq 0.30$, and blue – $r \leq 0.20$. *Top.* RVs versus time for the first CARMENES VIS season. *Bottom Left.* Histogram of the r Pearson correlation coefficient when comparing the RVs from individual lines to the CRX. The criteria for the sub-samples are illustrated here. *Bottom Right.* Zoomed-in GLS periodograms around the signal of interest of the RVs of the sub-samples. The orange sub-sample still shows little power at 2.23 d, whereas the blue sub-sample does not but it is noise limited.

This would be clear if the RV scatter decreased for the orange or blue datasets. However, since we do not observe such a decrease, it is difficult to discern what is causing the periodogram behavior. The increase in the RV scatter could be caused by increasing photon noise in the RVs of the orange and blue datasets (because we are using a smaller number of lines to compute the RVs, hence less signal). Then, the decrease in the periodogram power could be due to this increasing noise, and not to a decrease in the activity signal.

We further investigated why we do not observe a decrease in the recomputed RV scatter. When using this approach for the other stars, the correlations are much stronger and clearer than in AD Leo (the mean correlation coefficient r is $\sim$ -0.2 and some of them show $r \geq 0.8$ for the correlation with the CRX, while for AD Leo, the mean is at 0 and very few lines have $r \geq 0.6$). This lack of clear correlations indicates that the correlations that we find for AD Leo do not have much information related to the activity of the star, and this could be why we are not able to effectively mitigate the stellar activity signal in the RVs.

This difference in the correlation strength could be due to the different RV amplitudes of the stars. AD Leo shows a small RV amplitude compared to the other considered stars: $K \sim 25\,\mathrm{m\,s^{-1}}$ in comparison to e.g., $\sim$100 $\mathrm{m\,s^{-1}}$ for EV Lac. Both stars have similar spectral types and activity levels (for EV Lac, pEW(Hα) = -4.983$\pm$0.021, as computed from the CARMENES observations, Schöfer et al., 2019), so the difference in RV amplitudes seems to be caused by different spot configurations. AD Leo has a relatively low inclination ($i \sim 13°$) in comparison to EV Lac or the other considered stars ($\geq 60°$, see e.g. Morin et al., 2008).

This close to pole-on inclination could cause any visible co-rotating spots to induce a smaller modulation in the RVs simply because $v \sin i$ is smaller. Also, the photosphere of AD Leo could be more homogeneously spotted, also inducing smaller RV modulations.

To summarize, we tried to recompute RVs using only the lines least affected by activity in the AD Leo spectra, and observed a significant decrease in the periodogram peak at 2.23 d (0.1 % to 10 %), however there was still some residual power. This could be due to AD Leo having a different activity signal in the RVs than other stars with similar characteristics, for which we observe a clear mitigation of activity.

Table 6.3: Model comparison of RV fits done with `juliet` comparing a Keplerian model, a red-noise model, and a mixture of both for the various instrument datasets: CARMENES VIS1, CARMENES NIR1, and all datasets. The selected best model is boldfaced (refer to Sect. 6.5.6 for details on the priors used, model choice, and discussion of results). The columns refer to which model was being used, whereas the rows correspond to the model parameter.

	circ.	ecc.	GP	circ. + GP	ecc. + GP
CARMENES VIS1					
$P_{\rm stable}$	$2.2365^{+0.0050}_{-0.0054}$	$2.2344^{+0.0028}_{-0.0029}$	...	$2.2378^{+0.0038}_{-0.0039}$	$2.2341^{+0.0033}_{-0.0034}$
$K_{\rm stable}$	$25.9^{+1.5}_{-1.5}$	$28.42^{+0.93}_{-0.97}$	...	$26.0^{+1.3}_{-1.4}$	$28.1^{+1.2}_{-1.3}$
$P_{\rm GP}$	...	...	$2.2330^{+0.0033}_{-0.0039}$	$2.353^{+0.092}_{-0.099}$	$2.225^{+0.016}_{-0.017}$
ecc.	0.0 (fixed)	$0.192^{+0.030}_{-0.029}$	...	0.0 (fixed)	$0.188^{+0.035}_{-0.040}$
$\sigma_{\rm GP,\ CARMENES\ VIS}$	...	...	40^{+17}_{-15}	$4.7^{+2.1}_{-1.2}$	$0.43^{+2.50}_{-0.39}$
$\sigma_{\rm CARMENES\ VIS}$	$4.32^{+1.00}_{-0.82}$	$1.4^{+1.0}_{-1.2}$	$1.1^{+1.1}_{-1.1}$	$1.34^{+1.00}_{-0.81}$	$1.86^{+0.92}_{-0.91}$
$\Delta \ln \mathcal{Z}$	-6.20	**0.0**	-2.95	-1.97	1.89
CARMENES NIR1b					
$P_{\rm stable}$	$2.267^{+0.018}_{-0.013}$	$2.285^{+0.013}_{-0.015}$	...	$2.270^{+0.039}_{-0.026}$	$2.291^{+0.024}_{-0.010}$
$K_{\rm stable}$	$17.7^{+2.5}_{-2.8}$	$22.7^{+4.2}_{-3.9}$	...	$15.2^{+4.1}_{-4.1}$	$19.5^{+3.8}_{-5.0}$
$P_{\rm GP}$	...	...	$2.279^{+0.036}_{-0.038}$	$2.334^{+0.110}_{-0.086}$	$2.350^{+0.092}_{-0.090}$
ecc.	0.0 (fixed)	$0.53^{+0.12}_{-0.15}$	...	0.0 (fixed)	$0.457^{+0.092}_{-0.210}$
$\sigma_{\rm GP,\ CARMENES\ NIR}$	...	...	$18.9^{+15.0}_{-6.0}$	$7.1^{+6.5}_{-6.7}$	$5.2^{+5.1}_{-4.8}$
$\sigma_{\rm CARMENES\ NIR}$	$2.1^{+5.2}_{-2.0}$	$0.43^{+3.40}_{-0.39}$	$0.24^{+2.00}_{-0.21}$	$0.20^{+3.10}_{-0.17}$	$0.26^{+1.70}_{-0.22}$
$\Delta \ln \mathcal{Z}$	**0.0**	0.85	-0.34	2.42	1.92
HIRES + HARPS-S + CARMENES VIS + CARMENES NIR + HARPS-N + GIANO-B + HPF					
$P_{\rm stable}$	$2.226229^{+0.000026}_{-0.000026}$	$2.226229^{+0.000025}_{-0.000025}$	...	$2.226333^{+0.000082}_{-0.000079}$	$2.226326^{+0.000062}_{-0.000061}$
$K_{\rm stable}$	$17.07^{+0.57}_{-0.58}$	$17.14^{+0.58}_{-0.58}$	...	$12.8^{+1.7}_{-1.7}$	$13.0^{+1.9}_{-1.8}$
$P_{\rm GP}$	...	...	$2.2248^{+0.0020}_{-0.0019}$	$2.2249^{+0.0017}_{-0.0018}$	$2.2239^{+0.0019}_{-0.0019}$
ecc.	0.0 (fixed)	$0.060^{+0.051}_{-0.041}$	...	0.0 (fixed)	$0.037^{+0.050}_{-0.027}$
$\sigma_{\rm GP,\ HIRES}$	...	...	$24.4^{+4.1}_{-3.2}$	$22.0^{+3.7}_{-2.9}$	$21.4^{+3.1}_{-2.6}$
$\sigma_{\rm GP,\ HARPS\text{-}S}$	...	...	$31.3^{+6.4}_{-4.9}$	$28.3^{+5.6}_{-4.4}$	$27.1^{+4.6}_{-3.9}$
$\sigma_{\rm GP,\ CARMENES\ VIS1}$	...	...	$23.6^{+7.5}_{-5.4}$	$17.6^{+6.4}_{-4.4}$	$18.3^{+6.0}_{-4.4}$
$\sigma_{\rm GP,\ CARMENES\ NIR1}$	...	...	$23.7^{+16.0}_{-9.9}$	$0.51^{+2.60}_{-0.45}$	$0.12^{+0.61}_{-0.09}$
$\sigma_{\rm GP,\ HARPS\text{-}N1}$	...	...	$24.0^{+6.9}_{-4.9}$	$17.2^{+4.4}_{-3.5}$	$22.3^{+6.3}_{-5.4}$
$\sigma_{\rm GP,\ HARPS\text{-}N2}$	...	...	$14.8^{+6.4}_{-4.3}$	$13.4^{+6.2}_{-4.5}$	$10.3^{+4.9}_{-3.8}$
$\sigma_{\rm GP,\ GIANO\text{-}B1}$	...	...	$0.38^{+3.30}_{-0.34}$	$1.06^{+4.10}_{-0.89}$	$4.3^{+7.7}_{-3.3}$
$\sigma_{\rm GP,\ GIANO\text{-}B2}$	...	...	$1.6^{+14.0}_{-1.5}$	$1.5^{+18.0}_{-1.4}$	14^{+15}_{-11}
$\sigma_{\rm GP,\ CARMENES\ VIS2}$	...	...	$15.5^{+6.2}_{-4.0}$	$6.7^{+5.0}_{-2.8}$	$4.3^{+2.6}_{-1.9}$
$\sigma_{\rm GP,\ CARMENES\ NIR2}$	...	...	$11.2^{+11.0}_{-6.1}$	$1.3^{+6.3}_{-1.2}$	$3.8^{+6.4}_{-2.8}$
$\sigma_{\rm GP,\ HPF1}$	...	...	$26.5^{+13.0}_{-9.3}$	$6.0^{+12.0}_{-4.5}$	$15.1^{+10.0}_{-8.4}$
$\sigma_{\rm GP,\ HPF2}$	...	...	$7.7^{+2.2}_{-1.7}$	$8.4^{+2.0}_{-1.7}$	$8.6^{+2.1}_{-1.7}$
$\sigma_{\rm HIRES}$	$16.8^{+1.9}_{-1.7}$	$16.9^{+2.0}_{-1.7}$	$1.4^{+1.2}_{-1.2}$	$1.2^{+1.1}_{-1.0}$	$1.62^{+0.94}_{-0.83}$
$\sigma_{\rm HARPS\text{-}S}$	$18.1^{+2.0}_{-1.7}$	$18.1^{+1.9}_{-1.7}$	$0.94^{+0.49}_{-0.51}$	$0.81^{+0.48}_{-0.52}$	$1.00^{+0.36}_{-0.29}$
$\sigma_{\rm CARMENES\ VIS1}$	$7.4^{+1.4}_{-1.1}$	$7.5^{+1.3}_{-1.1}$	$0.56^{+1.40}_{-0.51}$	$0.22^{+1.20}_{-0.19}$	$1.06^{+1.20}_{-0.76}$
$\sigma_{\rm CARMENES\ NIR1}$	$0.89^{+5.30}_{-0.84}$	$1.1^{+5.3}_{-1.0}$	$0.74^{+5.40}_{-0.69}$	$2.7^{+5.4}_{-2.5}$	$1.1^{+6.8}_{-1.0}$
$\sigma_{\rm HARPS\text{-}N1}$	$11.0^{+1.4}_{-1.1}$	$11.0^{+1.4}_{-1.2}$	$1.56^{+0.35}_{-0.30}$	$1.54^{+0.34}_{-0.29}$	$1.62^{+0.35}_{-0.30}$
$\sigma_{\rm HARPS\text{-}N2}$	$9.2^{+1.7}_{-1.4}$	$9.2^{+1.8}_{-1.3}$	$4.2^{+1.2}_{-1.0}$	$4.1^{+1.4}_{-1.1}$	$4.2^{+1.4}_{-1.1}$
$\sigma_{\rm GIANO\text{-}B1}$	$0.48^{+4.90}_{-0.44}$	$0.5^{+4.9}_{-0.5}$	$0.37^{+3.50}_{-0.33}$	$1.8^{+5.5}_{-1.5}$	$0.32^{+1.20}_{-0.26}$
$\sigma_{\rm GIANO\text{-}B2}$	$2.0^{+12.0}_{-1.9}$	$1.9^{+11.0}_{-1.9}$	$0.38^{+3.90}_{-0.34}$	$0.57^{+5.50}_{-0.52}$	$0.07^{+0.38}_{-0.05}$
$\sigma_{\rm CARMENES\ VIS2}$	$0.109^{+0.400}_{-0.084}$	$0.14^{+0.44}_{-0.11}$	$0.09^{+0.34}_{-0.07}$	$0.15^{+0.36}_{-0.11}$	$0.46^{+0.51}_{-0.27}$
$\sigma_{\rm CARMENES\ NIR2}$	$4.5^{+6.2}_{-4.2}$	$4.3^{+6.1}_{-4.2}$	$0.40^{+3.00}_{-0.36}$	$0.18^{+1.30}_{-0.15}$	$0.2^{+1.1}_{-0.2}$
$\sigma_{\rm HPF1}$	$10.0^{+4.7}_{-2.8}$	$9.7^{+4.2}_{-2.6}$	$0.49^{+6.40}_{-0.44}$	$10.0^{+6.3}_{-5.3}$	$4.4^{+7.2}_{-3.6}$
$\sigma_{\rm HPF2}$	$12.1^{+1.8}_{-1.5}$	$12.2^{+1.8}_{-1.5}$	$2.98^{+0.77}_{-0.61}$	$2.45^{+0.68}_{-0.57}$	$2.49^{+0.64}_{-0.54}$
$\Delta \ln \mathcal{Z}$	-150.70	-156.60	-14.94	**0.0**	1.87

aUpper limits denote the 95% upper credibility interval of fits. bPriors for the NIR arm are slightly different because of the lower data quality. The period priors are wider, $\mathcal{U}(2.2, 2.5)$.

6.6 Discussion and future studies

In this analysis, we have presented new CARMENES VIS+NIR data that cover a wide wavelength range well into the red part of the spectrum to test the origin of the 2.23 d signal found in the RVs for AD Leo. The presence of stellar activity is confirmed with CARMENES through the proof of wavelength- and time-dependence. Solely focusing on the CARMENES data, the wavelength dependence of the amplitude can be attributed to a star-spot configuration following Reiners et al. (2010). C20 (Carleo et al., 2020) also found an amplitude decrease between the HARPS-N and GIANO-B data, i.e., from $33\,\mathrm{m\,s^{-1}}$ to less than $23\,\mathrm{m\,s^{-1}}$ between the instruments and from $33\,\mathrm{m\,s^{-1}}$ to $13\,\mathrm{m\,s^{-1}}$ between seasons. However, given the large errorbars of the GIANO-B data ($\sim$$20\,\mathrm{m\,s^{-1}}$), it was only possible to identify an amplitude decrease, but not to constrain whether there even is a signal present in these data at 2.23 d. Likewise, the high-precision NIR data from HPF R20 (Robertson et al., 2020) show a much smaller RV amplitude, inconsistent with that suggested in the bluer regime, and there is also an inconsistency even between HPF seasons, i.e., RMS scatter dropped from $23\,\mathrm{m\,s^{-1}}$ to $6.4\,\mathrm{m\,s^{-1}}$. This decrease in amplitude is also seen in the overlapping, optical HARPS-N data and second season of CARMENES data (see again Fig. 6.1). Nonetheless, both our results and those in C20 and R20 agree that the signal's amplitude does indeed decrease rather than increase. We conclude that the effect of the spots on the RVs is dominated by temperature differences rather than the Zeeman effect (see Reiners et al., 2013), in accordance with the other evidence at hand such as photometric variability (presented in T18).

Stable stellar-spot signal In the community it is common to model activity-induced RVs with GPs (e.g., Rajpaul et al., 2015, and further citations), as they are non-deterministic models that can sufficiently fit to stochastic models. Given that we claim that the RV signal found for AD Leo is solely due to stellar activity, it was expected that the GP-only model should have been the winning model. The modeling instead showed that neither a stable-only (i.e., sinusoid) model or red-noise-only (i.e., GP-only) model can correctly describe the whole dataset given the many amplitude jumps and phase shifts. A mixed model of a stable and variable component is rather the winning model, where the stable model has an amplitude of $K_{stable} = 12.8 \pm 1.8\,\mathrm{m\,s^{-1}}$, lower than the value of $19\,\mathrm{m\,s^{-1}}$ proposed by T18. We do not claim that the stable component is due to a planetary companion, but rather due to stellar activity exhibiting a constant behavior.

This should raise the question of whether a signal with an amplitude of $\sim$$13\,\mathrm{m\,s^{-1}}$ that is fully stable over all these observations ($\sim$19 yrs) in such an M dwarf is possible. In fact, it is not so surprising that spot-induced RV fluctuations for M dwarfs are long-lived (e.g., Günther et al., 2020). Though evidence of stable stellar activity behavior have previously been shown in photometry (e.g., GJ 1243, Davenport et al., 2020) and RVs (e.g., α Tau, Hatzes et al., 2015) over time, this paper demonstrates the first case for modeling RVs over time and wavelength. In future potential cases where there is a presumed planetary and stellar activity signal with two instruments covering a wide wavelength range, e.g., with CARMENES, it is crucial to adequately model the wavelength dependence of the stellar activity to ensure the most precise planetary parameters. AD Leo in this regard is an interesting case study to perform such fits.

Limitations Either we are limited by our modeling approaches, by our astrophysical knowledge of star-spot configurations, or a combination of both. Continuing on, the spectral line analysis is inconclusive considering that there still exists power at the periodicity of interest when only considering spectral lines that should not be affected by stellar activity.

Additional data may not be what is necessary as much as is a better understanding of the effects stellar spots impose on the star and how we choose to model them. We face the limitations of various RV modeling techniques, in particular regarding the question whether we could ascertain the presence of a planet with an orbital period comparable to that of the star's rotation. Determining the planetary parameters would then become rather challenging as one would have to disentangle the contribution of stellar activity from the Keplerian signal. Future studies performing simulations with software packages such as StarSim 2.0 (Herrero et al., 2016) or SOAP 2.0 (Dumusque et al., 2014) using various star-spot configurations may also shed light on why a signal can stay persistent over many years (Herrero et al., 2016; Rosich et al., 2020). Utilizing StarSim 2.0 to compare RV-CRX correlations between simulated and real data as performed by Baroch et al. (2020), with YZ CMi as a case study, could be beneficial in determining the star-spot temperature difference, the star-spot filling factor, and the location of the spot. A first test with a simple assumption (i.e., one big polar spot) could reproduce well the RVs and CRX values of AD Leo (Baroch priv. comm.). But such an approach can become degenerate when considering so many instruments and various star-spot configurations. Additionally, our spectral line analysis could be applied to not only the CARMENES data, but to all the other instruments as well to determine if the signal disappears. Either way, AD Leo certainly serves as a particularly intriguing system for studying the impact of a stable spot periodicity on the search for planetary signals.

6.7 Conclusions

In this paper, we have presented new CARMENES optical and near-infrared spectroscopic data for a known nearby, active M dwarf, AD Leo. The stellar rotation period of 2.23 d is clearly present in the RVs, and we address the question of whether there could be a planet hidden within. Taking advantage of the wide wavelength range of the CARMENES instrument, we have demonstrated the wavelength dependency of the RV semi-amplitudes to be in agreement with what is expected for a star-spot temperature difference configuration as suggested by Reiners et al. (2010) – a drop in amplitude into a steady plateau. The anti-correlation found between CRX-RV and BIS-RV for the CARMENES VIS data are additional signs of stellar activity.

When incorporating all available RVs (HARPS-S , HIRES, CARMENES, and the recent HARPS-N, GIANO-B, and HPF data), it became evident that the signal has undergone various amplitude fluctuations as well as phase shifts, behavior that cannot be attributed to the presence of a planetary companion. A closer look into the model comparison showed that a mixed model of a sinusoid + quasi-periodic red-noise model best explained the data, where the RV discrepancies (phase shifts and amplitude jumps) were modeled by the GP and then a stable component remained with $\mathrm{K_{stable}} = 12.8 \pm 1.8\,\mathrm{m\,s^{-1}}$. This is again consistent with a pureply stellar origin of the RV variations. The alternative, a planet plus intrinsic variations, both with almost exactly the same period, with similar amplitudes, and with the same phase, appears overly contrived.

Based on all this evidence and the given data at hand, we conclude the 2.23 d periodic signal found in AD Leo is due to stellar activity.

6.8 Appendix

6.8.1 RV data

6.8.2 Stellar activity

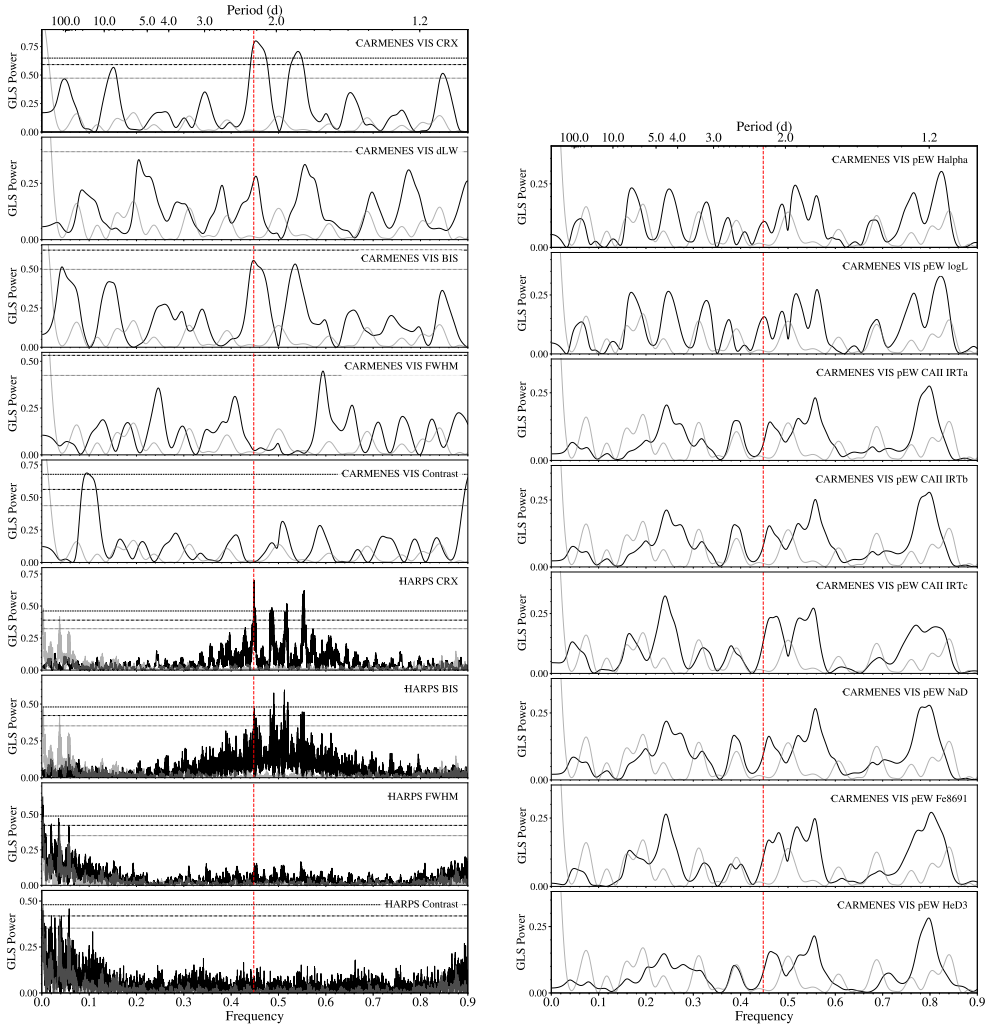

Figure 6.9: Presented here are the GLS periodograms for the various stellar activity indicators as marked. The red vertical dashed line represents $P = 2.23\,d$ and the grey line corresponds to the GLS periodogram of the sampling of the data. The chromatic index peaks both for the CARMENES VIS arm and for HARPS.

Table 6.4: CARMENES VIS RV and accompanying data for AD Leo used in this paper.

BJD	RV ($m\,s^{-1}$)	σ_{RV} ($m\,s^{-1}$)	BIS ($m\,s^{-1}$)	σ_{BIS} ($m\,s^{-1}$)	CRX ($m\,s^{-1}\,Np^{-1}$)	σ_{CRX} ($m\,s^{-1}\,Np^{-1}$)
2458199.311	17.262	3.180	-21.883	12.406	-73.157	33.190
2458199.434	-0.853	2.680	-23.081	11.889	-54.187	27.725
2458199.534	-7.023	2.704	-5.860	12.444	-34.792	29.000
2458200.308	-13.304	1.614	-1.688	6.022	27.535	14.683
2458200.336	-12.725	1.914	3.821	6.749	40.564	17.928
2458200.527	-0.806	2.852	-15.595	10.867	38.547	29.896
2458205.338	18.225	1.621	-13.597	5.505	-23.211	14.505
2458205.431	23.513	1.588	-17.053	5.201	-35.261	13.324
2458205.570	24.396	2.420	-27.654	5.246	-101.634	19.986
2458209.356	-6.661	1.375	-0.196	5.613	34.251	12.659
2458209.475	3.287	1.755	-7.623	6.040	19.473	17.697
2458210.314	21.811	7.247	-41.783	23.616	-173.475	78.389
2458211.332	-15.822	4.554	3.207	16.837	38.021	50.335
2458211.336	-12.851	3.160	2.057	11.040	66.880	32.558
2458212.361	32.086	2.450	-23.655	7.079	-58.094	24.650
2458212.567	25.084	2.778	-28.603	9.363	-59.675	29.101
2458213.411	-23.284	2.342	-6.122	5.534	85.570	17.877
2458213.514	-22.324	2.309	10.287	5.919	69.535	19.663
2458215.315	-22.164	2.026	8.406	5.256	77.002	16.401
2458215.442	-31.141	2.082	4.443	5.074	97.095	14.682
2458215.547	-25.314	2.174	15.019	6.137	81.567	18.273
2458216.367	5.911	3.267	14.926	12.667	-28.008	35.184
2458217.358	-7.135	3.323	17.290	13.209	42.821	34.909
2458218.355	-8.167	4.462	1.289	20.040	42.837	47.894
2458225.342	9.429	1.612	-7.484	5.163	-20.644	14.806
2458225.575	24.922	2.989	-24.363	8.225	-127.299	26.443
2458893.395	21.103	2.582	-35.130	9.071	-75.302	24.422
2458893.397	18.666	2.958	-23.245	9.476	-67.877	30.613
2458893.564	18.291	2.494	-20.626	7.835	-76.978	21.987
2458893.566	16.846	2.353	-20.263	8.312	-39.604	22.495
2458893.694	14.182	2.177	-9.675	7.376	-14.559	21.852
2458893.696	14.001	1.909	-10.158	7.305	-25.436	18.192
2458894.394	-14.037	2.121	-3.602	7.007	12.725	20.607
2458894.396	-9.738	2.554	-4.889	8.243	11.973	25.954
2458894.403	-12.885	2.223	-1.781	8.113	-30.402	21.260
2458894.404	-11.998	2.115	-5.520	7.191	20.364	19.870
2458894.555	-15.423	1.895	2.907	6.572	24.764	16.766
2458894.556	-17.371	1.863	-5.361	6.374	32.564	15.680
2458894.703	-16.274	2.499	-9.047	9.130	-28.602	25.081
2458894.704	-15.279	2.148	0.554	8.440	24.094	20.744
2458895.390	11.952	2.905	-16.044	8.810	-108.760	26.294
2458895.391	7.185	2.462	-7.704	7.990	-67.194	23.196
2458895.541	14.161	2.465	-7.461	7.658	-63.689	23.025
2458895.542	16.960	2.616	-25.839	7.698	-109.544	20.019
2458895.719	21.550	3.842	-37.095	11.487	-112.046	38.849
2458895.720	16.964	3.149	-19.707	12.000	-34.862	34.328

Table 6.5: CARMENES NIR RV and accompanying data for AD Leo used in this paper.

BJD	RV ($m\,s^{-1}$)	σ_{RV} ($m\,s^{-1}$)	BIS ($m\,s^{-1}$)	σ_{BIS} ($m\,s^{-1}$)	CRX ($m\,s^{-1}\,Np^{-1}$)	σ_{CRX} ($m\,s^{-1}\,Np^{-1}$)
2458199.311	-9.744	9.774	128.655	271.113	-13.856	47.054
2458199.434	-1.476	9.802	299.253	285.273	-82.019	42.550
2458199.534	-21.526	7.614	474.841	408.498	-24.338	35.578
2458200.308	-16.578	5.697	248.593	194.021	-3.904	25.393
2458200.336	-24.462	6.468	401.588	169.933	-14.225	29.212
2458200.527	5.426	24.786	-23.488	189.071	-172.600	146.180
2458205.337	13.424	6.568	224.574	246.577	9.884	31.169
2458205.431	27.808	5.842	172.484	129.209	-39.130	25.986
2458205.570	9.749	5.848	199.243	157.705	-3.844	28.305
2458209.356	-5.053	5.925	250.392	560.589	-6.177	27.754
2458209.476	-11.000	7.327	276.582	179.008	4.798	34.759
2458210.314	-5.641	23.891	369.179	697.732	-77.821	114.552
2458211.333	-24.691	13.568	516.923	529.345	-18.558	65.525
2458211.336	-21.722	9.165	-97.249	854.758	-51.458	41.690
2458212.361	26.485	5.109	177.989	463.934	3.115	22.698
2458212.567	7.251	7.699	-12.666	974.904	-24.789	35.395
2458213.411	-14.934	6.095	271.100	133.299	27.398	27.297
2458213.514	-16.770	5.906	390.612	147.820	20.938	26.754
2458215.315	-7.967	4.841	229.797	181.218	44.411	19.346
2458215.442	-6.856	5.625	319.263	140.135	53.233	22.731
2458215.547	-11.641	7.331	342.710	191.254	52.782	32.821
2458216.367	-7.236	9.653	220.862	494.561	-56.264	43.835
2458217.357	6.592	23.424	-365.758	832.370	-136.725	126.590
2458218.355	-9.437	11.831	482.920	2471.627	23.443	51.119
2458225.342	10.316	7.203	151.238	153.577	-47.491	30.473
2458225.575	-1.853	10.241	120.345	349.901	13.307	49.952
2458893.395	17.178	5.808	125.946	381.853	-8.073	27.328
2458893.397	31.122	12.162	411.763	192.137	-39.706	58.468
2458893.564	8.587	7.675	278.024	242.809	-53.653	34.818
2458893.566	6.394	10.360	341.030	223.494	-41.571	49.886
2458893.694	-2.563	11.054	272.567	227.187	-46.666	56.208
2458893.696	15.986	13.104	35.100	308.979	-60.278	72.350
2458894.394	-1.520	7.948	102.542	266.843	52.372	37.643
2458894.396	-3.073	12.019	175.041	242.795	95.912	55.872
2458894.403	15.022	8.899	431.392	196.544	-13.316	43.932
2458894.404	0.833	6.928	189.464	209.898	17.274	34.044
2458894.555	-2.677	7.319	454.943	151.880	109.503	24.685
2458894.556	-13.377	7.024	147.783	190.984	8.611	34.748
2458894.703	-27.149	11.604	440.286	550.565	29.497	66.496
2458894.704	-15.439	39.109	390.301	2184.474	72.229	210.431
2458895.390	18.247	6.221	38.575	213.213	-1.538	29.522
2458895.391	2.498	8.465	189.111	224.290	21.353	41.155
2458895.541	10.290	7.525	62.516	233.144	-7.111	36.255
2458895.542	-1.025	10.475	238.110	697.333	-84.146	47.719
2458895.719	13.870	14.447	-208.217	467.657	-148.940	68.649
2458895.720	5.277	18.570	-78.051	589.230	-90.176	95.535

Table 6.6: HARPS-S RV and accompanying data for AD Leo used in this paper, first processed using `serval` (Zechmeister et al., 2018) and then corrected for nightly zero points (Trifonov et al., 2020).

BJD	RV ($m\,s^{-1}$)	σ_{RV} ($m\,s^{-1}$)	CRX ($m\,s^{-1}\,Np^{-1}$)	σ_{CRX} ($m\,s^{-1}\,Np^{-1}$)
2452986.859	28.070	1.890	13.000	20.159
2453511.548	-19.611	1.007	-4.245	10.718
2453520.521	-15.617	1.003	2.884	9.969
2453543.482	13.687	1.256	15.835	10.623
2453544.453	-9.503	0.916	-18.846	7.702
2453550.460	39.003	2.319	26.920	17.033
2453728.866	39.050	1.031	15.394	13.352
2453758.755	-21.829	0.743	-21.824	8.058
2453760.755	-12.088	0.759	-2.911	6.578
2453761.781	18.336	0.665	15.041	7.187
2453783.726	-7.396	0.702	-6.299	6.387
2453785.727	-18.553	0.691	-8.912	7.319
2453809.661	-2.499	0.562	-1.806	4.409
2453810.677	10.933	0.676	11.065	5.885
2453811.676	8.043	0.661	1.208	5.026
2453812.664	-9.525	0.959	5.075	6.431
2453813.659	20.683	0.656	6.963	7.532
2453814.655	-20.455	0.851	-0.534	9.155
2453815.571	26.142	0.719	22.369	10.634
2453815.622	25.400	0.661	13.410	7.969
2453815.736	24.429	0.629	20.990	8.004
2453816.544	-14.430	0.742	-9.739	6.122
2453816.656	-19.395	0.650	-15.177	6.308
2453816.722	-21.994	0.681	-13.612	8.283
2453817.551	24.312	0.626	11.168	8.608
2453817.676	26.218	0.672	12.594	8.891
2453829.615	-1.066	0.615	4.834	6.330
2453830.540	-7.151	0.787	0.934	7.607
2453831.670	8.613	0.573	4.967	5.390
2453832.650	-11.771	0.623	-9.305	5.808
2453833.628	23.401	0.565	4.902	7.568
2453834.611	-27.058	0.628	-13.951	7.869
2453835.656	27.560	0.629	19.856	9.256
2453836.617	-19.536	0.592	-4.588	6.511
2453861.594	-1.222	0.694	-17.284	5.373
2453863.569	-22.081	0.692	-15.951	9.720
2453864.535	29.032	0.660	8.074	9.991
2453867.542	-13.933	0.687	-12.659	7.521
2453868.518	22.203	0.704	7.105	6.462
2453871.563	19.013	0.620	7.025	6.087
2456656.850	-36.789	0.868	-21.209	10.883
2456656.861	-35.189	0.864	-23.665	11.996
2456657.853	39.908	0.883	42.631	15.776
2456658.865	-45.305	0.880	-30.079	13.736
2456658.876	-45.601	0.863	-46.556	15.645
2456659.859	43.229	1.171	34.436	16.024
2456797.513	-29.239	0.574	-9.592	11.402

Table 6.7: HIRES RV data for AD Leo used in this paper produced by Tal-Or et al. (2019).

BJD	RV ($\mathrm{m\,s^{-1}}$)	σ_{RV} ($\mathrm{m\,s^{-1}}$)
2452064.857	-4.468	2.240
2452334.017	28.754	1.890
2452602.130	-17.428	1.940
2452652.102	8.909	1.966
2452653.010	-5.158	1.975
2452711.932	-4.572	1.799
2452712.956	-5.290	2.081
2452804.841	-14.890	2.397
2452828.763	5.108	2.120
2453044.883	17.332	2.097
2453339.121	13.734	2.022
2453340.137	-24.866	2.031
2453398.917	16.050	1.944
2453398.925	12.701	1.816
2453724.005	22.431	2.108
2453724.012	20.593	1.881
2453748.003	-21.621	1.733
2453749.896	-21.389	1.723
2453749.903	-24.097	1.832
2453750.913	15.301	1.546
2453751.934	-12.646	3.191
2453753.007	17.959	1.746
2453753.013	28.222	2.163
2453753.949	-12.153	1.706
2453753.956	-9.321	1.725
2453776.074	-0.548	1.694
2453776.080	-0.766	1.586
2453777.061	-22.006	1.646
2453777.067	-17.444	1.734
2453777.886	8.686	1.561
2453778.145	0.708	1.787
2453778.825	-26.816	1.709
2453837.868	19.003	1.988
2453837.875	17.744	1.827
2453841.864	10.578	1.912
2453841.870	8.420	1.790
2454130.101	-36.013	1.896
2454130.107	-37.321	1.896
2454130.996	5.955	2.173
2454490.992	-31.712	1.935
2455197.957	26.649	2.726
2455905.110	-31.066	2.005
2456641.070	-58.130	1.941

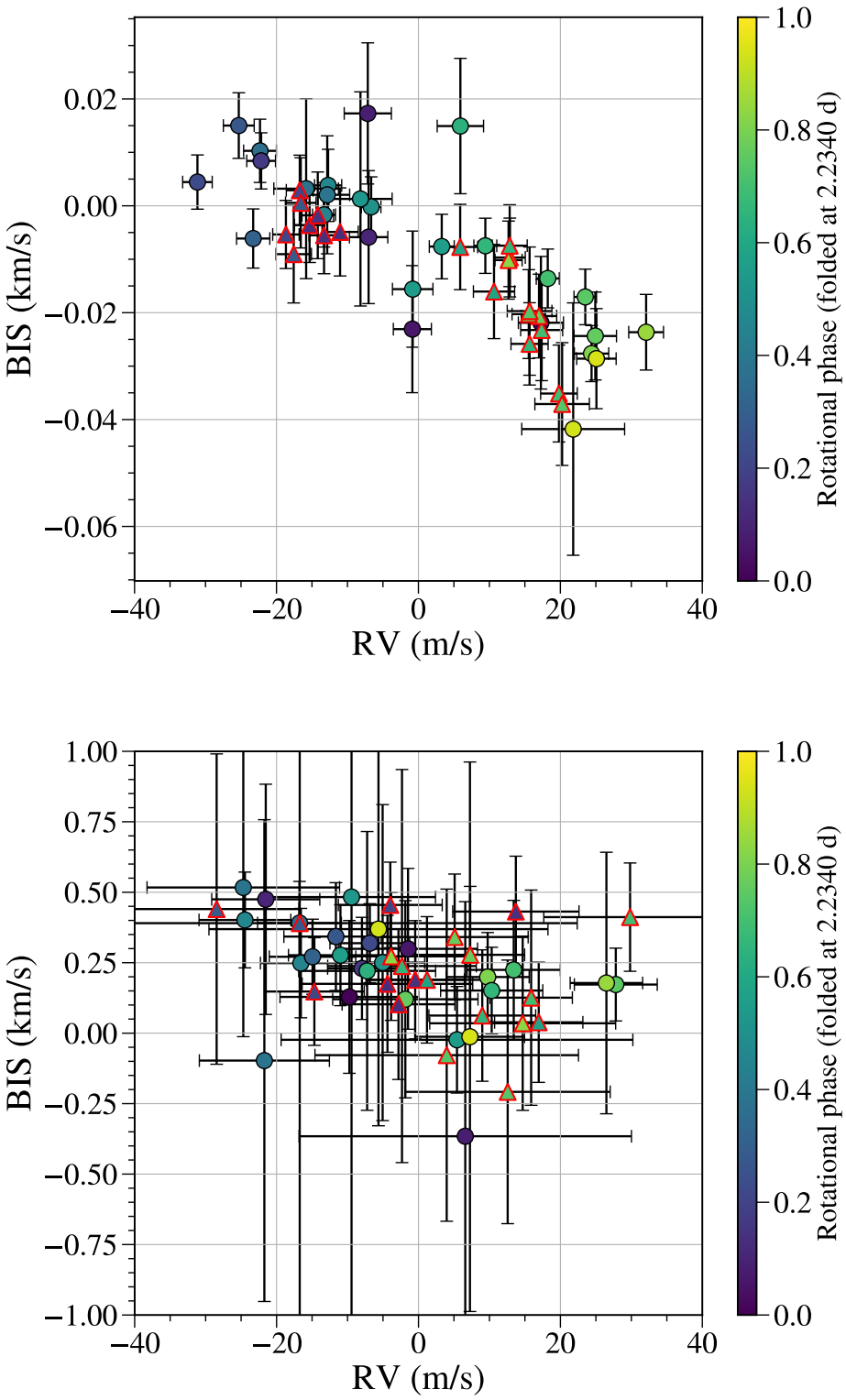

Figure 6.10: Correlations between the CCF BIS and the RVs for CARMENES VIS (left) and NIR (right). The red outlined triangles represent the second season. Note the different y-axis range.

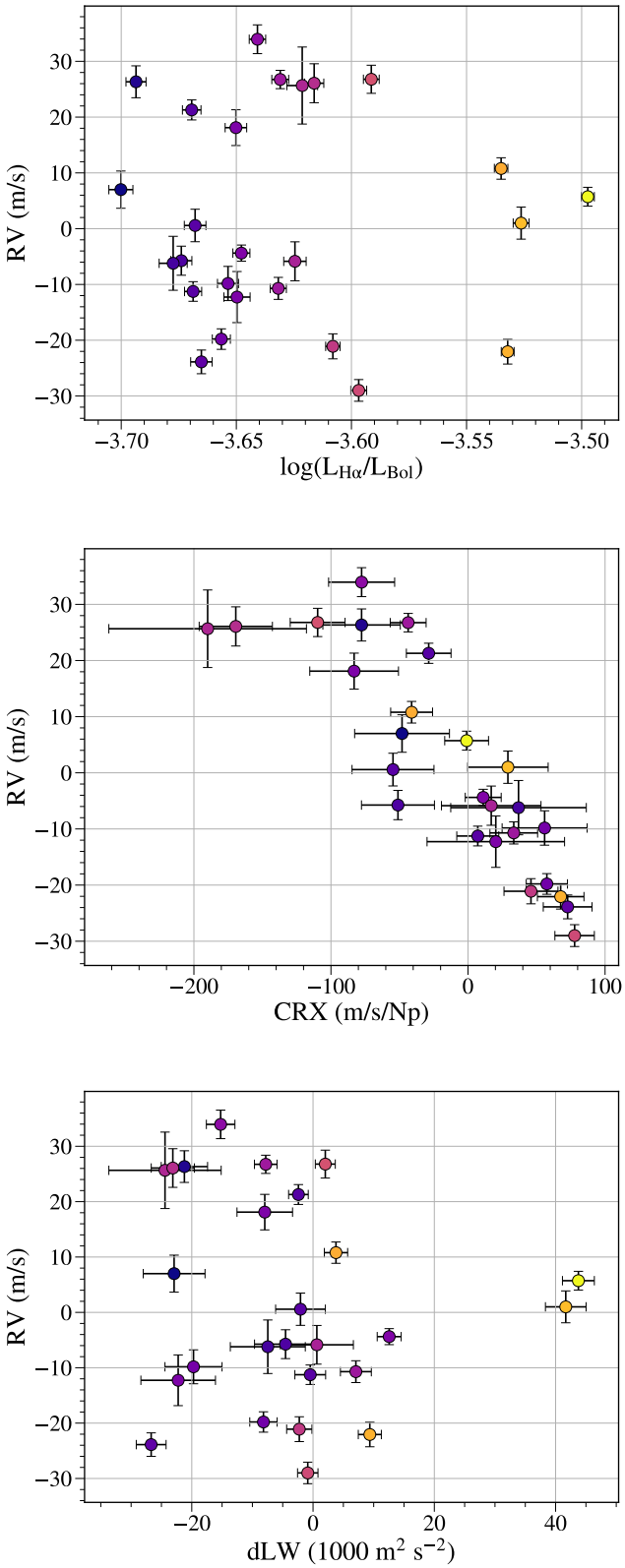

Figure 6.11: Above are various correlation plots that are also presented in Tal-Or et al. (2018) to prove the activity level of an M dwarf.

7 Conclusions and future outlook

"*The more I learn, the more I realize how much I don't know.*"

Albert Einstein (14 March 1879 - 18 April 1955)

7.1 Summary

Large transit surveys continually churn out abundances of exoplanets and it is the job of planet hunters to establish which ones are promising for future studies in order to gain a better grasp on how they form and evolve. In doing so, it is important to obtain precise planetary parameters which can be done by combining multiple datasets provided by different detection methods and implementing the right modeling approach. Within this thesis, I conveyed the importance of employing a standardized modeling approach within the Bayesian framework in order to properly interpret signals. This especially holds true for radial velocity data where short time baselines can make it difficult to determine whether a significant signal is a potential non-transiting planetary companion. Likewise, the presence of stellar activity can be prominent. In fact, the effects of stellar activity within this thesis were ironically gradually introduced, where the two hot Jupiters were clear of the behavior, the system with the transiting mini-Neptune contained some stellar presence, and the active M dwarf AD Leo was fully encapsulated by activity.

The first part of this thesis focused on setting out a standardized modeling approach within the framework of Bayesian statistics. The second part showcased the wide application of these approaches in appropriately characterizing planets as well as describing stellar activity behavior.

7.1.1 Promising targets for follow-up studies

With the impending launch of *JWST* shortly approaching, one of the purposes of the *TESS* mission was to distinguish which transiting planets should be prioritized for atmospheric characterization. As part of the CARMENES-TESS working group, I have contributed to a number of studies based on *TESS* discoveries followed-up with CARMENES spectroscopic data, outlined in Section 1.4. Furthermore, I presented a transiting mini-Neptune TOI-1201 b (Chapter 5). Outside of the group, I introduced two transiting hot Jupiters, TOI-

150 b and TOI-163 b (Chapter 4). I have provided precise planetary parameters for these targets, demonstrated that they serve as promising targets in their own respective manners, providing knowledge for the next steps in answering formation and evolution theories.

Chapter 4: TOI-150 b and TOI-163 b

The two hot Jupiters, TOI-150 b and TOI-163 b, uncovered by the 30-min cadence *TESS* FFIs, both orbit F-type stars on very close-in orbits, 5.8 d and 4.2 d, respectively. Both are great follow-up candidates for their respective reasons listed below.

Most hot Jupiters are found in circular orbits. TOI-150 b is particularly interesting in that regard because it has a relatively high eccentricity ($e \sim 0.26$), which was only possible to determine with enough follow-up spectroscopic data (cf., Cañas et al., 2019). A high eccentric orbit for a close-in planet challenges various migration theories, namely disk migration (e.g., Goldreich & Tremaine, 1980) and high-eccentricity migration due to the interaction with another body (e.g., Owen & Wu, 2013). The obliquity, i.e., measuring the spin-orbit alignment of the star to the planet, can paint a better picture of the configuration of the system, and in turn aid in deciphering how the hot Jupiter may have been formed (Valsecchi & Rasio, 2014). Additionally, the stellar host TOI-150 lies right on the effective temperature boundary, of which hotter stars with close-orbiting giant planets have a much broader obliquity distribution (Winn et al., 2010; Louden et al., 2021). TOI-150 b can be easily followed-up for measuring its obliquity which would provide more information on the formation of hot Jupiters.

TOI-163 b, on the other hand, follows a circular orbit, but that does not make this target any less intriguing. Like TOI-150 b, this target is also very promising for measuring its obliquity, whose stellar host also lies right on the mentioned boundary. More so, its a great candidate for transmission spectroscopy as it would be observed for ∼200 d since it resides in the *JWST* CVZ, where it would reach an expected atmospheric signal of 70 mm. TOI-150 b is one of the hot Jupiters with an inflated radius, where many exhibit radii larger than expected (e.g., Thorngren & Fortney, 2018b). Hence, characterizing the atmosphere of TOI-163 b over a long time baseline will able to deliver more insight on its existence.

Chapter 5: TOI-1201 b

This transiting mini-Neptune was detected in the *TESS* data and alerted as a TOI. Upon taking follow-up photometric observations, it was quickly uncovered that the dip in the light curve was actually due to TOI-1201 and not the bound companion falling on the same *TESS* pixel just ∼8 arcsec away. This system thus showcased the importance of follow-up observations. Further follow-up data from CARMENES spectroscopy was able to confirm the presence of the transiting planet and provide a mass determination with 14 % precision. The RVs also showed two peaks, i.e., the presumed stellar rotation period of $19 - 23$ d based on long-term photometry and stellar activity indicators, and a long-term unknown signal around ∼100 d that would need further monitoring to determine its origin.

The transiting mini-Neptune itself is a truly prime target for further studies since only a handful discovered around M dwarfs thus far are promising candidates. Namely, the spin-orbit alignment measured via the Rossiter-Mclaughin effect would be easily attainable using the current state-of-the-art spectrographs (i.e., ESPRESSO) which would shed light

on its obliquity (as mentioned above for TOI-150 b and TOI-163 b). Only six planets of resemblance to TOI-1201 b have measured obliquities, where just one is highly misaligned (i.e., GJ 436 b Bourrier et al., 2018). With the upcoming *JWST*, TOI-1201 b is among one of the most promising targets for transmission spectroscopy in the near- and mid-IR. On top of this, because its host star has an almost identical nearby companion, TOI-1201 b is also excellent for low-to-mid-resolution ground-based transit spectroscopy covering the optical regime. Characterizing the atmosphere over a wide wavelength range is the key in deducing the true composition of this world, which is believed to have a 0.3% H-He envelope (following theoretical models in Zeng et al., 2019). Additionally, this target finds itself in a wide (>300 AU) binary system, which does not make it prone to suffer from gravitational perturbations (e.g., Raghavan et al., 2010). However, the planet occurrence rate is lacking for planets orbiting M dwarf binary systems, and finding more planets like TOI-1201 allows this statistic to grow. Overall, it is evident that TOI-1201 b will stick around and find itself in future works.

7.1.2 Investigating stellar activity in RV data

The effect of stellar activity manifests itself in RV data as quasi-periodic entities, mainly due to the lingering but also fleeing nature of spots co-rotating on the stellar surface. Due to its stochastic nature, it is common to use non-parametric models, i.e., GPs, to model its correlated behavior. Due to the recent innovation of incorporating GPs into the final model, there is still much to learn on how to correctly apply them to describe the stellar activity.

Chapter 6: AD Leo

The enigmatic case of AD Leo had been debated in the literature over the course of many years, now accumulating RV data spanning ∼19 years. It was proposed that a massive planet orbits the star at the same periodicity of the 2.23 d stellar rotation since a star-spot model could not account for the combined simultaneous photometric and RV data (Tuomi et al., 2018). Follow-up studies (Carleo et al., 2020; Robertson et al., 2020) presented spectroscopic data that exhibited clear time- and wavelength-dependence of the presumed signal, thus refuting the planetary claim and attributing the signal to solely stellar activity. We were able to take advantage of the CARMENES-NIR arm instrument to clearly see the amplitude variation as a function over a wide wavelength range fitting to a plausible star-spot configuration (following theoretical models from Reiners et al., 2010). The conclusion was inline with the disapproval of a planetary companion and the signal is solely due to stellar activity.

I took it one step further by combining all RV datasets to see how we can model the stellar activity over the wide wavelength range and over a large amount of time. The winning model suggested that the data is best represented by a stable component and a variable component. While it is not so surprising for spots to stay for long periods of time (Günther et al., 2020), the appropriate modeling technique was questioned since many in the community usually apply GP-only models to account for it. Likewise, we tested out the approach suggested by Dumusque (2018), to recompute the RVs using presumed non-active spectral lines. The method was not as conclusive as hoped, thus showing there is room for improvement. To

summarize, AD Leo serves as a good case study for studying the stable and variable nature of stellar spots on M dwarfs.

7.2 Future outlook

August 1, 2017: 3 600 exoplanets
April 1, 2021: 4 375 exoplanets

No question is the field of exoplanets rapidly evolving with detections of exoplanets on the exponential rise. Even within just my time as a doctoral student, the incorporation of Bayesian statistics had simplified the process of computing the log-evidence for model comparison, and GPs started to dominate how to model correlated behavior. The field is, as I am, still learning how to handle such powerful tools to ensure no misuse and false claims are made.

7.2.1 Homogeneous studies

I will start with an example before making my point. In Chapter 4, I showed how the relatively high eccentricity of TOI-150 b is particularly unusual as to why some HJs are highly eccentric and others are not as this can shed light on formation theories and answer the questions of how did they migrate in. In order to address such questions, it is imperative that the derived eccentricities are reliable. Figure 4.8 demonstrated the discrepancy between how different modeling approaches can impact the interpretation of the results, i.e., an eccentricity of zero does not necessarily correspond to a circular model winning over an eccentric one, but rather it could be that an eccentric model was never attempted and the default winning model is a circular one. Even more so, this statistical plot can be skewed because not enough spectroscopic data was even taken to detect an eccentricity (e.g., as in the case in Cañas et al., 2019, for TOI-150 b). This is just one instance where the lack of data led to a different set of planetary parameters compared to a proper amount of data.

On a bigger scale, such instances, i.e., not taking enough data or incorrect modeling, can create a huge impact on the planetary parameters which can then trickle down to the exoplanet demographics and lead to false inferences. When analyzing exoplanet demographic statistics, each system often has its own nuances that it is nearly impossible to know each of these minute differences between various systems. More homogeneous studies (e.g., Torres et al., 2008) need to take place. This is indeed a daunting task but it is required considering we are reaching stages where exoplanet demographics can make or break intepretations, affecting theoretical models and beliefs.

7.2.2 Understanding stellar activity in RVs

The current struggle in the RV community is to understand how to mitigate the effects of stellar activity behavior, particularly due to stellar spots co-rotating on the surface. There will most likely never exist an empirical model as this process is stochastic and it is the equivalent of trying to predict how water flows. Thus, we can try modeling the intrinsic behavior to the best of our ability, i.e., with forward modeling Dumusque et al. (2014);

Herrero et al. (2016), though, the astrophysical knowledge is still lacking. For this reason, the GP acts as a great tool to model the quasi-periodic behavior.

In Chapter 6, I presented AD Leo, a good case-study where stellar activity was best modeled with a constant stable component alongside a GP. This demonstrated that the GP alone was not flexible enough to account for those variations. Additionally, one could wonder, what if there were indeed a planetary signal within this stellar rotation signal, would we be able to disentangle this from the stellar activity? Currently, no. And most likely in the future, also no, given its complexity. However, what we can learn form this example is that it is possible to use a GP including many instruments over a wide wavelength range to account for the achromaticity of stellar activity. This is of particular interest because it ensures that if a planetary signal is also present, i.e., at a different period than that of the stellar rotation, then we would be able to constrain its parameters better, e.g., the semi-amplitude of its RV signal. Otherwise, without the GP, the wavelength-dependence would not be properly modeled.

Nonetheless, understanding how to model stellar activity is an ongoing field of research. We are limited by two things, namely, our own physical understanding as well as how to approach the data with various modeling techniques. We are continually testing out our best models on real, noisy data, for which we do not even know the "true" solution for. Therefore, we are not really sure what to expect when comparing the Bayesian log-evidences from runs on real data, yet we make inferences on our results. Thus, to solve this, the next step would be to generate various simulated datasets where Keplerians are injected, certain stellar-spot configurations are injected, and as well a combination of both. In doing so in a controlled environment, we know what the results should reflect, e.g., if a GP was injected then the GP-only model should win and not a Keplerian-only model. If it is found that there are discrepancies, then this would signal that our modeling is not adequate and we need to accommodate for this.

As a whole, the signals we find in data are detected via indirect methods, meaning we will never be able to know the "truth", and we can only attempt our best in describing what we observe. This thesis demonstrated the best tactics in doing so, yet also showcased the shortcomings we currently are facing. We will never know what is really happening, yet it does not stop us from trying.

List of publications

These scientific publications have been submitted and published during my studies, or are in preparation for publication. The following articles are partially or fully presented within this thesis:

1st AUTHOR PUBLICATIONS

1. **Kossakowski D.**; Espinoza, N., 2019, MNRAS, 490, 1094;
   "TOI-150 b and TOI-163 b: two transiting hot Jupiters, one eccentric and one inflated, revealed by TESS near and at the edge of the JWST CVZ"

   [Chapter 4 in this PhD Thesis]

2. **Kossakowski D.** et al., to be submitted
   "TOI-1201 b: a mini-Neptune transiting a bright and relatively young M dwarf"

   [Chapter 5, soon-to-be submitted to the A&A Journal]

3. **Kossakowski D.** et al., to be submitted
   "AD Leonis: stable radial-velocity variations at the stellar rotation period"

   [Chapter 6, soon-to-be submitted to the A&A Journal]

CONTRIBUTIONS TO PUBLICATIONS INCLUDED IN THIS THESIS

1. Dreizler, S., Crossfield, I. J. M., **Kossakowski, D.** et al. 2020 A&A, 644, A127
   "The CARMENES search for exoplanets around M dwarfs. LP 714-47 b (TOI 442.01): populating the Neptune desert"

   [Parts summarized in Section 1.4]

2. Kemmer, J., Stock, S., **Kossakowski, D.** et al. 2020 A&A, 642, A236 "Discovery of a hot, transiting, Earth-sized planet and a second temperate, non-transiting planet around the M4 dwarf GJ 3473 (TOI-488)"

   [Parts summarized in Section 1.4]

3. Luque, R., Pallé, E., **Kossakowski, D.** et al. 2019 A&A, 628, A39
   "Planetary system around the nearby M dwarf GJ 357 including a transiting, hot, Earth-sized planet optimal for atmospheric characterization"

   [Parts summarized in Section 1.4]

4. Espinoza, N., **Kossakowski, D.** Brahm, R. 2019, MNRAS, 490, 2262E;
   "`juliet`: a versatile modelling tool for transiting and non-transiting exoplanetary systems"

   [Parts summarized in Chapter 3]

PUBLICATIONS NOT INCLUDED IN THIS THESIS

1. Addison, B., Wright, D., Nicholson, B., ..., incl. **Kossakowski, D.** et al. 2021, MNRAS, 502, 3704A
   "TOI-257 b (HD 19916b): a warm sub-saturn orbiting an evolved F-type star"

2. Brahm, R., Nielsen, L. D., Wittenmyer, R. A., ..., incl. **Kossakowski, D.** et al. 2020 AJ, 160, 235
   "TOI-481 b and TOI-892 b: Two Long-period Hot Jupiters from the Transiting Exoplanet Survey Satellite"

3. Nowak, G., Luque, R., Parviainen, H., Pallé, E., ..., **Kossakowski, D.** et al. 2020 A&A, 642, A173
   "The CARMENES search for exoplanets around M dwarfs. Two planets on opposite sides of the radius gap transiting the nearby M dwarf LTT 3780"

4. Bauer, F. F.; Zechmeister, M.; Kaminski, A.; Rodríguez López, C.; Caballero, J. A.; Azzaro, M.; Stahl, O. **Kossakowski, D.** et al. 2020 A&A, 640, A50
   "The CARMENES search for exoplanets around M dwarfs. Measuring precise radial velocities in the near infrared: The example of the super-Earth CD Cet b "

5. Bluhm, P., Luque, R., Espinoza, N., Pallé, E., ..., **Kossakowski, D.** et al. 2020 A&A, 639, A132
   "Precise mass and radius of a transiting super-Earth planet orbiting the M dwarf TOI-1235: a planet in the radius gap?"

6. Nielsen, L. D., Brahm, R., Bouchy, F., Espinoza, N., ..., **Kossakowski, D.** et al. 2020 A&A, 639, A76
   "Three short-period Jupiters from TESS. HIP 65Ab, TOI-157 b, and TOI-169 b"

7. Trifonov, T., Lee, M. H., KÃ¼rster, M., Henning, Th., ..., **Kossakowski, D.** et al. 2020 A&A, 638, A16
   "The CARMENES search for exoplanets around M dwarfs. Dynamical characterization of the multiple planet system GJ 1148 and prospects of habitable exomoons around GJ 1148 b"

8. Jordán, A., Brahm, R., Espinoza, N., Henning, T., ..., **Kossakowski, D.** et al. 2020 AJ, 159, 145
   "TOI-677 b: A Warm Jupiter (P = 11.2 days) on an Eccentric Orbit Transiting a Late F-type Star"

9. Stock, S., Kemmer, J., Reffert, S., Trifonov, T., ..., **Kossakowski, D.** et al. 2020 A&A, 636, A119
   "The CARMENES search for exoplanets around M dwarfs. Characterization of the nearby ultra-compact multiplanetary system YZ Ceti"

10. Nielsen, L. D., Gandolfi, D., Armstrong, D. J., Jenkins, J. S., ..., **Kossakowski, D.** et al. 2020 MNRAS, 492, 5399N
    "Mass determinations of the three mini-Neptunes transiting TOI-125"

11. Espinoza, N., Brahm, R., Henning, T., Jordán, A., ..., **Kossakowski, D.** et al. 2020 MNRAS, 491, 2982E
"HD 213885 b: a transiting 1-d-period super-Earth with an Earth-like composition around a bright (V = 7.9) star unveiled by TESS"

12. Morales, J. C., Mustill, A. J., Ribas, I., Davies, M. B., Reiners, A., Bauer, F. F., **Kossakowski, D.** et al. 2019 Science, 365, 1441
"A giant exoplanet orbiting a very-low-mass star challenges planet formation models"

13. Brahm, R., Espinoza, N., Jordán, A., Henning, T., ..., **Kossakowski, D.** et al. 2019 AJ, 158, 45
"HD 1397 b: A Transiting Warm Giant Planet Orbiting A $V = 7.8$ mag Subgiant Star Discovered by TESS"

14. Zechmeister, M., Dreizler, S., Ribas, I., Reiners, A., ..., **Kossakowski, D.** et al. 2019 A&A, 627, A49
"The CARMENES search for exoplanets around M dwarfs. Two temperate Earth-mass planet candidates around Teegarden's Star"

15. Deacon, N., Henning, T., **Kossakowski, D.** 2019 MNRAS, 486, 251D
"Data-driven stellar parameters for southern TESS FGK targets"

16. Wang, S., Jones, M., Shporer, A., Fulton, B., Paredes, L., Trifonov, T., **Kossakowski, D.** et al. 2019 AJ, 157, 51
"HD 202772A b: A Transiting Hot Jupiter around a Bright, Mildly Evolved Star in a Visual Binary Discovered by TESS"

17. Luque, R., Nowak, G., Pallé, E., ..., **Kossakowski, D.** et al. 2018 A&A, 620, A171
"The CARMENES search for exoplanets around M dwarfs. The warm super-Earths in twin orbits around the mid-type M dwarfs Ross 1020 (GJ 3779) and LP 819-052 (GJ 1265)"

18. Trifonov, T., Kürster, M., Reffert, S., Zechmeister, M., ..., **Kossakowski, D.** et al. 2018 RNAAS, 2, 180
"New HARPS and FEROS Observations of GJ 1046"

Bibliography

Abell, G. O. 1959, Publications of the Astronomical Society of the Pacific, 71, 517 133

Adams, F. C., & Laughlin, G. 2006, ApJ, 649, 1004 84

Addison, B. C., Horner, J., Wittenmyer, R. A., et al. 2020, arXiv e-prints, 2006, arXiv:2006.13675 114

Aerts, C., Christensen-Dalsgaard, J., & Kurtz, D. W. 2010, Asteroseismology, Astronomy and Astrophysics Library (Springer Netherlands), doi:10.1007/978-1-4020-5803-5 19

Agol, E., Steffen, J., Sari, R., & Clarkson, W. 2005, Monthly Notices of the Royal Astronomical Society, 359, 567 15

Akaike, H. 1998, in Selected Papers of Hirotugu Akaike, ed. E. Parzen, K. Tanabe, & G. Kitagawa, Springer Series in Statistics (New York, NY: Springer), 199–213 35

Alam, S., Albareti, F. D., Allende Prieto, C., et al. 2015, The Astrophysical Journal Supplement Series, 219, 12 99

Aller, A., Lillo-Box, J., Jones, D., Miranda, L. F., & Barceló Forteza, S. 2020, Astronomy and Astrophysics, 635, A128 94

Alonso, R. 2018, in Handbook of Exoplanets, ed. H. J. Deeg & J. A. Belmonte (Cham: Springer International Publishing), 1–26 15

Alonso-Floriano, F. J., Morales, J. C., Caballero, J. A., et al. 2015, Astronomy and Astrophysics, 577, A128 17, 97, 130, 132, 133

Ambikasaran, S., Foreman-Mackey, D., Greengard, L., Hogg, D. W., & O'Neil, M. 2015, IEEE Transactions on Pattern Analysis and Machine Intelligence, 38, doi:10.1109/TPAMI.2015.2448083 50, 145

Anderson, E. R., Duvall, Jr., T. L., & Jefferies, S. M. 1990, The Astrophysical Journal, 364, 699 44, 100

Anglada-Escudé, G., & Butler, R. P. 2012, The Astrophysical Journal Supplement Series, 200, 15 17, 24

Anglada-Escudé, G., & Tuomi, M. 2012, Astronomy and Astrophysics, 548, A58 22

Anglada-Escudé, G., Tuomi, M., Gerlach, E., et al. 2013, Astronomy and Astrophysics, 556, A126 22

Angus, R., Morton, T., Aigrain, S., Foreman-Mackey, D., & Rajpaul, V. 2018, Monthly Notices of the Royal Astronomical Society, 474, 2094 44

Argelander, F. W. A. 1860, Bonn : Adolf Marens, 1860; 1 v. ; in 4.; XI.4.6 132, 133

Astudillo-Defru, N., Díaz, R. F., Bonfils, X., et al. 2017, Astronomy and Astrophysics, 605, L11 50

Bailey, E., & Batygin, K. 2018, The Astrophysical Journal Letters, 866, L2 64

Balega, I., Bonneau, D., & Foy, R. 1984, Astronomy and Astrophysics Supplement Series, 57, 31 134, 135

Balega, Y. Y., & Balega, I. I. 1985, Soviet Astronomy Letters, 11, 47 134, 135

Baluev, R. V. 2009, Monthly Notices of the Royal Astronomical Society, 393, 969 33, 41, 51

—. 2013, Astronomy and Computing, 2, 18 51

—. 2018, Astronomy and Computing, 25, 221 51

Barclay, T., Pepper, J., & Quintana, E. V. 2018, The Astrophysical Journal Supplement Series, 239, 2 63

Barnes, J. R., Jenkins, J. S., Jones, H. R. A., et al. 2014, MNRAS, 439, 3094 144

Barnes, J. W. 2007, Publications of the Astronomical Society of the Pacific, 119, 986 10

Barnes, R., Jackson, B., Raymond, S. N., West, A. A., & Greenberg, R. 2009, The Astrophysical Journal, 695, 1006 92

Baroch, D., Morales, J. C., Ribas, I., et al. 2020, arXiv e-prints, arXiv:2006.16608 153

Barrado y Navascués, D. 1998, A&A, 339, 831 133

Barragán, O., Gandolfi, D., & Antoniciello, G. 2019, Monthly Notices of the Royal Astronomical Society, 482, 1017 51

Batalha, N. E., Lewis, T., Fortney, J. J., et al. 2019, The Astrophysical Journal Letters, 885, L25 15

Bauer, F. F., Reiners, A., Beeck, B., & Jeffers, S. V. 2018, A&A, 610, A52 144

Bauer, F. F., Zechmeister, M., & Reiners, A. 2015, Astronomy and Astrophysics, 581, A117 24

Bauer, F. F., Zechmeister, M., Kaminski, A., et al. 2020, arXiv e-prints, arXiv:2006.01684 142

Bean, J. L., Raymond, S. N., & Owen, J. E. 2021, Journal of Geophysical Research (Planets), 126, e06639 28, 92

Benneke, B., & Seager, S. 2013, The Astrophysical Journal, 778, 153 92, 115

Bianchi, L., Herald, J., Efremova, B., et al. 2011, Astrophysics and Space Science, 335, 161 98

Bidelman, W. P. 1985, ApJS, 59, 197 133

Bluhm, P., Luque, R., Espinoza, N., et al. 2020, Astronomy and Astrophysics, 639, A132 50

Bluhm, P., Palle, E., Molaverdikhani, K., et al. 2021, arXiv e-prints, 2103, arXiv:2103.01016 25, 47, 50, 56

Blum, J. R., Kiefer, J., & Rosenblatt, M. 1961, The Annals of Mathematical Statistics, 32, 485, publisher: Institute of Mathematical Statistics 48

Boeshaar, P. C. 1976, PhD thesis, journal Abbreviation: Ph.D. Thesis Publication Title: Ph.D. Thesis 130

Bonfils, X., Gillon, M., Udry, S., et al. 2012, Astronomy and Astrophysics, 546, A27 92

Bonfils, X., Delfosse, X., Udry, S., et al. 2013, A&A, 549, A109, publisher: EDP Sciences 19

Borucki, W. J., & Summers, A. L. 1984, Icarus, 58, 121 10

Borucki, W. J., Koch, D., Basri, G., et al. 2010, Science, 327, 977 63, 91, 131

Boué, G., Montalto, M., Boisse, I., Oshagh, M., & Santos, N. C. 2013, Astronomy and Astrophysics, 550, A53 114

Bourrier, V., Lovis, C., Beust, H., et al. 2018, Nature, 553, 477 114, 163

Brahm, R., Jordán, A., & Espinoza, N. 2017a, Publications of the Astronomical Society of the Pacific, 129, 034002 69

Brahm, R., Jordán, A., Hartman, J., & Bakos, G. 2017b, Monthly Notices of the Royal Astronomical Society, 467, 971 72, 74

Brahm, R., Jordán, A., Hartman, J. D., et al. 2015, The Astronomical Journal, 150, 33 72, 74

Brahm, R., Espinoza, N., Jordán, A., et al. 2018, Monthly Notices of the Royal Astronomical Society, 477, 2572 73

—. 2019a, The Astronomical Journal, 158, 45 28

—. 2019b, The Astronomical Journal, 158, 45 50

Brahm, R., Espinoza, N., Rabus, M., et al. 2019c, Monthly Notices of the Royal Astronomical Society, 483, 1970 73

Brandt, T. D., Kuzuhara, M., McElwain, M. W., et al. 2014, The Astrophysical Journal, 786, 1 133, 135

Brown, T. M., Baliber, N., Bianco, F. B., et al. 2013, Publications of the Astronomical Society of the Pacific, 125, 1031 66, 95

Buccino, A. P., Lemarchand, G. A., & Mauas, P. J. D. 2007, Icarus, Volume 192, Issue 2, p. 582-587., 192, 582 130

Buchner, J., Georgakakis, A., Nandra, K., et al. 2014, Astronomy and Astrophysics, 564, A125 50

Burke, C. J. 2008, The Astrophysical Journal, 679, 1566 10

Butler, R. P., Vogt, S. S., Marcy, G. W., et al. 2004, The Astrophysical Journal, 617, 580 92

Butler, R. P., Vogt, S. S., Laughlin, G., et al. 2017, AJ, 153, 208 138

Caballero, J. A. 2010, Astronomy and Astrophysics, 514, A18 99

Caballero, J. A., Cortés-Contreras, M., Alonso-Floriano, F. J., et al. 2016a, 148, conference Name: 19th Cambridge Workshop on Cool Stars, Stellar Systems, and the Sun (CS19) 23

—. 2016b, 148, conference Name: 19th Cambridge Workshop on Cool Stars, Stellar Systems, and the Sun (CS19) 24, 98, 132, 135

Cañas, C. I., Stefansson, G., Monson, A. J., et al. 2019, The Astrophysical Journal Letters, 877, L29 64, 65, 162, 164

Carleo, I., Malavolta, L., Lanza, A. F., et al. 2020, Astronomy and Astrophysics, 638, A5 130, 131, 134, 139, 152, 163

Castelli, F., & Kurucz, R. L. 2003, 210, A20, conference Name: Modelling of Stellar Atmospheres Place: eprint: arXiv:astro-ph/0405087 72

Cegla, H. 2019, Geosciences, 9, 114 19

Charbonneau, D., Berta, Z. K., Irwin, J., et al. 2009, Nature, 462, 891 92

Chen, G., Pallé, E., Parviainen, H., et al. 2021, Monthly Notices of the Royal Astronomical Society, 500, 5420 115

Chen, X., Feroz, F., & Hobson, M. 2019, arXiv e-prints, 1908, arXiv:1908.04655 36

Chen, X., Hobson, M., Das, S., & Gelderblom, P. 2018, arXiv e-prints, 1803, arXiv:1803.06387 33

Cifuentes, C., Caballero, J. A., Cortés-Contreras, M., et al. 2020, Astronomy and Astrophysics, 642, A115 97, 98, 132, 133

Claret, A. 2000, Astronomy and Astrophysics, 363, 1081 52

Claudi, R., Benatti, S., Carleo, I., et al. 2017, European Physical Journal Plus, 132, 364 131, 139

Cloutier, R., & Menou, K. 2020, The Astronomical Journal, 159, 211 92

Cloutier, R., Eastman, J. D., Rodriguez, J. E., et al. 2020, The Astronomical Journal, 160, 3 92, 93

Collier Cameron, A., & Jardine, M. 2018, MNRAS, 476, 2542 84

Collins, K. A., Kielkopf, J. F., Stassun, K. G., & Hessman, F. V. 2017, The Astronomical Journal, 153, 77 65

Cortés-Contreras, M. 2016, PhD thesis, Universidad Complutense de Madrid, Spain 133

Cortés-Contreras, M., Béjar, V. J. S., Caballero, J. A., et al. 2017, Astronomy and Astrophysics, 597, A47 92, 93, 134, 135

Cosentino, R., Lovis, C., Pepe, F., et al. 2012, in Ground-based and Airborne Instrumentation for Astronomy IV, Vol. 8446 (International Society for Optics and Photonics), 84461V 139

Crespo-Chacón, I., Montes, D., García-Alvarez, D., et al. 2006, A&A, 452, 987 133

Cretignier, M., Dumusque, X., Allart, R., Pepe, F., & Lovis, C. 2020, Astronomy and Astrophysics, 633, A76 21, 130

Crida, A., & Batygin, K. 2014, 217, conference Name: SF2A-2014: Proceedings of the Annual meeting of the French Society of Astronomy and Astrophysics 85

Crossfield, I. J. M., & Kreidberg, L. 2017, The Astronomical Journal, 154, 261 92

Curtis, J. L., Agüeros, M. A., Mamajek, E. E., Wright, J. T., & Cummings, J. D. 2019, The Astronomical Journal, 158, 77 102

Cutri, R. M., Skrutskie, M. F., van Dyk, S., et al. 2003, "The IRSA 2MASS All-Sky Point Source Catalog, NASA/IPAC Infrared Science Archive. http://irsa.ipac.caltech.edu/applications/Gator/" 74, 98, 99, 132

Daemgen, S., Siegler, N., Reid, I. N., & Close, L. M. 2007, The Astrophysical Journal, 654, 558 135

Damasso, M., Pinamonti, M., Scandariato, G., & Sozzetti, A. 2019, Monthly Notices of the Royal Astronomical Society, 489, 2555 19

Davenport, J. R. A., Mendoza, G. T., & Hawley, S. L. 2020, AJ, 160, 36, publisher: American Astronomical Society 22, 152

Dawson, R. I., & Fabrycky, D. C. 2010, The Astrophysical Journal, 722, 937 49, 50, 141

Dawson, R. I., & Johnson, J. A. 2018, Annual Review of Astronomy and Astrophysics, 56, 175 64

Dawson, R. I., Huang, C. X., Brahm, R., et al. 2021, The Astronomical Journal, 161, 161 28

Deacon, N. R., Kraus, A. L., Mann, A. W., et al. 2016, Monthly Notices of the Royal Astronomical Society, 455, 4212 93

Deeg, H. J., & Belmonte, J. A. 2018, Handbook of Exoplanets, doi:10.1007/978-3-319-55333-7 11

Désert, J.-M., Charbonneau, D., Torres, G., et al. 2015, The Astrophysical Journal, 804, 59 14

Desidera, S., & Barbieri, M. 2007, Astronomy and Astrophysics, 462, 345 115

Desort, M., Lagrange, A. M., Galland, F., Udry, S., & Mayor, M. 2007, A&A, 473, 983 142

Diamond-Lowe, H., Berta-Thompson, Z., Charbonneau, D., & Kempton, E. M.-R. 2018, AJ, 156, 42, publisher: American Astronomical Society 115

Díaz, R. F. 2018, in Asteroseismology and Exoplanets: Listening to the Stars and Searching for New Worlds, ed. T. L. Campante, N. C. Santos, & M. J. P. F. G. Monteiro, Astrophysics and Space Science Proceedings (Cham: Springer International Publishing), 199–224 33

Docobo, J. A., Tamazian, V. S., Balega, Y. Y., & Melikian, N. D. 2006, The Astronomical Journal, 132, 994 135

Dong, J., Huang, C. X., Dawson, R. I., et al. 2021, arXiv e-prints, 2104, arXiv:2104.01970 28

Dreizler, S., Crossfield, I. J. M., Kossakowski, D., et al. 2020, Astronomy and Astrophysics, 644, A127 25, 47, 92

Dressing, C. D., & Charbonneau, D. 2013, The Astrophysical Journal, 767, 95 92

—. 2015, The Astrophysical Journal, 807, 45 92, 130

Dumusque, X. 2016, Astronomy and Astrophysics, 593, A5 22

—. 2018, Astronomy and Astrophysics, 620, A47 21, 130, 147, 163

Dumusque, X., Boisse, I., & Santos, N. C. 2014, The Astrophysical Journal, 796, 132 22, 41, 153, 164

Dumusque, X., Santos, N. C., Udry, S., Lovis, C., & Bonfils, X. 2011a, Astronomy and Astrophysics, 527, A82 20, 41

Dumusque, X., Lovis, C., Ségransan, D., et al. 2011b, Astronomy and Astrophysics, 535, A55 19

Dumusque, X., Pepe, F., Lovis, C., et al. 2012, Nature, 491, 207 41

Dumusque, X., Borsa, F., Damasso, M., et al. 2017, Astronomy and Astrophysics, 598, A133 22

Duquennoy, A., & Mayor, M. 1991, Astronomy and Astrophysics, 248, 485 93

Eastman, J., Gaudi, B. S., & Agol, E. 2013, Publications of the Astronomical Society of the Pacific, 125, 83 51, 55

Eggen, O. J. 1958, Monthly Notices of the Royal Astronomical Society, 118, 65 97

—. 1984, The Astronomical Journal, 89, 1358 97

El-Badry, K., & Rix, H.-W. 2018, Monthly Notices of the Royal Astronomical Society, 480, 4884 99, 100

Engelkemeir, D. 1959, Publications of the Astronomical Society of the Pacific, 71, 522 133

Epchtein, N., de Batz, B., Capoani, L., et al. 1997, The Messenger, 87, 27 99

Espinoza, N. 2018, Research Notes of the American Astronomical Society, 2, 209 52

Espinoza, N., & Jordán, A. 2015, Monthly Notices of the Royal Astronomical Society, 450, 1879 53, 76

—. 2016, Monthly Notices of the Royal Astronomical Society, 457, 3573 53, 76

Espinoza, N., Kossakowski, D., & Brahm, R. 2019a, Monthly Notices of the Royal Astronomical Society, 490, 2262, juliet 50, 51, 75, 77, 104, 106, 145, 146

Espinoza, N., Rackham, B. V., Jordán, A., et al. 2019b, Monthly Notices of the Royal Astronomical Society, 482, 2065 115

Espinoza, N., Brahm, R., Henning, T., et al. 2020, Monthly Notices of the Royal Astronomical Society, 491, 2982 50

Eylen, V. V., & Albrecht, S. 2015, ApJ, 808, 126, publisher: IOP Publishing 52, 56

Fabrycky, D., & Tremaine, S. 2007, The Astrophysical Journal, 669, 1298 114

Feroz, F., & Hobson, M. P. 2008, Monthly Notices of the Royal Astronomical Society, 384, 449 38, 39

—. 2014, Monthly Notices of the Royal Astronomical Society, 437, 3540 22

Feroz, F., Hobson, M. P., & Bridges, M. 2009, Monthly Notices of the Royal Astronomical Society, 398, 1601 50

Feroz, F., & Skilling, J. 2013, 1553, 106, conference Name: Bayesian Inference and Maximum Entropy Methods in Science and Engineering: 32nd International Workshop on Bayesian Inference and Maximum Entropy Methods in Science and Engineering Place: eprint: arXiv:1312.5638 38

Fischer, D. A., Anglada-Escude, G., Arriagada, P., et al. 2016, Publications of the Astronomical Society of the Pacific, 128, 066001 17

Ford, E. B. 2006, The Astrophysical Journal, 642, 505 41, 55

Ford, E. B., Quinn, S. N., & Veras, D. 2008, The Astrophysical Journal, 678, 1407 59

Foreman-Mackey, D. 2018, Research Notes of the American Astronomical Society, 2, 31 44, 100

—. 2019, Astrophysics Source Code Library, ascl:1910.005 51

Foreman-Mackey, D., Agol, E., Ambikasaran, S., & Angus, R. 2017, The Astronomical Journal, 154, 220 45, 50, 65

Fressin, F., Torres, G., Charbonneau, D., et al. 2013, ApJ, 766, 81, publisher: American Astronomical Society 14

Frith, J., Pinfield, D. J., Jones, H. R. A., et al. 2013, Monthly Notices of the Royal Astronomical Society, 435, 2161 97

Fulton, B. J., & Petigura, E. A. 2018, The Astronomical Journal, 156, 264 92

Fulton, B. J., Petigura, E. A., Blunt, S., & Sinukoff, E. 2018, Publications of the Astronomical Society of the Pacific, 130, 044504 18, 50, 145

Fulton, B. J., Petigura, E. A., Howard, A. W., et al. 2017, The Astronomical Journal, 154, 109 26, 28, 92

Gaia Collaboration, Prusti, T., de Bruijne, J. H. J., et al. 2016, Astronomy and Astrophysics, 595, A1 99

Gaia Collaboration, Brown, A. G. A., Vallenari, A., et al. 2018, Astronomy and Astrophysics, 616, A1 26, 74, 99

Gaia Collaboration, Smart, R. L., Sarro, L. M., et al. 2020, arXiv e-prints, 2012, arXiv:2012.02061 13, 55, 97, 98, 99, 132, 133, 134

Gaidos, E., Mann, A. W., Lépine, S., et al. 2014, MNRAS, 443, 2561 133

Gardner, J. P., Mather, J. C., Clampin, M., et al. 2009, 10, 1, conference Name: Astrophysics in the Next Decade 13, 84, 92

Gaudi, B. S., & Winn, J. N. 2007, The Astrophysical Journal, 655, 550 15, 86, 114

Gelman, A., Carlin, J. B., Stern, H. S., et al. 2013, Bayesian Data Analysis (CRC Press), google-Books-ID: eSHSBQAAQBAJ 34

Gilbert, G. J., & Fabrycky, D. C. 2020, AJ, 159, 281, publisher: American Astronomical Society 25

Ginzburg, S., Schlichting, H. E., & Sari, R. 2016, The Astrophysical Journal, 825, 29 92

—. 2018, Monthly Notices of the Royal Astronomical Society, 476, 759 92

Gliese, W. 1957, Astron. Rechen-Institut, Heidelberg, 89 Seiten, 8 132

Goldreich, P., & Tremaine, S. 1980, The Astrophysical Journal, 241, 425 28, 162

Gomes da Silva, J., Santos, N. C., Bonfils, X., et al. 2011, A&A, 534, A30 144

González-Álvarez, E., Zapatero Osorio, M. R., Caballero, J. A., et al. 2020, Astronomy and Astrophysics, 637, A93 51, 93, 115

Goodwin, S. P., Kroupa, P., Goodman, A., & Burkert, A. 2007, Protostars and Planets V, 133 92

Goodwin, S. P., Nutter, D., Kroupa, P., Ward-Thompson, D., & Whitworth, A. P. 2008, Astronomy and Astrophysics, 477, 823 92

Gordon, K. C., & Kron, G. E. 1949, Publications of the Astronomical Society of the Pacific, 61, 210 133

Grandjean, A., Lagrange, A. M., Keppler, M., et al. 2020, A&A, 633, A44 133

Greene, T. P., Line, M. R., Montero, C., et al. 2016, The Astrophysical Journal, 817, 17 85

Gregory, P. 2005, Bayesian Logical Data Analysis for the Physical Sciences: A Comparative Approach with Mathematica® Support (Cambridge University Press), google-Books-ID: idkLAQAAQBAJ 34, 38

Gregory, P. C. 2012, arXiv e-prints, 1212, arXiv:1212.4058 22

Guerrero, N. M., Seager, S., Huang, C. X., et al. 2021, arXiv e-prints, 2103, arXiv:2103.12538 11, 14

Günther, M. N., & Daylan, T. 2019, Astrophysics Source Code Library, ascl:1903.003 51

Günther, M. N., Berardo, D. A., Ducrot, E., et al. 2020, arXiv e-prints, 2008, arXiv:2008.11681 22, 152, 163

Gupta, A., & Schlichting, H. E. 2019, Monthly Notices of the Royal Astronomical Society, 487, 24 92

—. 2021, arXiv e-prints, 2103, arXiv:2103.08785 92

Gurzadyan, G. A. 1971, A&A, 13, 348 133

Hadden, S., & Lithwick, Y. 2017, The Astronomical Journal, 154, 5 15

Hambly, N. C., MacGillivray, H. T., Read, M. A., et al. 2001, Monthly Notices of the Royal Astronomical Society, 326, 1279 99

Hara, N. C., Boué, G., Laskar, J., Delisle, J.-B., & Unger, N. 2019, Monthly Notices of the Royal Astronomical Society, 489, 738 55

Hardegree-Ullman, K. K., Cushing, M. C., Muirhead, P. S., & Christiansen, J. L. 2019, The Astronomical Journal, 158, 75 130

Hatzes, A. P. 2002, Astronomische Nachrichten, 323, 392 48

—. 2016, Astronomy and Astrophysics, 585, A144 21, 144

Hatzes, A. P., Cochran, W. D., Endl, M., et al. 2015, Astronomy and Astrophysics, 580, A31 20, 22, 144, 152

Hatzes, A. P., Endl, M., Cochran, W. D., et al. 2018, AJ, 155, 120 145

Hawley, S. L., & Pettersen, B. R. 1991, The Astrophysical Journal, 378, 725 133

Hawley, S. L., Allred, J. C., Johns-Krull, C. M., et al. 2003, The Astrophysical Journal, 597, 535 133

Haywood, R. D., Collier Cameron, A., Queloz, D., et al. 2014, Monthly Notices of the Royal Astronomical Society, 443, 2517 20, 130

Hébrard, G., Désert, J.-M., Díaz, R. F., et al. 2010, Astronomy and Astrophysics, 516, A95 114

Heng, K., & Demory, B.-O. 2013, The Astrophysical Journal, 777, 100 82

Henry, T. J., Jao, W.-C., Subasavage, J. P., et al. 2006, The Astronomical Journal, 132, 2360 26, 92, 130

Herrero, E., Ribas, I., Jordi, C., et al. 2016, Astronomy and Astrophysics, 586, A131 22, 41, 147, 153, 165

Hill, G. 1993, 38, 127, conference Name: New Frontiers in Binary Star Research 17

Hirano, T., Krishnamurthy, V., Gaidos, E., et al. 2020a, The Astrophysical Journal Letters, 899, L13 114

—. 2020b, The Astrophysical Journal Letters, 899, L13 114

Hobson, M. J., Jofré, E., García, L., Petrucci, R., & Gómez, M. 2018, Revista Mexicana de Astronomia y Astrofisica, 54, 65 93

Hobson, M. J., Brahm, R., Jordán, A., et al. 2021, arXiv e-prints, 2103, arXiv:2103.02685 28

Høg, E., & Murdin, P. 2000, Encyclopedia of Astronomy and Astrophysics, 2862 74

Hogg, D. W., Bovy, J., & Lang, D. 2010, arXiv e-prints, 1008, arXiv:1008.4686 32, 34, 51

Hojjatpanah, S., Figueira, P., Santos, N. C., et al. 2019, Astronomy and Astrophysics, 629, A80 132

Holman, M. J., & Murray, N. W. 2005, Science, 307, 1288 15

Horch, E. P., Howell, S. B., Everett, M. E., & Ciardi, D. R. 2012, The Astronomical Journal, 144, 165 71

Horch, E. P., Veillette, D. R., Baena Gallé, R., et al. 2009, The Astronomical Journal, 137, 5057 71

Howard, A. W., Marcy, G. W., Fischer, D. A., et al. 2014, The Astrophysical Journal, 794, 51 93

Howarth, I. D. 2011, Monthly Notices of the Royal Astronomical Society, 418, 1165 54

Howell, S. B., Everett, M. E., Horch, E. P., et al. 2016, The Astrophysical Journal Letters, 829, L2 71

Howell, S. B., Sobeck, C., Haas, M., et al. 2014, Publications of the Astronomical Society of the Pacific, 126, 398 13, 91

Hoyer, S., López-Morales, M., Rojo, P., Minniti, D., & Adams, E. R. 2016a, Monthly Notices of the Royal Astronomical Society, 455, 1334 84

Hoyer, S., Pallé, E., Dragomir, D., & Murgas, F. 2016b, The Astronomical Journal, 151, 137 84

Huang, C. X., Burt, J., Vanderburg, A., et al. 2018, The Astrophysical Journal Letters, 868, L39 65

Huber, D., Chaplin, W. J., Christensen-Dalsgaard, J., et al. 2013, The Astrophysical Journal, 767, 127 55, 56

Huitson, C. M., Désert, J.-M., Bean, J. L., et al. 2017, The Astronomical Journal, 154, 95 115

Hunt-Walker, N. M., Hilton, E. J., Kowalski, A. F., Hawley, S. L., & Matthews, J. M. 2012, Publications of the Astronomical Society of the Pacific, 124, 545 133

Hunt-Walker, N. M., Hilton, E. J., Kowalski, A. F., Hawley, S. L., & Matthews, J. M. 2012, PASP, 124, 545 134

Janson, M., Bergfors, C., Brandner, W., et al. 2014, The Astrophysical Journal, 789, 102 93

Janson, M., Hormuth, F., Bergfors, C., et al. 2012, The Astrophysical Journal, 754, 44 93

Jeffers, S. V., & Keller, C. U. 2009, 1094, 664, conference Name: 15th Cambridge Workshop on Cool Stars, Stellar Systems, and the Sun 45, 101

Jeffers, S. V., Schöfer, P., Lamert, A., et al. 2018, Astronomy and Astrophysics, 614, A76 101, 144

Jeffreys, H. 1961, Theory of Probability, 3rd edn. (Oxford, England: Oxford University Press) 36

Jenkins, J. M., Twicken, J. D., McCauliff, S., et al. 2016, 9913, 99133E, conference Name: Software and Cyberinfrastructure for Astronomy IV 13, 48, 65, 94

Jenkins, J. S., Pozuelos, F. J., Tuomi, M., et al. 2019, Monthly Notices of the Royal Astronomical Society, 490, 5585 50, 56

Jensen, E. 2013, Astrophysics Source Code Library, ascl:1306.007 65

Johnson, H. L., & Morgan, W. W. 1953, ApJ, 117, 313 133

Johnson, J. L., & Li, H. 2012, The Astrophysical Journal, 751, 81 93

Jones, D. E., Stenning, D. C., Ford, E. B., et al. 2017, arXiv e-prints, 1711, arXiv:1711.01318 130

Jones, M. I., Brahm, R., Espinoza, N., et al. 2019, Astronomy and Astrophysics, 625, A16 64

Jontof-Hutter, D., Ford, E. B., Rowe, J. F., et al. 2016, The Astrophysical Journal, 820, 39 15

Kaiser, N., Burgett, W., Chambers, K., et al. 2010, 7733, 77330E, conference Name: Ground-based and Airborne Telescopes III 98

Kaminski, A., Trifonov, T., Caballero, J. A., et al. 2018, Astronomy and Astrophysics, 618, A115 93

Kanodia, S., Cañas, C. I., Stefansson, G., et al. 2020, The Astrophysical Journal, 899, 29 92

Kass, R. E., & Raftery, A. E. 1995, Journal of the American Statistical Association, 90, 773, publisher: Taylor & Francis _eprint: https://www.tandfonline.com/doi/pdf/10.1080/01621459.1995.10476572 37

Kaufer, A., & Pasquini, L. 1998, 3355, 844, conference Name: Optical Astronomical Instrumentation 69

Keenan, P. C., & McNeil, R. C. 1989, ApJS, 71, 245 133

Kemmer, J., Stock, S., Kossakowski, D., et al. 2020, Astronomy and Astrophysics, 642, A236 25, 47, 56, 93, 109

Kempton, E. M.-R., Bean, J. L., Louie, D. R., et al. 2018, Publications of the Astronomical Society of the Pacific, 130, 114401 25, 92, 114

Kipping, D. M. 2010, Monthly Notices of the Royal Astronomical Society, 408, 1758 75

—. 2013a, Monthly Notices of the Royal Astronomical Society, 435, 2152 54, 76, 104

—. 2013b, Monthly Notices of the Royal Astronomical Society, 434, L51 55

—. 2014, Monthly Notices of the Royal Astronomical Society, 444, 2263 55

Kipping, D. M., & Sandford, E. 2016, Monthly Notices of the Royal Astronomical Society, 463, 1323 52

Kirkpatrick, J. D., Henry, T. J., & McCarthy, Jr., D. W. 1991, The Astrophysical Journal Supplement Series, 77, 417 130

Kjeldsen, H., Bedding, T. R., Butler, R. P., et al. 2005, The Astrophysical Journal, 635, 1281 19

Kjurkchieva, D., Dimitrov, D., Vladev, A., & Yotov, V. 2013, Monthly Notices of the Royal Astronomical Society, 431, 3654 52, 53

Klutsch, A., Freire Ferrero, R., Guillout, P., et al. 2014, A&A, 567, A52 133

Knapp, W., & Nanson, J. 2019, Journal of Double Star Observations, 15, 21 99, 100

Knutson, H. A., Charbonneau, D., Cowan, N. B., et al. 2009, The Astrophysical Journal, 690, 822 16

Kochanek, C. S., Shappee, B. J., Stanek, K. Z., et al. 2017, Publications of the Astronomical Society of the Pacific, 129, 104502 96

Kordopatis, G., Gilmore, G., Steinmetz, M., et al. 2013, The Astronomical Journal, 146, 134 97

Kossakowski, D., Espinoza, N., Brahm, R., et al. 2019, Monthly Notices of the Royal Astronomical Society, 490, 1094 50, 63

Kovács, G., Zucker, S., & Mazeh, T. 2002, Astronomy and Astrophysics, 391, 369 57, 65

Kreidberg, L. 2015, Publications of the Astronomical Society of the Pacific, 127, 1161 50

—. 2018, Handbook of Exoplanets, 100 15

Kürster, M., Trifonov, T., Reffert, S., Kostogryz, N. M., & Rodler, F. 2015, Astronomy and Astrophysics, 577, A103 19

Kürster, M., Endl, M., Rouesnel, F., et al. 2003, Astronomy and Astrophysics, 403, 1077 21, 144

Lafarga, M., Ribas, I., Lovis, C., et al. 2020, Astronomy and Astrophysics, 636, A36 24, 96, 97, 99, 132, 133, 144, 147

Lagrange, A.-M., Desort, M., & Meunier, N. 2010, Astronomy and Astrophysics, 512, A38 20

Lambrechts, M., Morbidelli, A., Jacobson, S. A., et al. 2019, A&A, 627, A83, publisher: EDP Sciences 25

Lang, K. R., Bookbinder, J., Golub, L., & Davis, M. M. 1983, The Astrophysical Journal Letters, 272, L15 133

Lawrence, A., Warren, S. J., Almaini, O., et al. 2007, Monthly Notices of the Royal Astronomical Society, 379, 1599 99

Leggett, S. K. 1992, ApJS, 82, 351 133

Lehmer, O. R., & Catling, D. C. 2017, The Astrophysical Journal, 845, 130 92

Lépine, S., & Gaidos, E. 2011, The Astronomical Journal, 142, 138 97, 98, 99

Lépine, S., Hilton, E. J., Mann, A. W., et al. 2013, AJ, 145, 102 133

Liller, W. 1952, PASP, 67, 129 133

Lippincott, S. L. 1969, The Astronomical Journal, 74, 224 134

Lissauer, J. J. 2007, The Astrophysical Journal Letters, 660, L149 25

Lo Curto, G., Pepe, F., Avila, G., et al. 2015, The Messenger, 162, 9 138

Lomb, N. R. 1976, Astrophysics and Space Science, 39, 447 48

Lopez, E. D., & Fortney, J. J. 2014, The Astrophysical Journal, 792, 1 92

López-Santiago, J., Montes, D., Gálvez-Ortiz, M. C., et al. 2010, A&A, 514, A97 133

López-Santiago, J., Montes, D., Gálvez-Ortiz, M. C., et al. 2010, Astronomy and Astrophysics, 514, A97 132

Louden, E. M., Winn, J. N., Petigura, E. A., et al. 2021, The Astronomical Journal, 161, 68 28, 162

Luque, R., Pallé, E., Kossakowski, D., et al. 2019, Astronomy and Astrophysics, 628, A39 24, 47, 50, 56

MacConnell, D. J. 1968, ApJ, 153, 313 133

Mackay, D. J. C. 2003, Information Theory, Inference and Learning Algorithms, by David J. C. MacKay, pp. 640. ISBN 0521642981. Cambridge, UK: Cambridge University Press, October 2003., num Pages: 640 32

Mahadevan, S., Ramsey, L., Bender, C., et al. 2012, 8446, 84461S, conference Name: Ground-based and Airborne Instrumentation for Astronomy IV Place: eprint: arXiv:1209.1686 140

Mahadevan, S., Ramsey, L. W., Terrien, R., et al. 2014, 9147, 91471G, conference Name: Ground-based and Airborne Instrumentation for Astronomy V 140

Mahmud, N. I., Crockett, C. J., Johns-Krull, C. M., et al. 2011, ApJ, 736, 123 142

Mai Anh, T., Bastin, F., & Frejinger, E. 2014, On optimization algorithms for maximum likelihood estimation 35

Makarov, V. V., & Kaplan, G. H. 2005, The Astronomical Journal, 129, 2420 99

Mamajek, E. E., Bartlett, J. L., Seifahrt, A., et al. 2013, AJ, 146, 154 133

Mandel, K., & Agol, E. 2002, The Astrophysical Journal Letters, 580, L171 52, 53

Mann, A. W., Feiden, G. A., Gaidos, E., Boyajian, T., & von Braun, K. 2015, ApJ, 804, 64 133

Marcy, G. W., Weiss, L. M., Petigura, E. A., et al. 2014, Proceedings of the National Academy of Science, 111, 12655 92

Marocco, F., Eisenhardt, P. R. M., Fowler, J. W., et al. 2020, arXiv e-prints, 2012, arXiv:2012.13084 99

Martín, E. L., Lodieu, N., Pavlenko, Y., & Béjar, V. J. S. 2018, The Astrophysical Journal, 856, 40 97

Martin, J., Fuhrmeister, B., Mittag, M., et al. 2017, A&A, 605, A113 144

Mason, B. D., Wycoff, G. L., Hartkopf, W. I., Douglass, G. G., & Worley, C. E. 2001, The Astronomical Journal, 122, 3466 99, 134

Mathur, S., Huber, D., Batalha, N. M., et al. 2017, The Astrophysical Journal Supplement Series, 229, 30 91

Mayor, M., Pepe, F., Queloz, D., et al. 2003, The Messenger, 114, 20 69, 138

McArthur, B. E., Endl, M., Cochran, W. D., et al. 2004, The Astrophysical Journal Letters, 614, L81 49

McLaughlin, D. B. 1924, The Astrophysical Journal, 60, doi:10.1086/142826 15, 114

McQuillan, A., Mazeh, T., & Aigrain, S. 2013, The Astrophysical Journal Letters, 775, L11 131

Merrill, P. W., Deutsch, A. J., & Keenan, P. C. 1962, The Astrophysical Journal, 136, 21 17, 130

Meshkat, T., Mawet, D., Bryan, M. L., et al. 2017, AJ, 154, 245 133

Milbourne, T. W., Haywood, R. D., Phillips, D. F., et al. 2019, The Astrophysical Journal, 874, 107 19

Miller-Ricci, E., & Fortney, J. J. 2010, The Astrophysical Journal Letters, 716, L74 92

Monet, D. G., Levine, S. E., Canzian, B., et al. 2003, The Astronomical Journal, 125, 984 99

Montes, D., López-Santiago, J., Gálvez, M. C., et al. 2001, Monthly Notices of the Royal Astronomical Society, 328, 45 97, 132, 133

Montes, D., González-Peinado, R., Tabernero, H. M., et al. 2018, Monthly Notices of the Royal Astronomical Society, 479, 1332 93, 99

Morales, J. C., Mustill, A. J., Ribas, I., et al. 2019, Science, 365, 1441 23

Mordasini, C. 2020, Astronomy and Astrophysics, 638, A52 92

Mordasini, C., Alibert, Y., Klahr, H., & Henning, T. 2012, Astronomy and Astrophysics, 547, A111 25

Morin, J., Donati, J.-F., Petit, P., et al. 2008, Monthly Notices of the Royal Astronomical Society, 390, 567 130, 132, 134, 149

Mortier, A., & Collier Cameron, A. 2017, Astronomy and Astrophysics, 601, A110 141

Mortier, A., Faria, J. P., Correia, C. M., Santerne, A., & Santos, N. C. 2015, Astronomy and Astrophysics, 573, A101 141

Muheki, P., Guenther, E. W., Mutabazi, T., & Jurua, E. 2020, A&A, 637, A13 133

Muñoz, D. J., & Perets, H. B. 2018, The Astronomical Journal, 156, 253 15, 114

Nagel, E. 2019, PhD thesis, Universität Hamburg 24

Namekata, K., Maehara, H., Sasaki, R., et al. 2020, PASJ, arXiv:2005.04336 133

Nelson, B. E., Ford, E. B., Buchner, J., et al. 2020, The Astronomical Journal, 159, 73 35

Newton, E. R., Irwin, J., Charbonneau, D., Berta-Thompson, Z. K., & Dittmann, J. A. 2016, The Astrophysical Journal Letters, 821, L19 131

Nikolov, N., Sing, D. K., Gibson, N. P., et al. 2016, The Astrophysical Journal, 832, 191 115

Nobel Prize. 2019, Nobel Lecture: Didier Queloz, Nobel Prize in Physics 2019 17

Nowak, G., Luque, R., Parviainen, H., et al. 2020, Astronomy and Astrophysics, 642, A173 92, 93

Oliva, E., Origlia, L., Baffa, C., et al. 2006, 6269, 626919, conference Name: Society of Photo-Optical Instrumentation Engineers (SPIE) Conference Series 139

Osten, R. A., & Bastian, T. S. 2008, The Astrophysical Journal, 674, 1078 133

Owen, J. E., & Jackson, A. P. 2012, Monthly Notices of the Royal Astronomical Society, 425, 2931 119

Owen, J. E., & Wu, Y. 2013, The Astrophysical Journal, 775, 105 92, 162

—. 2017, The Astrophysical Journal, 847, 29 25, 92

Palle, E., Oshagh, M., Casasayas-Barris, N., et al. 2020, Astronomy and Astrophysics, 643, A25 114

Parmentier, V., & Crossfield, I. J. M. 2018, Handbook of Exoplanets, 116 16

Parviainen, H. 2017, in Handbook of Exoplanets, ed. H. J. Deeg & J. A. Belmonte (Cham: Springer International Publishing), 1–24 32, 34

Passegger, V. M., Schweitzer, A., Shulyak, D., et al. 2019, Astronomy and Astrophysics, 627, A161 97, 132, 133

Penev, K., Jackson, B., Spada, F., & Thom, N. 2012, The Astrophysical Journal, 751, 96 84

Penev, K., Hartman, J. D., Bakos, G. Á., et al. 2016, The Astronomical Journal, 152, 127 84

Pepe, F. A., Cristiani, S., Rebolo Lopez, R., et al. 2010, 7735, 77350F, conference Name: Ground-based and Airborne Instrumentation for Astronomy III 17

Perger, M., Scandariato, G., Ribas, I., et al. 2019, Astronomy and Astrophysics, 624, A123 93

Perryman, M. 2018, The Exoplanet Handbook by Michael Perryman, Cambridge University Press; Second Edition, 952 p., ISBN: 9781108419772 11, 12, 15, 16

Perryman, M. A. C., Brown, A. G. A., Lebreton, Y., et al. 1998, Astronomy and Astrophysics, 331, 81 97

Pettersen, B. R., Coleman, L. A., & Evans, D. S. 1984, ApJS, 54, 375 133

Pinamonti, M., Damasso, M., Marzari, F., et al. 2018, Astronomy and Astrophysics, 617, A104 93

Pollacco, D. L., Skillen, I., Collier Cameron, A., et al. 2006, PASP, 118, 1407 96

Porter, J., Yowell, E., & Smith, E. 1915, Publications of the Cincinnati Observatory, 18, 1 132

Powell, M. J. D. 1964, The Computer Journal, 7, 155 35

Queloz, D. 1995, 167, 221, conference Name: New Developments in Array Technology and Applications 17

Queloz, D., Mayor, M., Udry, S., et al. 2001a, The Messenger, 105, 1 144

Queloz, D., Henry, G. W., Sivan, J. P., et al. 2001b, Astronomy and Astrophysics, 379, 279 20, 22

Quirrenbach, A., Amado, P. J., Mandel, H., et al. 2010, 7735, 773513, conference Name: Ground-based and Airborne Instrumentation for Astronomy III 23, 24

Quirrenbach, A., Amado, P. J., Caballero, J. A., et al. 2014, 9147, 91471F, conference Name: Ground-based and Airborne Instrumentation for Astronomy V 23, 24, 96, 138

Quirrenbach, A., Amado, P. J., Ribas, I., et al. 2018, 0702, 107020W, conference Name: Ground-based and Airborne Instrumentation for Astronomy VII ISBN: 9781510619579 23, 96, 138

Raghavan, D., McAlister, H. A., Henry, T. J., et al. 2010, The Astrophysical Journal Supplement Series, 190, 1 93, 163

Rajpaul, V., Aigrain, S., Osborne, M. A., Reece, S., & Roberts, S. 2015, Monthly Notices of the Royal Astronomical Society, 452, 2269 22, 40, 130, 152

Rasio, F. A., & Ford, E. B. 1996, Science, 274, 954 28

Rasmussen, C. E., & Williams, C. K. I. 2006, Gaussian Processes for Machine Learning (MIT Press) 40

Rauer, H., Gebauer, S., Paris, P. V., et al. 2011, Astronomy and Astrophysics, 529, A8 130

Reichert, K., Reffert, S., Stock, S., Trifonov, T., & Quirrenbach, A. 2019, Astronomy and Astrophysics, 625, A22 20, 145

Reiners, A., Bean, J. L., Huber, K. F., et al. 2010, The Astrophysical Journal, 710, 432 22, 60, 130, 142, 143, 152, 153, 163

Reiners, A., Shulyak, D., Anglada-Escudé, G., et al. 2013, A&A, 552, A103 144, 152

Reiners, A., Zechmeister, M., Caballero, J. A., et al. 2018, Astronomy and Astrophysics, 612, A49 23, 97, 133, 135

Reuyl, D. 1943, The Astrophysical Journal, 97, 186 134

Ribas, I., Tuomi, M., Reiners, A., et al. 2018, Nature, 563, 365 23

Ricker, G. R., Winn, J. N., Vanderspek, R., et al. 2015, Journal of Astronomical Telescopes, Instruments, and Systems, 1, 014003 13, 63, 92

Robertson, P., Bender, C., Mahadevan, S., Roy, A., & Ramsey, L. W. 2016, ApJ, 832, 112 144

Robertson, P., Roy, A., & Mahadevan, S. 2015, ApJ, 805, L22 144

Robertson, P., Stefansson, G., Mahadevan, S., et al. 2020, The Astrophysical Journal, 897, 125 130, 131, 140, 152, 163

Robinson, R. D., Slee, O. B., & Little, A. G. 1976, ApJ, 203, L91 133

Roell, T., Neuhäuser, R., Seifahrt, A., & Mugrauer, M. 2012, Astronomy and Astrophysics, 542, A92 115

Rogers, L. A. 2015, The Astrophysical Journal, 801, 41 92

Rogers, L. A., Bodenheimer, P., Lissauer, J. J., & Seager, S. 2011, The Astrophysical Journal, 738, 59 92

Rogers, L. A., & Seager, S. 2010, The Astrophysical Journal, 712, 974 15, 28, 92

Rojas-Ayala, B., Covey, K. R., Muirhead, P. S., & Lloyd, J. P. 2012, ApJ, 748, 93 133

Rosich, A., Herrero, E., Mallonn, M., et al. 2020, arXiv e-prints, arXiv:2007.00573 153

Rossiter, R. A. 1924, The Astrophysical Journal, 60, doi:10.1086/142825 15, 114

Saar, S. H., & Linsky, J. L. 1985, The Astrophysical Journal Letters, 299, L47 133

Sandford, E., Espinoza, N., Brahm, R., & Jordán, A. 2019, Monthly Notices of the Royal Astronomical Society, 489, 3149 55

Santerne, A., Díaz, R. F., Moutou, C., et al. 2012, Astronomy and Astrophysics, 545, A76 14

Sarkis, P., Henning, T., Kürster, M., et al. 2018, AJ, 155, 257 142

Scargle, J. D. 1982, The Astrophysical Journal, 263, 835 48

Schlecker, M., Mordasini, C., Emsenhuber, A., et al. 2020a, A&A, doi:10.1051/0004-6361/202038554, publisher: EDP Sciences 25

Schlecker, M., Kossakowski, D., Brahm, R., et al. 2020b, The Astronomical Journal, 160, 275 28, 47, 52, 119

Schöfer, P., Jeffers, S. V., Reiners, A., et al. 2019, Astronomy and Astrophysics, 623, A44 21, 24, 97, 101, 130, 132, 142, 149

Schweitzer, A., Passegger, V. M., Cifuentes, C., et al. 2019, Astronomy and Astrophysics, 625, A68 97, 133

Seager, S., & Mallén-Ornelas, G. 2003, The Astrophysical Journal, 585, 1038 11, 53, 55

Sestovic, M., Demory, B.-O., & Queloz, D. 2018, Astronomy and Astrophysics, 616, A76 64, 84

Shappee, B. J., Prieto, J. L., Grupe, D., et al. 2014, The Astrophysical Journal, 788, 48 96

Shkolnik, E., Liu, M. C., & Reid, I. N. 2009, ApJ, 699, 649 133

Shporer, A. 2017, Publications of the Astronomical Society of the Pacific, 129, 072001 82

Simpson, D., Rue, H., Riebler, A., Martins, T. G., & Sørbye, S. H. 2017, Statistical Science, 32, 1, publisher: Institute of Mathematical Statistics 36

Skilling, J. 2004, 735, 395, conference Name: Bayesian Inference and Maximum Entropy Methods in Science and Engineering: 24th International Workshop on Bayesian Inference and Maximum Entropy Methods in Science and Engineering 33, 35, 38, 39

Smith, J. C., Stumpe, M. C., Van Cleve, J. E., et al. 2012, Publications of the Astronomical Society of the Pacific, 124, 1000 13, 94

Sozzetti, A., Torres, G., Charbonneau, D., et al. 2007, The Astrophysical Journal, 664, 1190 12, 55

Speagle, J. S. 2020, Monthly Notices of the Royal Astronomical Society, 493, 3132 38, 40, 50, 104, 145

Speagle, J. S., & Barbary, K. 2018, Astrophysics Source Code Library, ascl:1809.013 50, 104, 145

Stassun, K. G., Oelkers, R. J., Pepper, J., et al. 2018, The Astronomical Journal, 156, 102 13, 74, 98

Stefansson, G., Mahadevan, S., Maney, M., et al. 2020, The Astronomical Journal, 160, 192 114

Stephenson, C. B. 1986, AJ, 92, 139 133

Stock, S. 2021, PhD Thesis, Ruperto-Carola-University of Heidelberg 22, 58

Stock, S., & Kemmer, J. 2020, The Journal of Open Source Software, 5, 1771 50, 105, 141

Stock, S., Kemmer, J., Reffert, S., et al. 2020a, Astronomy and Astrophysics, 636, A119 19, 50, 105, 106, 130, 141

Stock, S., Nagel, E., Kemmer, J., et al. 2020b, Astronomy and Astrophysics, 643, A112 93

Stumpe, M. C., Smith, J. C., Catanzarite, J. H., et al. 2014, Publications of the Astronomical Society of the Pacific, 126, 100 13, 94

Stumpe, M. C., Smith, J. C., Van Cleve, J. E., et al. 2012, Publications of the Astronomical Society of the Pacific, 124, 985 13, 94

Sullivan, P. W., Winn, J. N., Berta-Thompson, Z. K., et al. 2015, The Astrophysical Journal, 809, 77 14

Tal-Or, L., Trifonov, T., Zucker, S., Mazeh, T., & Zechmeister, M. 2019, Monthly Notices of the Royal Astronomical Society, 484, L8 133, 138, 139, 158

Tal-Or, L., Zechmeister, M., Reiners, A., et al. 2018, Astronomy and Astrophysics, 614, A122 6, 22, 142, 160

Teitler, S., & Königl, A. 2014, The Astrophysical Journal, 786, 139 131

Teske, J., Wang, S. X., Wolfgang, A., et al. 2020, arXiv:2011.11560 [astro-ph], arXiv: 2011.11560 19

Thorngren, D. P., & Fortney, J. J. 2018a, The Astronomical Journal, 155, 214 64

—. 2018b, The Astronomical Journal, 155, 214 162

Tofflemire, B. M., Wisniewski, J. P., Kowalski, A. F., et al. 2012, The Astronomical Journal, 143, 12 130

Torres, G., Winn, J. N., & Holman, M. J. 2008, The Astrophysical Journal, 677, 1324 18, 164

Triaud, A. H. M. J. 2018, Handbook of Exoplanets, 2 28, 86

Trifonov, T. 2019, Astrophysics Source Code Library, ascl:1906.004 47, 105

Trifonov, T., Tal-Or, L., Zechmeister, M., et al. 2020, Astronomy and Astrophysics, 636, A74 24, 96, 138, 157

Trifonov, T., Kürster, M., Zechmeister, M., et al. 2017, Astronomy and Astrophysics, 602, L8 19

—. 2018, Astronomy and Astrophysics, 609, A117 93

Trifonov, T., Caballero, J. A., Morales, J. C., et al. 2021, arXiv e-prints, 2103, arXiv:2103.04950 24, 115

Trotta, R. 2008, Contemporary Physics, 49, 71 35, 36, 38, 104, 145

Tuomi, M., Jones, H. R. A., Barnes, J. R., et al. 2018, The Astronomical Journal, 155, 192 21, 130, 134, 163

Udry, S., & Mayor, M. 2008, 398, 13, conference Name: Extreme Solar Systems 20

Valsecchi, F., & Rasio, F. A. 2014, ApJ, 786, 102, publisher: IOP Publishing 28, 162

van de Kamp, P., & Lippincott, S. L. 1949, The Astronomical Journal, 55, doi:10.1086/106323 134

Van Eylen, V., Agentoft, C., Lundkvist, M. S., et al. 2018, Monthly Notices of the Royal Astronomical Society, 479, 4786 92

Van Eylen, V., & Albrecht, S. 2015, The Astrophysical Journal, 808, 126 55

Van Eylen, V., Astudillo-Defru, N., Bonfils, X., et al. 2021, arXiv e-prints, 2101, arXiv:2101.01593 92, 114, 117

van Leeuwen, F. 2007, Astronomy and Astrophysics, 474, 653 134

Vidotto, A. A., Jardine, M., Morin, J., et al. 2013, Astronomy and Astrophysics, 557, A67 130

Vogt, S. S., Allen, S. L., Bigelow, B. C., et al. 1994, 2198, 362, conference Name: Instrumentation in Astronomy VIII 138

Wakeford, H. R., Wilson, T. J., Stevenson, K. B., & Lewis, N. K. 2019, Research Notes of the AAS, 3, 7 85

Walkowicz, L. M., & Basri, G. S. 2013, Monthly Notices of the Royal Astronomical Society, 436, 1883 131

Wang, J., Fischer, D. A., Xie, J.-W., & Ciardi, D. R. 2014, The Astrophysical Journal, 791, 111 93

Wang, S., Jones, M., Shporer, A., et al. 2019, The Astronomical Journal, 157, 51 64

Weiss, L. M., Isaacson, H. T., Marcy, G. W., et al. 2018, AJ, 156, 254 25

Wilson, J., Gibson, N. P., Lothringer, J. D., et al. 2021, Monthly Notices of the Royal Astronomical Society, 503, 4787 115

Winn, J. N. 2010, arXiv e-prints, 1001, arXiv:1001.2010 11, 59

Winn, J. N., Fabrycky, D., Albrecht, S., & Johnson, J. A. 2010, The Astrophysical Journal Letters, 718, L145 28, 114, 162

Winters, J. G., Henry, T. J., Lurie, J. C., et al. 2015, The Astronomical Journal, 149, 5 92, 130

Winters, J. G., Henry, T. J., Jao, W.-C., et al. 2019, The Astronomical Journal, 157, 216 93

Wise, A. W., Dodson-Robinson, S. E., Bevenour, K., & Provini, A. 2018, The Astronomical Journal, 156, 180 21

Wright, J. T. 2005, Publications of the Astronomical Society of the Pacific, 117, 657 51

Wright, J. T., & Howard, A. W. 2009, The Astrophysical Journal Supplement Series, 182, 205 18

Wright, J. T., Marcy, G. W., Howard, A. W., et al. 2012, The Astrophysical Journal, 753, 160 28

Yi, S., Demarque, P., Kim, Y.-C., et al. 2001, The Astrophysical Journal Supplement Series, 136, 417 73, 74

Zacharias, N., Finch, C. T., Girard, T. M., et al. 2013, The Astronomical Journal, 145, 44 98, 100

Zechmeister, M., & Kürster, M. 2009, Astronomy and Astrophysics, 496, 577 48, 79, 105, 135

Zechmeister, M., Reiners, A., Amado, P. J., et al. 2018, Astronomy and Astrophysics, 609, A12 17, 22, 24, 96, 138, 142, 144, 157

Zechmeister, M., Dreizler, S., Ribas, I., et al. 2019, Astronomy and Astrophysics, 627, A49 23

Zellem, R. T., Swain, M. R., Roudier, G., et al. 2017, The Astrophysical Journal, 844, 27 85

Zellem, R. T., Fortney, J. J., Swain, M. R., et al. 2018, arXiv e-prints, 1803, arXiv:1803.07163 85

Zeng, L., Jacobsen, S. B., Sasselov, D. D., et al. 2019, Proceedings of the National Academy of Science, 116, 9723 114, 117, 163

Zucker, S. 2018, Monthly Notices of the Royal Astronomical Society, 474, L86 48

Zucker, S., & Mazeh, T. 1994, The Astrophysical Journal, 420, 806 140

Acknowledgements

"*Are you going to sit there like an idiot doing nothing or are you going to shoot for the stars?*"
Space Force

As cliche as it is and this is how everyone starts it...
It all began with a school field trip to the Lawrence Hall of Science in Berkeley. I will never forget that feeling and the rush of stars flying by me in the planetarium. (Also I tried strawberry flavored astronaut ice cream for the first time and I was sold). It was from that moment that I wanted to dig deeper into this grand astronomical world. Casual at first, I was just taking the right classes and then things got serious when I chose to study Astrophysics for my Bachelor's. I was considering not to but something in my gut told me to.

And now here I am.

I would first like to thank my thesis committee composed of Martin Kürster, Thomas Henning, and Sabine Reffert for making my PhD studies even possible to begin with.

Martin, you were very approachable and I was comfortable that I felt I could ask any question I ever wanted and not once did you judge. You believed in my work and ability which I truly appreciate. And when our philosophical talks came, you were the one to always remind why we chose our job: because it's fun. Not only were you supportive in my academic journey but also in my personal life. Your light humor and easy going approach to life resonated with mine. I feel lucky to have had you as my "Doktorvater".

Thomas, your words of encouragement were greatly appreciated and kept me going even when my motivation was temporarily suppressed. Overall, I admire the enthusiasm and dedication you have for the department and I hope you are proud of the environment you built and foster within the PSF department.

Thank you Sabine for your insightful feedback during the CARMENES Königsstuhl meetings. The scientific discussions we had would always get me thinking.

Many thanks to Dr. Trifon Trifonov. You were always so willing to take time out of your busy schedule and help whenever I had any questions, always responding to emails no matter the hour. Also, I am forever grateful to have the opportunity to experience an observing run with the HARPS instrument in La Silla, Chile. It gave me the chance to remind myself just how fascinating our job is.

Thank you Dr. Néstor Espinoza (a.k.a. compañero) for being the Chilean addicted to coke (Coca Cola). You enthusiasm was contagious and motivational, I enjoyed working with you. Heidelberg lost a good one but now you're taking Charm City by storm!

An overall thank you to the CARMENES consortium, specifically Jonas K., Stephan S., Paz B., Marcelo P., Sepideh S., Paula S., and also the others not part of the Heidelberg crew. It was a pleasure to be working with so many PhD students, helping each other out and carrying on fruitful scientific discussions. Special thanks to Jonas K. for very frequent insightful conversations and for providing very valuable feedback for my work in general and in this thesis (both for the writing and help with the German abstract). Likewise, thank you Stephan S., Paula S., and Martin S. for taking the time to look over my thesis and provide feedback. Also gracias to Dr. José Caballero for squeezing in time, being available, providing great insight, and answering (the most random) questions to help me progress. Thank you Paula S. for always smiling and lightening my day. You supported me no matter what and I had a blast supporting you too, huge congrats on your new opportunity. Thank you Herr Doktor Marcelo P. for being someone to count on, both academically and personally, and being the guy that is from 'Mexico' (referring to your Chicago trip). Thank you to Faustine C. for being a relatable "2" and for caring about the environment the way you do. Thank you to my IMPRS generation ("is that Ben?" - Amsterdam 2018). Special thanks to Martin S. for being such a great co-representative for our IMPRS generation (DM forever) and a great office mate who endured my strange German (was geht ab Diggaaa?). To the Nov 1 group, Giada P., Ben A., and Giulia M., you know what's up - glad we continue to entertain ourselves with all of our interesting stories. There are countless others that have made my experience enjoyable at MPIA.

And now to those outside who have kept me sane and supported me through the journey. Thank you Giulia M., my "Schatzi", whether it's Chloe Ting, Foodspring protein pancakes, or getting tiramisu almost for free, you always make me laugh and I consider Torino my (Italian) home away from home. Thank you Federica F. for being the go-to person for deep-talk walks. Thank you to the amaaazing Riccardo D.B., Carlo A., and Giada P. for making our times not bad. And just an overall thank you to the Italians for inspiring me to take Italian classes in Germany ("hai una barca?"). Thank you Sarah E. for being just as crazy as I am (or even more!), that it makes me feel more sane. What's life without adventure? Thank you to my loving and supporting boyfriend, Denis H. I honestly don't know how I could've finished this thesis during COVID without you. Somehow you found the patience and ability to handle my personalit(ies), and I'm shocked it didn't scare you off (yet). Jetzt kann ich berechtigterweise sagen, ich bin fertig :P

Of course, those back home, my best friend Laura H. (Lil L) - if the Oktoberfest wasn't enough to convince you to move to Germany then I don't know what would be; my Schwester Ania K. - they say you can't pick family though you can pick your friends, but with you, you're the unsolicited, chosen best friend (for life) and I can't complain; my parents - grateful that you guys support me no matter what I choose to do, I'll always be your little Myszka; and those abroad, Ditte L.P. - it's incredible how we are just on the same wavelength, thanks for always listening; Shaarroooonnn N. - knowledge IS power.

To finish, it's just amazing how grand the butterfly effect can be: I was just a kid sitting in a planetarium and little did I know that I'd be getting my PhD in Astronomy years down

the line. My only hope is that I can inspire others just like I was guided to where I am now.

Overall, astronomy has taught me that we often forget the bigger picture and get frustrated on the little details. But we need to remember to take life light, because, as the infamous song by Linkin Park played constantly in O'reilys put it,

"in the end, it doesn't even matter"

Declaration of Originality

Declaration of Originality

I hereby declare that this thesis is my own work and that I have used no other than the stated sources and aids.

Declaration

Ich versichere, dass ich diese Arbeit selbstständig verfasst habe und keine anderen als die angegebenen Quellen und Hilfsmittel benutzt habe.

Heidelberg, der 26. April 2021

(Diana Kossakowska)